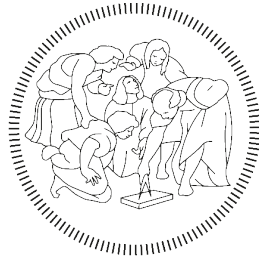


Self-organization and pattern formation in soft matter



POLITECNICO
MILANO 1863

CANDIDATE: Giulia Bevilacqua

ADVISOR:
Prof. Pasquale Ciarletta

CHAIR OF THE DOCTORAL PROGRAM:
Prof.ssa Irene Sabadini

Doctoral programme in
Mathematical Models
and Methods in Engineering

2020 - Cycle XXXIII

ABSTRACT

This thesis deals with the formulation and analysis of mathematical models for soft biological matter. More precisely, it focuses on two main aspects: self-organization and pattern formation.

Self-organization is a well-studied phenomenon in different forms. In this thesis, we characterize this aspect studying the equilibrium configurations of an agglomerate of soap bubbles to mimic the phenomenon of the cell mitosis in the embryo as well as extending recent results of so-called Kirchhoff-Plateau problem, in which the fixed boundary is replaced by an elastic rod and it represents a prototype of a membrane problem.

Pattern formation characterizes many aspects in nature: in this thesis we focus on describing growth and remodeling in living matter. First, we study the gyrification process, *i.e.* the formation of folded structures in brain organoids equipping a nonlinear elastic model with tissue surface tension and thanks to the competition between the elastic energy and the surface one, we correctly capture the experimental behavior of brain organoids.

Second, we deal with the c -looping process in the heart tube, which is the first-symmetry breaking in cardiac embryogenesis and we show that a torsional internal remodeling alone can drive the spontaneous onset and the fully nonlinear development of the c -looping within its physiological range of geometrical parameters. Third, we characterize the onset of Faraday waves in soft elastic solids proving that standing waves at the free surface can appear also in soft matter. Remarkably, we find that Faraday instability in soft slabs is characterized by a harmonic resonance in the physical range of the material parameters, and, thanks to a collaboration with the Mechanical Department at the Clemson University, we are able to develop an experimental procedure to distinguish solid-like from fluid-like responses of soft matter. Finally, we propose a mathematical description of cancer development involving the growth process of fluid-like tumor cells surrounded by a porous medium. We include an additional source term to the classical porous-media equation to model the cell division rate. In order to introduce a free-boundary model, which gives more realistic description of tumor growth, we extend the Aronson-Bénilan estimate on second order derivatives for the solution of the porous media equation for different fields of pressure and in all Lebesgue spaces.

RIASSUNTO

Questa tesi si occupa della formulazione e dell'analisi di modelli matematici per la materia biologica. Più precisamente, si concentra su due suoi aspetti principali: auto-organizzazione e formazione di pattern.

L'auto-organizzazione è un fenomeno ben studiato in diverse sue forme. In questa tesi, caratterizziamo questo aspetto studiando le configurazioni di equilibrio di un agglomerato di bolle di sapone per imitare il fenomeno della mitosi cellulare nell'embrione nonché estendendo recenti risultati del cosiddetto problema di Kirchhoff-Plateau, in cui il bordo fisso è sostituito da una trave elastica e rappresenta un prototipo per la rappresentazione di membrane.

La formazione di pattern caratterizza molti aspetti della natura: in questa tesi ci concentriamo sulla descrizione dei fenomeni di crescita e di rimodellamento nella materia vivente. Per prima cosa studiamo il processo di girificazione, cioè la formazione delle cosiddette rughe cerebrali negli organoidi aggiungendo ad un modello elastico non lineare la componente della tensione superficiale, e in questo modo, grazie alla competizione tra l'energia elastica e quella di superficie, rappresentiamo in maniera corretta il comportamento sperimentale degli organoidi. In secondo luogo, ci occupiamo del processo di c -looping nel tubo cardiaco, che rappresenta la prima rottura di simmetria nell'embriogenesi cardiaca e mostriamo che un rimodellamento interno da solo può guidare l'insorgenza spontanea e lo sviluppo non lineare del c -looping nell'intervallo fisiologico dei parametri geometrici. In terzo luogo, caratterizziamo lo sviluppo delle onde di Faraday nei solidi elastici soffici dimostrando che le onde stazionarie sulla superficie libera possono presentarsi anche in tali materiali. In più, troviamo che l'instabilità di Faraday nei solidi soffici è caratterizzata da una risonanza di tipo armonico e, grazie alla collaborazione con il Dipartimento di Meccanica della Clemson University, siamo in grado di sviluppare una robusta procedura sperimentale per distinguere una risposta di un solido da quella di un fluido viscoso. Infine, proponiamo una descrizione matematica dello sviluppo del cancro che coinvolge il processo di crescita di cellule tumorali modellizzate come fluidi che evolvono in un mezzo poroso ed includiamo un termine sorgente aggiuntivo alla classica equazione dei mezzi porosi per descrivere il tasso di divisione cellulare. Al fine di introdurre un modello che caratterizza il moto del bordo del tumore e che è di fatto una descrizione più realistica della crescita tumorale, estendiamo la stima di Aronson-Bénilan sulle derivate parziali del secondo ordine per la soluzione dell'equazione dei mezzi porosi, ottenendola per diversi campi di pressione e in tutti gli spazi di Lebesgue.

Contents

1	INTRODUCTION	1
1.1	Technical preliminaries for self-organization	4
1.1.1	Brief notions of Calculus of Variations	4
1.1.1.1	The Direct Methods of Calculus of Variations	6
1.1.1.2	Other strategies	11
1.2	Technical preliminaries for pattern formation	12
1.2.1	Brief notions of nonlinear elasticity	12
1.2.1.1	Hyperelasticity	13
1.2.2	Active processes	15
1.2.2.1	Morphoelasticity	16
1.2.2.2	Porous-Media Equation (PME)	19
2	SELF-ORGANIZATION OF SOFT MATTER	25
2.1	Symmetry break in the eight bubble compaction	28
2.1.1	Geometrical principle	30
2.1.1.1	Spatial arrangement	30
2.1.1.2	Coordinates	33
2.1.1.3	“bubble compaction”: tiling the central sphere	34
2.1.1.4	Geometrical optimality	36
2.1.1.5	Surfaces, edges and vertices	38
2.1.2	Mechanical balance	40
2.1.2.1	Tensional balance	40
2.1.2.2	Volume conservation	42
2.1.2.3	Results	43
2.1.3	Final remarks	44
2.2	The Kirchhoff-Plateau problem	46
2.2.1	Historical view on the Kirchhoff-Plateau Problem	46
2.2.2	Soap film spanning an elastic link	49
2.2.2.1	Formulation of the problem	52
2.2.2.2	Main results	64
2.2.2.3	Some simple experiments	72
2.2.3	Soap film spanning electrically repulsive elastic protein links	73
2.2.3.1	Formulation of the problem and main result	75

2.2.4	Dimensional reduction of the Kirchhoff-Plateau Problem	77
2.2.4.1	Physical motivation	79
2.2.4.2	Mathematical preliminaries	83
2.2.4.3	Setting of the problem and main result	85
2.2.4.4	Proof of the convergence result	91
A	APPENDIX TO CHAPTER 2	96
A.1	Dual tessellation of the central bubble	96
A.2	Polyedra with seven faces	97
A.3	Calculation of volumes	98
A.4	Equations of balance of tensions	104
3	PATTERN FORMATION IN SOFT MATTER	109
3.1	Surface tension controls the onset of gyrification in brain organoids	113
3.1.1	Intercellular adhesion generates surface tension in cellular aggregates	116
3.1.1.1	Estimation of the surface tension	117
3.1.2	Elastic model of brain organoids	119
3.1.2.1	Kinematics	119
3.1.2.2	Mechanical constitutive assumptions and force balance equations	121
3.1.2.3	Equilibrium radially-symmetric solution	123
3.1.3	Linear stability analysis	127
3.1.3.1	Incremental equations	127
3.1.3.2	Stroh formulation	128
3.1.3.3	Incremental solution for the lumen	130
3.1.3.4	Numerical procedure for the solution in the cortex	131
3.1.3.5	Discussion of the results	134
3.1.4	Post-buckling analysis	139
3.1.4.1	Description of the numerical method	139
3.1.4.2	Results of the finite element simulations	142
3.1.5	Discussion and concluding remarks	146
3.2	Morphomechanical model of the torsional c-looping in the embryonic heart	149
3.2.1	Mathematical model	152
3.2.1.1	Kinematics	152
3.2.1.2	Boundary-Value Problem (BVP)	154
3.2.1.3	Radially-symmetric solution	155
3.2.2	Linear stability analysis	158
3.2.2.1	Incremental BVP	159
3.2.2.2	Stroh formulation	160
3.2.2.3	Impedance matrix method	163
3.2.2.4	Marginal stability thresholds	165
3.2.3	Numerical simulations	169

3.2.3.1	Simulation results	171
3.2.4	Conclusions	179
3.3	Faraday waves in soft elastic solids	181
3.3.1	Experimental investigation of Faraday waves in soft materials	183
3.3.2	The nonlinear elastic problem and its ground state	185
3.3.3	Incremental equations	188
3.3.3.1	Subharmonic resonance	191
3.3.3.2	Harmonic resonance	195
3.3.4	Marginal stability analysis	199
3.3.4.1	Dimensionless parameters	199
3.3.4.2	Marginal stability thresholds	200
3.3.4.3	Asymptotic limit of Rayleigh-Taylor instability	206
3.3.5	Conclusions	207
3.4	Porous Media model of tissue growth: analytical estimates in the free bound- ary limit	209
3.4.1	The Aronson-Bénilan estimate and regularity theory of the PME	210
3.4.2	Population-based description of tissue growth	211
3.4.2.1	Free Boundary-based Description of Tissue Growth	213
3.4.3	Extension to two species	214
3.4.4	L^1 -type estimate	216
3.4.4.1	L^1 -Estimates when $G \equiv 0$	216
3.4.4.2	L^1 -estimates with $G \neq 0$	219
3.4.5	L^∞ -type Estimate	222
3.4.5.1	L^∞ -estimates when $G \equiv 0$	223
3.4.5.2	L^∞ -estimates when $G \neq 0$	229
3.4.6	L^2 -type estimate	230
3.4.6.1	L^2 -estimates when $G \equiv 0$. No weight.	231
3.4.6.2	L^2 -estimates when $G \equiv 0$. With weights.	232
3.4.6.3	L^2 -estimates when $G \neq 0$. With weights	235
3.4.7	Conclusions	238
B	APPENDIX TO CHAPTER 3	240
B.1	Computation of the incremental curvature	240
B.2	Role of the Matrigel embedment	241
B.3	Expressions of $\zeta_n, \tau_n, \sigma_n$	243
B.4	Expressions of Z_n, T_n, Σ_n	243
4	CONCLUSION AND PERSPECTIVES	245
	REFERENCES	276

Listing of figures

1.1	Scheme of the basic and perturbed variables. In the reference state, \mathbf{X} is the reference position vector, the tensor \mathbf{G} takes into account growth/remodeling, while F_e describes the elastic distortion. In the actual configuration, \mathbf{x} is the base solution and \mathbf{F} the deformation gradient. Finally, in the perturbed setting, $\bar{\mathbf{x}}$ is the perturbed position vector and $\bar{\mathbf{F}}$ the perturbed deformation gradient. . . .	17
2.1	(a) Top and (b) side view of the position and connections of the seven points on the spherical surface of the central bubble. The blue connections are the arcs of length a defined by Tammes' construction.	31
2.2	Stereographic (a) and spherical (b) projections of the Tammes' points on the spherical surface and their connecting arcs. Grey and thin lines, corresponding to arcs of length $1.34 a$, make the tessellation fully triangular.	32
2.3	Geometrical sketch of the latitude of the points A , B and C : the central angle β , the radius r of the sphere and the radius r_ϕ of the circumference laying in the plane defined by the triplet of points.	32
2.4	(a) Initial arrangement of the bubbles before compaction. Tangent points are denoted by a blue dot, red dots denote the center of each sphere. (b) Sketch of the "compaction process" between two bubbles driven by the parameter δ . . .	34
2.5	(a) Bottom view of the construction of the tessellation. (b) Top view of the construction of the tessellation.	35
2.6	(a) Sketch of four independent nodes V_1 , V_2 , V_3 and V_4 on the tessellation, highlighting the corresponding symmetry group. (b) Stereographic projection of the dual tassellation.	36
2.7	(a) Balance of tensions on an edge. (b) The bubble volume is the sum of a pyramidal frustum (with pink side boundaries) plus the polygonal-basis vault standing on it (light pink).	41
2.8	Compactification of peripheral bubbles around (a) the triangle, (b) a quadrilateral and (c) a pentagon. The corresponding peripheral bubble is removed for the sake of graphical representation. The yellow segment represents the radial height h of the intersection surface among three adjacent bubbles	42
2.9	Geometry of the problem.	50
2.10	γ_i ($i = 1, 2$) are simple links for H_i while $\gamma_3 \in F(\Lambda[\mathbf{w}])$. Even if K is not D -spanning for the whole system, notice how $\gamma_1 \cap K \neq \emptyset$	62

2.11	Results obtained by our configuration with two fixed linked rigid metallic wires.	73
2.12	Results obtained by our configuration with the mobile component.	74
2.13	A schematic representation of a knotted protein linked to another one.	74
2.14	Geometry of the problem.	75
2.15	A possible choice of h	76
A.1	Bottom view of the dual tessellation. The dashed lines represent the chord ℓ of the Tammes' construction. The centroid of the triangle A, B, C is the South Pole, called V_1 in the dual tessellation.	97
A.2	Different views of the tessellation: (a) top, (b) bottom and (c) side view. Black dots indicate the Tammes' points. Irrespective of the graphic illusion, the corners of the inscribed polyhedron are on the spherical surface; after restoring of the initial volume, they will be external. Yellow lines underline the sides of the different obtained polygons: (a) a triangle, (b) three quadrilaterals and (c) three pentagons.	97
A.3	Graphical representation, obtained through the software Plantri, of the five convex polygons among the 34 inscribed into a sphere which satisfy the first optimal criterium Eq. (2.7). The Tammes' dual tessellation is one of them, <i>i.e.</i> the last one.	98
A.4	In the plane passing through the projected Tammes points \tilde{D} , \tilde{E} and the origin O , the points C_D and C_E are the centres of the spheres of radius R_P , that eventually define the free surface of the bubble. The side of the pyramidal frustum is h_2	100
A.5	Geometrical representation of the lateral cut of the spherical cap.	103
A.6	Geometrical sketch of the rotation around the axis x by the angle ϕ_{pqr} . The coordinates ρ , θ and ϕ are the spherical ones set into a Cartesian frame of reference (x, y, z)	104
3.1	Cells in the bulk (left) and on the free surface (right) of a cellular lattice. Adhesion forces generated by the surrounding cells are denoted by the red arrows. The sum of all these forces on an internal cell is zero, while it is non-zero and perpendicular to the boundary for a cell on the free surface.	115
3.2	Plot of the marginal stability threshold g_{cr} and of the critical mode m_{cr} versus α_γ for (a) $\alpha_R = 0.9$ and (b) $\alpha_R = 0.95$	135
3.3	Plot of the critical value α_γ^{tr} at which the instability moves from the external surface to the interface versus α_R	136
3.4	Plot of the marginal stability threshold g_{cr} and of the critical mode m_{cr} versus α_R for (a) $\alpha_\gamma = 0$, (b) $\alpha_\gamma = 0.5$, (c) $\alpha_\gamma = 1$, (d) $\alpha_\gamma = 1.5$	138
3.5	Representation of the conformal mapping \mathbf{g} that maps the computational domain Ω_n to the reference configuration Ω_0	140
3.6	Mesh generated through GMSH for $\alpha_R = 0.9$. The maximum diameter of this mesh elements is 0.2488 while the minimum diameter is 0.0017.	141

3.7	Buckled configuration for (a) $\alpha_\gamma = 0$ and $g = 1.7556$ and (b) $\alpha_\gamma = 0.5$ and $g = 2.1646$	143
3.8	Bifurcation diagrams for (a) $\alpha_\gamma = 0$ and (b) $\alpha_\gamma = 0.5$. The orange square denotes the theoretical marginal stability threshold computed as exposed in Section 3.1.3. The good agreement between the linear stability analysis and the finite element code outcomes validates the numerical algorithm.	143
3.9	Plot of the ratio $E_{\text{num}}/E_{\text{th}}$ for (a) $\alpha_\gamma = 0$ and (b) $\alpha_\gamma = 0.5$. The orange square denotes the theoretical marginal stability threshold computed as exposed in Section 3.1.3.	144
3.10	Thickness of the cortex of ridges (blue) and furrows (green) for (a) $\alpha_\gamma = 0$ and (b) $\alpha_\gamma = 0.5$. The latter situation, in which the the thickness of ridges is higher than the one of furrows, corresponds to the “antiwrinkling” behavior described in [131].	145
3.11	Ventral views showing the positional and morphological changes of the embryonic heart tube between its first morphological appearance at Hamburger Hamilton (HH)-stage 10 [171] (A), the beginning of the c-looping, HH-stage 12/13 [171] (C), the end of the phase of dextral-looping at HH-stage 13 [171] and the transformation from the c-shaped loop into the s-shaped one (D)-(F). [c], primitive conus; [v], primitive ventricular bend; [a], primitive atria. Scale bar $100\mu\text{m}$. Figures adapted from [221].	151
3.12	Plot of (a) the axial force F_z and (b) the torque M versus the torsion rate γ fixing the external radius $R_o = 1$, the shear modulus $\mu = 1$, computing r_i through Eq. (3.64) and varying the ratio between the external and the internal radii within the range $\frac{R_o}{R_i} \in (1, 10)$	158
3.13	Plot of the critical values versus α_R , varying the initial thickness ratio $\alpha_R \in (1, 10)$. (a) Plot of the circumferential critical wavenumber m_{cr} versus α_R . Varying $\alpha_R \in (1, 2)$ and $\alpha_L = +\infty$, (b) plot of the critical axial wavenumber \tilde{k}_{cr} and (c) of the marginal stability threshold $\tilde{\gamma}_{\text{cr}}$ versus α_R . Varying $\alpha_R \in (2, 10)$, (d) plot of the critical circumferential wavenumber m_{cr} and (e) of the critical axial wavenumber \tilde{k}_{cr} versus α_R having chosen different values of $\alpha_L = \{4, 4.5, 5, 6, 7, 15, 30\}$	167
3.14	Plot of the marginal stability threshold $\tilde{\gamma}_{\text{cr}}$ versus α_R for thick cylinders, $\alpha_R \in (2, 10)$, varying $\alpha_L = \{14, 14.5, 15, 15.5, 16\}$. The inset shows a zoom of the curve with $\alpha_L = 14$	168
3.15	Plot of critical wavenumbers and the marginal stability threshold versus α_L , fixing the initial thickness ratio $\alpha_R = 2.85$. (a) The critical circumferential wavenumber is $m_{\text{cr}} = 1$. (b) The critical axial wavenumber \tilde{k}_{cr} and (c) of the marginal stability threshold $\tilde{\gamma}_{\text{cr}}$ decrease as α_L increases.	168
3.16	Mesh generated through MSHR for $\alpha_R = 2.85$ with local refinement.	169
3.17	Actual configuration of the buckled tube when $\alpha_R = 2.85$, $\alpha_L = 7$ and Eq. (3.91) is taken as the boundary condition at $z = 0, \alpha_L$. For such values, the linear stability analysis gives $\tilde{\gamma}_{\text{cr}} \simeq 0.881748$	172

3.18	(a) Plot of the different shapes of the mid-section $z = \alpha_L/2 = 3.5$ at different values of the torsion control parameter $\tilde{\gamma}$. The black dot is $O = (0, 0, \alpha_L/2)$, i.e. the centroid of the initial midsection of the original HT, while the red one is the centroid of the midsection in the current configuration. The shape of the section changes and the lumen is getting smaller causing the stop of the numerical simulation. (b) Bifurcation diagram where we show the dimensionless parameter $\Delta r/R_o$ defined in Eq. 3.93 versus the torsion control parameter $\tilde{\gamma}$ when $\alpha_R = 2.85$ and $\alpha_L = 7$. The numerical simulation is validated against the marginal stability threshold computed with the linear stability analysis (orange square, $\tilde{\gamma}_{cr} \simeq 0.881748$).	173
3.19	Plot of the bifurcation diagram varying the numbers of faces 30, 35, 40, 45, 50, 60, 70, 80 on the side of the cylinder [212]. In the inset, we highlight the behavior near the marginal stability threshold.	173
3.20	Actual configuration of the looped tube when $\alpha_R = 2.85$, $\alpha_L = 7$ and Eq. (3.92) is taken as boundary condition at $z = 0, \alpha_L$. In such conditions $\tilde{\gamma}_{cr} \simeq 0.881748$	174
3.21	Plot of the ratio E_{num}/E_{th} for (a) $\alpha_R = 2.85$ and Eq. (3.91) as boundary condition and (b) $\alpha_R = 2.85$ and (3.92) on the two bases versus the torsion control parameter $\tilde{\gamma}$. The orange square denotes the theoretical marginal stability threshold computed in Section 3.2.2.	175
3.22	Actual configuration of the buckled tube for when $\alpha_R = 2.85$ and $\alpha_L = 12$ and Eq. (3.91) is taken as BC. In such conditions $m_{cr} = 1$, $\tilde{k}_{cr} = 2\pi/\alpha_L$ and $\tilde{\gamma}_{cr} = 0.521594$	176
3.23	(a) Plot of the ratio E_{num}/E_{th} for $\alpha_R = 2.85$, $\alpha_L = 12$ and Eq. (3.91) is taken as boundary condition versus the torsion control parameter $\tilde{\gamma}$. (b) Bifurcation diagram where we show the dimensionless parameter $\Delta r/R_o$ versus the torsion control parameter $\tilde{\gamma}$ when $\alpha_R = 2.85$, $\alpha_L = 12$ and $z = \alpha_L/2 = 6$. The orange square denotes the theoretical marginal stability threshold computed in Section 3.2.2, i.e. $m_{cr} = 1$, $\tilde{k}_{cr} = 2\pi/\alpha_L$ and $\tilde{\gamma}_{cr} = 0.521594$	177
3.24	Actual configuration of the buckled tube when $\alpha_R = 1.35$, $\alpha_L = 7$ and Eq. (3.91) is taken as BC. In such conditions $m_{cr} = 2$, $\tilde{k}_{cr} = 2\pi/\alpha_L$ and $\tilde{\gamma}_{cr} \simeq 0.177001$	177
3.25	Actual configuration of the buckled tube for when $\alpha_R \rightarrow \infty$, $\alpha_L = 12$ and Eq. (3.91) is taken as BC. We choose $m_{cr} = 1$ and $\tilde{k}_{cr} = 2\pi/\alpha_L$	178
3.26	(a) Mesh generated through MSHR for $\alpha_R \rightarrow \infty$ with local refinements. (b) Bifurcation diagram showing the dimensionless parameter $\Delta r/R_o$ versus the torsion control parameter $\tilde{\gamma}$ when $\alpha_R \rightarrow \infty$, $\alpha_L = 12$ and $z = \alpha_L/2 = 6$. The orange square denotes the marginal stability threshold $\tilde{\gamma}_{cr} \simeq 0.8$ [164], with $m_{cr} = 1$ and $\tilde{k}_{cr} = 2\pi/\alpha_L$	179
3.27	Faraday waves in soft gels: (a) schematic of experimental setup, (b) typical wave pattern for a gel with shear modulus $\mu = 19\text{Pa}$ in a square container, as it depends upon driving frequency f , and (c) typical instability tongue plotting critical acceleration a against frequency f for a given mode in a circular container.	183

3.28	Sketch of the reference configuration of the model: L is the reference length of the elastic slab and H is its reference height. It is clamped to a rigid substrate and it is subjected to its own weight and to a vertical sinusoidal oscillation with amplitude a and frequency ω	186
3.29	Marginal stability curves showing the order parameter \tilde{a} versus the horizontal wavenumber \tilde{k} where we fix $\lambda_x = 1$, $\alpha_\gamma = 0$ and $\alpha_g = 0.1$. (a) $\alpha = 1/2$ and $\alpha_\omega = \{0.5, 1, 2, 2.5, 3, 3.1, \pi\}$; (b) $\alpha = 0$ and $\alpha_\omega = \{0.3, 0.6, 0.9, 1.3, 1.5, 1.56, \pi/2\}$. (c) Critical threshold \tilde{a}_{cr} versus α_ω fixing $\lambda_x = 1$, $\alpha_\gamma = 0$ and $\alpha_g = 0.1$: the blue line is the subharmonic case $\alpha = 1/2$ (SH), while the yellow one is the harmonic resonant mode $\alpha = 0$ (H).	201
3.30	Plot of the critical value \tilde{a}_{cr} and the critical wavenumber \tilde{k}_{cr} versus α_ω fixing $\lambda_x = 1$ and varying the physical quantities. (a) - (b) $\alpha_\gamma = 0$ and $\alpha_g = 0.001$, (c) $\alpha = 0$, $\alpha_\gamma = 0$ and $\alpha_g \in [1, 5]$ step 0.5 for graphical reasons, (d) $\alpha = 0$, $\alpha_\gamma = 0$ and $\alpha_g \in [0, 6.22]$ step 0.2, (e) - (f) $\alpha = 0$, $\alpha_g = 0.001$ and $\alpha_\gamma \in [0, 0.2]$ step 0.05. In (a) - (b), the yellow line is the harmonic solution while the blue one is the subharmonic one.	203
3.31	Plot of the critical values \tilde{a}_{cr} and the critical wavenumber \tilde{k}_{cr} versus α_ω fixing the first unstable resonant mode, <i>i.e.</i> $\alpha = 0$ and varying $\lambda_x \in [0.7, 1.4]$ step 0.1. (a) - (b) $\alpha_g = 0.001$, $\alpha_\gamma = 0$, (c) - (d) $\alpha_g = 0.1$, $\alpha_\gamma = 0$, (e) - (f) $\alpha_g = 0.001$, $\alpha_\gamma = 0.05$	204
3.32	Plot of the (a) critical values $(\alpha_g)^{\text{min}}$ and (b) $(\tilde{k}_{\text{cr}})^{\text{min}}$ versus λ_x in the limit of $\alpha_\omega \ll 1$ fixing $a = 0$ and $\alpha_\gamma = 0$	207
B.1	Marginal stability threshold g_{cr} (top) and critical wavenumber m_{cr} (bottom) versus α_γ for $\alpha_R = 0.9$ and $\alpha_k = 0, 0.5$	241

"PENSO CHE LA MATEMATICA SIA UNA DELLE MANIFESTAZIONI PIÙ SIGNIFICATIVE DELL'AMORE PER LA SAPIENZA E COME TALE LA MATEMATICA È CARATTERIZZATA DA UN LATO DA UNA GRANDE LIBERTÀ E DALL'ALTRO DA UNA INTUIZIONE CHE IL MONDO DICIAMO È GRANDISSIMO, È FATTO DI COSE VISIBILI E INVISIBILI, E LA MATEMATICA HA FORSE UNA CAPACITÀ UNICA TRA TUTTE LE SCIENZE DI PASSARE DALLA OSSERVAZIONE DELLE COSE VISIBILI ALL'IMMAGINAZIONE DELLE COSE INVISIBILI. QUESTO FORSE È IL SEGRETO DELLA FORZA DELLA MATEMATICA."

ENNIO DE GIORGI

Acknowledgments

In the first place, I would like to express my gratitude to my advisor Pasquale Ciarletta, for being a guide and a great font of mathematical inspiration. He taught me how mathematics can be extremely concrete and how it can be used to describe the surrounding reality, always supporting me and helping to overcome any difficulties encountered.

I wish to thank Davide Ambrosi for his contagious optimism, his endless patience and for giving me the opportunity to work together.

I would like to thank Benoît Perthame who kindly hosted me at *Laboratoire J.-Louis Lions* in Paris for six months and always encouraged my independence as a mathematician.

I also wish to thank Luca Lussardi and Alfredo Marzocchi, with whom I not only started a fruitful scientific collaboration but also an excellent human relationship, they were the first to believe in me and to introduce me into the fascinating world of research.

My deep gratitude goes to my coauthors, who have substantially contributed to the realization of part of this thesis: a big thanks to Davide Riccobelli and Markus Schmidtchen, who contributed to my mathematical growth with many stimulating discussions.

*Chi non conosce la matematica difficilmente
riesce a cogliere la bellezza, la più intima
bellezza, della natura.*

R.P. Feynman

1

Introduction

This thesis deals with the formulation and analysis of mathematical models for soft matter. More precisely, we focus on two main phenomena: self-organization and pattern formation.

The first one is a spontaneous process which gives a specific order to a disordered system thanks to the multiple interactions of particles or parts of the system and due to the presence of an external energy which drives the entire process. Examples can be found in different subjects, like in Physics [14], Chemistry [32] and Biology [76], but also in Economy [197], Sociology [311] and Technology [326]. For instance, we mention the protein

folding [2], which drives the system to equilibrium configuration, or the different shapes of liquid crystals [330], which strongly depend on the amount of available energy.

Pattern formation refers to the generation of complex configurations organized in space and time, for instance the pigmentation of seashells or the skin of animals. In this thesis, we mainly focus on modeling growth and remodeling in living matter and studying possible consequences due to the presence of these active phenomena. For instance, in soft elastic solids, the mentioned active processes change the internal microstructure and cause geometrical incompatibilities, which, in combination with physical nonlinearities of the material itself, may induce a topological transition. Indeed, residual mechanical stresses, which are present even in the absence of external loads, can arise and once they exceed a critical threshold, an elastic instability can occur driving to a morphological change. Examples in this setting are the windy development of tumor growth in the healthy tissue [157] or the formation of biological organs, like arteries [324, 146] and the intestine [26]. Moving to a fluid-like description, the phenomenon of growth characterizes cancer development. Indeed, considering the tumor cell density evolving in the healthy tissue, modeled as a porous medium, to take into account its cell division rate, an additional source term is included to the model. Hence, classical results have to be modified since this new term can lead to different analytical solutions [250] or, from a numerical point of view, the emergence of finger-like patterns [127, 214].

The results of this thesis are collected into two chapters. In Chapter 2, we focus on two different problems to characterize the self-organization phenomenon in soft matter. First, we propose a theoretical explanation for the symmetry break in the arrangement of eight cells undergoing optimal compaction driven by anisotropies in the mechanical cues, mimic the mitotic process in the embryo passing from the eight-cell stage to the sixteen one. Second, we present recent extensions of the so-called Kirchhoff-Plateau problem, in which the fixed boundary of the classical Plateau problem is replaced by an elastic rod and it can be

used as a prototype to study the process of absorption of a protein by a biological membrane.

In Chapter 3, we deal with different models to study growth and remodeling in living matter. First, we address the phenomenon of the gyrification, *i.e.* the formation of the folded structures in brain organoids by proposing an elastic model coupled with surface tension to correctly describe their experimental behavior. Second, we study the c -looping process in the heart tube, which is the first-symmetry breaking process in cardiac embryogenesis, by introducing an internal remodeling cell flow, and we show that this active process alone can drive the spontaneous onset and the fully nonlinear development of the c -looping. Third, we propose a new model to characterize the onset of Faraday instability in soft tissues showing that standing waves at the free surface can appear also in soft elastic solids. By studying the linear problem through the Floquet theory, we obtain that Faraday instability in soft solids is characterized by a harmonic resonance, which will also introduce a new experimental procedure to distinguish a fluid-like from a solid-like response. Finally, we characterize growth process in a fluid-like system by studying cancer invasion. We consider the evolution of a tumor cell density through the healthy tissue, modeled as a porous-medium and, to take into account the cell division rate, we introduce an additional source function. Since it is known that models of this type are equivalent, in the incompressible limit, to more realistic tumor growth ones formulated as free boundary problems, we extend the Aronson-Bénilan estimate on the second derivatives for porous media in different Lebesgue spaces and for all fields of pressure.

All the aforementioned problems are solved within Mathematical Physics framework, dealing with the definition of a suitable model to characterize the real and observable physical phenomenon. Then, this model can be studied using different mathematical tools: we exploit variational formulations to look for an absolute minimum, perturbative techniques to describe the behavior in a neighborhood of an equilibrium point, energy estimates to

control the evolution of a specific quantity or numerical methods to characterize the post-buckling behavior.

For sake of clarity, we collect in the following some preliminary notions for the benefit of the reader which will be used in the next chapters.

1.1 TECHNICAL PRELIMINARIES FOR SELF-ORGANIZATION

Self-organization is a process where some forms of overall order arise from local interactions between parts of an initially disordered system. In the following we study this phenomenon by introducing a powerful mathematical strategy to characterize all the equilibrium configurations of a system.

1.1.1 BRIEF NOTIONS OF CALCULUS OF VARIATIONS

Almost every phenomena in nature can be modeled using partial differential equations (PDE). However solving and studying a PDE could be hard and sometimes impossible. Hence, mathematicians prefer to use its variational form, to determine and characterize all the equilibrium solutions. Indeed, these solutions are minima of a specific and given functional related to, for instance, elasticity, solid and fluid mechanics, electromagnetism, gravitation, quantum mechanics, string theory, and many other examples. To perform this minimization process an old and famous method has been introduced: the *Direct Method of Calculus of Variations* [106]. For our specific purpose, this method can be formulated as follows.

Definition 1.1.1. Let

$$\mathcal{F}[\varphi] := \int_{\Omega_0} W(\mathbf{X}, \varphi(\mathbf{X}), \text{Grad } \varphi(\mathbf{X})) d\mathbf{X} \quad (1.1)$$

where

- $\Omega_0 \subset \mathbb{R}^N$ is a bounded set and $\mathbf{X} \in \Omega_0$;
- $\varphi : \Omega_0 \rightarrow \mathbb{R}^N$ is a function whose regularity will be specified later and $\text{Grad } \varphi$ is the Jacobian matrix of φ ;
- $W : \Omega_0 \times \mathbb{R}^N \times \mathbb{R}^{N \times n}$, $W = W(\mathbf{X}, \varphi, \mathbf{z})$ is a given function which will be characterized better later.

The minimization process can be formulated in the following way:

1. *Computing the Euler-Lagrange equations.* Let A be a function space. If $\forall \psi \in A$ the function

$$g_{\bar{\varphi}} : \mathbb{R} \times A \rightarrow \mathbb{R}$$

$$(t, \psi) \mapsto g_{\bar{\varphi}} := \mathcal{F}[\bar{\varphi} + t\psi]$$

satisfies the condition

$$g'_{\bar{\varphi}}(0, \psi) = 0, \tag{1.2}$$

we call Eq. (1.2) an *Euler-Lagrange equation* for the functional \mathcal{F} .

2. *Computing the minimum of the functional.* We wish to find $\bar{\varphi} \in A$ such that

$$m = \mathcal{F}[\bar{\varphi}] \leq \mathcal{F}[\psi] \quad \forall \psi \in A,$$

where

$$m := \inf\{\mathcal{F}[\psi], \psi \in A\}. \tag{1.3}$$

The minimum m of Eq. (1.3) is a stationary point, *i.e.* it is a solution of Eq. (1.2) and we call $\bar{\varphi} \in A$ a minimal point of \mathcal{F} .

There are several examples in the use of this variational form, especially in 1D. For example, the *brachistochrone problem* or the *minimal revolution surface* [106].

In the aforementioned examples, the minimum exists and it can be computed explicitly by assuming that the solution φ is regular enough, $\varphi \in C^2$ is for instance sufficient. However, there are many physical examples, particularly those dealing with partial derivatives (*i.e.* $n > 1$), in which considering the class of admissible functions (*i.e.* the space A) too small (*i.e.* the elements of A are too regular), is too strict and the minimum φ cannot be found. The essence of the Direct Methods of the Calculus of Variations is to split the minimization problem into two parts. First to enlarge the space of admissible functions, for example by considering spaces such as the Sobolev spaces $W^{1,p}$ so as to get a general existence theorem and then to prove some regularity results that should satisfy any minimizer of the considered problem. In the following, we do not address in studying any regularity results, but we are essentially concerned only with the first problem.

1.1.1.1 THE DIRECT METHODS OF CALCULUS OF VARIATIONS

The Direct Methods of Calculus of Variations is a very powerful strategy which consists in proving some steps. Since we want to provide a method to model physical problems, in the following we assume $N = n = 3$.

Let \mathcal{F} be a functional as in Eq. (1.1). We want to compute

$$\min_{\varphi \in A} \mathcal{F},$$

where A is a Banach space. To do so, we have to check the following requests:

1. \mathcal{F} is bounded from below and $\mathcal{F} \neq +\infty \forall \varphi \in A$
2. considering a minimizing sequence, *i.e.*

$$\lim_h \mathcal{F}[\varphi_h] = \inf_{\varphi \in A} \mathcal{F}[\varphi]$$

3. finding a subsequence $(\varphi_{h_k})_{k \in \mathbb{N}} \in A$ which "converges" to $\varphi \in A$
4. proving that \mathcal{F} is lower semicontinuous with respect to the topology introduced above, *i.e.*

$$\mathcal{F}[\varphi] \leq \liminf_j \mathcal{F}[\varphi_j].$$

Hence

$$\mathcal{F}[\varphi] \leq \liminf_k \mathcal{F}[\varphi_{h_k}] = \lim_h \mathcal{F}[\varphi_h] = \inf_{\varphi \in A} \mathcal{F}[\varphi], \quad (1.4)$$

which ensures that \mathcal{F} is bounded from below and it admits a minimum.

Immediately, we notice that the first two points are necessary but the last ones "fight" each other. Indeed, to be sure that a sequence converges, one can choose the weakest topology on which, unfortunately, proving the lower semicontinuity becomes harder. Hence, we are forced to consider reflexive spaces, like $W^{1,p}$, $p > 1$, to move to the weak topology, to use the weakly lower semicontinuity (WLSC) property of the functional \mathcal{F} and to require the coercivity condition on \mathcal{F} to prove the following theorem [106]

Theorem 1.1.2. *Let A be a reflexive Banach space and $\mathcal{F} : A \rightarrow \mathbb{R} \cup \{+\infty\}$ a proper function. If \mathcal{F} is WLSC and coercive on A , then the minimum exists.*

This theorem alone is not enough because we need to characterize the form of a weakly lower semicontinuous functional \mathcal{F} . Let $\mathcal{L}^+(\mathbb{R}^3)$ be the group (with respect to the operation of function composition) of all the linear applications with positive determinant belonging to the set of all the automorphisms of \mathbb{R}^3 , by requiring that W is a Carathéodory function, *i.e.* for all $\varphi \in \mathbb{R}^3$ and $\forall z \in \mathcal{L}^+(\mathbb{R}^3)$, $W(\cdot, \varphi, z)$ is a measurable function in Ω_0 and for almost every $X \in \Omega_0$, $W(\mathbf{X}, \cdot, \cdot)$ is continuous, the following result holds true [106]

Theorem 1.1.3. *Let Ω_0 be an open bounded set of \mathbb{R}^3 and $W : \Omega_0 \times \mathbb{R}^3 \times \mathcal{L}^+(\mathbb{R}^3) \rightarrow [0, +\infty)$ be a Carathéodory function such that a. e. $\mathbf{X} \in \Omega_0$ and $\forall \varphi \in \mathbb{R}^3$, $W(\mathbf{X}, \varphi, \cdot)$ is a convex*

function. Then, the functional \mathcal{F} in Eq. (1.1) is weakly lower semicontinuous with respect to the weak topology induced by $W^{1,p}$ with $p > 1$.

Precisely, if $N = n = 1$, \mathcal{F} is WLSC $\iff z \mapsto W(\mathbf{X}, \boldsymbol{\varphi}, z)$ is convex.

Thanks to Theorem 1.1.3, both the existence [137] and the uniqueness [195] of the solution of the mixed boundary value problem in linear elasticity can be proved.

Moving to nonlinear elasticity, proving the existence of a minimum becomes more complicated for two main reasons: first the convexity is incompatible with the constitutive assumption of continuum mechanics, such as frame-indifference and non-degeneracy of the strain energy density W [98, 88] and then we expect many equilibrium configurations, in contrast with the strict convexity of \mathcal{F} which guarantees the existence and the uniqueness of a minimum. Thus, different conditions, weaker than convexity, should be considered to exploit the Direct Method of Calculus of Variations for proving the existence of energy minimizers. The replaced necessary condition is the *quasiconvexity*

Definition 1.1.4. Let Ω_0 be an open set and $W : \mathcal{L}^+(\mathbb{R}^3) \rightarrow \mathbb{R}$ a continuous function. The strain energy density W is *quasiconvex* if, $\forall \mathbf{A} \in \mathcal{L}^+(\mathbb{R}^3)$ and $\forall \boldsymbol{\varphi} \in C_0^1(\Omega_0, \mathbb{R}^N)$ the following inequality holds

$$\int_{\Omega_0} W(\mathbf{A} + \text{Grad } \boldsymbol{\varphi}) dX \geq |\Omega_0| W(\mathbf{A}),$$

where C_0^1 denotes the set of all functions $g : \Omega_0 \rightarrow \mathbb{R}^3$ with compact support that are differentiable with a continuous first derivative and $|\cdot|$ is the Lebesgue measure of Ω_0 .

The definitions of convexity and quasiconvexity are not disjoint, since it is possible to prove that all convex function W are also quasiconvex. Moreover, if an energy functional is weakly lower semicontinuous, then the strain energy density is quasiconvex. However we need the converse implication which has been proved by Acerbi-Fusco [1], assuming suitable growth conditions, *i.e.*

Theorem 1.1.5. *Let Ω_0 be an open bounded set and $W : \Omega_0 \times \mathbb{R}^3 \times \mathcal{L}^+(\mathbb{R}^3) \rightarrow [0, +\infty)$ be a Carathéodory function which, given two constants $L \geq 0$ and $p > 1$, satisfies the following inequality*

$$0 \leq W(\mathbf{X}, \boldsymbol{\varphi}, \mathbf{z}) \leq L(1 + |\boldsymbol{\varphi}|^p + |\mathbf{z}|^p).$$

Moreover, the function $W(\mathbf{X}, \boldsymbol{\varphi}, \cdot)$ is assumed to be quasiconvex a.e. $\mathbf{X} \in \Omega_0$ and $\forall \boldsymbol{\varphi} \in \mathbb{R}^3$, then \mathcal{F} in Eq. (1.1) is weakly lower semicontinuous with respect to the weak convergence in $W^{1,p}(\Omega_0, \mathbb{R}^3)$.

However, quasiconvexity condition is hard to use since it is a non-local condition, hence it rarely provides an operative rule for constitutive modeling. A more restrictive property (but easier to prove) is the following one

Definition 1.1.6. A function $W : \mathcal{L}^+(\mathbb{R}^3) \rightarrow \mathbb{R} \cup \{+\infty\}$ of the form

$$W(\mathbf{A}) = h(\mathbf{A}, \text{Cof } \mathbf{A}, \det \mathbf{A}) \quad \forall \mathbf{A} \in \mathcal{L}^+(\mathbb{R}^3)$$

with $g : \mathbb{R}^{19} \rightarrow \mathbb{R} \cup \{+\infty\}$ a convex function, is said *polyconvex*.

It can be proved that a polyconvex function is quasiconvex, while the viceversa is not necessarily true [310]. Precisely if $n = N = 1$ all the previous definitions are equivalent.

This definition is fundamental to prove [30] the existence of minimizer for nonlinear elastic problems with polyconvex strain energy densities satisfying some conditions

Theorem 1.1.7. *Let $\Omega_0 \subset \mathbb{R}^3$ be an open, connected, bounded subset with regular boundary and $W : \Omega_0 \times \mathcal{L}^+(\mathbb{R}^3)$ be a strain energy density such that*

- (Polyconvexity) *There exists a Carathéodory function $g : \Omega_0 \times \mathcal{L}^+(\mathbb{R}^3) \times \mathcal{L}^+(\mathbb{R}^3) \times (0, +\infty) \rightarrow \mathbb{R}$ such that $g(\mathbf{X}, \cdot, \cdot, \cdot)$ is convex and such that*

$$\forall \mathbf{A} \in \mathcal{L}^+(\mathbb{R}^3) \quad W(\mathbf{X}, \mathbf{A}) = g(\mathbf{X}, \mathbf{A}, \text{Cof } \mathbf{A}, \det \mathbf{A})$$

- (Continuity at infinity) if $\mathbf{A}_h \rightarrow \mathbf{A}$, $\mathbf{C}_h \rightarrow \mathbf{C}$ and $\delta_h \rightarrow 0^+$, then

$$\lim_h g(\mathbf{X}, \mathbf{A}_h, \mathbf{C}_h, \delta_h) = +\infty$$

- (Coercivity) there exist $\alpha > 0$, $\beta \in \mathbb{R}$, $p \geq 2$, $q \geq p/(p-1)$, $r > 1$ such that $\forall \mathbf{A}, \mathbf{C} \in \mathcal{L}^+(\mathbb{R}^3)$ and $\delta > 0$

$$g(\mathbf{X}, \mathbf{A}, \mathbf{C}, \delta) \geq \alpha (|\mathbf{A}|^p + |\mathbf{C}|^q + \delta^r) + \beta.$$

We assume that there exist two disjoint subsets Γ_0 and Γ_1 such that $\partial\Omega_0 = \Gamma_0 \cup \Gamma_1$ and such that $|\Gamma_0| > 0$. Let $\mathbf{b} : \Omega_0 \rightarrow \mathbb{R}^3$ and $\mathbf{s}_0 : \Gamma_1 \rightarrow \mathbb{R}^3$ be measurable such that the functional

$$L[\varphi] := \int_{\Omega_0} \mathbf{b} \cdot \varphi \, dX + \int_{\Gamma_1} \mathbf{s}_0 \cdot \varphi \, dS$$

is continuous on $W^{1,p}(\Omega_0, \mathbb{R}^3)$. Finally, let $\varphi_0 : \Gamma_0 \rightarrow \mathbb{R}^3$ be a measurable function and such that the set

$$\begin{aligned} \mathcal{U} := \{ \varphi \in W^{1,p}(\Omega_0, \mathbb{R}^3) : \text{Cof Grad } \varphi \in L^q, \det \text{Grad } \varphi \in L^r, \\ \det \text{Grad } \varphi > 0 \text{ a. e. in } \Omega_0, \varphi = \varphi_0 \text{ on } \Gamma_0 \} \end{aligned} \quad (1.5)$$

is not empty. Then, defining $\mathcal{F} : \mathcal{U} \rightarrow \mathbb{R} \cup +\infty$ as

$$\mathcal{F}[\varphi] := \int_{\Omega_0} W(\mathbf{X}, \text{Grad } \varphi) - L[\varphi]$$

and assuming $\inf \mathcal{F}[\varphi] < +\infty$, then there exists

$$\min \mathcal{F}[\varphi].$$

Hence, in a nonlinear elastic problem, just by replacing the convexity condition with

polyconvexity on the strain energy density, we can prove the existence of the solution.

1.1.1.2 OTHER STRATEGIES

In the previous section, we specify the Direct Method of the Calculus of Variations just in a particular framework, *i.e.* when the functional \mathcal{F} has a specific form. However, the steps mentioned at the beginning of Section 1.1.1.1 are true for all types of problem, proving the compactness and lower-semicontinuity of the functional. Indeed, in the Plateau problem, which in its simplest form studies the existence of a surface spanning a given boundary, the shape of \mathcal{F} strongly depends on the chosen regularity. For instance, the Plateau problem can be defined in terms of finite perimeter sets [217] or in terms of currents [135]. In both cases, adding some additional hypothesis like imposing suitable regularity of the involved boundaries in the finite perimeter set approach or requiring finite mass for the current and its boundary in the currents description, the same steps presented in Section 1.1.1.1 are valid and the existence of a minimizer for the associated functional is obtained [237].

However, even if this method is very powerful, there are some problems in which the minimum cannot be explicitly computed and numerical computations are too expensive. Indeed, describing multiple interactions among different components in 3D should be hard since as the number of the involved parts grows, these links increase exponentially. Hence, using a typical technique of Rational Mechanics [313], we adopt another approach: giving a mechanical system, it reaches the equilibrium if the distribution of forces is suitable. Then, since any equilibrium configuration is not the minimal one, some physical criteria, which mimic nature's attitude to save energy and to choose the most favorable rearrangement, have to be introduced. If these criteria are satisfied, we might expect that the obtained configuration is the minimal one. We use this strategy to study the symmetry break in the eight bubbles configuration (see Section 2.1) since this method allows to face

immediately with the needed rearrangement, and then we can perform a quantitative analysis on this configuration computing the active tensions on the different surfaces.

1.2 TECHNICAL PRELIMINARIES FOR PATTERN FORMATION

Pattern formation refers to the generation of complex configurations in space and time.

In the following, we focus on modeling active phenomena, like growth and remodeling, in living matter, on characterizing their mathematical formulation in soft solids or a in fluid-like system and on describing possible consequences due to their presence.

1.2.1 BRIEF NOTIONS OF NONLINEAR ELASTICITY

Nonlinear elasticity has been introduced to describe deformed materials like rubbers and hydrogels since linear elasticity is not appropriate, especially in large deformations regimes [243, 180]. The most famous class, and the only one considered throughout the thesis, of nonlinear elastic materials is the hyperelastic one. Before describing this class of materials, we introduce the general form of the mixed Boundary Value Problem (BVP) in nonlinear elasticity.

Denoting by \mathbb{E}^3 the three-dimensional Euclidean space, we call reference configuration of the body a regular subset Ω_0 of \mathbb{E}^3 . Let $\mathbf{X} \in \Omega_0$ be the Lagrangian or Material coordinate of a point. The motion is described by the vector field $\varphi : \Omega_0 \times (0, +\infty) \rightarrow \mathbb{R}^3$, called deformation. We indicate with $\Omega := \varphi(\Omega_0, t)$ the deformed configuration of the body at time t . Let $\mathbf{x}(t) = \varphi(\mathbf{X}, t)$ be the Eulerian or spatial coordinate of the point \mathbf{X} at time t . We indicate with $\mathbf{F} = \text{Grad } \varphi(\mathbf{X}, t)$ the deformation gradient and we assume that $J = \det \mathbf{F} > 0$. The vector $\mathbf{u}(\mathbf{X}, t) = \varphi(\mathbf{X}, t) - \mathbf{X}$ is called the *displacement* of a point $\mathbf{X} \in \Omega_0$ at a time t , hence $\mathbf{F} = \mathbf{I} + \text{Grad } \mathbf{u}(\mathbf{X}, t)$.

By imposing the conservation of mass and the linear momentum [168], the general form

of mixed BVP in elasticity is given by

$$\begin{cases} \operatorname{Div} \mathbf{P} + \rho_0 \mathbf{B} = \rho_0 \frac{d^2 \mathbf{u}}{dt^2} & \text{in } \Omega_0 \\ \mathbf{u} = \mathbf{u}_0 & \text{on } \Gamma_0 \\ \mathbf{P}^T \mathbf{N} = \mathbf{s}_0 & \text{on } \Gamma_1, \end{cases}$$

where \mathbf{P} is the *first Piola-Kirchhoff stress tensor*, \mathbf{B} is the force density in the reference configuration, \mathbf{N} is the outer normal to the portion of the boundary Γ_1 and we choose to apply Dirichlet boundary conditions on a portion Γ_0 with $|\Gamma_0| > 0$ and Neumann boundary conditions on Γ_1 with $\Gamma_0 \cap \Gamma_1 = \emptyset$ and $\Gamma_0 \cup \Gamma_1 = \partial\Omega_0$ [243].

1.2.1.1 HYPERELASTICITY

To model nonlinear elastic materials, a constitutive equation has to be imposed to link the first Piola-Kirchhoff stress tensor \mathbf{P} with the deformation gradient \mathbf{F} . A material is said to be *hyperelastic* if there exists a free energy density $W : \Omega_0 \times \mathcal{L}^+(\mathbb{R}^3)$, also known as *strain energy density*, depending only on the deformation gradient and satisfying the following relation

$$\mathbf{P} = \frac{\partial W(\mathbf{X}, \mathbf{F})}{\partial \mathbf{F}}.$$

Moreover, W is an elastic potential if it satisfies the following axioms

- Frame indifference The strain energy density W has to be independent on the selected reference system, *i.e.*

$$W(\mathbf{X}, \mathbf{F}) = W(\mathbf{X}, \mathbf{QF}) \quad \forall \mathbf{X} \in \Omega_0, \forall \mathbf{F} \in \mathcal{L}^+(\mathbb{R}^3) \text{ and } \forall \mathbf{Q} \in \mathcal{O}^+(\mathbb{R}^3), \quad (1.6)$$

where $\mathcal{O}^+(\mathbb{R}^3)$ is the set of rigid rotations. Using the polar decomposition theorem

[168], Eq. (1.6) is true if and only if

$$W(\mathbf{X}, \mathbf{F}) = \hat{W}(\mathbf{X}, \mathbf{C}),$$

where $\mathbf{C} := \mathbf{F}^T \mathbf{F}$ is the *right Cauchy-Green tensor*. Precisely, for an isotropic material, *i.e.* $W(\mathbf{X}, \mathbf{F}) = W(\mathbf{X}, \mathbf{F}\mathbf{Q}) \forall \mathbf{Q} \in \mathcal{O}^+(\mathbb{R}^3)$, this frame-indifference condition implies that the strain energy function W is a function of the principal invariants of the right Cauchy-Green tensor \mathbf{C} [275], namely $W = W(I_1, I_2, I_3)$, where

$$I_1 = \text{tr } \mathbf{C}, \quad I_2 = \frac{(\text{tr } \mathbf{C})^2 - \text{tr } \mathbf{C}^2}{2}, \quad I_3 = \det \mathbf{C}.$$

- Non-degeneracy To avoid energetic paradoxes, we require

$$\begin{aligned} W(\mathbf{X}, \mathbf{F}) &\rightarrow +\infty && \text{if } J \rightarrow 0^+ \\ W(\mathbf{X}, \mathbf{F}) &\rightarrow +\infty && \text{if } |\mathbf{F}| \rightarrow +\infty, \end{aligned} \tag{1.7}$$

where $|\mathbf{F}| = \sqrt{\text{tr } \mathbf{C}}$.

There are many examples of hyperelastic strain energy densities [232, 220]. In the following, we only consider the simplest one: our elastic materials behave as *neo-Hookean* ones and the strain energy density is given by

$$W(\mathbf{F}) = \frac{\mu}{2} (\text{tr } \mathbf{C} - 3),$$

where μ is the shear modulus.

1.2.2 ACTIVE PROCESSES

One of the possible outcomes of an *active process*, where active refers to an open thermodynamical system working in out of equilibrium conditions, is the change of the macroscopic shape thanks to the microscopic rearrangement of matter [10]. This rearrangement is called *remodeling* where there is no generation of mass and *growth* otherwise [293, 69, 10, 250, 161].

The mathematical description of these phenomena strongly depends on which material we are considering: for solid matter these active phenomena generate residual stresses, defined as the remained stress field present even in the absence of external loading or thermal gradients [178] and the most famous approach is the *multiplicative decomposition* of the deformation gradient. Moving to a liquid-type description, one of the most important examples is the tumor cells proliferation and their motion in tissue environment. In this context, where usually an Eulerian form is adopted, one of the most used approach is the evolution of a tumor cell density through a *porous-medium* with an additional and specified source term. The obtained PDE is not the classical porous-media equation (PME), implying the modulation of classical known analytical estimates [250, 110] or a morphological change of the interfaces, leading for instance to the emergence of finger-like patterns [214, 215].

In the following sections, first we characterize the presence of active processes in soft-elastic solids, which can cause several topological transitions and the appearance of an instability pattern [10, 26, 161, 273]. Then, moving to the mathematical description of cancer development, we study the “modified” porous-media equation in which a source additional term is taken into account to model the cell division rate [250, 214, 65, 110].

1.2.2.1 MORPHOELASTICITY

In solid soft matter, the presence of active processes can lead to a local inelastic distortion, hence inducing geometrical incompatibilities, like for instance change of shapes, variations of mass or direction of fibers. To restore the geometrical compatibility lost and to balance external and internal forces, an elastic distortion is necessary [293]. The introduction of the elastic contribution generates residual stresses, which are very common in biological soft materials: they have been found in blood vessels [209, 324, 146], heart [245], intestine [26] and many others [161].

The most famous approach to model the response of residually stressed materials has been first introduced in elasto-plasticity by Kröner [196] and Lee [204] and, then widely employed in continuum mechanics models [276]. It is based on a *multiplicative decomposition* of the deformation gradient into two contributions

$$\mathbf{F} = \mathbf{F}_e \mathbf{G},$$

where \mathbf{G} takes into account purely the growth/remodeling process, *i.e.* it describes the inelastic change of shape induced by the microstructural rearrangement of the matter, while \mathbf{F}_e restores the geometrical compatibility by inducing an elastic deformation. The main advantage of this approach is that it describes the effect growth and remodeling without specifying the inner mechanisms involved [10].

From a physical point of view, the presence of residual stresses and the non-uniqueness of the solution in nonlinear elasticity lead to several morphological transitions, governed by geometrical and constitutive parameters. *Morphoelasticity* investigates the emergence of complex patterns in soft tissue which occur for an elastic instability.

The oldest problem is the buckling of a column subjected by a load: a critical load τ_{cr}

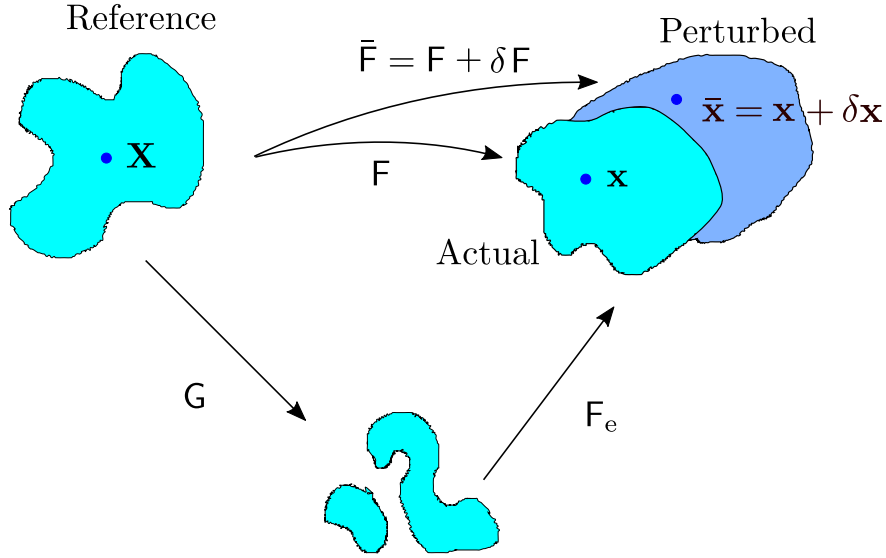


Figure 1.1: Scheme of the basic and perturbed variables. In the reference state, \mathbf{X} is the reference position vector, the tensor G takes into account growth/remodeling, while F_e describes the elastic distortion. In the actual configuration, \mathbf{x} is the base solution and F the deformation gradient. Finally, in the perturbed setting, $\bar{\mathbf{x}}$ is the perturbed position vector and \bar{F} the perturbed deformation gradient.

can be computed which implies that, if the column is subjected to a higher force than τ_{cr} , then it will buckle, *i.e.* it will deviate from its straight configuration. Not only an external load can drive the onset of an elastic bifurcation but, as we mentioned before, also the excessive accumulation, *i.e.* beyond a critical threshold, of residual stresses can lead to a pattern formation in the material, due to the introduced geometrical incompatibility in the micro-structure.

Methods of perturbation theory can be applied to study the stability of solutions in finite elasticity [54, 56]. The one adopted in this thesis is the *method of incremental deformations superposed on finite deformations*, first introduced by Ogden [243], see Fig. 1.1. Similar to the stability study of a nonlinear ODE, the main idea of this method, which will be detailed in Sections 3.1 - 3.3 - 3.2 for different problems and geometries, is to introduce a small perturbation $\delta \mathbf{x}$ and to sum it to the base solution \mathbf{x} , *i.e.*

$$\bar{\mathbf{x}} = \mathbf{x} + \delta \mathbf{x},$$

where we assume that $\delta\mathbf{x}$ is small with respect to the $W^{1,\infty}(\Omega, \mathbb{R}^3)$ of the base solution \mathbf{x} . We are characterizing the initial shape of the material, given by \mathbf{x} and its morphology after a possible bifurcation, expressed by $\delta\mathbf{x}$. Hence, a linearization process of the nonlinear problem about the actual configuration can be performed, and the results is the construction of a incremental BVP where the unknown is the increment $\delta\mathbf{x}$.

The BVP is hard to numerically solve, hence the *Stroh formalism* [297] is introduced: it allows to transform the system of BVP into an hamiltonian system of first order ordinary differential equations with initial conditions [144]. Then, since the problem is still numerically stiff, the *surface impedance matrix* is introduced [59, 242] to transform the vectorial ODE into a Riccati equation which can be efficiently numerically solved by using standard iterative methods.

This vibrant research field has rapidly developed in the last decade, pushed on a hand by the technological availability of experimental devices controlling the extreme deformations of soft incompressible materials, like hydrogels [307], and on the other one by the development of even more efficient computational resources, fundamental to run sophisticated numerical algorithms without losing too much time [273].

Studying mechanical instabilities and topological transitions in soft elastic solids has highlighted some similarities, yet several relevant differences, with the instability characteristics of hydrodynamic systems, even if their BVP are completely different. For example, if the surface tension in fluid drives the formation of droplets, which spontaneously break down [265], such a dynamics can be also seen due to elastic effects in soft solid cylinders [234], thus driving the emergence of stable beads-on-a-string patterns [303]. Another interesting example is the effect of gravity on one or more elastic layers attached to a rigid substrate [235, 272]. The interplay between elastic and gravity waves has a regularizing effect: it changes and in particular reduces the typical velocity of propagation of the Rayleigh waves, always computed in a fluid-like system [213, 308]. In Section 3.3, we prove that a

well-known phenomenon in fluid dynamics can display a completely different behavior if elastic effects are taken into account opening the path for using Faraday waves for a precise and robust experimental method that is able to distinguish solid-like from fluid-like responses of soft matter.

1.2.2.2 POROUS-MEDIA EQUATION (PME)

In the last decades the study of cancer development increases thanks to the introduction of new mathematical models [69, 250] and efficient numerical algorithms [4] to describe the last and the worst part of tumor growth, *i.e.* its invasion through the healthy tissue and the formation of metastases.

The main mechanical model is based on considering the evolution of the tumor density, called in the following $n(t, x)$ through a porous medium, *i.e.* the healthy tissue, with an additional source term G to characterize the cell division rate. Hence, its mathematical formulation is given by

$$\frac{\partial n}{\partial t} + \operatorname{div}(n \nabla p) = nG(p), \quad (1.8)$$

where p denotes the *pressure*. Since the equation, in its current form, is not closed, a *constitutive pressure law*, also referred to as *equation of state*, is chosen to close the equation. Such a law relates the pressure directly to the quantity, n , affected by the pressure, *i.e.* $p = p(n)$. Precisely, Eq. (1.8), both with and without G , can be used in many practical applications, reaching from problems related to ground water flow [107], nonlinear heat transfer [329], and population dynamics, [167, 187, 238], to name just a few of them. For an extensive and elaborate treatise of the porous medium equation, we refer the reader to the homonymous book by Vázquez [316], and references therein.

One of the most fascinating properties of nonlinear diffusion phenomena is the finite speed of propagation. While solutions of the linear diffusion equation have an instant-

neous regularizing effect, *i.e.* solutions become positive and smooth after an arbitrarily short time, solutions of the porous medium equation exhibit a behavior quite different from that of the linear case – solutions remain with limited regularity and compactly supported if they were compactly supported initially, a phenomenon often referred to as *finite speed of propagation*. In [244], the Authors introduce a notion of weak solutions and give an existence and uniqueness result of weak solutions to the filtration equation,

$$\frac{\partial n}{\partial t} = \frac{\partial^2}{\partial x^2} \phi(n), \quad (1.9)$$

for a certain class of functions ϕ . Moreover, they show that the equation is satisfied in the classical sense in neighborhoods of points, (t, x) , where $n(t, x) > 0$, and, that solutions, emerging from compactly supported initial data, have compact support for all times.

In a later paper, [192], more properties of the porous medium equation were shown. In particular, invaded regions will remain covered with the density, n , *cf.* [192, Lemma 2] for all times, every point in space will be invaded by the density after a sufficiently long time, [192, Lemma 3] and regions of vacuum do not fill up spontaneously, *cf.* [192, Lemma 3].

Intrigued by the fact that the support of any solution emanating from compactly supported initial data is bounded by two free boundaries, or *interfaces*, *cf.* [192], Aronson proved a characterization of the free boundary speed which is directly related to the pressure gradient which acts as the formal velocity in Eq. (1.8) with $G \equiv 0$, see [18]. In this paper, it is assumed that some initial data supported on an interval $I = (a_1, a_2)$ are given. In order to establish the aforementioned characterization of the speed of the moving boundary, Aronson remarks that some control of the quantity “ p_{xx} ” is required for the analysis. However, the author was able to construct a counterexample explaining that this type of regularity cannot, in general, be expected, which was already known in the case of the explicit Barenblatt-Pattle solution, discovered in 1952, *cf.* [31, 247]. In fact, in [17], he pro-

vides smooth initial data (of C^∞ -regularity) that exhibit blow-up of “ p_{xx} ” in finite time. Assuming a Power-law for the pressure, *i.e.*

$$p = n^\gamma, \tag{1.10}$$

Aronson investigates the behavior of the following one-dimension Cauchy problem

$$\begin{cases} \frac{\partial p}{\partial t} = \gamma p p_{xx} + p_x^2 \\ p(x, 0) = \cos^2(x) \end{cases} \tag{1.11}$$

and he proves that, in general, it is not possible to estimate the second derivatives of the solution of Eq. (1.11) in terms of the bounds for the derivatives of the initial data. Indeed, he obtains that the second derivative of the pressure behaves like

$$p_{xx} = \frac{2T}{T-t}, \quad \text{where} \quad T = \frac{m-1}{2m(m-1)}, \tag{1.12}$$

which implies that it exceeds any bound in finite time; for more details one can refer to [17, Theorem 1]. Moreover, a similar result can be obtained when the initial data has compact support, *cf.* [17, p. 301], Example 2.

Thus a different type of control is necessary. In [18, Lemma 2], Aronson proves that if

$$\operatorname{ess\,inf}_I \frac{\partial^2 p}{\partial x^2}(0, x) \geq -\alpha, \tag{1.13}$$

for some $\alpha \geq 0$, then

$$\frac{\partial^2 p}{\partial x^2}(t, x) \geq -\alpha, \tag{1.14}$$

for all (t, x) such that $n(t, x) > 0$. To the best of our knowledge, this is the first time this

type of lower bound on the Laplacian* of the pressure is obtained. At the same time, this observation acts as the foundation of the more refined version with less restrictions on the initial data, obtained in [19], in 1979.

The lower bound on the Laplacian of the pressure is achieved by regularizing the initial data in the following way:

$$p_0^n(x) = (k_n \star p_0)(x) + 2^{2-n}K, \quad (1.15)$$

where K is the Lipschitz constant of p_0 and k_n is a sequence of smoothing kernels converging to a Dirac delta. For the smoothed and strictly positive initial data classical solutions exist, *cf.* [244], and an equation for the second derivative of the pressure, p_{xx} , can be found. Aronson observes that the resulting equation for p_{xx} can be cast into a form whose parabolic operator satisfies the maximum principle presented in [184, Theorem 8]. Ultimately, this allows to deduce the uniform bound from below on the second derivative of the pressure.

Later, Aronson and Bénéilan show that a similar estimate (known as Aronson-Bénéilan estimate, *i.e.* AB-estimate) can be obtained in the multi-dimensional case, *cf.* [19]. Under no additional assumptions† they show that

$$\Delta p \geq -\frac{c}{t}, \quad (1.16)$$

for some constant $c > 0$. Let us note that the same result is already mentioned in [18] as a note, since the regularizing effect was not the main focus in the derivation of the boundary speed characterization in one dimension.

In 1982, Crandall and Pierre generalize the Aronson-Bénéilan estimate for the initial-

*At this time, the results by Oleinik, Kalashnikov, and Aronson only concern the one-dimensional case.

†only exponents "large enough", *cf.* their paper

value problem associated to the filtration equation, *cf.* Eq. (1.9), given by

$$\begin{cases} \partial_t n = \Delta \phi(n), \\ n(0, x) = n_0(x), \end{cases} \quad (1.17)$$

for $t > 0$, and $x \in \mathbb{R}^N$, where ϕ is a non-negative, non-decreasing, continuous function with $\phi(0) = 0$, *cf.* [102]. They prove that if ϕ satisfies an inequality, *cf.* [102, Eq. (3)] which formally controls the growth of ϕ , the solution n of Eq. (1.17) satisfies

$$\partial_t \phi(n) \geq \frac{K}{t} (\phi(n) + a), \quad (1.18)$$

for some constants $K > 0$ and $a \geq 0$. In the Power-law case, $\phi(n) = n^\gamma$, with $a = 0$ and

$$K \geq \frac{\gamma}{\gamma - 1 + 2/N},$$

obtained from the aforementioned inequality, *cf.* [102, Eq. (3)], the solution n underlies the same regularizing effect as that of [19]. With this approach, they are able to extend the AB-type estimate to cover a larger class of problems, including, for instance, the Stefan problem (see [71]) which holds for $a = 1$, $K = N/2$.

The first proposed macroscopic model, *i.e.* Eq. (1.8), is widely studied with many numerical and analytical tools but it does not capture correctly the biological vision of tumor growth. Hence, tissue growth can be described by devising a free boundary model, where tissue growth is due to the motion of its boundary. It is a more geometrical approach and it allows to better study the motion and the dynamics of cancer. Moreover, they are not independent, since there is a well-developed technique to establish a link between these two approaches, the so-called *incompressible limit*, which implies that the pressure becomes stiff.

FREE BOUNDARY-BASED DESCRIPTION OF TISSUE GROWTH Besides its huge impact on the regularity theory of solutions to the porous medium equation and the free boundaries thereof, the AB-estimate proves to be a crucial tool for building a bridge between a density-based description and a geometric description of tissue growth. The link between the two models is established through a rigorous study of the *incompressible limit* of the porous medium pressure equation, *i.e.* for a general pressure law

$$\partial_t p = |\nabla p|^2 + qw, \quad (1.19)$$

where

$$q(p) := np'(n) \quad \text{and} \quad w := \Delta p + G(p),$$

and the limit is obtained as the pressure law becomes stiffer and stiffer. For instance, in Power-Law case, where $p = n^\gamma$, the incompressible limit holds when *i.e.* $\gamma \rightarrow \infty$. An incompressible model has to satisfy two relations. The first, $p(n - 1) = 0$, implies the absence of any pressure in zones that are not saturated ($\{n < 1\}$), while the second one, also referred to as *complementarity relation*, yields an equation satisfied by the pressure on $\{p > 0\}$, which is of the form

$$p(\Delta p + G(p)) = 0.$$

It is immediately apparent that strong regularity is needed to obtain such an expression, which is provided by (adaptations) of the AB-estimate — bounds on the Laplacian of the pressure are enough to infer strong compactness of the pressure gradient. This was first observed in [250] to be equivalent to being able to pass to the limit in the porous medium pressure equation and obtain the incompressible limit.

*Una cosa è matematicamente ovvia dopo che la
si è capita.*

R. D. Carmichael

2

Self-organization of soft matter

The main focus of this chapter is to study the ordered rearrangement of different physical structures in the space.

In this chapter, first we aim to study the symmetry break of an equilibrium multi-bubbles configuration proving that Geometry and Mechanics have both a relevant role in determining the three-dimensional packing of 8 bubbles. In Section 2.1.1.1, we define the spatial arrangement of bubbles assuming that it obeys a geometrical principle maximizing the minimum mutual distance between the bubble centroids. Then, in Section 2.1.1.3, we construct the compacted structure by radially packing the bubbles under constraint of volume

conservation. We generate a polygonal tiling on the central sphere and peripheral bubbles with both flat and curved interfaces. Since this configuration is not obtained through a minimization process, in Section 2.1.1.4, we verify that the obtained polyhedron is optimal under suitable physical criteria. In Section 2.1.2, we enforce the mechanical balance imposing the constraint of conservation of volume and we find an anisotropy in the distribution of the field of forces: surface tensions of bubble-bubble interfaces with normal oriented in the circumferential direction of bubbles aggregate are larger than the ones with normal unit vector pointing radially out of the aggregate. We suggest that this mechanical cue is key for the symmetry break of this bubbles configuration. Finally, in Section 2.1.3, we add few concluding remarks.

Then, we generalize the so called Kirchhoff-Plateau problem. The first existence result, in its general form, appears in 2017, thanks to Giusteri *et al.* [156]. The rest of the chapter is devoted to present our investigations on this famous problem.

First, in Section 2.2.2, we consider a more complex configuration of the bounding loop: we study the equilibrium problem of a system consisting by several Kirchhoff rods linked in an arbitrary way and tied by a soap film. Precisely, for the sake of simplicity we will consider throughout the section just two thin elastic three-dimensional closed rods. In Section 2.2.2.1, we formulate the problem similar to [156], but while the first loop has a prescribed frame at a point, the second one does not have a fixed position in space. Then, in Section 2.2.2.2, we prove the existence of a solution with minimum energy. Finally, in Section 2.2.2.3, we perform experiments confirming the kind of surface predicted by the model, showing its irregularity in some points.

Second, in Section 2.2.3, we study the equilibrium problem of a mechanical system consisting of two Kirchhoff rods linked in an arbitrary way and also forming knots, constrained not to touch themselves by means of electrical repulsion and tied by a soap film. This is not only a simple model to describe the interaction between an electrically charged pro-

tein and a biomembrane but, from a mathematical point of view, it is a generalization of the Kirchhoff-Plateau problem with a single component, studied by Fried *et al.* in [156], and with several Kirchhoff rods, studied by Bevilacqua *et al.* in [47]. Since the mathematical model is exactly the same as the one in Section 2.2.2, in Section 2.2.3, we underline the major differences. Precisely, to give a more realistic, physical and biological background to take into account processes like the adsorption of a protein by a biomembrane [181], we introduce an additional repulsional energy between the two rods. Finally, the same conclusion can be achieved: we prove the existence of a solution with minimum total energy, which may be quite irregular, as expected from the physical problem.

Finally, in Section 2.2.4, we obtain the minimal energy solution of the Plateau problem with elastic boundary as a variational limit of the minima of the Kirchhoff-Plateau problems with a rod boundary when the cross-section of the rod vanishes. First, in section 2.2.4.1 we sketch the physical motivations that support the fact that the limit curve can sustain also a twisting energy, proving that a “*memory*” of the twist is preserved. Then, in sections 2.2.4.2 and 2.2.4.3 we define the rigorous setting of the problem and we state the Γ -convergence result and its most important consequence. Precisely, we obtain (Theorems 2.2.20 and 2.2.21) that the approximating problems have minima which converge weakly to the minimum energy solution of the limit problem, as well as the corresponding value of the energy. This also shows that the Plateau solution with elastic boundary may be approximated by solutions of the problems with a rod border. Indeed, the limit boundary is a framed curve that can sustain bending and twisting. Finally, section 2.2.4.4 contains the proof of the main theorem.

The results of this Chapter lead to the following publications:

- G. Bevilacqua; *Symmetry break in the eight bubble compaction*; preprint <https://arxiv.org/pdf/2007.15399.pdf>, [45].

- G. Bevilacqua, L. Lussardi, A. Marzocchi; *Soap film spanning electrically repulsive elastic protein links*; Atti Accad. Peloritana Pericolanti Cl. Sci. Fis. Mat. Natur. 96 (2018), suppl. 3, A1, 13 pp, [48].
 - G. Bevilacqua, L. Lussardi, A. Marzocchi; *Soap film spanning an elastic loop*; Quart. Appl. Math. (2019) 77:3, 507-523, doi:10.1090/qam/1510 (2019), [47].
 - G. Bevilacqua, L. Lussardi, A. Marzocchi; *Dimensional reduction of the Kirchhoff-Plateau problem*; J. Elasticity 140, no. 1, 135-148, doi:10.1007/s10659-020-09763-y (2020), [49].
-

2.1 SYMMETRY BREAK IN THE EIGHT BUBBLE COMPACTION

Often used for children's enjoyment, soap bubbles are the simplest physical example of a lot of mathematical problems: they are the solution of the minimal surface problem [253], they solve a stability problem since their longevity is limited [284] and when two or more bubbles cluster together, their configuration obeys a shape optimality problem [53]. Assembling several bubbles traps pockets of gas in a liquid and results in *foam*: the surfactants added to the liquid stabilize the bubbles by reducing the surface tension and by arranging themselves at the liquid/gas interfaces [322].

Regarding the behavior of a single soap bubble, everything is known. What is not completely understood is the geometrical and mechanical properties of a cluster of many bubbles, known as a foam. For instance, its optimal rearrangement in space is still matter of debate.

In 2D there are more results: Hales proved the *honeycomb conjecture*, which states that the partition of the plane into regular hexagons of equal area has least perimeter, *i.e.* it minimizes the perimeter fixing the area [170]. In this context, some years later, Morgan proved that the optimal (*i.e.* minimal) configuration exists for N clusters [237] and Cox *et al.* obtained their numerical visualizations up to $N = 200$ [100]. Due to the non linearity of the problem, in a lot of physical situations, the equilibrium solution is only stable with respect to *small displacements*, *i.e.* it is not a global minimum of the system. This aspect leads to mechanical instabilities which break the symmetry of the system [62, 101, 321, 139].

If we move to 3D, the problem is minimizing the area functional and few exact result exist. The only rigorous one is the proof of *the Double Bubble Conjecture* [183], which states that the standard double bubble provides the least-area enclose and separates two regions of prescribed volume in \mathbb{R}^3 . As regarding the numerical results, Kelvin [312] proposed an optimal candidate structure with *identical cells*, which has been numerically refuted in [320]: by numerical calculations, an agglomerate of two different types of bubbles has less perimeter, for fixed area.

The aim of this section is to study the symmetry break of a eight bubble compaction in 3D, *i.e.* we want to investigate the mechanical cues driving the three-dimensional packing of 8 bubbles displayed in a recalling foam structure. To circumvent the difficulty of a variational approach, *i.e.* the minimization of an area functional satisfying some geometrical constraints, we follow a different strategy. First of all, we fix the geometrical arrangement of the eight bubbles as the solution of the Tamme's problem [306]: we exploit a geometrical principle of maximal mutual distance between neighbor points on a spherical surface obtaining seven symmetrical peripheral spheres tangent to the central one [228]. Then, compaction is produced by packing the outer bubbles along the radial direction of the aggregate. The obtained agglomerate recalls the foam structure [77]: the central sphere is

completely covered, while the peripheral ones have a free-curved surface. While our construction does not ensure that the obtained final configuration is the minimal one, we will prove that the our tessellation on the central sphere is the optimal one among all the possible [64] according to physical assumptions: the liquid/liquid interface is favored versus the liquid/gas one and it maximizes the volume [322].

2.1.1 GEOMETRICAL PRINCIPLE

2.1.1.1 SPATIAL ARRANGEMENT

In this section, we introduce a geometrical principle that we exploit to describe the spatial arrangement of the 8-bubbles configuration, to determine the position of the seven bubbles surrounding the central one. The coordinates of the peripheral bubbles centroids are given as solution of the classical *Tammes's Problem* [306]: determine the arrangement of n points on the surface of a sphere maximizing the minimum distance between nearest points (*maxmin principle*). This is equivalent to determine (up to rigid rotations) the n unit vectors $\{\mathbf{r}_i\}$ such that

$$\lim_{m \rightarrow +\infty} \left\{ \frac{1}{|\mathbf{r}_i - \mathbf{r}_j|^m} : 1 \leq i < j \leq n \right\}, \quad (2.1)$$

is maximum, where the limit $m \rightarrow +\infty$ selects the distance among closest points only.

In our case $n = 7$; we want to find the position of seven points on a sphere with minimum distance from their nearest neighbors.

Here, we exploit the *graph theory* [323] to find this maximizing configuration. A set of n points on a sphere forms a graph G of n points connected by arcs of great circles of length a [287]. The maximal spatial arrangement of seven points can be obtained by the projective argument presented in [287]. Consider a frame of reference centered in $O = (0, 0, 0)$ and the coordinates on the spherical surface (r, θ, ϕ) , where $\theta \in [0, 2\pi)$ (longitude) and

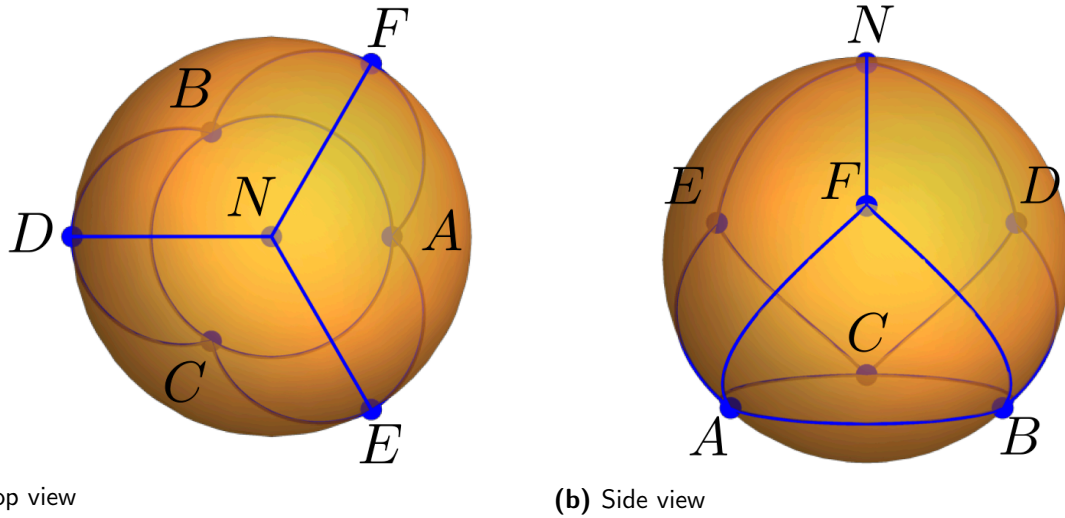


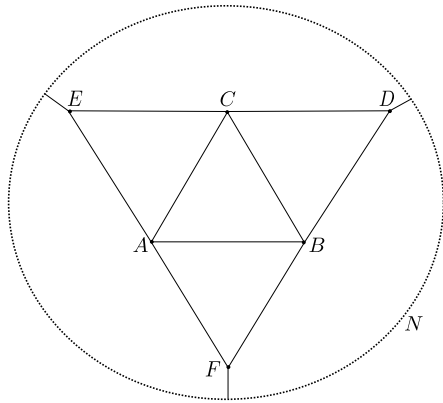
Figure 2.1: (a) Top and (b) side view of the position and connections of the seven points on the spherical surface of the central bubble. The blue connections are the arcs of length a defined by Tamme's construction.

$\phi \in [0, \pi]$ (latitude) on S^2 , namely

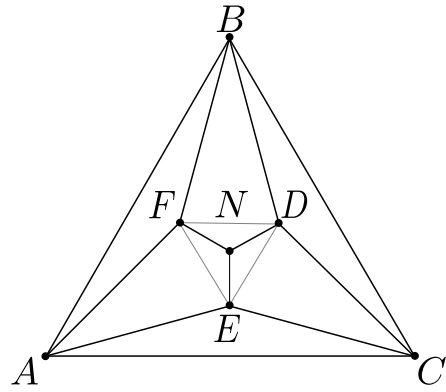
$$S^2 = \{r, 0 \leq \theta < 2\pi, 0 \leq \phi \leq \pi\},$$

where r is the radius of the sphere N and S the North and South Pole, respectively. Three points $\{A, B, C\}$ are placed at the same latitude on the surface of the central sphere, such that they are connected by arcs of length a and they form an equilateral triangle centered in S . Three more identical triangles are then created, adjacent to the former ones, with vertices D, E and F : they share the same latitude too. The final step is then to connect D, E and F with N and vary the radius r (for fixed a) until also the latter arcs have length a , * (see Fig. 2.1). The associated extremal graph defines four triangles and three quadrangles on the spherical surface, as illustrated in Fig. 2.2.

*In a fully equivalent way, one can fix the radius r and vary the chord length a .



(a) Stereographic projection



(b) Spherical projection

Figure 2.2: Stereographic (a) and spherical (b) projections of the Tamme's points on the spherical surface and their connecting arcs. Grey and thin lines, corresponding to arcs of length $1.34 a$, make the tessellation fully triangular.

Fundamental relations of spherical trigonometry tell us that the internal angle of an equilateral spherical triangle is $\alpha = \frac{4\pi}{9}$, while the arc angle β with respect to the centre of the sphere β is given by [42]

$$\cos \beta = \frac{\cos \frac{4\pi}{9}}{1 - \cos \frac{4\pi}{9}}, \quad (2.2)$$

as illustrated in Fig. 2.3.

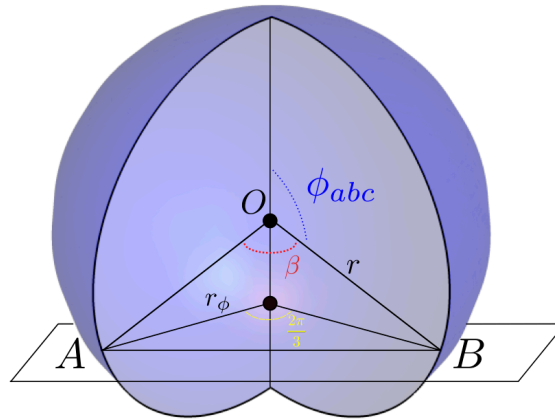


Figure 2.3: Geometrical sketch of the latitude of the points A , B and C : the central angle β , the radius r of the sphere and the radius r_ϕ of the circumference laying in the plane defined by the triplet of points.

This allows to find explicitly the linear relation between arc length and radius, *i.e.* $a =$

βr .

The length ℓ of the chord between closest points is

$$\ell = 2r \sin\left(\frac{\beta}{2}\right).$$

2.1.1.2 COORDINATES

By construction, the spherical distance on S^2 of the points D, E and F from N is equal to a , so their latitude is the angle $\phi_{pqr} = \beta$. For the triplet of points $\{A, B, C\}$, the calculations are a little bit more elaborated. Let r_ϕ be the radius of the circumference defined by the intersection of the sphere and the plane where A, B and C are. The following relation holds

$$r_\phi = r \sin(\phi_{abc}), \quad (2.3)$$

where ϕ_{abc} is the latitude of the points A, B and C .

Since the chord length is the same for the spherical arc and for the in-plane circle, we find

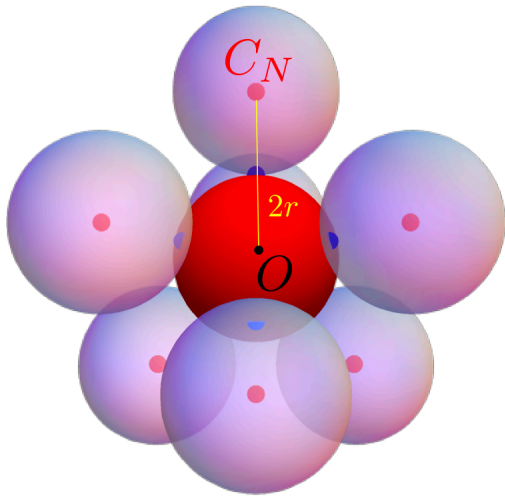
$$\frac{\ell}{2} = r_\phi \sin\left(\frac{1}{2} \frac{2\pi}{3}\right) = r \sin\left(\frac{\beta}{2}\right). \quad (2.4)$$

By combining Eqs. (2.3) and (2.4) we get

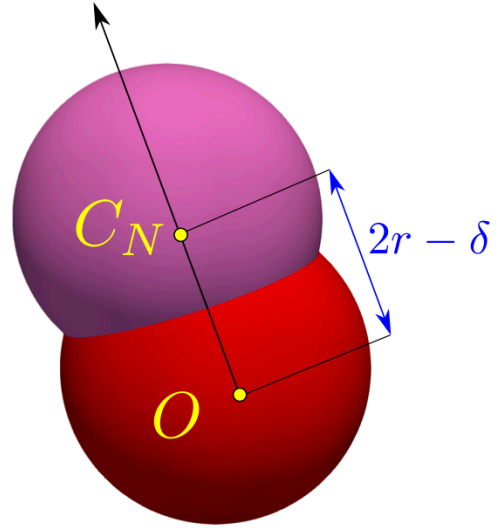
$$\sin \phi_{abc} = \frac{2}{\sqrt{3}} \sin\left(\frac{\beta}{2}\right). \quad (2.5)$$

Summarizing, the coordinates of the seven Tammes points depicted in Fig. 2.1 are

$$\begin{aligned} A &= (r, 0, \phi_{abc}) & B &= \left(r, \frac{2\pi}{3}, \phi_{abc}\right) & C &= \left(r, \frac{4\pi}{3}, \phi_{abc}\right), \\ D &= \left(r, \frac{\pi}{3}, \phi_{pqr}\right) & E &= (r, \pi, \phi_{pqr}) & F &= \left(r, \frac{5\pi}{3}, \phi_{pqr}\right) & N &= (r, 0, 0). \end{aligned} \quad (2.6)$$



(a) Before compaction



(b) Compaction process

Figure 2.4: (a) Initial arrangement of the bubbles before compaction. Tangent points are denoted by a blue dot, red dots denote the center of each sphere. (b) Sketch of the “compaction process” between two bubbles driven by the parameter δ .

This configuration, given by the *maxmin principle* (2.1), is here adopted as the ideal reference bubble arrangement: seven spheres are tangent to the former one in the Tamme’s points, as illustrated in Fig. 2.4a.

2.1.1.3 “BUBBLE COMPACTION”: TILING THE CENTRAL SPHERE

The tessellation of the spherical surface illustrated in the previous sections, is composed by four equilateral triangles and three quadrilaterals, see Fig. 2.2a. However it can be made of triangles only by connecting points $\{D, E, F\}$, see Fig. 2.2b. The triangle $\{D, E, N\}$ is not equilateral, since the distance between D and E is equal to $1.34a$. On the basis of such a triangular tessellation we can produce a *dual* tessellation connecting the circumcenters of the triangles: the locus where the axis of the edges cross each other (Fig. 2.5).

The Tamme’s points are the centroids of the polygons that define the dual tessellation (see Fig. 2.5 and for more mathematical details Appendix A.1).

The bubble packing is obtained ideally moving each peripheral bubble, initially tangent

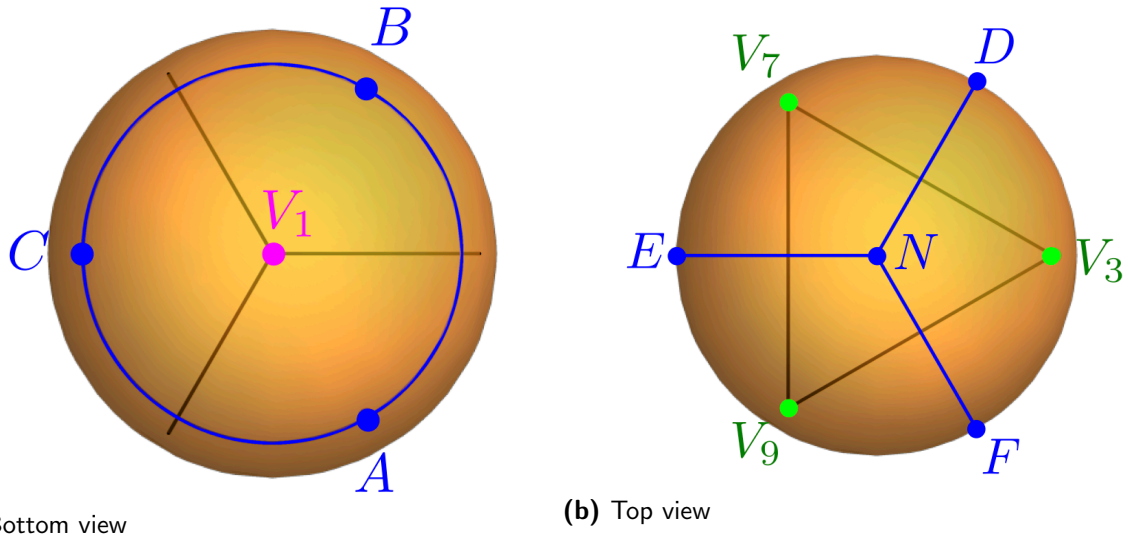


Figure 2.5: (a) Bottom view of the construction of the tessellation. (b) Top view of the construction of the tessellation.

to the central one in the Tamme's points, towards the origin O along the radial direction, as illustrated in Fig. 2.4b, while enforcing the volume conservation. In other words, to pack the bubbles aggregate we generate a collection of flat surfaces of contact among bubbles starting from the *maxmin* distribution of the tangent points: each peripheral bubble adheres to the central one moving centripetally, see Fig. 2.4b. At the same time we shuffle the peripheral and the central spheres to preserve the initial volume \mathcal{V} . The contact surfaces between central and peripheral bubbles obtained by such a *dive and shuffle* procedure are nothing but the polygons obtained connecting the points of the dual tessellation defined above.

The final configuration is a tiling of the spherical surface of the central bubble with seven polygons, as illustrated in Fig. 2.6:

- an equilateral triangle centered in N (area $\simeq 0.66 a^2$),
- three quadrilaterals centered in A, B, C (area $\simeq 0.7 a^2$),
- three pentagons centered in D, E, F (area $\simeq 0.74 a^2$).

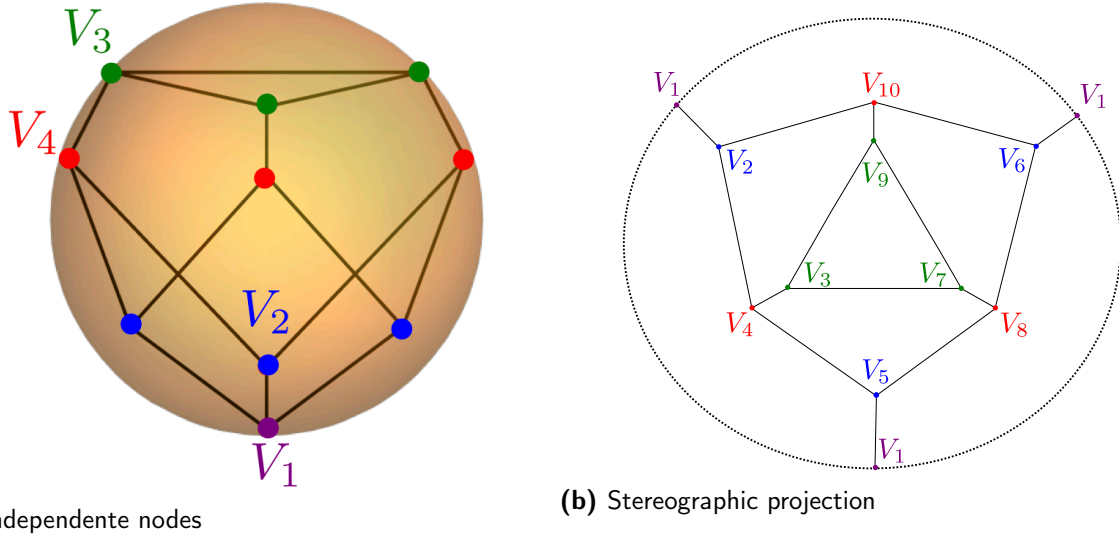


Figure 2.6: (a) Sketch of four independent nodes V_1 , V_2 , V_3 and V_4 on the tessellation, highlighting the corresponding symmetry group. (b) Stereographic projection of the dual tessellation.

2.1.1.4 GEOMETRICAL OPTIMALITY

While the produced polygonal surface covers the central sphere, it naturally arises the question if such a tiling is optimal according to some suitable criterion. The problem to cover a spherical surface with polygons is old, rigorous results dating back to Cauchy [82]. In the present context, all the bubbles are identical and it is therefore tempting the idea to cover the central bubble with identical polygons. Unfortunately, this is not allowed by Euler's Polyhedron Formula[†].

There is no regular heptahedron. In order to prove if our tiling is optimal, we can con-

[†]Euler's Polyhedron Formula has been proved by Cauchy [82] and it gives a relation among the number of faces, edges and vertices of a polyhedron, such as

$$F + V - E = 2.$$

The number of vertices and edges are related with the number of faces faces F as follows

$$E = \frac{Fn}{2} \quad V = \frac{2E}{m} = \frac{Fn}{m},$$

where n is the number of edges of the polygon at hand, while m is the number of faces which insist on the same vertex. We are interested in the case $F = 7$. By elementary calculations one can easily see that there is no n for which a suitable integer m exists.

struct all the convex polyhedra with 7 faces which can be inscribed into a sphere of fixed radius r . By the software Plantri [64], we find 34 convex polytopes with seven faces. They can be classified in terms of number of edges and number of vertices, see Table 2.1.

Number of vertices	Number of polyhedra	Number of edges
6	2	11
7	8	12
8	11	13
9	8	14
10	5	15

Table 2.1: Classification of the 34 convex polytopes with respect to the number of vertices (from left to right) or in terms of edges (from right to left).

The packing rearrangement of soap bubbles is dictated by both geometrical and mechanical motivations. Moreover, the optimal configuration is the one which minimizes the energy maximizing the volume. From the physics of the problem, we know that creating an interface liquid/liquid energetically costs less than one liquid/air [322]. Hence, we can assume that the final shape of the central bubble has the maximum numbers of edges, *i.e.*

$$\tilde{\mathcal{P}} = \max_{E=11}^{15} E_{\mathcal{P}_i} \quad i = 1, \dots, 34. \quad (2.7)$$

where $E_{\mathcal{P}_i}$ is the number of edges the i -polyhedron. In this way, we can reduce the number of polyhedra: we pass from 34 convex polytopes with 7 faces to just 5 in which our tiling is included. In Appendix A.2, we show these 5 polyhedra obtained and drawn by the software Plantri. So, we need another condition to select just one configuration. From the isoperimetric inequality, we know that the sphere is the solid that, fixing the area, it maximizes the volume and viceversa. For this reason, the shape of a single bubble is spherical. When two bubbles enter in contact, the surface of the agglomerate is lower than the surface of the two bubbles. Therefore, we search among the favorable energetically configura-

tions, the one that has the maximum volume, such as

$$\bar{\mathcal{P}} = \max_{i=1}^5 (\mathcal{L}^3(\tilde{\mathcal{P}}_i)), \quad (2.8)$$

where \mathcal{L}^3 is the volume measure. By numerically computing the five volumes, we find that the tiling obtained as the dual of the Tamme's one is the one with the maximum volume, *i.e.* the optimal one according to our criteria.

Remark 2.1.1. Since each polyhedron is not regular, we do not have an explicit formula to compute the volume. However, each polyhedron can be divided into 7 pyramids, where the basis is a face. Using this geometrical argument, the total volume can be computed as the sum of the volumes of the pyramids.

2.1.1.5 SURFACES, EDGES AND VERTICES

The dual tessellation defines ten nodes and it belongs to $\mathcal{C}_{3z}(1, 3, 3, 3)$.[‡] We denote the nodes of the dual tessellation on the basis of the vertices of the Tamme's triangles they belong to, such as

$$\begin{aligned} V_1 &= (A, B, C), \\ V_2 &= (A, F, B), \quad V_3 = (E, F, N), \quad V_4 = (A, E, F), \\ V_5 &= (A, E, C), \quad V_6 = (B, D, C), \quad V_7 = (D, E, N), \\ V_8 &= (B, D, E), \quad V_9 = (D, F, N), \quad V_{10} = (B, D, F). \end{aligned}$$

Because of the symmetry of the problem, there are only four independent nodes, as depicted in Fig. 2.6a.

[‡] \mathcal{C}_{nz} is the group of a cyclic symmetry after a rotation $2\pi/n$ with respect to the axis z [96, 283]: the configuration is invariant for rotations of an angle $2\pi/3$ around the z axis. The notation $(1, 3, 3, 3)$ denotes how many nodes of the tessellation share the same longitude.

The dual tessellation is formed by 15 edges, only 4 of them being independent. Each edge is identified by the polygons it belongs to on the tiled surface and the boldface denotes the unit vector parallel to the edge. Therefore, $\mathbf{c}_1 = \overline{V_1V_2}$ denotes the edge between two quadrilaterals, $\mathbf{c}_2 = \overline{V_2V_3}$ separates a quadrilateral and a pentagon, $\mathbf{c}_3 = \overline{V_3V_4}$ separates a pentagon and a pentagon and $\mathbf{c}_4 = \overline{V_2V_3}$ is between a pentagon and the triangle.

We generate a three dimensional structure projecting radially the dual tessellation, by an height to be fixed later on the basis of volume conservation arguments. Each vertex of the tessellation on the central bubble has therefore a corresponding outer one that we denote by V_i^h , $i = 1, 2, 3, 4$. The connection between inner, outer and side surfaces is defined by two classes of edges:

- $\mathbf{c}_5 = \overline{V_1V_1^h}$, $\mathbf{c}_6 = \overline{V_2V_2^h}$, $\mathbf{c}_7 = \overline{V_3V_3^h}$, $\mathbf{c}_8 = \overline{V_4V_4^h}$ point radially,
- $\mathbf{c}_9 = \overline{V_1^hV_2^h}$, $\mathbf{c}_{10} = \overline{V_2^hV_3^h}$, $\mathbf{c}_{11} = \overline{V_3^hV_4^h}$, $\mathbf{c}_{12} = \overline{V_2^hV_3^h}$, are parallel to the ones on the tessellation of the central bubble.

At this stage the geometrical characterization of the 8-bubbles configuration derived on the basis of a maximum-minimum distance of the centroids of the peripheral bubbles is completed. The inner bubble has no free surface: it is surrounded by contact interfaces with other bubbles only. The external ones have the shape of a pyramidal frustum covered by a laterally cut spherical cap: the lower basis is the polygon generated by the adhesion with the central bubble, lateral sides are flat too, their edges being radially oriented, the upper basis of the frustum is a radial projection of the lower one. The upper geometrical structure is a spherical vault on a polygonal frustum, intriguingly known since the Middle Age in Sicilian architecture [147]. The radius of the spherical cap and the height of the frustum are to specified on the basis of balance and conservation arguments discussed below.

2.1.2 MECHANICAL BALANCE

In this section, we compute the surface tensions that make the geometrical packing mechanically equilibrated. We remark that the central sphere has only bubble–bubble contact interfaces, while the peripheral ones also possess a traction–free surface. Each bubble–bubble interface and each free surface is characterized by a tension τ_i , defined as the energy density per unit area of the liquid/liquid or liquid/air interfaces [279]. Thus, we have ten unknown independent tensions τ_i : three on the central bubble, four on lateral bubble–bubble interfaces and three at the free surface denoted by

$$\tau_Q, \tau_P, \tau_T, \tau_{QQ}, \tau_{PQ}, \tau_{PP}, \tau_{PT}, \tau_Q^s, \tau_P^s, \tau_T^s, \quad (2.9)$$

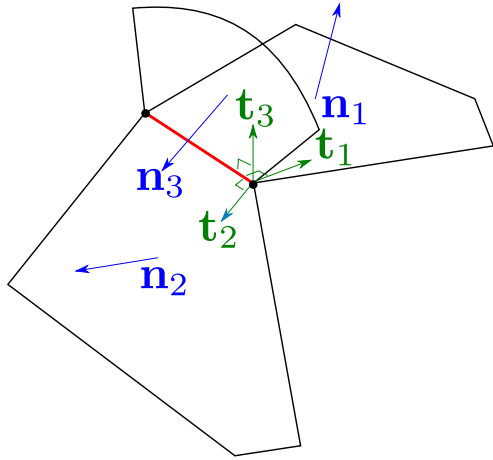
where the subscript identifies the surface of the polygon it applies to and the superscript s specifies the tensions at the free surfaces.

2.1.2.1 TENSIONAL BALANCE

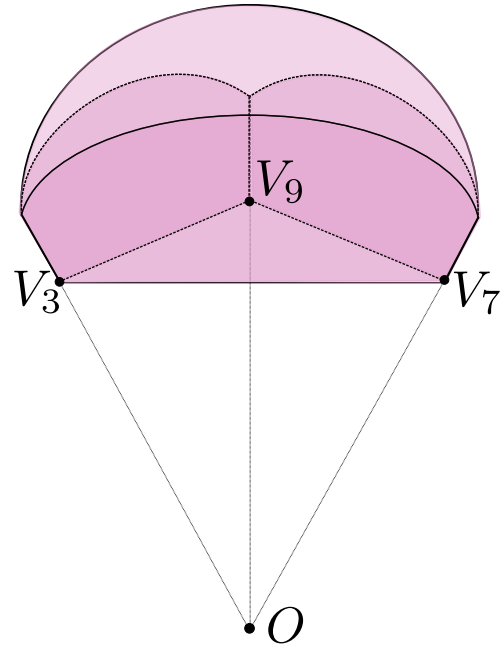
First, we enforce the mechanical equilibrium imposing that the surface tensions are balanced on each independent edge \mathbf{c}_i , where $i = 1, \dots, 12$ (see Fig. 2.7a). Three (flat or curved) surfaces are attached to each edge, their local orientation being denoted by the normal unit vectors \mathbf{n}_j^i , $j = 1, 2, 3$. The balance of tensions on each edge is defined by the sum of the tensions, oriented orthogonally to the edge and in-plane with the corresponding interface (see Fig. 2.7a). Therefore it must hold

$$\sum_{j=1}^3 \mathbf{t}_j \tau_j = \sum_{j=1}^3 \mathbf{c}_i \times \mathbf{n}_j^i \tau_j = \mathbf{c}_i \times \sum_{j=1}^3 \mathbf{n}_j^i \tau_j = 0 \quad \Rightarrow \quad \sum_{j=1}^3 \mathbf{n}_j^i \tau_j = 0 \quad i = 1, \dots, 12 \quad (2.10)$$

Eq. (2.10) defines 36 scalar equations, 12 of them being trivially null because all the summed vectors are in the plane orthogonal to the edge under consideration. With the help of a



(a) Balance on a edge



(b) Volume of a peripheral sphere

Figure 2.7: (a) Balance of tensions on an edge. (b) The bubble volume is the sum of a pyramidal frustum (with pink side boundaries) plus the polygonal-basis vault standing on it (light pink).

symbolic software [§], we eventually find that, given the unit vectors \mathbf{n}_j^i only 10 of them are independent.[¶] The equations are detailed in Appendix A.4 in Tables A.1 - A.2 - A.3.

The linear system Eq. (2.10) is however not closed because, while the direction orthogonal to the flat surfaces is uniquely defined, the edge contribution of the tension defined on the free surface depends on the curvature of the surface itself. Curvature, tension and pressure gap on the free surface of the peripheral bubbles obey the Young-Laplace equation [33] in the following way

$$\Delta p = \frac{4\tau_i^s}{R_i} \quad i = P, Q, T, \quad (2.11)$$

where R_i is the radius of curvature of the free surface of the i -th bubble and Δp is the difference between the outer and the inner of pressure and there is an extra factor 2 since the

[§]We used Mathematica (Wolfram Inc., Version 12).

[¶]The orientation of the normal unit vectors is not defined according any specific rule because it is expected to affect only the sign of tension, that we know to be positive.

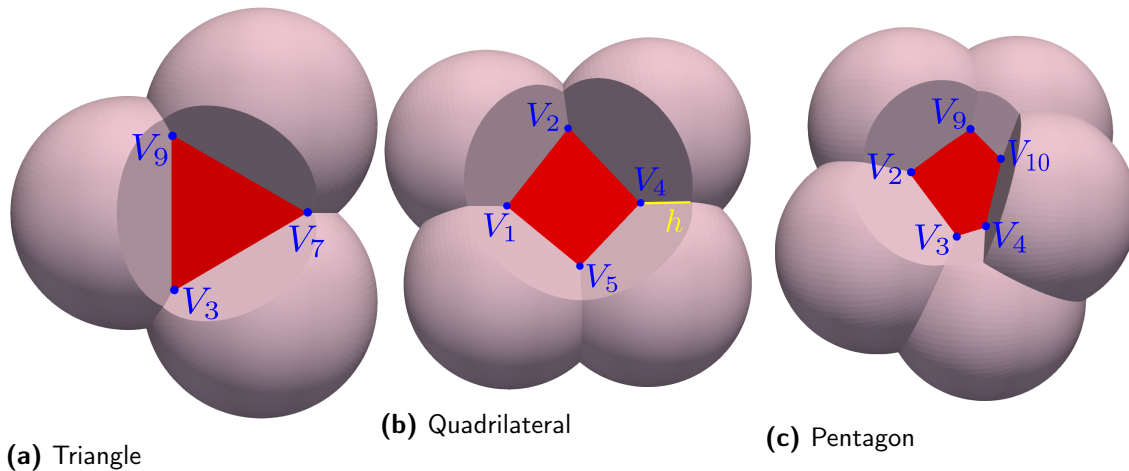


Figure 2.8: Compactification of peripheral bubbles around (a) the triangle, (b) a quadrilateral and (c) a pentagon. The corresponding peripheral bubble is removed for the sake of graphical representation. The yellow segment represents the radial height h of the intersection surface among three adjacent bubbles

surface of the bubble is composed by two leaflets. Since we have only three independent types of polygons on the tessellation, Eq. (2.11) gives three independent equations.

2.1.2.2 VOLUME CONSERVATION

Finally, we have to impose the conservation of bubble volume under compaction. While the central (packed) bubble is bounded by flat interfaces, the peripheral ones have the shape of a pyramidal frustum covered with a spherical vault (see Fig. 2.7b). The basis of the pyramidal frustum are

- the interface with the central bubble;
- its radially directed homothetic projection, by a factor $\frac{r+h}{r}$, where h is the radial height of the intersection surface among three adjacent cells (see the yellow segment in Fig. 2.8).

The value of h has to be fixed on the basis of volume conservation arguments: the sum of the pyramidal and apsal volumes must be equal to the common volume of all bubbles.

Details about the calculation of these volumes are given in Appendix A.3. As the area of each polygonal basis and the curvature radius of the apse are different, the radial height h of the cells is not actually the same; however differences are below 1%.

2.1.2.3 RESULTS

We can solve the system of 16 equations given by Eqs. (2.10)-(2.11), constrained to volume conservation, with respect the 16 unknowns: 10 tensions, 3 curvature radii and 3 heights. Using some experimental data coming from the foam literature, [77], we can fix the pressure difference $\Delta p = 50$ Pa and the radius of the round bubble as $r = 1$ mm, before the compaction process. Numerical solution of the nonlinear system of equations predicts the following surface tensions

$$\left\{ \begin{array}{lll} \tau_P = 51 \frac{mN}{m} & \tau_T = 45 \frac{mN}{m} & \tau_Q = 47 \frac{mN}{m} \\ \tau_{PP} = 69 \frac{mN}{m} & \tau_{QQ} = 58 \frac{mN}{m} & \tau_{PT} = 63 \frac{mN}{m} & \tau_{PQ} = 65 \frac{mN}{m} \\ \tau_P^s = 41 \frac{mN}{m} & \tau_T^s = 35 \frac{mN}{m} & \tau_Q^s = 39 \frac{mN}{m}. \end{array} \right. \quad (2.12)$$

The computed radii of curvature are

$$R_P = 3.5 \text{ mm}, \quad R_T = 2.5 \text{ mm}, \quad R_Q = 3.1 \text{ mm}. \quad (2.13)$$

The obtained surface tensions are consistent with experimental results [77]: to create a soap bubble, the surface tension has to be less than the one of water, which is $\tau_{\text{water}} \simeq 73$ mN/m, otherwise the bubble cannot exist. The obtained field of forces Eq. (2.12) is the one at the equilibrium. We immediately notice that there is an anisotropy in the distribution of the field of forces: surface tensions of bubble-bubble interfaces with normal oriented in the circumferential direction of bubbles aggregate (second line of Eq. (2.12)) are

larger than the ones with normal unit vector pointing radially out of the aggregate (first and third line of Eq. (2.12)).

This result supports our conjecture: the anisotropy in the mechanical cues may be the cause of the symmetry break, *i.e.* there might be a preferential direction of the next topological instability [101]. Indeed, from experiments and numerical results, it is known that a similar aggregate, due to some physical involved parameters, can develop an asymmetry or a topological transition [321]. The study of the stability of this configuration is out of this section. This result wants just to show that the distribution of forces in the equilibrium configuration itself is not symmetric, hence we can state that any small perturbations can change the rearrangement of forces inside the system and can develop a topological transition which breaks the starting symmetrical structure.

2.1.3 FINAL REMARKS

In this section, we studied the symmetry break of a particular configuration of 8 spheres, showing the anisotropy in the distribution of the field of forces of the equilibrium position, that might possible originate a topological transition and break the symmetric structure of the starting agglomerate [101, 321]. This result can be applied to a physical situation, *i.e.* the study of foam, since the selected rearrangement of spheres remembers the one of soap bubbles in a single module of the foam structure [77].

We considered 7 identical spheres symmetrically surrounding a central one: their initial position is dictated by the solution of the Tammes' problem [306]. Neglecting any dynamical process, the final configuration is obtained by a compaction process which results into a full tiling of the central sphere. By introducing physical criteria of optimality dictated by the energy minimality, Eq. (2.7), and by the volume maximality, Eq. (2.8), we proved that our polyhedra is the optimal one among all the 34 convex polytopes inscribed into a sphere with radius r [64], since due to Euler Polyhedra Formula no regular heptahedrons

exist [82].

Fixing this geometrical arrangement, we looked for the force balance that realizes such a configuration: we computed balance of forces on every edge, we forced the conservation of volume (by experimental evidences soap bubbles can be assumed to be incompressible [133]) and we imposed the Laplace law on the possibly curved free surface. We obtained a force field, Eq. (2.12), which fulfills an acceptable physical range [77], but it shows an anisotropy in its orientation, see second line in Eq. (2.12). This result suggests that a difference in tension, generated by a purely mechanical principle, might be crucial for next topological transitions and for the development of anisotropies [321]. In this respect, we conjecture that the expulsion of a single bubble, dictated by any small perturbations, in the *flower cluster* in 2D [101] can be replicated in higher dimensions, breaking the symmetrical structure.

The main drawback of this work is that we expect that the obtained configuration is the minimal one due to the geometrical intuitions in Section 2.1.1.4 but we cannot state that it is the minimal one since it has not been formulated as a minimization problem. Indeed, we decided not to follow such a research line due to the high difficulty in writing down the energy functional, which has to take into account many interactions among all the bubbles. Hence, future efforts will be devoted to numerically study the dynamical evolution of this agglomerate and then to reproduce this system in a laboratory.

The main novelty is the application of a mathematical method, to a particular context, *i.e.* the symmetry break of a 8-bubble compaction. In general, the study of the geometrical rearrangement and the change of shape of a configuration by mechanical and geometrical considerations might introduce a new non-destructive approach to better understand different physical phenomena. For instance, it can be used to design new meta-materials, where it is fundamental to know a priori the balance of forces, or to study the mitosis of cells. Indeed, just by knowing their geometrical rearrangement at a fixed stage, we can deter-

mine if the distribution of forces has an anisotropy which can favor the duplication process along a particular direction. This means that our method can give an insight on a more detail comprehension on the mechanics of morphogenesis of a variety of tissues.

2.2 THE KIRCHHOFF-PLATEAU PROBLEM

In this Section, we will extend recent results of the *Plateau problem*, a milestone in Calculus of Variations which in its simplest form studies the existence of a surface spanning a given boundary. Precisely, We solve the so called *Kirchhoff-Plateau problem*, in which the fixed boundary is replaced by an elastic rod adding another unknown to the problem.

2.2.1 HISTORICAL VIEW ON THE KIRCHHOFF-PLATEAU PROBLEM

Liquid films spanning rigid frames have been of longstanding interest to physicists and mathematicians, thanks to the sheer beauty of the countless observable shapes. After the experimental investigations of Plateau [254], the first satisfactory proofs of the existence of a surface of least area bounded by a fixed contour were provided only in the twentieth century by Douglas [126] and Radó [260]. This first result, formally, establishes that in the equilibrium any liquid surface is a minimizer of the potential energy caused by the molecular forces. Since for soap films such a energy is proportional to the area, they can be viewed as physical models for stable minimal surfaces. Thanks to Douglas and Radó, who won the first Fields medal for this original contribution, the Plateau problem becomes a milestone in the field of Calculus of Variations giving rise to a great variety of beautiful generalizations in Mathematics.

For instance, in contrast with Plateau problem, in which a soap film spans a fixed frame, the Kirchhoff-Plateau problem concerns the equilibrium shapes of a system in which a *flexible* filament has the form of a closed loop spanned by a liquid film. The filament form-

ing the loop is assumed to be thin enough to be modeled faithfully by a Kirchhoff rod, an unshearable inextensible rod which can sustain bending of its midline and twisting of its cross sections, see [15, Ch. 8]. In this way the problem becomes “elasto-variational”.

Furthermore, the physical presence of the bounding loop requires a proper treatment of the constraint of noninterpenetration of matter, which is clearly at play in real experiments and even becomes essential, since the bounding loop can sustain large deflections but remains constrained when self-contact occurs. If, in particular, the relative strength of surface tension with respect to the elastic response of the filament becomes large, then the compliance of the mathematical solution with physical requirements can only be guaranteed by including the noninterpenetration constraint. Thanks to the description of the elastic rod provided in [286], all these properties can be included in a variational framework.

The first existence results of the Kirchhoff-Plateau problem were given by Bernatzky [43] and Bernatzky and Ye [44] who employed the theory of currents, but their elastic energy fails to satisfy the physical requirement of invariance under superposed rigid transformations. Furthermore, a strong hypothesis is used to avoid self-contact. Giomi and Mahadevan in [154] investigated the bifurcation from the flat state and provide also numerical examples. The Kirchhoff-Plateau problem, where a 3-dimensional elastic rod plays the role of the boundary of the soap film, was first formulated by Giusteri et al. [155] where the authors derive general equilibrium and linear stability conditions by considering the first and second variations of the energy functional. Stability properties of flat circular solutions under various conditions regarding the material properties of the rod have been investigated also by Chen and Fried [84], Biria and Fried [57, 58], and Hoang and Fried [177].

However, in all of these studies the boundary of the spanning surface is assumed to coincide with the rod midline and not to lie on the surface of the rod. Moreover, the surface is viewed as diffeomorphic to a disk, except in [44].

The most delicate point in the description of the elasto-variational problem is a good definition of spanning surface, since it is not prescribed *a priori* the region where the soap film touches the surface of the spanning loop.

To overcome this problem, different approaches have been proposed: the theories of integral currents and of varifolds were applied to the Plateau problem by Federer and Fleming [136] and Almgren [5], respectively. However, their approaches also fail either to cover all the physical soap film solutions to the Plateau problem or to furnish a sufficiently general existence result. An alternate route was initiated by Reifenberg [268], who treated the surface as a point set that minimizes the two-dimensional Hausdorff measure. This purely spatial point of view, adopted also by De Pauw [248] and David [109], deals nicely with the topology of solutions, but makes it difficult to handle a generic boundary condition.

A more complete treatment is the definition of *spanning surface* introduced by Harrison [173] based on the concept of *linking number*, which is a numerical invariant well-known in topology. Even if this approach describes all soap-film solutions [173, 172], it needs much strong regularity, which can be achieved through a recent and powerful reformulation by De Lellis *et al.* [112], who formulate the Plateau problem in a particular notion of *spanning*. Precisely, this result [112] has been generalized in every codimension, for general energies and allowing multiplicities respectively in [113, 252, 281]. In [112], the authors make use of the weak* topology of measures for the convergence for surfaces. Precisely, in the extension [252] to any codimension and general energies, a convergence in Hausdorff topology is provided in homological classes. In this way the minimum of the problem is defined as the support of a Radon measure, [109, 248, 268]. Hence, this approach has the advantage of considering also non-rectifiable or not fixed boundaries but it is not easy to apply since the minimization of Hausdorff measures on classes of compact sets could cause lack of lower semicontinuity (it depends on the notion of convergence adopted), which is fun-

damental, as we mentioned before, for the direct method of the Calculus of Variations. To avoid these difficulties they combine Preiss rectifiability theorem [255] for Radon measure in combination with some variational arguments, such as the introduction of cone and cup competitors. However, an important simplification is that, following the proof in [206], the use of the deep Preiss Theorem can be avoided, using instead a soft argument with Caccioppoli sets (see [206, Section 3.2]).

Using these recent works, the first existence result for the Kirchhoff-Plateau problem has been given by Giusteri et al. [156] where the functional to be minimized is composed by the elastic energy of the rod, the weight of the rod and the area of the soap film spanned by the rod. Even if the gravity is relatively easy to treat from the mathematical point of view since it is a continuous perturbation of the rest of the energy, it cannot be neglected since there is a significant separation of scales between the typical thickness of the liquid film and the cross-sectional thickness of the filaments, at least two orders of magnitude. Hence, in their work which is the pioneer in this sector, they model the liquid film as a two-dimensional set, while the bounding loop is a three-dimensional object.

The main novelty of this work, which was our starting point in developing different prospective of the Kirchhof-Plateau problem (see Sections 2.2.2 - 2.2.3 - 2.2.4), is the strong link with the experimental observations justified also by the dimensional reduction performed by expressing the total energy of the system (bounding loop plus spanning surface) as a functional of the geometric descriptors of the bounding loop only. Indeed, this step is motivated by the existence of a solution to the problem of finding an area-minimizing surface spanning a three-dimensional bounding loop.

2.2.2 SOAP FILM SPANNING AN ELASTIC LINK

This kind of problem has been investigated in [156] by Giusteri *et al.* where they consider only a filament, while our aim is to study more complex configurations of the bounding

loop, like a finite number of them linked in an arbitrary way. For the sake of simplicity we will consider throughout the section two thin elastic three-dimensional closed rods, *i.e.* two loops, linked in a simple but nontrivial way: we impose that the midline of each rod has to have linking number equal to one with the other one: this implies that they form what is called a link (see Fig. 2.9), but the case of a number of N loops possibly non isotopic to a torus and arbitrarily linked can be easily treated with the same technique and minor changes. In this way, the major difference with respect to [156] is the fact that the second loop doesn't have a fixed position in space, while the first has a prescribed frame at a point. To take into account all of these requests we have to impose some physically moti-

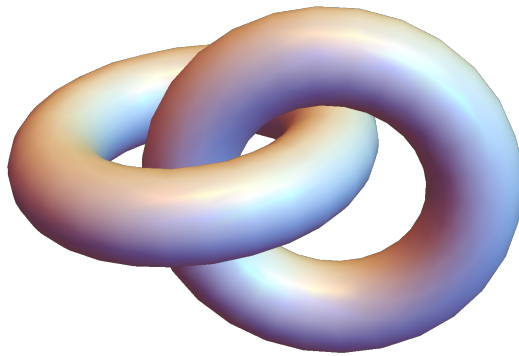


Figure 2.9: Geometry of the problem.

vated constraints, such as local and global non-interpenetration of matter (though allowing for points on the surface of the bounding loop to come into contact), and other already introduced by Schuricht [286], adding the necessary specifications in considering a link and not a single loop.

As for the energy functional of the system, we consider three contributions: the elastic and the potential energy for the link and the surface tension energy of the film. Precisely,

we do not take into account the energy associated with the liquid/solid interface since it is less than the one between the liquid/air interface. However, for the future it could be a parameter to add to the problem in order to give a more physical description also for the spanning surface.

The most delicate point in our elasto-variational problem is a good definition of spanning surface, since we do not prescribe *a priori* the region where the soap film touches the surface of the spanning loop.

To overcome this problem we use the definition of *spanning surface* introduced by Harrison [173] based on the concept of *linking number*, which is a numerical invariant well-known in topology. Even if this approach describes all soap-film solutions [173, 172], it needs much strong regularity. Therefore, like in [156], we use a recent and powerful reformulation by De Lellis *et al.* [112], who formulate the Plateau problem in a particular notion of *spanning*. We quote that the result [112] has been generalized in every codimension, for general energies and allowing multiplicities respectively in [113, 252, 281]. In [112] the authors make use of the weak* topology of measures for the convergence for surfaces. We also mention that in the extension [252] to any codimension and general energies, a convergence in Hausdorff topology is provided in homological classes. In this way the minimum of the problem is defined as the support of a Radon measure, [109, 248, 268]. Hence, this approach has the advantage of considering also non-rectifiable or not fixed boundaries but it is not easy to apply since the minimization of Hausdorff measures on classes of compact sets could cause lack of lower semicontinuity (it depends on the notion of convergence adopted), which is fundamental for the direct method of the Calculus of Variations. To avoid these difficulties they combine Preiss rectifiability theorem [255] for Radon measure in combination with some variational arguments, such as the introduction of cone and cup competitors. However, we point out that, following the proof in [206] we could avoid the use of the deep Preiss Theorem, using instead a soft argument with Caccioppoli sets (see

[206, Section 3.2]).

2.2.2.1 FORMULATION OF THE PROBLEM

We consider two continuous bodies whose reference, or material, configurations are two right cylinders of lengths L_1, L_2 . The arc-length parameter s of the axis of each cylinder identifies a material (cross) section $\mathcal{A}(s)$, which consists of all points on a plane perpendicular to the axis at s belonging to a simply connected and compact subset of the plane. Like in [15, Ch. 8] we describe each rod by three vector-valued functions $[0, L_i] \rightarrow \mathbb{R}^3$ given by $s \mapsto (\mathbf{r}_i(s), \mathbf{u}_i(s), \mathbf{v}_i(s))$ ($i = 1, 2$).

Now we fix a point O in the euclidean space \mathbb{E}^3 and describe the position in space of each point of the i th rod. Setting $G_i(s) - O = \mathbf{r}_i(s)$ (the so-called *midline*), where $G_i(s)$ is the center of mass of the cross-sections and considering \mathbf{u}_i and \mathbf{v}_i as applied vectors in $G_i(s)$, a generic point P_i of the rod in space is given by the knowledge of the vector

$$\mathbf{p}_i(s, \zeta_1, \zeta_2) = P_i - O = \mathbf{r}_i(s) + \zeta_1 \mathbf{u}_i(s) + \zeta_2 \mathbf{v}_i(s), \quad (2.14)$$

where $(s, \zeta_1, \zeta_2) \in \Omega_i := \{(s, \zeta_1, \zeta_2) \mid s \in [0, L_i], (\zeta_1, \zeta_2) \in \mathcal{A}_i(s)\}$. Hence, Ω_i is the closure of an open set in \mathbb{R}^3 . Moreover, ζ_1 and ζ_2 are not completely free: we require that our body is “*longer than broad*”, so there exists an $R > 0$, the maximum thickness, which has to be small compared to the length L_i , such that $|\zeta_1| < R$ and $|\zeta_2| < R$ for any (s, ζ_1, ζ_2) .

Moreover, we also assume that the rod is *unshearable*, *i.e.* the cross section at any point of the midline remains in the plane orthogonal to the midline at that point, so that \mathbf{u} and \mathbf{v} are orthogonal to the midline, and that this line is *inextensible*. Hence, by these assumptions, we can choose the Kirchhoff rod as a model for the first rod, which is a special case of a Cosserat rod.

Given the function $\mathcal{A}_i(s)$, the position of the midline of each rod is then completely de-

terminated by three scalar parameters with a physical meaning: k'_i and k''_i are the *flexural densities* and ω the *twist density*. The vectors $\mathbf{r}_i, \mathbf{u}_i, \mathbf{v}_i$ satisfy the system of Ordinary Differential Equations

$$\begin{cases} \dot{\mathbf{r}}_i(s) = \mathbf{w}_i(s), \\ \dot{\mathbf{u}}_i(s) = -\omega(s)\mathbf{w}_i(s) - k'_i(s)\mathbf{v}_i, \\ \dot{\mathbf{v}}_i(s) = k'_i(s)\mathbf{u}_i(s) + k''_i(s)\mathbf{w}_i(s); \end{cases} \quad (2.15)$$

where $i = 1, 2$ and $\mathbf{w} = \mathbf{u} \times \mathbf{v}$ is tangent to the midline.

Up to now, the two rods are defined in the same way. We now suppose that the first one is “clamped” by assigning an initial value to its system, *i.e.*

$$(\mathbf{r}_1(0), \mathbf{u}_1(0), \mathbf{v}_1(0)) = (\hat{\mathbf{r}}_1, \hat{\mathbf{u}}_1, \hat{\mathbf{v}}_1). \quad (2.16)$$

Since clearly

$$\dot{\mathbf{w}}_1(s) = -\omega_1(s)\mathbf{u}_1(s) - k''_1(s)\mathbf{v}_1(s)$$

the triple $(\mathbf{u}_1, \mathbf{v}_1, \mathbf{w}_1)$ satisfies a non-autonomous linear system and therefore, then by classical results [174], if the densities k'_1, k''_1 and ω belong to $L^p([0, L_1]; \mathbb{R})$ for some $p \in (1, \infty)$, then the initial-value problem has a unique solution, with $\mathbf{r}_1 \in W^{2,p}([0, L_1]; \mathbb{R}^3)$ and $\mathbf{u}_1, \mathbf{v}_1 \in W^{1,p}([0, L_1]; \mathbb{R}^3)$. It is easy to verify that if $(\hat{\mathbf{u}}_1, \hat{\mathbf{v}}_1, \hat{\mathbf{w}}_1)$ is orthonormal, so is $(\mathbf{u}_1(s), \mathbf{v}_1(s), \mathbf{w}_1(s))$ for every $s \in [0, L_1]$. For every $(\hat{\mathbf{u}}_1, \hat{\mathbf{v}}_1, \hat{\mathbf{w}}_1) \in (\mathbb{R}^3)^3$ we then set

$$\mathbf{z}_1 = (k'_1, k''_1, \omega_1) \in V_1 := L^p([0, L_1]; \mathbb{R}^3).$$

As for the second rod, since we do not know *a priori* its position in space, we need some information also on the orientation of one of its orthonormal frames. Therefore we seek a

solution of the form

$$\mathbf{z}_2 = (k_2', k_2'', \omega_2, \hat{\mathbf{r}}_2, \hat{\mathbf{u}}_2, \hat{\mathbf{v}}_2, \hat{\mathbf{w}}_2) \in V_2 := L^p([0, L_2]; \mathbb{R}^3) \times \mathbb{R}^3 \times \mathbb{R}^3 \times \mathbb{R}^3 \times \mathbb{R}^3$$

where $\hat{\mathbf{u}}_2, \hat{\mathbf{v}}_2, \hat{\mathbf{w}}_2$ are orthonormal and $\hat{\mathbf{r}}_2$ gives their application point.

Now the system (2.15)_{2,3} and (2.16), together with the knowledge of $\hat{\mathbf{r}}_2$, fully fixes the position in space of the second midline.

Since we want to deal with closed loops, we have to restrict to a suitable subclass of descriptors by imposing topological constraints. Obviously we impose the closure of the midlines, *i.e.*

$$\mathbf{r}_i(0) = \mathbf{r}_i(L_i) \quad (i = 1, 2) \quad (2.17)$$

and, since we do not want interpenetration, we need to have also continuity of the tangent vectors, so that for $i = 1, 2$

$$\mathbf{w}_i(0) = \mathbf{w}_i(L_i). \quad (2.18)$$

The simple determination of the midline, however, does not completely fix the shape of the loops if they are three-dimensional. Indeed, the same midline may correspond to different bodies if the cross-sections $\mathcal{A}_i(s)$ are rotated around the midline before being glued, and the final rotation angle depends on the shape of the cross-section. On the other hand, since they are undeformable, the information to be encoded reduces to fixing a point in every section. First of all we recall the notion of *isotopy*, which will be useful also later on.

Definition 2.2.1. Let $\eta_i : [a, b] \rightarrow \mathbb{R}^3$, with $i = 1, 2$, be two continuous curves with $\eta_i(a) = \eta_i(b)$. η_1 and η_2 are said to be *isotopic*, $\eta_1 \simeq \eta_2$, if there are open neighborhoods N_1 of $\eta_1([a, b])$, N_2 of $\eta_2([a, b])$ and a continuous mapping $\Phi : N_1 \times [0, 1] \mapsto \mathbb{R}^3$ such that $\Phi(N_1, \tau)$ is homeomorphic to N_1 for all $\tau \in [0, 1]$, $\Phi(\cdot, 0)$ is the identity, $\Phi(N_1, 1) = N_2$ and $\Phi(\eta_1([a, b]), 1) = \eta_2([a, b])$.

The isotopy class is then stable with respect to diffeomorphism and define also the *knot type*. Another very useful notion is the linking number.

Definition 2.2.2. Let η_1, η_2 be two absolutely continuous disjoint closed curves in \mathbb{E}^3 .

The number

$$L(\eta_1, \eta_2) = \frac{1}{4\pi} \int_a^b \int_a^b \frac{\eta_1(s) - \eta_2(t)}{|\eta_1(s) - \eta_2(t)|^3} \cdot (\eta_1'(s) \times \eta_2'(t)) ds dt$$

is called the *linking number* between η_1 and η_2 .

It is well-known [241] that L is always an integer and that is invariant in the isotopy class of the two curves.

To encode a possible rotation of the cross-sections, we then proceed as follows for each of the two rods. Since the thickness is nonzero, we can consider a curve “near” the midline \mathbf{r}_i , which could be not a closed one since the endpoints may be different. Joining them without intersecting the midline, we obtain a closed curve which has a certain linking number with the midline. Of course, every possible midline has to preserve this number, so we will impose this constraint on the midline. At this point, once we know the midline, the position of the nearby curve is fixed and so is its every cross-section, thus completely defining[‡] the shape of the loops, which we will indicate by $\Lambda[\mathbf{z}]$, see Fig. 2.10.

Finally, we want to impose that the two loops form a link. We then come back to the two midlines, and we suppose that they are linked with a given linking number $L_{12} \in \mathbb{Z}$. As they are closed sets, they admit disjoint neighborhoods, which we can suppose tubular without loss of generality ([239] pp. 199-223). By a further shrinking to the diameter of $\mathcal{A}(s)$ we have that both rods are disjoint and linked one each other with the given linking number.

At this point, the shape of the two solids is assigned once we know $\mathbf{z}_1, \mathbf{z}_2$, but we still have to avoid local and global interpenetration, which is clearly unphysical. To this end,

[‡]Up to a set of \mathcal{L}^1 -zero measure which is irrelevant.

we first introduce the elastic and potential energy stored in the loops.

In the following, since the elastic energy density depends only on a single scalar variable and to introduce a more comprehensible notation to treat this problem, we refer to it using the classical notation f . The elastic energy is supposed to be of the classical form (see for instance [106, Ch. 2])

$$E_{\text{el}_i}[\mathbf{z}_i] := \int_0^{L_i} f_i(\mathbf{z}_i(s), s) ds \quad (2.19)$$

where $f_i(\cdot, s)$ are continuous and convex for any $s \in [0, L_i]$ and $f_i(a, \cdot)$ is measurable for any $a \in \mathbb{R}^3$. Since we are going to apply the Direct Method of the Calculus of Variations, we suppose that there exist positive constants C_i, D_i such that In view of this, the total elastic energy

$$E_{\text{el}}[\mathbf{z}] = E_{\text{el}_1}[\mathbf{z}_1] + E_{\text{el}_2}[\mathbf{z}_2] := \int_I f(\mathbf{z}(\xi), \xi) d\xi,$$

where $I = [0, L_1] \times [0, L_2]$, $\mathbf{z} = (\mathbf{z}_1, \mathbf{z}_2)$ and ξ is a vector variable, is easily seen to be coercive on $V := V_1 \times V_2$.

$$f_i(a, s) \geq C_i |a|^p + D_i \quad \forall (a, s) \in \mathbb{R}^3 \times [0, L_i]. \quad (2.20)$$

As for the potential energy of the weight, it is given for each loop by

$$E_{\mathbf{g}_i}[\mathbf{z}_i] = - \int_0^{L_i} \rho_i(s) \mathbf{g} \cdot (G_i(s) - O) ds$$

where $\rho_i > 0$ stand for the mass of each section of the rod and \mathbf{g} denotes the acceleration of gravity.

It is worth insisting on the fact that the weight plays a different role in the two rods: in the first it acts essentially deforming only the midline, while in the second it influences the global positioning of the rod, and could draw it away without appropriate conditions of non intersection, that we will introduce below.

We also set

$$E_{\text{loop}}[\mathbf{z}] = E_{\text{el}_1}[\mathbf{z}_1] + E_{g_1}[\mathbf{z}_1] + E_{\text{el}_2}[\mathbf{z}_2] + E_{g_2}[\mathbf{z}_2].$$

We now need to set sufficient conditions for the local and global non-interpenetration of our configuration.

As for the first, it is well known ([15, Thm. 6.2]) that for Kirchhoff rods the condition is equivalent to the existence of two convex, homogeneous functions $g_i(\xi_1, \xi_2, s)$ such that $g(0, 0, s) = 0$ and

$$g_i(k_i'(s), k_i''(s), s) < 1 \quad \text{for a.e. } s \in [0, L_i], \quad (i = 1, 2). \quad (2.21)$$

However, this will not define a weakly closed set in the space of solutions, due to the strict inequality. Therefore, we will require the weaker condition

$$g_i(k_i'(s), k_i''(s), s) \leq 1 \quad \text{for a.e. } s \in [0, L_i], \quad (i = 1, 2). \quad (2.22)$$

even if this could let some point to infinite compression, and to prevent this we impose the natural growth condition on the elastic energy as

$$f_i(\mathbf{z}_i(s), s) \rightarrow +\infty \quad \text{as} \quad g_i(k_i'(s), k_i''(s), s) \rightarrow 1, \quad (i = 1, 2) \quad (2.23)$$

i.e. the elastic energy approaches infinity under complete compression (remember that f_i may depend on g_i). By this assumption we have that the equality in (2.21) can occur only on a set of measure zero for configurations with finite energy.

At this point it is not difficult to prove the next theorem.

Theorem 2.2.3. *Let $\mathbf{z} = (\mathbf{z}_1, \mathbf{z}_2) \in V = V_1 \times V_2$ satisfies (2.22), f_i with $i = 1, 2$ satisfies (2.23) and $E_{\text{el}}(\mathbf{z}) < +\infty$. Then the mapping $(s, \zeta_1, \zeta_2) \mapsto \mathbf{p}[\mathbf{z}](s, \zeta_1, \zeta_2) = (\mathbf{p}_1, \mathbf{p}_2)[\mathbf{z}_1, \mathbf{z}_2](s, \zeta_1, \zeta_2)$ is*

locally injective on $\text{int } \Omega$. Moreover, this mapping is open on $\text{int } \Omega$.

Proof. The proof can be made easily by following the proof presented in [156] taking into account the fact that we can study the two rods separately since it is sufficient to reduce the proof in an open neighborhood well-contained in each rod. \square

As for the global injectivity, we must distinguish each loop and their union. First of all, Ciarlet and Nečas [89] proved that if this condition holds (2.24)

$$\int_{\Omega_i} \det \frac{\partial \mathbf{p}_i(s, \zeta_1, \zeta_2)}{\partial (s, \zeta_1, \zeta_2)} d(s, \zeta_1, \zeta_2) \leq \mathcal{L}^3(\mathbf{p}_i[\mathbf{z}_i](\Omega_i)), \quad (2.24)$$

the global injectivity is true. Moreover, in our case it can be rewritten as

$$\int_{\Omega_i} (1 - \zeta_1 k_i'(s) - \zeta_2 k_i''(s)) d(s, \zeta_1, \zeta_2) \leq \mathcal{L}^3(\mathbf{p}_i[\mathbf{z}_i](\Omega_i)). \quad (2.25)$$

Hence, assuming (2.25) true, one has the global injectivity of the functions \mathbf{p}_i on each rod. Roughly speaking, this condition guarantees that parts of the rod which are far away from each other in the reference configuration, cannot penetrate each other after large deformations.

We will then suppose (2.25) for the non-interpenetration of each rod. At this point, for the union of the two, we notice that the midlines (which are closed sets) have to be disjoint and therefore there exist $R > 0$ such that the maximum diameter of the sections is less than R it holds

$$\forall \mathbf{z} \in V \quad \mathbf{p}_1[\mathbf{z}_1](\Omega_1) \cap \mathbf{p}_2[\mathbf{z}_2](\Omega_2) = \emptyset. \quad (2.26)$$

We will then suppose the sections so small that (2.26) is verified.

Now we can prove the following result.

Theorem 2.2.4. *Let \mathbf{z} be an element of $V = V_1 \times V_2$ such that $E_{\text{loop}}[\mathbf{w}] < +\infty$ and f_i with*

$i = 1, 2$ satisfy (2.23). Suppose that $\mathbf{p}_1[\mathbf{z}](\Omega_1) \cap \mathbf{p}_2[\mathbf{z}](\Omega_2) = \emptyset$ and \mathbf{z}_i satisfies (2.22) and (2.25). Then the mapping $(s, \zeta_1, \zeta_2) \mapsto \mathbf{p}[\mathbf{z}](s, \zeta_1, \zeta_2)$ is globally injective on $\text{int } \Omega$.

Proof. By (2.26) it suffices to show the global injectivity of \mathbf{p}_1 and repeat the arguments for \mathbf{p}_2 . Let us fix a configuration $\mathbf{z}_1 \in V_1$, by Theorem 2.2.3 there is a set \mathcal{I}_0 of measure zero such that

$$\limsup_{(\tilde{s}, \tilde{\zeta}_1, \tilde{\zeta}_2) \rightarrow (s, \zeta_1, \zeta_2)} \frac{\|\mathbf{p}_1(\tilde{s}, \tilde{\zeta}_1, \tilde{\zeta}_2) - \mathbf{p}_1(s, \zeta_1, \zeta_2)\|}{\|(\tilde{s}, \tilde{\zeta}_1, \tilde{\zeta}_2) - (s, \zeta_1, \zeta_2)\|} < \infty \quad \forall (s, \zeta_1, \zeta_2) \in \Omega'_1,$$

where Ω'_1 is defined as $\Omega_1 \setminus \Omega_1(\mathcal{I}_0)$ and

$$\Omega_1(\mathcal{I}_0) = \{(s, \zeta_1, \zeta_2) \in \Omega_1 : s \in \mathcal{I}_0\}.$$

Obviously** $\mathcal{L}^3(\mathbf{p}_1[\mathbf{z}_1](\Omega_1(\mathcal{I}_0)))$ is equal to zero. By the coarea formula^{††} ([135], pp. 243-244), we have

$$\int_{\Omega'_1} (1 - \zeta_1 k'_1 - \zeta_2 k''_1) \, d(s, \zeta_1, \zeta_2) = \int_{\mathbf{p}_1(\Omega'_1)} \text{card}\{\mathbf{p}_1^{-1}(\mathbf{q})\} \, d\mathbf{q}, \quad (2.27)$$

**The complete proof of this statement is in [286]. However, we can give a simple and empirical idea of the proof: since \mathcal{I}_0 has measure zero, the cross-sections such that their arc-length parameter s belongs to \mathcal{I}_0 are the elements of the set $\Omega_1(\mathcal{I}_0)$. Hence, $\mathcal{L}^3(\Omega_1(\mathcal{I}_0)) = 0$. But now, since \mathbf{p}_1 is a regular function, we can think that *sets of measure zero are mapped into sets of measure zero*.

^{††}Let consider two locally Lipschitz continuous functions $f : \mathbb{R}^n \rightarrow \mathbb{R}$ and $g : \mathbb{R}^n \rightarrow \mathbb{R}^m$ with $m \leq n$. Then

$$\int_{\mathbb{R}^n} f(x) \sqrt{\det [dg(x)(dg(x))^T]} \, d\mathcal{L}^n(x) = \int_{\mathbb{R}^m} \left(\int_{g^{-1}(y)} f(x) \, d\mathcal{H}^{n-m}(x) \right) d\mathcal{L}^m(y).$$

If $m = n$, the quantity $\mathcal{H}^0 = \text{card}$, *i.e.* the function which counts the elements of a set [135].

where \mathbf{p}_1^{-1} is the inverse of the mapping \mathbf{p}_1 . Therefore, using (2.25) and (2.27), it yields

$$\begin{aligned} \mathcal{L}^3(\mathbf{p}_1[\mathbf{z}_1](\Omega_1)) &= \int_{\mathbf{p}_1[\mathbf{z}_1](\Omega_1)} d\mathbf{q} = \int_{\mathbf{p}_1[\mathbf{z}_1](\Omega_1(\mathcal{I}_0))} d\mathbf{q} \leq \\ &\int_{\mathbf{p}_1[\mathbf{z}_1](\Omega_1(\mathcal{I}_0))} \text{card}\{\mathbf{p}_1^{-1}(\mathbf{q})\} d\mathbf{q} = \int_{\Omega'_1} (1 - \zeta_1 k'_1 - \zeta_2 k''_1) d(s, \zeta_1, \zeta_2) = \\ &\int_{\Omega_1} (1 - \zeta_1 k'_1 - \zeta_2 k''_1) d(s, \zeta_1, \zeta_2) \leq \mathcal{L}^3(\mathbf{p}_1[\mathbf{z}_1](\Omega_1)). \end{aligned}$$

Hence,

$$\text{card}\{\mathbf{p}_1^{-1}(\mathbf{q})\} = 1 \quad \text{for almost all } \mathbf{q} \in \mathbf{p}_1[\mathbf{z}_1](\Omega_1), \quad (2.28)$$

which combined with Theorem 2.2.3 ensure the injectivity of \mathbf{p}_1 on $\text{int } \Omega_1$ and then the global injectivity of \mathbf{p} on $\text{int } \Omega$. \square

Finally, the energy stored in a film that will deform the link is defined as

$$E_{\text{film}}(S) = 2\sigma \mathcal{H}^2(S), \quad (2.29)$$

where \mathcal{H}^d represents the d -dimensional Hausdorff measure. When a soap film is in stable equilibrium, as in eq. (2.29), any small change in its area, S , will produce a corresponding change in its energy E , providing σ remains constant. As E_{film} is minimized when the film is in stable equilibrium, S will be minimized. Precisely, in (2.29), we do not consider what happens between the film and the bounding loop, *i.e.* the energy associated with the liquid/solid interface.

Anyway, we still cannot provide the final expression for the energy since we have not yet specified how the film is attached to each loop. Since in our case we have a boundary with non vanishing thickness, to formulate the idea of a solution we have to give a good definition of the terms *surface*, *area* and *contact*, which we will call *span*. We need also a precise mathematical formulation of the conditions which explain how the liquid film spans

the bounding loop without detaching from it, after which we will end up with the final expression of the functional to be minimized. We begin with some recalls of topology.

Definition 2.2.5. Let $H = \bigcup_{j \in J} H_j$ be a closed compact 3-dimensional submanifold of \mathbb{E}^3 consisting of connected components H_j . We say that a circle γ embedded in $\mathbb{E}^3 \setminus H$ is a *simple link* of H if there exists $i \in J$ such that the linking numbers $L(\gamma, H_j)$ verify

$$|L(\gamma, H_i)| = 1, \quad L(\gamma, H_j) = 0 \quad j \neq i.$$

Clearly, a simple link “winds around” only one component of H (see figure 2.10). Precisely, the definition of the linking number between a closed subset and a curve is exactly the one given before (Definition 2.2.2) by considering compactification of the \mathbb{E}^3 (for more details see [278], pp.132-136).

Definition 2.2.6. We say that a compact subset $K \subseteq \mathbb{E}^3$ *spans* H if every simple link of H intersects K .

This idea is crucial: we need spanning sets (in simple cases, surfaces) crossing every simple link: in this way it is impossible for K to be “detached” from H , or having “holes” which are not occupied by other components of H (see figure 2.10).

However, in our case we need a still more general definition, because in our problem H is not given a priori since $H = \Lambda[\mathbf{z}]$, *i.e.* it depends on the considered configuration.

Now let H be an arbitrary closed subset of \mathbb{E}^3 and consider the family

$$C_H = \{\gamma : \mathbb{S}^1 \rightarrow \mathbb{E}^3 \setminus H : \gamma \text{ is a smooth embedding of } \mathbb{S}^1 \text{ into } \mathbb{E}^3\}.$$

A set $C \subseteq C_H$ is said to be *closed by homotopy* (with respect to H) if it contains all elements belonging to the same homotopy class.

Definition 2.2.7. Given $C \subseteq C_H$ closed by homotopy, we say that a relatively closed sub-

set $K \subset \mathbb{E}^3 \setminus H$ is a C -spanning set of H if

$$K \cap \gamma \neq \emptyset \quad \forall \gamma \in C.$$

We denote by $F(H, C)$ the family of all C -spanning sets of H .

Notice that the set spanned by the surface, can be any closed set in \mathbb{E}^3 , so we can consider $H = \Lambda[\mathbf{z}]$ with finite cross-section, as in our case and not only a line as in the Plateau's problem. Nevertheless, the spanning surface depends only on the choice of the homotopy class and not to the configuration \mathbf{z} . Hence, we can give the following definition.

Definition 2.2.8. We call a set $D_{\Lambda[\mathbf{z}]} \subseteq C_{\Lambda[\mathbf{z}]}$ a $D_{\Lambda[\mathbf{z}]}$ -spanning set of $\Lambda[\mathbf{z}]$ if it contains all the smooth embeddings γ which are not homotopic to a constant and which have linking number one with both rods. For the sake of brevity, we will write D in place of $D_{\Lambda[\mathbf{z}]}$.

Finally, we denote $F(\Lambda[\mathbf{z}], D)$ the family of D -spanning sets of $\Lambda[\mathbf{z}]$ with linking number one with both components (see Fig 2.10).

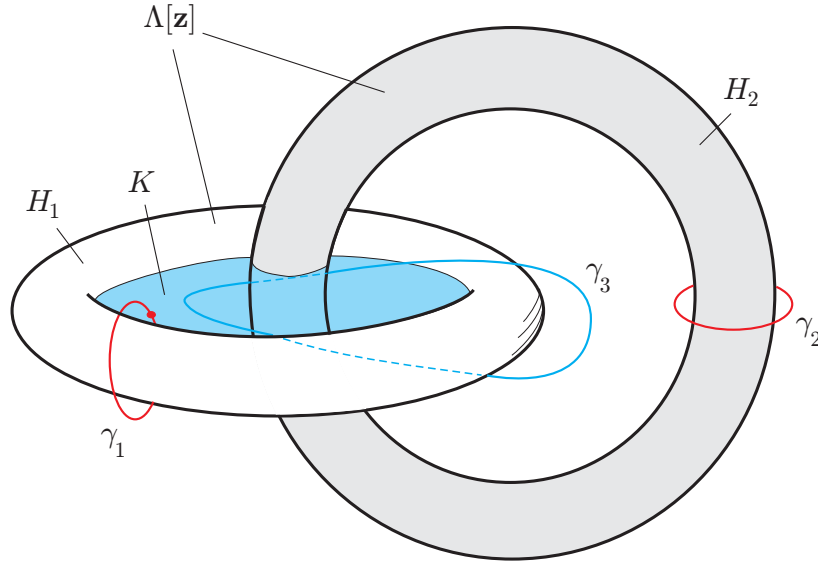


Figure 2.10: γ_i ($i = 1, 2$) are simple links for H_i while $\gamma_3 \in F(\Lambda[\mathbf{w}])$. Even if K is not D -spanning for the whole system, notice how $\gamma_1 \cap K \neq \emptyset$.

We are now in position to set the energy functional for our problem. We set

$$E_{\text{KP}}[\mathbf{z}] := E_{\text{loop}}[\mathbf{z}] + \inf\{E_{\text{film}}(S) : S \text{ is a } D\text{-spanning set of } \Lambda[\mathbf{z}]\}, \quad (2.30)$$

where $\mathbf{z} \in V$ and verifies all the above-mentioned constraints. Precisely, the inf in the equation (2.30) is necessary since we want to eliminate the dependence on the spanning surface S and writing everything in the terms of the configuration \mathbf{z} only.

At this point a first important result holds.

Theorem 2.2.9. *Let two circumferences $\eta_i : [0, L_i] \rightarrow \mathbb{E}^3$ and $M \in \mathbb{R}$ and $n_1, n_2 \in \mathbb{Z}$ three constants be given. Then, the set*

$$\begin{aligned} U_{M, n_i, \eta_i} := \{ \mathbf{z} = (\mathbf{z}_1, \mathbf{z}_2, \hat{\mathbf{r}}_2, \hat{\mathbf{u}}_2, \hat{\mathbf{v}}_2) \in V = V_1 \times V_2 : E_{\text{loop}}[\mathbf{z}] < M; \\ (2.17), (2.18), (2.25) \text{ and } (2.26) \text{ hold}; L(\mathbf{z}_i) = n_i; \\ L_{12} = 1 \text{ and } (\mathbf{r}_1[\mathbf{z}_1], \mathbf{r}_2[\mathbf{z}_2]) \simeq (\eta_1, \eta_2) \} \end{aligned} \quad (2.31)$$

is weakly closed in V .

Proof. If $U_{M, n_i, \eta_i} = \emptyset$ the thesis is obviously true.

If $U_{M, n_i, \eta_i} \neq \emptyset$, it is an extension to Schuricht's theorems 3.9, 4.5 and 4.6 [286], by remembering that

$$\mathbf{p} = (\mathbf{p}_1, \mathbf{p}_2) \quad \mathbf{z} = (\mathbf{z}_1, \mathbf{z}_2).$$

Moreover, since \mathbf{p}_i are two open maps and Ω_i are the closure of two open sets in \mathbb{E}^3 , condition (2.26) yields the intersection of two closed sets, which is obviously a closed set and concludes the proof. \square

2.2.2.2 MAIN RESULTS

Now we want to prove the existence of a solution to the Kirchhoff-Plateau problem, *i.e.* the existence of a minimizer of E_{KP} given by (2.30) in the class U_{M,n_i,η_i} . As a first step we find a minimizer of each its two terms. Obviously, we cannot say that the solution of our problem will be the sum of them, but this will be useful to prove the main result.

ENERGY MINIMIZER FOR THE BOUNDING LOOP For the first term in the right-hand side of (2.30) we use a quite straightforward application of the direct method of the Calculus of variations. Recall that its expression is

$$\begin{aligned} E_{\text{loop}}[\mathbf{z}] &: V \rightarrow \mathbb{R} \cup \{+\infty\} \\ \mathbf{z} \mapsto E_{\text{loop}}[\mathbf{z}] &= E_{\text{el}}[\mathbf{z}] + E_{\text{g}}[\mathbf{z}] = \int_I f(\mathbf{z}(\xi), \xi) d\xi + E_{\text{g}}[\mathbf{z}]. \end{aligned}$$

In order to verify if we can apply this method to E_{loop} , we follow the following steps.

First, we need to show that E_{loop} is bounded from below and proper, *i.e.* $E_{\text{loop}} \neq +\infty$. E_{el} is proper by definition. As for the boundedness, we can focus only on E_{el} , because E_{g} is always bounded from below, since the midline is bounded. Therefore, by (2.20) we immediately obtain

$$E_{\text{el}_i}[\mathbf{z}] \geq C_i \int_0^{L_i} |\mathbf{z}_i|^p ds + D_i L_i \geq D_i L_i > -\infty. \quad (2.32)$$

Hence, E_{loop} is bounded from below and moreover $E_{\text{loop}}[\mathbf{z}] = +\infty$ only under complete compression.

Next, consider a sequence $\{\mathbf{z}_k\}_{k \in \mathbb{N}}$ such that

$$\lim_k E_{\text{loop}}[\mathbf{z}_k] = \inf_{\mathbf{z} \in V} E_{\text{loop}}[\mathbf{z}] = m.$$

Obviously, it exists \bar{k} such that $\forall k \geq \bar{k}$

$$E_{\text{loop}}[\mathbf{z}_k] \leq m + 1.$$

Now, we notice that this sequence is bounded: this follows easily from the boundedness of the clamping parameters and by coercitivity, since

$$\int_0^{L_i} |\mathbf{z}_{i_k}|^p dx \leq \frac{1}{C_i} \int_0^{L_i} f_i(\mathbf{z}_{i_k}(s), s) ds - \frac{D_i L_i}{C_i} \leq \frac{1}{C_i}(m + 1) - \frac{D_i L_i}{C_i} \leq A,$$

where $A > 0$ is a constant. Since V is a reflexive space, \mathbf{z}_k admits a weakly convergent subsequence, *i.e.* up to subsequences one has

$$\exists \mathbf{z} \in V : \quad \mathbf{z}_k \rightharpoonup \mathbf{z}.$$

Now we show that $E_{\text{loop}}[\mathbf{z}]$ is weakly-lower semicontinuous (wlsc) in V . Remember that $E_{\text{loop}} = E_{\text{el}} + E_{\text{g}}$ and all linear functionals are wlsc, so we can focus on the total stored energy E_{el} . By assumptions made on E_{el_i} , *i.e.* the hypotheses made on f_i , we obtain first that E_{el} is wlsc and then the total energy associated to the bounding loop.

To introduce and to prove the following theorem, we have to remember that we are looking for the solution of our problem not in a generic Banach space but in U_{M,n,η_i} , *i.e.* it has to satisfy the physical and the topological constraints imposed to the problem. Therefore:

Theorem 2.2.10. *If there is at least one admissible*

$$\bar{\mathbf{z}} = (\bar{\mathbf{z}}_1, \bar{\mathbf{z}}_2) \in U_{M,n_i,\eta_i}$$

with $M \in \mathbb{R}$, $n_i \in \mathbb{N}$ and $\eta_i : [0, L_i] \rightarrow \mathbb{E}^3$, then the variational problem described above has a

minimizer, i.e. there exists a minimizer $\mathbf{z} \in U_{M,n_i,\eta_i}$ for the loop energy functional.

Proof. Since $\bar{\mathbf{z}} \in U_{M,n_i,\eta_i}$, i.e. it is a competitor, $U_{M,n_i,\eta_i} \neq \emptyset$. So, let $\{\mathbf{z}_k\}_{k \in \mathbb{N}} \in U_{M,n_i,\eta_i}$ a minimizing sequence such that $E_{\text{loop}}[\mathbf{z}_k] < M$ for some $M \in \mathbb{R}$ be given.

By the coercitivity of f_i with $i = 1, 2$, we obtain that U_{M,n_i,η_i} is a bounded subset in V . So, we can extract a weakly converging subsequence $\mathbf{z}_{k_h} \rightharpoonup \mathbf{z}$. Moreover, as U_{M,n_i,η_i} is weakly closed in V (Theorem 2.2.9), so $\mathbf{z} \in U_{M,n_i,\eta_i}$.

Finally, the weak lower semicontinuity of $E_{\text{loop}}[\mathbf{z}]$ yields

$$E_{\text{loop}}[\mathbf{z}] \leq \liminf_h E_{\text{loop}}[\mathbf{z}_{k_h}] = \lim_k E_{\text{loop}}[\mathbf{z}_k] = \inf_{\mathbf{z} \in U_{M,n_i,\eta_i}} E_{\text{loop}}[\mathbf{z}],$$

where \mathbf{z}_{k_h} is a subsequence of the chosen minimizing sequence \mathbf{z}_k . Therefore, the weak limit \mathbf{z} is a global minimizer. □

AREA-MINIMIZING SPANNING SURFACE Up to now, we only proved the existence of an energy-minimizing configuration for the bounding loop in the absence of the liquid film.

Now we want to show the existence of an area-minimizing spanning surface for the link. If $\Lambda[\mathbf{z}]$ is rigid, De Lellis *et al.* [112] proved an important result:

Theorem 2.2.11. *Fix $\mathbf{z} \in V$. If*

$$m_0 := \inf\{E_{\text{film}}(S) : S \in F(\Lambda[\mathbf{z}], D)\} < +\infty,$$

then

1. $F(\Lambda[\mathbf{z}], D)$ is a good class;
2. there exists $K[\mathbf{z}]$ a relatively closed subset of $\mathbb{R}^3 \setminus \Lambda[\mathbf{z}]$ such that $K[\mathbf{z}] \in F(\Lambda[\mathbf{z}], D)$ and $K[\mathbf{z}]$ is a minimizer, i.e. $E_{\text{film}}(K[\mathbf{z}]) = m_0$;

3. $K[\mathbf{z}]$ is a countably \mathcal{H}^2 -rectifiable set and it is an $(M, 0, \infty)$ -minimal set in $\mathbb{R}^3 \setminus \Lambda[\mathbf{z}]$ in the sense of Almgren.

For a precise definition of *good class* and $(M, 0, \infty)$ -minimal set in the sense of Almgren, see respectively [112] and [5]. In our case the first one is just a family of subsets in which we can control their measures. Namely, it exists a selected and well-defined competitor L with finite 2-dimensional Hausdorff measure which control the measure of each element of the good class. The second one, instead, is a property of regularity on the subset $K[\mathbf{z}]$. The theorem is just a combination of Theorem 2 and 3 in [112].

MAIN RESULT Now we come to our main result. Since we are dealing with approximating surfaces, we need to specify the notion of convergence of surfaces. We do this following Giusteri *et al.* [156].

Definition 2.2.12. Let A, B be two non empty subsets of a metric space (M, d_M) . The *Hausdorff distance* between A and B is defined by

$$d_H(A, B) := \max\left\{\sup_{a \in A} \inf_{b \in B} d_M(a, b), \sup_{b \in B} \inf_{a \in A} d_M(a, b)\right\}.$$

If we consider all non-empty subsets of M , then d_H is a *pseudo-metric*, *i.e.* we can always find two subsets A, B with $A \neq B$ such that $d_H(A, B) = 0$. However, the set $K(M)$ of non empty *compact* subsets of M is a metric space. Moreover, the topology induced by d_H on all closed non empty subsets of M does not depend on d_M and it is said *Hausdorff topology*.

The problem we have to solve is connected to the fact that $\Lambda[\mathbf{z}_k]$, the closed subset in \mathbb{R}^3 occupied by the whole link, changes along the minimizing sequence. So we have to consider sequences of nonempty closed sets, possibly converging to a closed set, which might be our minimal link.

Theorem 2.2.13. *Let Λ_k a sequence of closed non empty subsets of \mathbb{E}^3 converging in the Hausdorff topology to a closed set $\Lambda \neq \emptyset$. Assume that*

i) $\forall k \in \mathbb{N}, S_k \in F(\Lambda_k[\mathbf{z}], D)$, where $F(\Lambda_k[\mathbf{z}], D)$ is a good class;

ii) S_k is a countably \mathcal{H}^2 -rectifiable set;

iii) $\mathcal{H}^2(S_k) = \inf\{\mathcal{H}^2(S) : S \in F(\Lambda_k[\mathbf{z}], D)\} < +\infty$.

Then the sequence of measures $\mu_k := \mathcal{H}^2 \llcorner S_k$ is a bounded sequence, $\mu_k \xrightarrow{} \mu$, up to subsequences, and*

$$\mu \geq \mathcal{H}^2 \llcorner S_\infty, \text{ where } S_\infty = (\text{supt } \mu) \setminus \Lambda \text{ and it is a } \mathcal{H}^2\text{-rectifiable set.}$$

Proof. Let $\mu_k = \mathcal{H}^2 \llcorner S_k$ and $S_k \in F(\Lambda_k[\mathbf{z}], D)$. Since $F(\Lambda_k[\mathbf{z}], D)$ is a good class, for all $J \in F(\Lambda_k[\mathbf{z}], D)$ one has

$$\mu_k(J) = \mathcal{H}^2 \llcorner S_k(J) = \mathcal{H}^2(S_k \cap J) \leq \mathcal{H}^2(J) \leq \mathcal{H}^2(L) < +\infty,$$

where L is the generic competitor in the *good class*. Hence, μ_k is a bounded Radon measure, therefore ([132], pp. 54-59), up to a subsequence (not relabeled), $\mu_k \xrightarrow{*} \mu$.

Now let $f \in C_c^\infty(\mathbb{R}^n)$ with $0 \leq f \leq \chi_{B(x,r)}$; by the weak* convergence of μ_k we have

$$\int_{B(x,r)} f d\mu = \lim_k \int_{B(x,r)} f d\mu_k \leq \liminf_k \mu_k(B(x,r))$$

so that $\mu(B(x,r)) \leq \liminf_k \mu_k(B(x,r))$.

Since $\Lambda_k \xrightarrow{H} \Lambda$, for any $x \in S_\infty = (\text{supt } \mu) \setminus \Lambda$ we can find a radius r such that

$$0 < r < d(x, \Lambda) \iff d(x, \Lambda_k) > \frac{1}{2} d(x, \Lambda).$$

Moreover, if we assume that $\mu(\mathbb{R}^n) = \lim_k \mu_k(\mathbb{R}^n)$, combining De Lellis' result with this additional specification, we have that

$$\mu = \theta \mathcal{H}^2 \llcorner S_\infty \text{ with } S_\infty = (\text{supt } \mu) \setminus \Lambda.$$

Indeed

$$\begin{aligned} \mu(\mathbb{R}^n) &= \lim_k \mu_k(\mathbb{R}^n) \geq \liminf_k \mu_k(\mathbb{R}^n) = \\ &= \liminf_k \mu_k(B(x, r)) + \liminf_k \mu_k(\mathbb{R}^n \setminus \overline{B(x, r)}) \\ &\geq \mu(B(x, r)) + \mu(\mathbb{R}^n \setminus \overline{B(x, r)}) = \mu(\mathbb{R}^n), \end{aligned} \quad (2.33)$$

where the last equivalence is true because if a set $\{r > 0 : \mu(\partial B(x, r)) \neq 0\}$ is countable, then its Lebesgue measure is zero. Finally, $\mu(\mathbb{R}^n) = \lim_k \mu_k(\mathbb{R}^n)$ is obviously true because of the definition of μ_k and the convergence in the Hausdorff topology.

Let's see that S_∞ is a \mathcal{H}^2 -rectifiable set. If we fix $x \in S_\infty$, *i.e.* $d(x, \Lambda) > 0$, the function $r \mapsto \mu(B(x, r))/r^n$ is increasing on $(0, d(x, \Lambda_k))$ (see, for instance, the Step two of the proof of [112, Thm.2]). By using Preiss' results [255], we can find immediately that

$$\mu = \theta \mathcal{H}^2 \llcorner \tilde{K}$$

where \tilde{K} is a \mathcal{H}^2 -rectifiable set. By the definition of the support of a measure $\tilde{K} = S_\infty$. □

However, this is still not enough. Up to now, we proved in a separate way that the two functionals, the one associated with the elastic link and the other with the film, admit global minimizers.

Now, first we have to rewrite the second result in terms of the configurations of our sys-

tem since we only prove the existence of the minimal surface in the presence of a changing boundary, and then we have to write the solution to our problem, *i.e.* making a balance of the two contributions.

Theorem 2.2.14. *Let us suppose that*

i) $\{\mathbf{z}_k\}_{k \in \mathbb{N}} \subseteq U_{M, n_i, \eta_i}$ a sequence such that $\mathbf{z}_k \rightarrow \mathbf{z}$ with $\mathbf{z} \in U_{M, n_i, \eta_i}$;

ii) $S_k \in F(\Lambda[\mathbf{z}_k], D)$;

iii) γ is a smooth embedding like the one defined in Definition 2.2.8.

Then there exist two constants $\varepsilon > 0$ and $M = M(\varepsilon) > 0$ such that $U_{2\varepsilon}(\gamma) \subseteq \mathbb{E}^3 \setminus \Lambda[\mathbf{z}]$ and $\forall k \geq k_0$

$$\mathcal{H}^2(S_k \cap U_\varepsilon(\gamma)) \geq M,$$

where $U_r(\gamma)$ denotes the tubular neighborhood of radius $r > 0$ around γ , namely the union of all balls of radius r centered at the points of γ .

Moreover, Theorem 2.2.14 says that the intersection between the sequence of the surface $\{S_k\}$, for large k , and a neighborhood of the smooth embedding γ is not a point but a set with positive measure. Since the tubular neighborhood $U_\varepsilon(\gamma)$ depends only on the embedding γ , we can state that the surface S_∞ which realizes the area minimal set (Theorem 2.2.13) belongs to $F(\Lambda[\mathbf{z}], D)$. This theorem is fundamental in order to rewrite everything in terms of the configuration \mathbf{z} only, *i.e.* we solve the first gap mentioned before. Indeed, suppose true Theorem 2.2.13 and 2.2.14; if we assume by contradiction that $S_\infty \notin F(\Lambda[\mathbf{z}], D)$, this would mean that

$$\exists \gamma \in D_{\Lambda[\mathbf{z}]} : \begin{cases} \gamma \cap S_\infty = \emptyset \\ L(\gamma, \mathbf{r}_1) \neq 1 \\ L(\gamma, \mathbf{r}_2) \neq 1. \end{cases}$$

If $\gamma \cap S_\infty = \emptyset$, we have $\mu(U_\varepsilon(\gamma)) = 0$, with ε defined in Theorem 2.2.14. Hence

$$0 = \mu(U_\varepsilon(\gamma)) \geq \mathcal{H}^2 \llcorner S_\infty(U_\varepsilon(\gamma)) = \mathcal{H}^2(S_\infty \cap U_\varepsilon(\gamma)) = \lim_k \mathcal{H}^2(S_k \cap U_\varepsilon(\gamma))$$

which implies

$$\lim_k \mathcal{H}^2(S_k \cap U_\varepsilon(\gamma)) = 0,$$

which contradicts the thesis of Theorem 2.2.14. Precisely, both $L(\gamma, \mathbf{r}_1) \neq 1$ and $L_n(\gamma, \mathbf{r}_2) \neq 1$ cannot be achieved because the sequence of Λ_k converges in the Hausdorff topology, *i.e.* it implies a uniform convergence. Hence, we can state that $F(\Lambda[\mathbf{z}], D)$ is a weakly closed subset with respect to the weak* convergence.

Now, for the proof of Theorem 2.2.14, we can say that it is similar to the one presented by Giusteri et al. [156] with some modifications. Remember that we are considering a link so, for example, the constant ε is the same for the whole system and we have to consider the embedding which has the linking number equal to one with both the filaments.

We are now ready to prove our final and main result.

Theorem 2.2.15. *Let $M \in \mathbb{R}$, $n_i \in \mathbb{N}$ and $\eta_i : [0, L_i] \rightarrow \mathbb{E}^3$ two circumferences be given. If there exists $\tilde{\mathbf{z}} = (\bar{\mathbf{z}}_1, \bar{\mathbf{z}}_2) \in U_{M, n_i, \eta_i}$, then there exists a solution $\mathbf{z} \in U_{M, n_i, \eta_i}$ to the Kirchhoff-Plateau problem, *i.e.* there exists a minimizer \mathbf{z} for the energy functional E_{KP} .*

Proof. Let $\{\mathbf{z}_k\}$ be a minimizing sequence for E_{KP} . First of all, by coercivity, we have

$$E_{\text{loop}}[\mathbf{z}_k] \leq C_1 \quad \mathcal{H}^2(S_k) \leq C_2,$$

where $C_1, C_2 > 0$ and $S_k \in F(\Lambda[\mathbf{z}], D)$. Precisely, if $\mathbf{z}_k \in U_{M, n_i, \eta_i}$, by weak closure we can extract a subsequence \mathbf{z}_{k_i} such that

$$\mathbf{z}_{k_i} \rightharpoonup \mathbf{z},$$

where $\mathbf{z} \in U_{M, n_i, \eta_i}$. Now E_{KP} is wlsc on V . Indeed, by Theorem 2.2.10, E_{loop} is wlsc, so we only need to show that the functional

$$\mathbf{z} \mapsto \inf\{\mathcal{H}^2(S) : S \in F(\Lambda[\mathbf{z}], D)\} \quad \text{is WLSC.} \quad (2.34)$$

To this end, consider $S_k \in F(\Lambda[\mathbf{z}_k], D)$ such that

$$\mathcal{H}^2(S_k) = \inf\{\mathcal{H}^2(S) : S \in F(\Lambda[\mathbf{z}_k], D)\} < \infty.$$

Notice that since $\mathbf{z}_k \rightarrow \mathbf{z}$ in V we can say that the sequence of corresponding midlines converges uniformly. Hence, $\Lambda[\mathbf{z}_k]$ converges in the Hausdorff topology to $\Lambda[\mathbf{z}]$. By Theorem 2.2.13, we find immediately that

$$\mu \geq \mathcal{H}^2 \llcorner S_\infty,$$

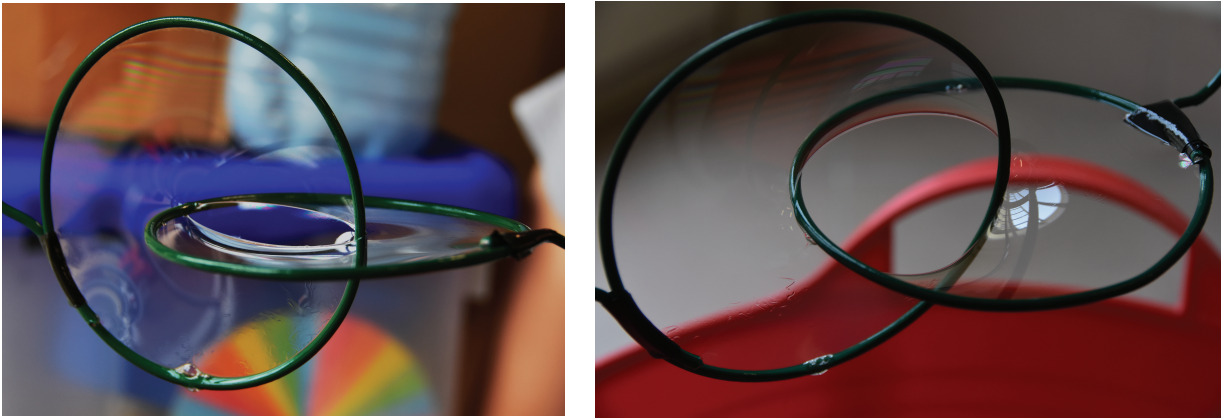
where $S_\infty = \text{supt } \mu \setminus \Lambda[\mathbf{z}]$ and it belongs to $F(\Lambda[\mathbf{z}], D)$, by the previous remarks. Hence, we obtain the chain of inequalities

$$\begin{aligned} \liminf_k \inf\{\mathcal{H}^2(S) : S \in F(\Lambda[\mathbf{z}_k], D)\} \\ \geq \liminf_k (\mathcal{H}^2(S_k)) = \liminf_k \mu_k(\mathbb{R}^3) = \mu(\mathbb{R}^3) \\ \geq \mathcal{H}^2(S_\infty) \geq \inf\{\mathcal{H}^2(S) : S \in F(\Lambda[\mathbf{z}], D)\}, \end{aligned} \quad (2.35)$$

which establishes the lower semicontinuity of the functional (2.34) and so the existence of the solution. □

2.2.2.3 SOME SIMPLE EXPERIMENTS

Finally, we tried to get some hint and confirmation reproducing our problem in the laboratory. The film was a solution of 81% water, 16% glycerine, 3% of common dish soap and



(a) Top view

(b) Side view

Figure 2.11: Results obtained by our configuration with two fixed linked rigid metallic wires.

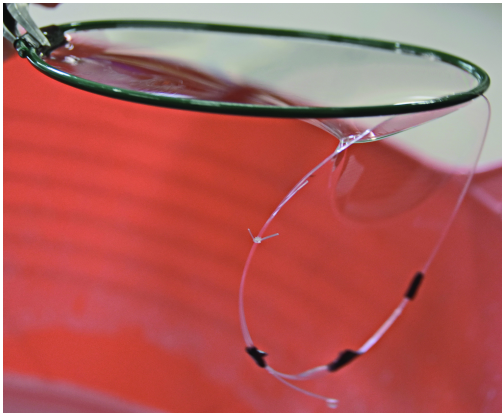
we added a spoon of baking powder to make it more resistant.

In the first example we took two fixed linked rigid metallic wires in the configuration of fig. 2.14, and we observed first a locally minimal configuration consisting of a plane surface and a D -spanning set in the sense of our definition. Once the extra surface was removed, the remaining surface seemed to be the minimum surface (fig. 2.11).

In the second experiment, for practical reasons, we took a fixed rigid metallic wire as first rod, while the second was a 0.5 mm thick slender fishing line, twisted of 4 turns and then glued together. The pictures (fig. 2.12) show the existence of a configuration balancing the weight of the line with the energy coming from the film.

2.2.3 SOAP FILM SPANNING ELECTRICALLY REPULSIVE ELASTIC PROTEIN LINKS

The existence of knotted proteins is widely known (see for instance [226]). In addition, they may also form links with other proteins or molecules. Such proteins are in general extremely complicated and made up by repeated subunits, so that a sort of “macroscopic modeling” as a filament is reasonable. Of course, since everything is immersed in a biological fluid, it is natural to take into account the action of a liquid film spanning the filament.



(a) Top view



(b) Side view

Figure 2.12: Results obtained by our configuration with the mobile component.

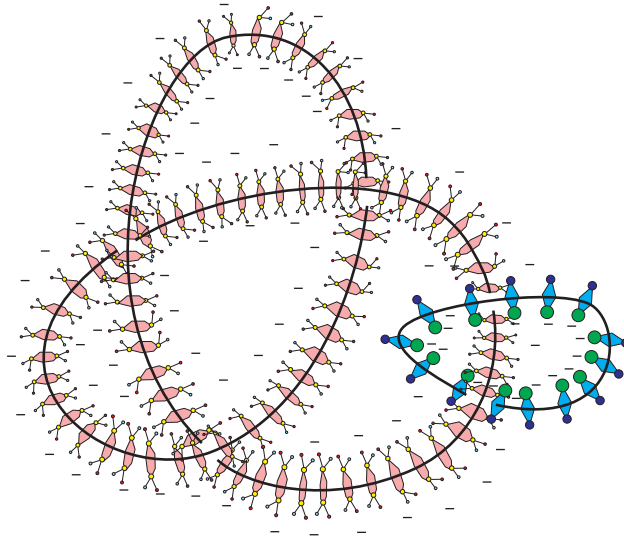


Figure 2.13: A schematic representation of a knotted protein linked to another one.

Therefore, we use the same mathematical description as the one presented in Section 2.2.2: we consider flexible filaments of the form of a closed loop spanned by a liquid film and we model our filament as a Kirchhoff rod (see for instance Antman [15] Ch. 8). Moreover, in order to consider somewhat more complicated shapes, as the ones exhibited by proteins, we consider two thin elastic three-dimensional closed rods linked in a simple but nontrivial way: we impose that the midline of each rod has to have linking number equal

to one with the other one: this implies that they form what is called a link (see Fig. 2.14).

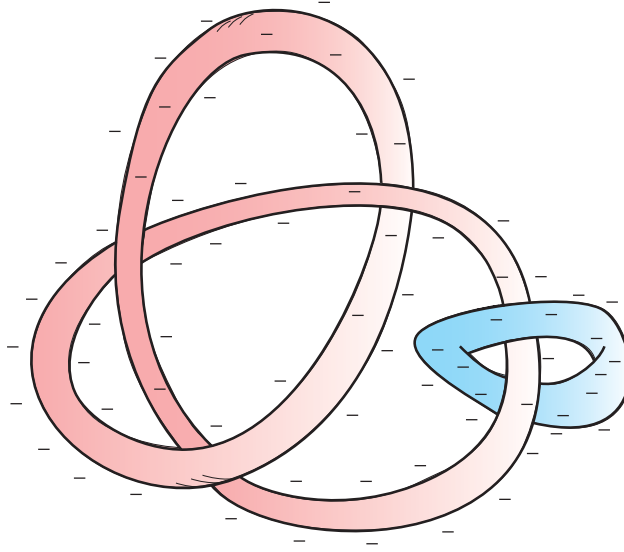


Figure 2.14: Geometry of the problem.

The major achievement with respect to [47] is the introduction of a contribution into the energy functional of the system: we take into account the elastic and the potential energy for the link, the repulsion between the two loops and the surface tension energy of the film. Then, by using the Direct Method of the Calculus of Variations, we are able to prove the existence of the minimum, *i.e.* the solution of our problem.

2.2.3.1 FORMULATION OF THE PROBLEM AND MAIN RESULT

As we have already mentioned, the problem is exactly the same presented in Section 2.2.2.1 with two main novelties:

1. since we want to avoid the possibility for the two loops to touch themselves, we need to modify the energy of the loop, and it is given by

$$E_{\text{loop}}[\mathbf{z}] = E_{\text{el}_1}[\mathbf{z}_1] + E_{\text{g}_1}[\mathbf{z}_1] + E_{\text{el}_2}[\mathbf{z}_2] + E_{\text{g}_2}[\mathbf{z}_2] + E_{\text{rep}}[\mathbf{r}],$$

where $E_{\text{rep}}[\mathbf{r}]$ is a kind of electrical potential energy which, physically, encodes the repulsion between the two rods. This idea is linked to the fact that the amino acids can link together by peptide bonds, but some of them, because of their chemical structure, can repel (see for instance Alberts [2] Ch. 3). Its mathematical form is given by

$$E_{\text{rep}}[\mathbf{r}] := \int_0^{L_1} \int_0^{L_2} \frac{c}{h(\|\mathbf{r}_1(s_1) - \mathbf{r}_2(s_2)\|)} ds_1 ds_2, \quad (2.36)$$

where $\mathbf{r} = (\mathbf{r}_1, \mathbf{r}_2)$, $s_1 \in [0, L_1]$, $s_2 \in [0, L_2]$, c is a constant and h is an increasing non-negative and continuous function. A possible choice for h is represented in Fig. 2.15.

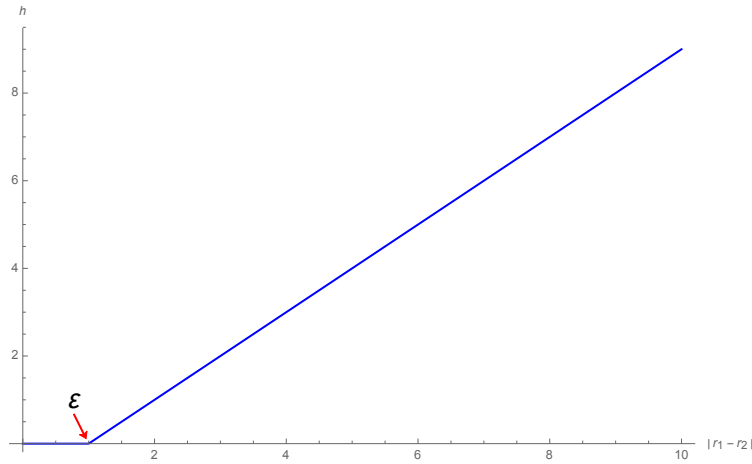


Figure 2.15: A possible choice of h

Notice that with this choice we are introducing a positively unbounded energy, which may be infinite if the midlines are sufficiently close (this happens if the set where $\|\mathbf{r}_1 - \mathbf{r}_2\| < \varepsilon$ is large enough). However, notice also that we cannot take ε too large otherwise we do not get any linked rods with finite repulsion energy. Since we are only assuming that h is increasing, nonnegative and continuous for $r > \varepsilon$ we will also assume that ε is small enough so that the rods have finite repulsion energy. Moreover, by the introduction of this repulsive component in the loop energy, with an appropriate choice of ε , we ensure not only the possibility of non-interpenetration

between the two rods but also we avoid the contact.

2. the proof of the WLSC of the energy of the loop has to take into account an additional term which can be easily considered using the Fatou's lemma, *i.e.*

$$\begin{aligned}
E_{\text{rep}}[\mathbf{r}] &= \int_0^{L_1} \int_0^{L_2} \liminf_j \frac{c}{h(\|\mathbf{r}_1^j(s_1) - \mathbf{r}_2^j(s_2)\|)} ds_1 ds_2 \\
&\leq \liminf_j \int_0^{L_1} \int_0^{L_2} \frac{c}{h(\|\mathbf{r}_1^j(s_1) - \mathbf{r}_2^j(s_2)\|)} ds_1 ds_2 \\
&= \liminf_j E_{\text{rep}}[\mathbf{r}_j] = \lim_k E_{\text{rep}}[\mathbf{r}_k] \leq m.
\end{aligned}$$

As in Sec. 2.2.2.1, we are able to prove the existence of a solution to the Kirchhoff-Plateau problem, *i.e.* the existence of a minimizer of E_{KP} given by (2.30) in the class U_{M, n_i, η_i} , defined in Theorem 2.2.9.

2.2.4 DIMENSIONAL REDUCTION OF THE KIRCHHOFF-PLATEAU PROBLEM

The Plateau problem with elastic boundary curve, a precursor of the Kirchhoff-Plateau problem, has been investigated only in recent years. The first existence results were given by Bernatzky [43] and Bernatzky and Ye [44] who employed the theory of currents, but their elastic energy fails to satisfy the physical requirement of invariance under superposed rigid transformations. Furthermore, a strong hypothesis is used to avoid self-contact. Giomi and Mahadevan in [154] investigated the bifurcation from the flat state and provide also numerical examples. The Kirchhoff-Plateau problem, where a 3-dimensional elastic rod plays the role of the boundary of the soap film, was first formulated by Giusteri et al. [155] where the authors derive general equilibrium and linear stability conditions by considering the first and second variations of the energy functional. Stability properties of flat circular solutions under various conditions regarding the material properties of the rod have been investigated also by Chen and Fried [84], Biria and Fried [57, 58], and Hoang and

Fried [177]. The first existence result for the Kirchhoff-Plateau problem has been given by Giusteri et al. [156] where the functional to be minimized is composed by the elastic energy of the rod, the weight of the rod and the area of the soap film spanned by the rod. The presence of the gravity here is relatively easy to treat from the mathematical point of view since it is a continuous perturbation of the rest of the energy, but at the same time it is interesting from the physical point of view. For instance, the weight of the rod could be a non-negligible contribution when considering two or more linked rods and only one of them is clamped: in this situation (see Bevilacqua et al. [48] and [47]) there is a competition between the weight of the non-clamped rods and the surface tension of the soap films created by the structure of linked rods. In order to treat successfully the soap film part in Giusteri et al. [156] the authors employed the recent approach by De Lellis et al. [112] which used a concept of contact between film and rod, called *spanning*, introduced by Harrison and Pugh [173]. This can be also generalized to complicated topologies of the rod, like knots, and even to links as said before (see Bevilacqua et al. [48] and [47]).

In the Kirchhoff-Plateau problem a sufficiently thin rod is considered, in order to avoid self-intersection which is unphysical. As a consequence, a natural question arises: what happens when the thickness of the rod vanishes, that is the rod shrinks to a line? The limit should give a more physical way to state the Plateau problem with elastic boundary curve. The first attempt is clearly to look for simple cases and the first one, the linear twisted case sketched below, already shows that in the linear case the elastic energy tends to zero as a certain power of the radius of the cross-section of the rod. The same happens in nonlinear elasticity, showing that the elastic contribution to the total energy, duly rescaled, may be expressed in the limit with a density that depends only on the mid-line parameters. Therefore we assume such an expression be generally true (as in all the above mentioned problems) and we perform the passage to the limit. Moreover, it turns out that the limiting curve may retain some “memory” of the twisting, showing that some-

thing more than the simple image of the curve must be given in order to model the associated elastic energy. The same conclusion comes also from another experiment: suppose to force a regular elastic curve to belong to a plane. Then every deformed curve will have zero torsion, but some energy associated to it will be present and will be compensated by the reaction of the plane, so that an energy associated to twist is perfectly conceivable.

2.2.4.1 PHYSICAL MOTIVATION

AN EXAMPLE IN LINEAR ELASTICITY Let us consider a rod in space, which can sustain bending and torsion within the linear theory of elasticity. If we split the total stored energy of the rod into the corresponding contributions E_b and E_t , we may find their densities expressions in the literature (see, for example [202]) as

$$E_b = \frac{\pi}{8} E \varepsilon^4 k^2 \quad \text{and} \quad E_t = \frac{\pi}{4} G \varepsilon^4 \omega^2, \quad (2.37)$$

where E is the Young's modulus and G is the shear modulus, both carry the physical dimensions of pressure, ε is the radius of the section of the rod which can be thought, for simplicity, as a circular section, k is the curvature of the rod, the inverse of a length, and $\omega = \theta/L$, where θ is the angle of twist and ω is the twist density, also the inverse of a length, and finally L is the length of the rod. Therefore the quantities in (2.37) are energy densities per unit length and in order to get the total stored energy we have to integrate along the rod, getting

$$E_{\text{rod}} = \int_0^L (E_b + E_t) ds = \frac{\pi}{8} L E \varepsilon^4 k^2 + \frac{\pi}{4} L G \varepsilon^4 \omega^2. \quad (2.38)$$

Then, given E_b and E_t in a more general way, the expression (2.38) suggests that if we wish to obtain something not trivial as Γ -limit we should consider

$$E_{\text{rod}}^\varepsilon = \int_0^L \frac{1}{\varepsilon^4} (E_b + E_t) ds.$$

Notice that the rescaled density energy, in the linear case, given by

$$\frac{1}{\varepsilon^4} (E_b + E_t) = \frac{\pi}{8} Ek^2 + \frac{\pi}{4} G\omega^2,$$

does not depend on ε .

NONLINEAR ELASTICITY Let us now model our rod as a cylinder made of an isotropic, hyperelastic, incompressible material assuming for simplicity a neo-Hookean strain energy function ψ

$$\psi(\mathbf{F}) = \frac{\mu}{2} (\text{tr } \mathbf{C} - 3),$$

where \mathbf{F} is the deformation gradient and $\mathbf{C} = \mathbf{F}\mathbf{F}^T$ and μ is the shear modulus. The material can sustain both bending and torsion but for simplicity we take into account only torsion. Always looking for the correct rescaling of the energy to use in the abstract set of Γ -convergence, we want also justify the geometrical setting of the framed curves we are going to introduce. The cylinder has axial length L and external radius ε in the fixed reference configuration Ω_0 described by the cylindrical coordinates (R, Θ, Z) . The deformation mapping $\chi : \Omega_0 \rightarrow \mathbb{R}^3$ brings the material point represented by $\mathbf{X} = \mathbf{X}(R, \Theta, Z)$ to the point represented by $\mathbf{x} = \mathbf{x}(r, \theta, z) = \chi(\mathbf{X})$, where (r, θ, z) are the coordinates in the deformed configuration. Hence, following Truesdell and Noll [314], the deformation of a

cylinder subjected to a finite torsion rate γ is given by

$$r = R, \quad \theta = \Theta + \gamma Z, \quad z = Z,$$

where its gradient can be easily computed as

$$\mathbf{F} = \begin{pmatrix} 1 & 0 & 0 \\ 0 & 1 & \gamma R \\ 0 & 0 & 1 \end{pmatrix}.$$

Taking into account the constraint of incompressibility ($\det \mathbf{F} = 1$), the Piola stress tensor and the Cauchy stress tensor are given by

$$\mathbf{S} = \mu \mathbf{F} - p \mathbf{F}^{-\text{T}} \quad \text{and} \quad \mathbf{T} = \mathbf{S} \mathbf{F}^{\text{T}} = \mu \mathbf{F} \mathbf{F}^{\text{T}} - p \mathbf{I}, \quad (2.39)$$

where p is the Langrangian multiplier which enforces the incompressibility. The balance equation is given by

$$\operatorname{div} \mathbf{T} = 0, \quad \text{in } \Omega = \chi(\Omega_0),$$

where $\Omega_0 = \{0 < R < \varepsilon, 0 < \Theta < 2\pi, 0 < Z < L\}$. It turns out that p is only radial, so by assuming zero stress on the lateral surface it is not difficult to see that the total stored energy in the cylinder is given by

$$E_{\text{cyl}} = \frac{\mu L \pi \gamma^2}{4} \varepsilon^4.$$

As before, the area contribution is proportional to ε^4 . So, the nonlinear case is in agreement with the linear one, so we obtain that, for a more general stored energy $\psi(\mathbf{F})$ the

simplest rescaling of the functional is

$$E_{\text{cyl}}^\varepsilon = \frac{1}{\varepsilon^4} \int_{\Omega_0} \psi(\mathbf{F}) R \, dR \, d\Theta \, dZ. \quad (2.40)$$

Moreover, when the cylinder has a finite radius, every reference system with \mathbf{e}_3 as an axis in the original configuration is rotated by a fixed angle proportional to the value of the Z coordinate. The interesting fact is that, in the limit case, *i.e.* when the radius vanishes, this geometrical feature remains unaltered. This is in accordance with the notion of *framed curve* and the well-known fact that the torsion is not continuous with respect to uniform convergence. For example, helices on the finite cylinders have finite and strictly positive torsion independent of the radius of the cylinder, while their limit is a straight line and therefore has zero torsion. Notice that we can rewrite (2.40) as

$$E_{\text{cyl}}^\varepsilon = \int_0^L \left(\frac{1}{\varepsilon^4} \int_0^{2\pi} \int_0^\varepsilon \psi(\mathbf{F}) R \, dR \, d\Theta \right) dZ, \quad (2.41)$$

and, as in the linear case, we notice that the rescaled density, given by

$$f(\gamma) = \frac{1}{\varepsilon^4} \int_0^{2\pi} \int_0^\varepsilon \psi(\mathbf{F}) R \, dR \, d\Theta = \frac{\mu}{4} \pi \gamma^2,$$

does not depend on ε , so that we have

$$E_{\text{cyl}}^\varepsilon = \int_0^L f(\gamma(s)) \, ds.$$

Both examples show that there exists a rescaled energy density which is a function of some variables of the limiting midline only, and which may retain some terms related to the original three-dimensional configuration. Therefore we may think, as an assumption, that there exists an elastic energy density f which is a function of the line variables only.

Notice that this is not equivalent to say that the elastic energy is the same irrespective of the section of the rod attached to the midline, since all constraints that we will introduce (e.g. the non-interpenetration or the knot type) depend on the shape of the section and therefore they may affect the minimizers during the limiting process, as well as the extension of the film, which exerts a tension. So, our problem differs from the very interesting one in which the full 3D elastic energy is rescaled to the midline, which seems on the other part very difficult in view of our constraints.

We will also introduce the weight of the rod in the total energy expression, but this may be treated in several ways: if one wants to see a heavy curve in the limit, then an appropriate rescaling of the density is necessary; if on the contrary the rescaling is not performed, the weight in the limit vanishes and one sees only the condition of passing through the curve—which by the way exerts an elastic traction, which is physically strange. Anyway, from the mathematical point of view, these terms are relatively easy to treat and their presence do not affect deeply our main result.

2.2.4.2 MATHEMATICAL PRELIMINARIES

GEOMETRY OF CLOSED CURVES In this paragraph we recall some classical notions of the theory of curves and knots. Let $L > 0$ and $\mathbf{x}_1, \mathbf{x}_2: [0, L] \rightarrow \mathbb{R}^3$ be two continuous and closed curves. We define their *linking number* as

$$\text{Link}(\mathbf{x}_1, \mathbf{x}_2) = \frac{1}{4\pi} \int_0^L \int_0^L \frac{\mathbf{x}_1(s) - \mathbf{x}_2(t)}{|\mathbf{x}_1(s) - \mathbf{x}_2(t)|^3} \cdot \mathbf{x}'_1(s) \times \mathbf{x}'_2(t) ds dt.$$

It turns out that the linking number is always integer. We say that \mathbf{x}_1 and \mathbf{x}_2 are *isotopic*, and we use the notation $\mathbf{x}_1 \simeq \mathbf{x}_2$, if there exists an open neighborhood N_1 of $\mathbf{x}_1([0, L])$, an open neighborhood N_2 of $\mathbf{x}_2([0, L])$ and a continuous map $\Phi: N_1 \times [0, 1] \rightarrow \mathbb{R}^3$ such that

$\Phi(N_1, \tau)$ is homeomorphic to N_1 for all τ in $[0, 1]$ and

$$\Phi(\cdot, 0) = \text{Identity}, \quad \Phi(N_1, 1) = N_2, \quad \Phi(\mathbf{x}_1([0, L]), 1) = \mathbf{x}_2([0, L]).$$

Roughly speaking, two closed curves are isotopic if and only if they have the same knot type. Following Gonzalez et al. [160], we define the *minimal global radius of curvature* of a closed curve $\mathbf{x} \in W^{1,p}([0, L]; \mathbb{R}^3)$, with $p > 1$, by

$$\Delta(\mathbf{x}) = \inf_{s \in [0, L]} \inf_{\sigma, \tau \in [0, L] \setminus \{s\}} R(\mathbf{x}(s), \mathbf{x}(\sigma), \mathbf{x}(\tau)),$$

where $R(x, y, z)$ denotes the radius of the smallest circle containing x, y, z , with the convention $R(x, y, z) = +\infty$ if x, y, z are collinear. The global radius of curvature has been introduced to see if a tubular neighborhood of a curve has self-intersections. More precisely, if $r > 0$ we define the *r-tubular neighborhood of \mathbf{x}* by

$$U_r(\mathbf{x}) = \bigcup_{s \in [0, L]} B_r(\mathbf{x}(s)).$$

Accordingly to Ciarlet and Nečas [89] we say that $U_r(\mathbf{x})$ is *not self-intersecting* if for any $p \in \partial U_r(\mathbf{x})$ there exists a unique $s \in [0, L]$ such that $\|p - \mathbf{x}(s)\| = r$. The following result holds true (see Gonzalez et al. [160]).

Lemma 2.2.16. *Let $\mathbf{x} \in W^{1,p}([0, L]; \mathbb{R}^3)$ be a closed curve and let $r > 0$. Then $\Delta(\mathbf{x}) \geq r$ if and only if $U_r(\mathbf{x})$ is not self-intersecting. In particular, if $\Delta(\mathbf{x}) > 0$ then \mathbf{x} is simple, that is $\mathbf{x}: [0, L] \rightarrow \mathbb{R}^3$ is injective.*

PLATEAU PROBLEM Now we recall how to solve the Plateau problem using one of the most recent result based on a new notion of spanning condition which dates back to Harrison and Pugh [173] and has been also developed by De Lellis et al. [112]. In particular,

we will follow the notation of De Lellis et al. [112] choosing a suitable class of loops, particularly appropriate for the Kirchhoff-Plateau problem (see Giusteri et al. [156]). Let H be a closed set in \mathbb{R}^3 . We denote by \mathcal{C}_H the set of all smooth embeddings $\gamma: S^1 \rightarrow \mathbb{R}^3 \setminus H$ which are not homotopic to a constant in $\mathbb{R}^3 \setminus H$. Given $K \subset \mathbb{R}^3$ we say that K spans H if $K \subset \mathbb{R}^3 \setminus H$ is relatively closed in $\mathbb{R}^3 \setminus H$ and $K \cap \gamma(S^1) \neq \emptyset$ for every γ in \mathcal{C}_H . Then, in De Lellis et al. [112] the following theorem is proved.

Theorem 2.2.17. *Assume that there exists $S \subset \mathbb{R}^3$ such that $\mathcal{H}^2(S) < +\infty$ and that spans $\mathbb{R}^3 \setminus H$. Then the problem $\min\{\mathcal{H}^2(S) : S \text{ spans } \mathbb{R}^3 \setminus H\}$ has a solution^{‡‡}.*

2.2.4.3 SETTING OF THE PROBLEM AND MAIN RESULT

THE ROD Let $L > 0$, let $p \in (1, +\infty)$ and let $\kappa_1, \kappa_2, \omega \in L^p([0, L])$. We let $w = (\kappa_1, \kappa_2, \omega) \in L^p([0, L]; \mathbb{R}^3)$. Let $\mathbf{x}_0, \mathbf{t}_0, \mathbf{d}_0 \in \mathbb{R}^3$ with $\mathbf{t}_0 \perp \mathbf{d}_0$ and $|\mathbf{t}_0| = |\mathbf{d}_0| = 1$. Denote by $\mathbf{x}[w] \in W^{2,p}([0, L]; \mathbb{R}^3)$ and $\mathbf{t}[w], \mathbf{d}[w] \in W^{1,p}([0, L]; \mathbb{R}^3)$ the unique solution of the Cauchy problem

$$\begin{cases} \mathbf{x}[w]'(s) = \mathbf{t}[w](s), \\ \mathbf{t}[w]'(s) = \kappa_1(s)\mathbf{d}[w](s) + \kappa_2(s)\mathbf{t}[w](s) \times \mathbf{d}[w](s), \\ \mathbf{d}[w]'(s) = \omega(s)\mathbf{t}[w](s) \times \mathbf{d}[w](s) - \kappa_1(s)\mathbf{t}[w](s), \\ \mathbf{x}[w](0) = \mathbf{x}_0, \mathbf{t}[w](0) = \mathbf{t}_0, \mathbf{d}[w](0) = \mathbf{d}_0. \end{cases}$$

It is easy to prove that $\mathbf{t}[w](s) \perp \mathbf{d}[w](s)$ and $|\mathbf{t}[w](s)| = |\mathbf{d}[w](s)| = 1$ for any $s \in [0, L]$ which means that the frame $(\mathbf{t}[w](s), \mathbf{d}[w](s), \mathbf{t}[w](s) \times \mathbf{d}[w](s))$ is an orthonormal frame in \mathbb{R}^3 for any $s \in [0, L]$. For any $s \in [0, L]$ let $\mathcal{A}(s) \subset \mathbb{R}^2$ be compact and simply connected

^{‡‡}It is possible to prove that the solution belongs also to the class of Almgren minimal sets. We do not enter in details since we will not make use of them. We refer to Almgren [6] for a precise definition. Here we just stress that they seem to be the best model for soap films because they have, thanks to a celebrated theorem by Taylor [309], the singularities of Plateau type.

such that $B_\eta(\mathbf{0}) \subset \mathcal{A}(s) \subset B_\nu(\mathbf{0})$ for any $s \in [0, L]$ and for some $\eta, \nu > 0$. For any $\varepsilon > 0$ let

$$\Omega_\varepsilon = \{(s, \zeta_1, \zeta_2) : s \in [0, L] \text{ and } (\zeta_1, \zeta_2) \in \varepsilon \mathcal{A}(s)\}.$$

For any $w \in L^p([0, L]; \mathbb{R}^3)$ let then

$$\mathbf{p}_\varepsilon[w]: \Omega_\varepsilon \rightarrow \mathbb{R}^3, \quad \mathbf{p}_\varepsilon[w](s, \zeta_1, \zeta_2) = \mathbf{x}[w](s) + \zeta_1 \mathbf{d}[w](s) + \zeta_2 \mathbf{t}[w](s) \times \mathbf{d}[w](s). \quad (2.42)$$

Moreover, we set $\Lambda_\varepsilon[w] = \mathbf{p}_\varepsilon[w](\Omega_\varepsilon)$.

THE CONSTRAINTS Before defining the energy it is convenient to fix the constraints. The fact that the midline is a closed curve can be readily expressed by

$$(C1) \quad \mathbf{x}[w](L) = \mathbf{x}[w](0) = \mathbf{x}_0.$$

The closure of the midline is supplemented with the closure of the tangent vectors

$$(C2) \quad \mathbf{t}[w](L) = \mathbf{t}[w](0) = \mathbf{t}_0,$$

and the assignment of the other clamping condition

$$(C3) \quad \mathbf{d}[w](0) = \mathbf{d}_0.$$

To prescribe how many times the ends of the rod are twisted before being glued together we close up the curve $\mathbf{x}[w] + \tau \mathbf{d}[w]$, for $\tau > 0$ fixed and small enough, defining, as in Schuricht [286],

$$\tilde{\mathbf{x}}_\tau[w](s) = \begin{cases} \mathbf{x}[w](s) + \tau \mathbf{d}[w](s), & \text{if } s \in [0, L], \\ \mathbf{x}[w](L) + \tau(\cos(\varphi_w(s-L))\mathbf{d}[w](L) + \sin(\varphi_w(s-L))\mathbf{t}[w](L) \times \mathbf{d}[w](L)), & \text{if } s \in [L, L+1], \end{cases}$$

where $\varphi_w \in [0, 2\pi)$ is the unique angle between \mathbf{d}_0 and $\mathbf{d}[w](L)$ such that $\varphi_w - \pi$ has the same sign as $\mathbf{d}_0 \times \mathbf{d}[w](L) \cdot \mathbf{t}_0$. We trivially identify $\mathbf{x}[w]$ with its extension $\mathbf{x}[w](s) = \mathbf{x}(L)$ for any $s \in [L, L + 1]$ and therefore we require that

$$(C4) \quad \text{Link}(\mathbf{x}[w], \tilde{\mathbf{x}}_\tau[w]) = L_0, \text{ for some fixed } L_0 \in \mathbb{Z}.$$

To encode the knot type of the midline we fix a continuous mapping $\ell: [0, L] \rightarrow \mathbb{R}^3$ such that $\ell(L) = \ell(0)$ and require that

$$(C5) \quad \mathbf{x}[w] \simeq \ell.$$

Finally, in order to prevent self-intersections also in the limit we require that

$$(C6) \quad \Delta(\mathbf{x}[w]) \geq \Delta_0, \text{ for some prescribed } \Delta_0 > 0.$$

We denote by V the set of all constraints, namely

$$V = \{w \in L^p([0, L]; \mathbb{R}^3) : (C1)–(C6) \text{ hold true}\}.$$

It turns out that V is weakly closed in $L^p([0, L]; \mathbb{R}^3)$ (see Gonzalez et al. [160] and Schuricht [286]).

Remark 2.2.18. Following Ciarlet and Nečas [89] the non-interpenetration of matter can be enforced through the global injectivity condition

$$\int_{\Omega_\varepsilon} \det D\mathbf{p}_\varepsilon[w] \, ds d\zeta_1 d\zeta_2 \leq \mathcal{L}^3(\mathbf{p}_\varepsilon[w](\Omega_\varepsilon)),$$

which follows from (C6) and Lemma 2.2.16 if ε is small enough.

THE ENERGY CONTRIBUTIONS AND THE CONVERGENCE RESULT In what follows, without loss of generality $\varepsilon \in (0, 1)$. First, let $f: \mathbb{R}^3 \times [0, L] \rightarrow \mathbb{R} \cup \{+\infty\}$ be bounded from below such that:

- (a) $f(\cdot, s)$ is continuous and convex for any s in $[0, L]$,
- (b) $f(a, \cdot)$ is measurable for any $a \in \mathbb{R}^3$,
- (c) $f(a, s) \geq c_1|a|^p + c_2$ for some $c_1 > 0$ and c_2 in \mathbb{R} .

Taking into account the discussion in Section 2.2.4.1 we define the elastic energy of the bounding rod $E^{\text{el}}: V \rightarrow \mathbb{R} \cup \{+\infty\}$ as

$$E^{\text{el}}(w) = \int_0^L f(w(s), s) ds. \quad (2.43)$$

The second energy contribution we want to take into account is the weight of the rod. Let $\Omega = \Omega_1$ and let $\rho \in L^\infty(\Omega)$ with $\rho \geq 0$ be the mass density function and \mathbf{g} be the gravitational acceleration. Let us define $E_\varepsilon^{\text{g}}: V \rightarrow \mathbb{R} \cup \{+\infty\}$ as

$$E_\varepsilon^{\text{g}}(w) = \frac{1}{\varepsilon^2} \int_{\Omega_\varepsilon} \rho(s, \zeta_1, \zeta_2) \mathbf{g} \cdot \mathbf{p}_\varepsilon[w](s, \zeta_1, \zeta_2) ds d\zeta_1 d\zeta_2,$$

where \mathbf{p}_ε is defined as in (2.42). The last contribution is the soap film energy. We define $E_\varepsilon^{\text{sf}}: V \rightarrow \mathbb{R} \cup \{+\infty\}$ as

$$E_\varepsilon^{\text{sf}}(w) = 2\sigma \inf \{ \mathcal{H}^2(S) : S \subset \mathbb{R}^3 \text{ and } S \text{ spans } \Lambda_\varepsilon[w] \},$$

where $\sigma > 0$ is a constant called *surface tension*.

Remark 2.2.19. Assume that

$$\inf_V E_\varepsilon < +\infty.$$

Then (see Giusteri et al. [156]) there exists $w_\varepsilon \in V$ be such that

$$E_\varepsilon(w_\varepsilon) = \min_V E_\varepsilon.$$

Let now introduce the limit energy functional. Let $\rho_0: [0, L] \rightarrow \mathbb{R}$ be given by

$$\rho_0(s) = \lim_{(\xi_1, \xi_2) \rightarrow (0,0)} \rho(s, \xi_1, \xi_2).$$

For any $w \in V$ we let

$$E_0(w) = \int_0^L f(w(s), s) ds + \int_0^L |\mathcal{A}(s)| \rho_0(s) \mathbf{g} \cdot \mathbf{x}[w](s) ds \\ + 2\sigma \inf \{ \mathcal{H}^2(S) : S \subset \mathbb{R}^3 \text{ spans } \mathbf{x}[w]([0, L]) \}.$$

The functional E_0 is an energy on framed curves: when dealing with minimization of E_0 we are finding a soap film spanning an elastic and heavy boundary curve. Existence and approximation of such a solutions follow in a standard way (using the theory of Γ -convergence, see Theorem 2.2.21) from the next theorem.

Theorem 2.2.20. *For any $\varepsilon > 0$ let $E_\varepsilon: V \rightarrow \mathbb{R} \cup \{+\infty\}$ be given by*

$$E_\varepsilon(w) = E^{\text{el}}(w) + E_\varepsilon^{\text{g}}(w) + E_\varepsilon^{\text{sf}}(w).$$

Let (ε_h) be a sequence with $\varepsilon_h \rightarrow 0$ as $h \rightarrow +\infty$ and let (w_h) be a sequence in V with $E_{\varepsilon_h}(w_h) \leq c$ for some $c > 0$. Then, up to a subsequence, $w_h \rightarrow w$ in $L^p([0, L]; \mathbb{R}^3)$ and $w \in V$. Moreover, the family $\{E_\varepsilon\}_{\varepsilon>0}$ Γ -converges to E_0 as $\varepsilon \rightarrow 0^+$ with respect to the weak topology of $L^p([0, L]; \mathbb{R}^3)$, namely:

- (a) *for any sequence (ε_h) with $\varepsilon_h \rightarrow 0$, for any $w \in V$ and for any sequence (w_h) in V with $w_h \rightarrow w$ in $L^p([0, L]; \mathbb{R}^3)$ we have*

$$E_0(w) \leq \liminf_{h \rightarrow +\infty} E_{\varepsilon_h}(w_h); \tag{2.44}$$

- (b) *for any $w \in V$ there is a sequence (ε_h) with $\varepsilon_h \rightarrow 0$ and a sequence (\bar{w}_h) in V with*

$\bar{w}_h \rightharpoonup w$ in $L^p([0, L]; \mathbb{R}^3)$ such that

$$E_0(w) \geq \limsup_{h \rightarrow +\infty} E_{\varepsilon_h}(\bar{w}_h). \quad (2.45)$$

Proof. The compactness statement is Proposition 2.2.22 below. Inequality (2.44) follows combining (2.49), (2.50) and (2.51) with the subadditivity of the liminf operator. Next, for any $w \in V$ let $w_h = w$. Of course $\bar{w}_h \rightharpoonup w$ in $L^p([0, L]; \mathbb{R}^3)$. Inequality (2.45) follows easily combining (2.50) and (2.53) with the superadditivity of the limsup operator. \square

Theorem 2.2.21. *Let (ε_h) be such that $\varepsilon_h \rightarrow 0$ as $h \rightarrow +\infty$. Assume that*

$$\inf_V E_{\varepsilon_h} < +\infty, \quad \forall h \in \mathbb{N},$$

and for any $h \in \mathbb{N}$ let $w_h \in V$ be such that

$$E_{\varepsilon_h}(w_h) = \min_V E_{\varepsilon_h}.$$

Then, up to a subsequence $w_h \rightharpoonup w_0$ in $L^p([0, L]; \mathbb{R}^3)$,

$$E_0(w_0) = \min_V E_0, \quad (2.46)$$

and

$$\lim_{h \rightarrow +\infty} \min_V E_{\varepsilon_h} = \min_V E_0. \quad (2.47)$$

Proof. The proof is standard in the theory of Γ -convergence but for the sake of completeness we add the details. Since $f(a, s) \geq c_1|a|^p + c_2$ we deduce that $\|w_h\|_p$ is bounded, which says that, up to a subsequence, $w_h \rightharpoonup w_0$ in $L^p([0, L]; \mathbb{R}^3)$. Let $w \in V$. Accordingly with

(2.45) let $\bar{w}_h \rightharpoonup w$ in $L^p([0, L]; \mathbb{R}^3)$ such that

$$E_0(w) \geq \limsup_{h \rightarrow +\infty} E_{\varepsilon_h}(\bar{w}_h).$$

By (2.44) we obtain

$$E_0(w_0) \leq \liminf_{h \rightarrow +\infty} E_{\varepsilon_h}(w_h) = \liminf_{h \rightarrow +\infty} \min_V E_{\varepsilon_h} \leq \limsup_{h \rightarrow +\infty} \min_V E_{\varepsilon_h} \leq \limsup_{h \rightarrow +\infty} E_{\varepsilon_h}(\bar{w}_h) \leq E_0(w), \quad (2.48)$$

that is

$$E_0(w_0) = \min_V E_0.$$

Finally, putting $w = w_0$ in (2.48) we deduce that

$$\lim_{h \rightarrow +\infty} \min_V E_{\varepsilon_h} = \min_V E_0,$$

and this ends the proof. □

2.2.4.4 PROOF OF THE CONVERGENCE RESULT

Fix a sequence $\varepsilon_h \rightarrow 0$ as $h \rightarrow +\infty$.

Proposition 2.2.22. (compactness) *Let (w_h) be a sequence in V with $E_{\varepsilon_h}(w_h) \leq c$ for some $c > 0$. Then, up to a subsequence, $w_h \rightharpoonup w$ in $L^p([0, L]; \mathbb{R}^3)$ and $w \in W$.*

Proof. Since $f(a, s) \geq c_1|a|^p + c_2$ we can say that $\|w_h\|_p$ is bounded. Then, up to a subsequence, $w_h \rightharpoonup w$ in $L^p([0, L]; \mathbb{R}^3)$. Moreover, $w \in V$ since V is weakly closed in $L^p([0, L]; \mathbb{R}^3)$ and this yields the conclusion. □

Proposition 2.2.23. (lower semicontinuity of the elastic energy) *Let $w \in W$. Then for any sequence (w_h) in V with $w_h \rightharpoonup w$ in $L^p([0, L]; \mathbb{R}^3)$ we have*

$$\int_0^L f(w(s), s) ds \leq \liminf_{h \rightarrow +\infty} E^{\text{el}}(w_h). \quad (2.49)$$

Proof. Inequality (2.49) follows easily by the fact that V is weakly closed in $L^p([0, L]; \mathbb{R}^3)$ and the functional

$$u \mapsto \int_0^L f(u(s), s) ds$$

is weakly lower semicontinuous in $L^p([0, L]; \mathbb{R}^3)$ because $f(\cdot, s)$ is convex. \square

The study of the weight term is easy since the weak convergence $w_h \rightharpoonup w$ implies the uniform convergence of the midlines.

Proposition 2.2.24. (convergence of the weight) *For any $w \in W$ and for any sequence (w_h) in V with $w_h \rightharpoonup w$ in $L^p([0, L]; \mathbb{R}^3)$ we have*

$$\lim_{h \rightarrow +\infty} E_{\varepsilon_h}^{\text{g}}(w_h) = \int_0^L |\mathcal{A}(s)| \rho_0(s) \mathbf{g} \cdot \boldsymbol{\alpha}[w](s) ds. \quad (2.50)$$

Proof. By the change of variables $\zeta_i = \varepsilon_h \eta_i$, $i = 1, 2$, we obtain

$$\begin{aligned} & \frac{1}{\varepsilon_h^2} \int_{\Omega_{\varepsilon_h}} \rho(s, \zeta_1, \zeta_2) \mathbf{g} \cdot \mathbf{p}_{\varepsilon_h}[w_h](s, \zeta_1, \zeta_2) ds d\zeta_1 d\zeta_2 \\ &= \frac{1}{\varepsilon_h^2} \int_{\Omega_{\varepsilon_h}} \rho(s, \zeta_1, \zeta_2) \mathbf{g} \cdot (\boldsymbol{\alpha}[w_h](s) + \zeta_1 \mathbf{d}[w_h](s) + \zeta_2 \mathbf{t}[w_h](s) \times \mathbf{d}[w_h](s)) ds d\zeta_1 d\zeta_2 \\ &= \int_{\Omega} \rho(s, \varepsilon_h \eta_1, \varepsilon_h \eta_2) \mathbf{g} \cdot (\boldsymbol{\alpha}[w_h](s) + \varepsilon_h \eta_1 \mathbf{d}[w_h](s) + \varepsilon_h \eta_2 \mathbf{t}[w_h](s) \times \mathbf{d}[w_h](s)) ds d\eta_1 d\eta_2. \end{aligned}$$

Passing to the limit as $h \rightarrow +\infty$, using the fact that $\boldsymbol{\alpha}[w_h] \rightarrow \boldsymbol{\alpha}[w]$ uniformly on $[0, L]$ and applying the Dominated Convergence Theorem we conclude. \square

The main difficulty is to pass to the limit in the soap film part of the energy. First of

all we need the following Lemma whose proof requires minor modifications of the proof of Theorem 2 in De Lellis et al. [112] (see also Lemma 3.4 in Giusteri et al. [156]).

Lemma 2.2.25. *Let (Λ_h) be a sequence of closed subsets of \mathbb{R}^3 converging in the Hausdorff topology to a closed set $\Lambda \neq \emptyset$. For any $h \in \mathbb{N}$ let $S_h \subset \mathbb{R}^3$ be such that*

$$\mathcal{H}^2(S_h) = \min \{ \mathcal{H}^2(S) : S \text{ spans } \Lambda_h \}.$$

Let $\mu_h = \mathcal{H}^2 \llcorner S_h$. Then, up to a subsequence, $\mu_h \xrightarrow{} \mu$ and*

$$\mu \geq \mathcal{H}^2 \llcorner S_\infty,$$

where $S_\infty = \text{spt}(\mu) \setminus \Lambda$ is a countably \mathcal{H}^2 -rectifiable set.

Proposition 2.2.26. (lower estimate for the soap film energy) *For any $w \in W$ and for any sequence (w_h) in V with $w_h \rightharpoonup w$ in $L^p([0, L]; \mathbb{R}^3)$ we have*

$$2\sigma \inf \{ \mathcal{H}^2(S) : S \text{ spans } \mathbf{x}[w]([0, L]) \} \leq \liminf_{h \rightarrow +\infty} E_{\varepsilon_h}^{\text{sf}}(w_h). \quad (2.51)$$

Proof. Let $S_h \subset \mathbb{R}^3$ be such that

$$\mathcal{H}^2(S_h) = \min \{ \mathcal{H}^2(S) : S \text{ spans } \Lambda_{\varepsilon_h}[w_h] \}.$$

Since $\mathbf{x}[w_h] \rightarrow \mathbf{x}[w]$ uniformly on $[0, L]$ we easily deduce that $\Lambda_{\varepsilon_h}[w_h] \rightarrow \mathbf{x}[w]([0, L])$ in the Hausdorff topology. Let $\mu_h = \mathcal{H}^2 \llcorner S_h$. Then, using Lemma 2.2.25 we can say that, up to a subsequence, $\mu_h \xrightarrow{*} \mu$ and

$$\mu \geq \mathcal{H}^2 \llcorner S_\infty,$$

where $S_\infty = \text{spt}(\mu) \setminus \mathbf{x}[w]([0, L])$ is a countably \mathcal{H}^2 -rectifiable set. We now prove that S_∞

spans $\mathbf{x}[w]([0, L])$. Let $\gamma \in \mathcal{C}_{\mathbf{x}[w]}([0, L])$. The key point is to show that for any $r > 0$ such that $U_{2r}(\gamma) \subset \mathbb{R}^3 \setminus \mathbf{x}[w]([0, L])$, there exists $M = M(r) > 0$ such that, for h large enough,

$$\mathcal{H}^2(S_h \cap U_r(\gamma)) \geq M. \quad (2.52)$$

The proof of (2.52) can be done as in the proof of Lemma 3.5 in Giusteri et al. [156]: indeed the proof uses essentially the fact that $\Lambda_{\varepsilon_h}[w_h] \rightarrow \mathbf{x}[w]([0, L])$ in the Hausdorff topology. Using (2.52) we can show that S_∞ spans $\mathbf{x}[w]([0, L])$. Assume by contradiction that there exists $\gamma \in \mathcal{C}_{\mathbf{x}[w]}([0, L])$ with $\gamma(S^1) \cap S_\infty = \emptyset$ and take $r > 0$ as before. We then find that $\mu(U_r(\gamma)) = 0$ and, therefore, that

$$\lim_h \mathcal{H}^2(S_h \cap U_r(\gamma)) = 0,$$

which contradicts (2.52). Finally, we obtain

$$\begin{aligned} & \liminf_h 2\sigma \inf\{\mathcal{H}^2(S) : S \text{ spans } \Lambda_{\varepsilon_h}[w_h]\} \\ &= 2\sigma \liminf_h \mathcal{H}^2(S_h) \\ &\geq 2\sigma \mathcal{H}^2(S_\infty) \\ &\geq 2\sigma \inf\{\mathcal{H}^2(S) : S \text{ spans } \mathbf{x}[w]([0, L])\}, \end{aligned}$$

and this yields the conclusion. □

Now we prove the upper estimate.

Proposition 2.2.27. (upper estimate for the soap film energy) *For any $w \in V$ we have*

$$2\sigma \inf\{\mathcal{H}^2(S) : S \text{ spans } \mathbf{x}[w]([0, L])\} \geq \limsup_{h \rightarrow +\infty} E_{\varepsilon_h}^{\text{sf}}(w). \quad (2.53)$$

Proof. Without loss of generality, we can assume that

$$\inf\{\mathcal{H}^2(S) : S \text{ spans } \mathbf{x}[w]([0, L])\} < +\infty.$$

otherwise (2.53) becomes trivial. Let $S_\infty \subset \mathbb{R}^3$ be such that

$$\mathcal{H}^2(S_\infty) = \min\{\mathcal{H}^2(S) : S \text{ spans } \mathbf{x}[w]([0, L])\}.$$

We have to construct $S_h \subset \mathbb{R}^3$ which spans $\Lambda_{\varepsilon_h}[w]$ and such that $\mathcal{H}^2(S_h) \leq \mathcal{H}^2(S_\infty)$. The idea is to look S_∞ outside $\Lambda_{\varepsilon_h}[w]$. Let $S_h = S_\infty \setminus \Lambda_{\varepsilon_h}[w]$. We claim that S_h spans $\Lambda_{\varepsilon_h}[w]$. This is straightforward since for any $\gamma \in \mathcal{C}_{\Lambda_{\varepsilon_h}[w]}$ we have $\gamma(S^1) \cap (S_\infty \setminus \Lambda_{\varepsilon_h}[w]) \neq \emptyset$. Of course we have $\mathcal{H}^2(S_h) \leq \mathcal{H}^2(S_\infty)$. As a consequence,

$$\begin{aligned} \limsup_{h \rightarrow +\infty} E_{\varepsilon_h}^{\text{sf}}(w) &\leq 2\sigma \limsup_{h \rightarrow +\infty} \mathcal{H}^2(S_h) \\ &\leq 2\sigma \mathcal{H}^2(S_\infty) \\ &= 2\sigma \inf\{\mathcal{H}^2(S) : S \text{ spans } \mathbf{x}[w]([0, L])\}, \end{aligned}$$

and this ends the proof. □

Remark 2.2.28. It is likely that the condition

$$S \text{ spans } \mathbf{x}[w]([0, L]), \quad \mathbf{x}[w] \in W^{2,p}([0, L]; \mathbb{R}^3),$$

carries some more informations on its boundary. For instance, is it true that S assumes $\mathbf{x}[w]([0, L])$ as a boundary in a more classical sense? We do not know the answer, and this seems to be challenging since very few results are known about boundary regularity for Plateau problem.

A

Appendix to Chapter 2

A.1 DUAL TESSELLATION OF THE CENTRAL BUBBLE

A visual three-dimensional representation of the dual tessellation produced on the central sphere by the bubble packing is depicted in Figs. [A.1](#) and [A.2](#). The polygons representing the flat bubble–bubble interfaces are here plotted inside the original spherical bubble of radius r *before* reshuffling the polyhedron to recover the original bubble volume.

As we can see from Figs. [A.1-A.2](#), the projection of Tammes' points along the radial direction represents the centroid of each polygon on the dual tessellation. Viceversa, the

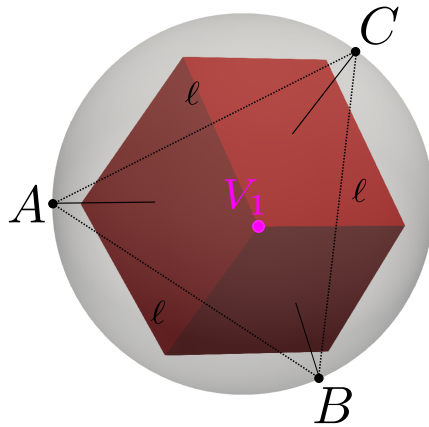


Figure A.1: Bottom view of the dual tessellation. The dashed lines represent the chord ℓ of the Tamme's construction. The centroid of the triangle A, B, C is the South Pole, called V_1 in the dual tessellation.

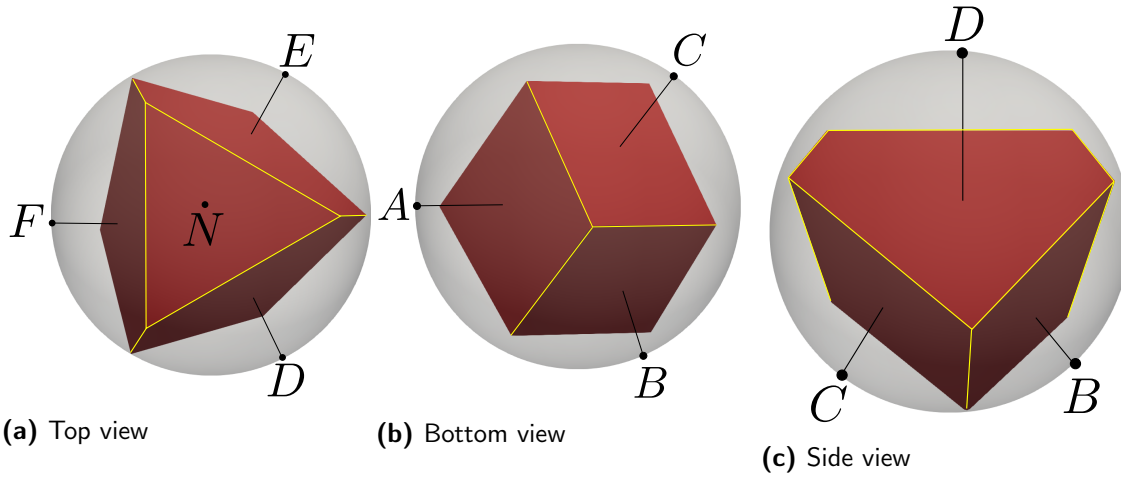


Figure A.2: Different views of the tessellation: (a) top, (b) bottom and (c) side view. Black dots indicate the Tamme's points. Irrespective of the graphic illusion, the corners of the inscribed polyhedron are on the spherical surface; after restoring of the initial volume, they will be external. Yellow lines underline the sides of the different obtained polygons: (a) a triangle, (b) three quadrilaterals and (c) three pentagons.

vertices V_i with $i = 1, \dots, 10$ are the centroids of the triangles of the modified Tamme's tessellation, see Fig. 2.2b.

A.2 POLYEDRA WITH SEVEN FACES

In this appendix, we want to show the five polyhedra among all the 34 convex polytopes with seven faces inscribed into a sphere of a fixed radius r , which satisfies the first optimal

criterium, *i.e.* Eq. (2.7). By the software Plantri, we can draw them and their graphical representation is presented in Fig. A.3.

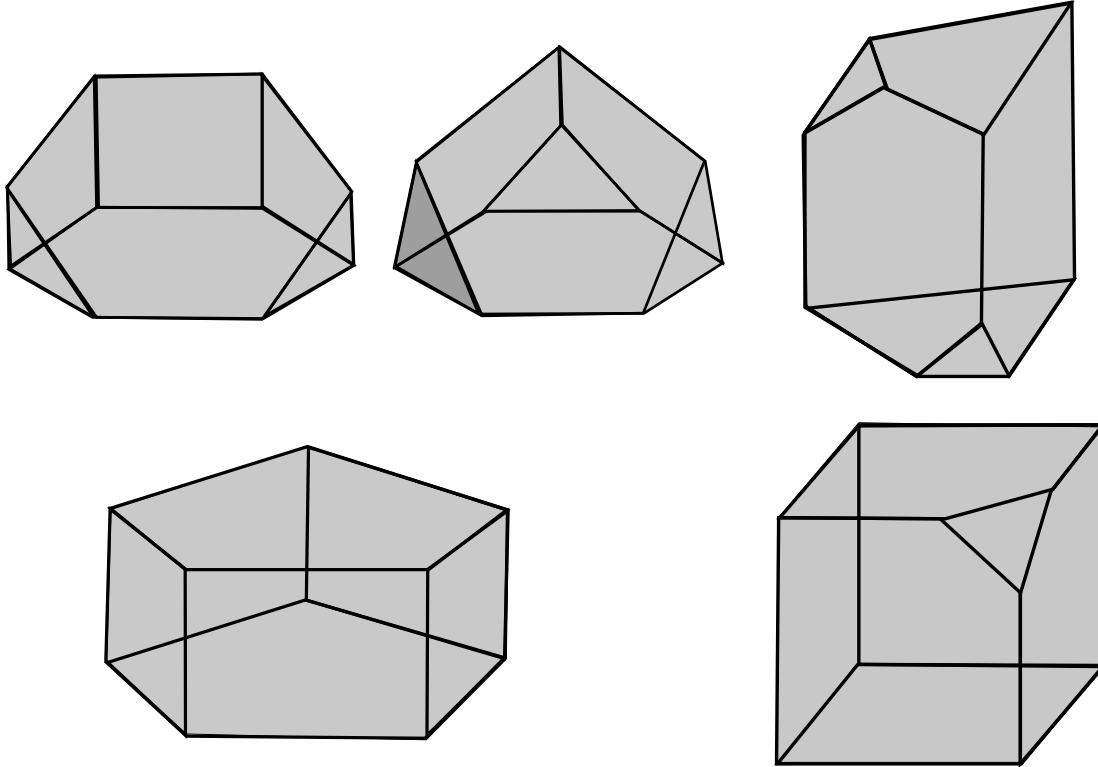


Figure A.3: Graphical representation, obtained through the software Plantri, of the five convex polygons among the 34 inscribed into a sphere which satisfy the first optimal criterium Eq. (2.7). The Tammes' dual tessellation is one of them, *i.e.* the last one.

A.3 CALCULATION OF VOLUMES

In order to compute the volume of the peripheral bubbles, we have to mathematically describe the shape of a pyramidal frustum covered by a vault. The vault is obtained radially cutting slices of a spherical cap drawn on the vertices of the external basis of the frustum, by prolongation of the lateral surfaces of the frustum itself (see Figs. 2.7b and A.5). From a mathematical point of view, this calculation is a bit technical since the final solid is not a known or a common one.

First of all, we have to better clarify which are the involved unknowns. As it concerns the packing parameter, which is used to define the position of the vertices on the free surface and it is obtained through the interaction among three surfaces, we a priori have four different values of packing parameter, *i.e.*

$$h_1 = h(Q, Q, Q) \quad h_2 = h(P, P, T) \quad h_3 = h(Q, P, Q) \quad h_4 = h(Q, P, P), \quad (\text{A.1})$$

where the letters into brackets denote the interaction between three polygons, *i.e.* P for pentagons, Q for quadrilaterals and T for the triangle.

We denote with the symbol $\tilde{}$ the centroids of the dual tessellation polygon: $\tilde{A}, \tilde{B}, \tilde{C}, \dots$, the center of the sphere passing through the vertices of the homotetically projected polygons is C_i , with $i = A, B, C, D, E, F, N$. Since we have three type of polygons, we make the calculations only on a representative of each class, such as on the quadrilateral A , on the pentagon D and on the triangle N .

We define $h_P = \tilde{D} - C_D$, $h_Q = \tilde{A} - C_A$ and $h_T = \tilde{N} - C_N$ (see Fig. A.4) the distance between the centre of the sphere associated with the vault curvature and the centroid of the polygonal inner basis of the frustum (the projection of the Tammes' points on the central bubble interfaces). These distances are to be fixed in order to enforce conservation of volumes of the peripheral bubbles.

Depending on the type of adjacent polygons (pentagon-pentagon, pentagon-triangle,....), a different packing parameter h_i with $i = 1, 2, 3, 4$ is expected (see Eq. (A.1)). For illustrative purposes, here below we only show how the radial height h_2 , obtained by the intersection among the sphere constructed on the triangle and on the two adjacent pentagons. We are going to show that it can be rewritten as a function of h_P (Fig. A.4).

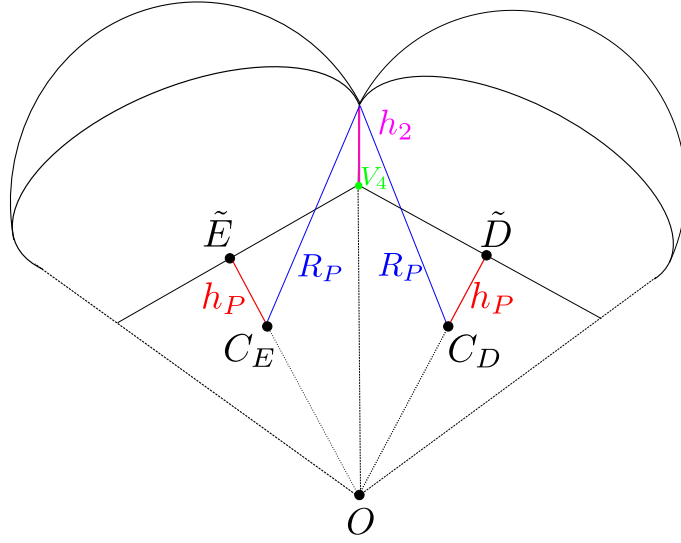


Figure A.4: In the plane passing through the projected Tammes points \tilde{D} , \tilde{E} and the origin O , the points C_D and C_E are the centres of the spheres of radius R_P , that eventually define the free surface of the bubble. The side of the pyramidal frustum is h_2 .

The sphere of radius R_P , centered in C_D is defined by the equation

$$(x - x_{C_D})^2 + (y - y_{C_D})^2 + (z - z_{C_D})^2 = R_P^2, \quad (\text{A.2})$$

where the coordinates of C_D are

$$C_D = (dx_{\tilde{D}}, dy_{\tilde{D}}, dz_{\tilde{D}}) \quad \text{with} \quad d = 1 - \frac{h_P}{r}.$$

Analogously, we construct the sphere on the adjacent pentagon E , so that

$$(x - x_{C_E})^2 + (y - y_{C_E})^2 + (z - z_{C_E})^2 = R_P^2. \quad (\text{A.3})$$

The same compation parameter d scales the coordinates $(x_{C_E}, y_{C_E}, z_{C_E})$ because both D and E are pentagons.

The intersection between the two spheres is a circumference, and the edge $\mathbf{c}_3 = \overline{V_3V_4}$

lies on it. In the same way, we can also consider another circumference obtained by the intersection of, for instance, the sphere centered in C_D and the adjacent constructed on the triangle, *i.e.* centered in C_N . The length of the side of the frustum h_2 is the distance between the node V_4 of the dual tessellation and the outer intersection point of the two circumferences defined above. The parametric representation of the radial line passing through $V_4 = (x_{V_4}, y_{V_4}, z_{V_4})$ is given by

$$\begin{cases} x = tx_{V_4}, \\ y = ty_{V_4}, \\ z = tz_{V_4}, \end{cases} \quad (\text{A.4})$$

where t is a positive real parameter. The intersection between the two spherical surfaces Eqs. (A.2) and (A.3) with the line Eq. (A.4) is the point \mathbf{x}_0 on the free surface with the following coordinates (where $z_{V_4} \neq 0$ by construction)

$$\mathbf{x}_0 : \begin{cases} x = \frac{x_{V_4}}{z_{V_4}} z \\ y = \frac{y_{V_4}}{z_{V_4}} z \\ z = \frac{(-x_{C_P}^2 + x_{C_Q}^2 - y_{C_P}^2 + y_{C_Q}^2 - z_{C_P}^2 + z_{C_Q}^2)z_{V_4}}{-2(x_{C_P} + x_{C_Q})x_{V_4} - 2(y_{C_P} + y_{C_Q})y_{V_4} - 2(z_{C_P} + z_{C_Q})z_{V_4}}. \end{cases} \quad (\text{A.5})$$

Hence, we define

$$h_2 = |\mathbf{x}_0 - V_4|. \quad (\text{A.6})$$

This procedure can be repeated on all the lateral interfaces in order to calculate all the h_i with $i = 1, 2, 3, 4$.

The second and final step is to write down the volume of the solid (pyramidal frustum plus spherical vault) as a function of h_P , h_T and h_Q calculated as in Eq. (A.5). The vol-

ume of the pyramidal frustum is

$$\mathcal{V}_{\text{py}}^i = \frac{\left(A_{\text{bottom}}^i + A_{\text{top}}^i + \sqrt{A_{\text{bottom}}^i A_{\text{top}}^i} \right) H_{\text{py}}^i}{3} \quad i = P, Q, T, \quad (\text{A.7})$$

where A_{bottom}^i is the area of the i -th polygon on the dual tessellation, $A_{\text{top}}^i = \frac{r+h}{r} A_{\text{bottom}}^i$ is the area of the upper basis, and H_{py}^i is the height of the pyramidal frustum.

The volume of the spherical vault is nothing but the volume of the laterally cut spherical cap. For the sake of simplicity, we consider here the spherical vault based on the triangle N . We use local coordinates with origin in C_N , the centroid of the triangle is in $\tilde{N} = (0, 0, h_T)$.

In terms of the local coordinates (x', y', z') , the volume of the spherical cap is

$$\Omega' = \{(x', y', z') \in \mathbb{R}^3 : (x')^2 + (y')^2 + (z')^2 \leq R_T^2, z' \geq h + h_T\}.$$

and its measure is obtained by standard volume integration. We have to subtract to the measure of Ω' the volume of the slices obtained by prolongation of the flat interface defined by the vertices V_3V_7 (and so on). It is worth to remark that the plane attached to V_3V_7 is not perpendicular to basis of the spherical cap. So, first of all, the expression of the area of a circular segment of radius ρ and chord b is

$$\mathcal{A}_{\text{cir}} = \rho^2 \left(\arcsin \left(\frac{b}{2\rho} \right) - \frac{b}{2\rho} \right). \quad (\text{A.8})$$

Here ρ and b are functions of the quote $z' \in [h + h_T, h_{\text{max}}]$ and h_{max} has to be determined, see Fig. A.5. The value of h_{max} is fixed at the z' -level such that the homothetic projection of the inner triangle is circumscribed into the circumference. Namely, a plane at given z' crosses the plane defined by V_3V_7 along a line, that we represent by its equation $ax' + by' +$

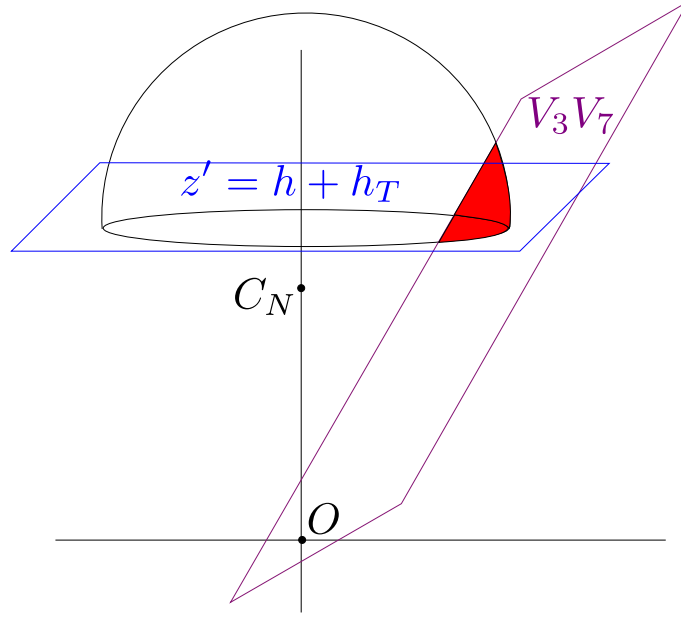


Figure A.5: Geometrical representation of the lateral cut of the spherical cap.

$c = 0$. To obtain the upper integration bounds in z' we impose

$$\frac{|a\bar{x}' + b\bar{y}' + c|}{\sqrt{a^2 + b^2}} = \sqrt{R_T^2 - (z')^2}, \quad (\text{A.9})$$

where $\bar{x}' = 0$, $\bar{y}' = 0$ and the left-hand-side of Eq. (A.9) is exactly the radius ρ of the circumference at fixed z' .

By solving (A.9), we get

$$z'_{1,2} = \frac{-cd \pm \sqrt{c^2 d^2 - (a^2 + b^2 + c^2)(d^2 - R_T^2 a^2 - R_T^2 b^2)}}{c^2 + a^2 + b^2},$$

where $a = 2.48 - 2.96h_T$, $b = 0$, $c = 1$ and $d = 0.42 - h_T$ and h_{\max} is the positive value, since it belongs to Ω' .

Finally, the volume of the bubble constructed on the triangle is given by

$$\mathcal{V}_T = |\Omega'| - 3 \int_{h+h_T}^{h_{\max}} \mathcal{A}_{cir} d\alpha,$$

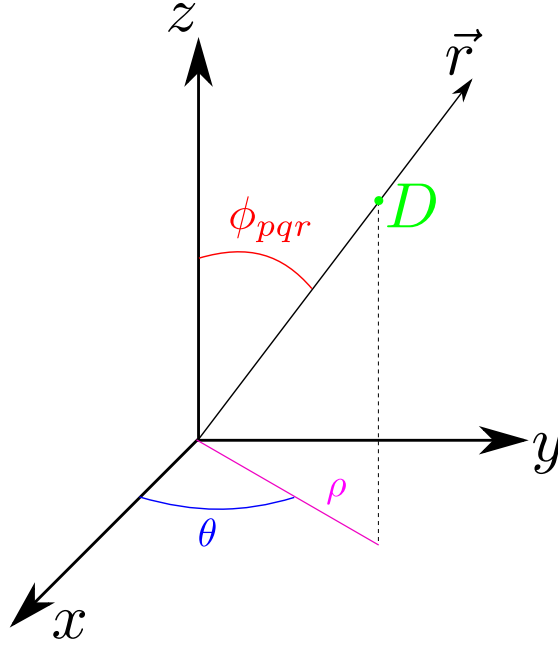


Figure A.6: Geometrical sketch of the rotation around the axis x by the angle ϕ_{pqr} . The coordinates ρ , θ and ϕ are the spherical ones set into a Cartesian frame of reference (x, y, z) .

where $|\cdot|$ denotes the measure of the volume of Ω' . All the calculations are computed numerically by using the Newton's method with the software *Mathematica* 11.3 (Wolfram Research, Champaign, IL, USA). For the other polygons, the computation is similar up to a rotation which has to be done before computing the translation of the centre of the frame of reference, see Fig. A.6.

A.4 EQUATIONS OF BALANCE OF TENSIONS

The detailed expressions of Eqs. (2.10) and their geometrical representation are listed in Tables A.1-A.3. We introduce different superscripts to distinguish the different directions. The unit vectors denoting the direction of the force on the side edge is denoted by the symbol \mathbf{t} , \mathbf{t}^r for the ones oriented in the radial direction, \mathbf{t}^s on the free surface.

In the following tables, the unit vector normal to the free surface applied in the homothetical vertex of the dual Tamme's tessellation are not reported due to absence of space.

We collect them below, *i.e.*

$$\mathbf{n}_D^s = (-0.18 + 0.39h_2 + 0.62h_P, 0.53 + 0.68h_2, -0.4 - 0.64h_2 - 0.13h_P)$$

$$\mathbf{n}_E^s = (0.55 + 0.39h_2 - 0.3h_P, 0.11 + 0.67h_2 + 0.58h_P, -0.4 - 0.64h_2 - 0.13h_P)$$

$$\mathbf{n}_A^s = (0.48 + 0.83h_4 + 0.23h_Q, -0.31 + 0.3h_Q, 0.11 + 0.56h_4 + 0.43h_Q)$$

$$\mathbf{n}_B^s = (0.35 - 0.44h_Q, 0, 0.46 + h_4 + 0.43h_Q)$$

$$\mathbf{n}_N^s = (0.31 + 0.39h_3, -0.53 - 0.67h_3, -0.09 - 0.64h_3 - 0.53h_T),$$

where h_P , h_Q and h_T are the distance between the center of the sphere associated with the vault curvature and the centroid of the polygonal inner basis of the frustum, for more details see Appendix [A.3](#).

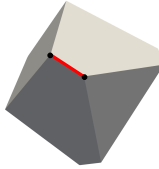
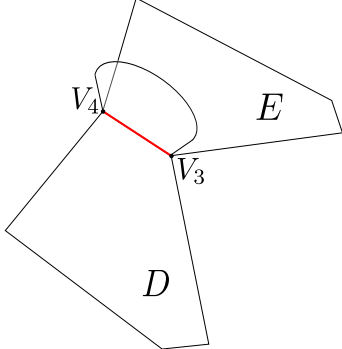
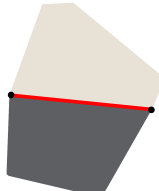
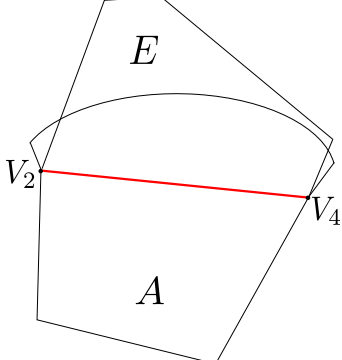
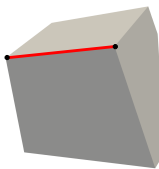
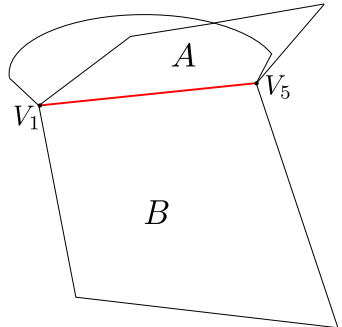
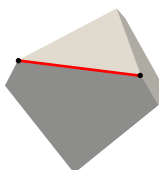
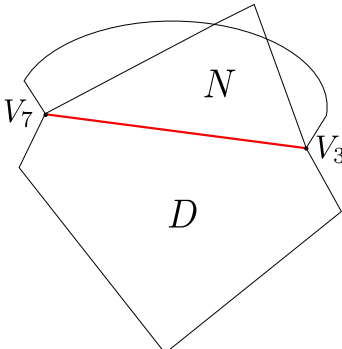
Adjacent polygons	Edges	Vectors	Equation
pentagon–pentagon 		$V_3 = (-0.3, -0.53, 0.51)$ $V_4 = (-0.38, -0.66, 0.2)$ $\mathbf{n}_D = (0.78, 0, -0.16)$ $\mathbf{n}_E = (-0.38, 0.67, -0.16)$ $\mathbf{n}_{DE} = (-0.3, 0.13, 0)$ $\mathbf{c}_3 = (0.078, 0.14, 0.3)$	$\tau_P \mathbf{t}_D$ $+\tau_P \mathbf{t}_E$ $+\tau_{PP} \mathbf{t}_{DE}$ $= 0$
quadrilateral– pentagon 		$V_2 = (-0.66, 0, -0.45)$ $V_4 = (-0.38, -0.66, 0.2)$ $\mathbf{n}_E = (0.78, 0, -0.16)$ $\mathbf{n}_A = (0.28, 0.5, 0.55)$ $\mathbf{n}_{AE} = (-0.3, 0.3, 0.44)$ $\mathbf{c}_2 = (-0.27, 0.66, -0.65)$	$\tau_Q \mathbf{t}_A$ $+\tau_P \mathbf{t}_E$ $+\tau_{PQ} \mathbf{t}_{AE}$ $= 0$
quadrilateral– quadrilateral 		$V_1 = (0, 0, -0.79)$ $V_5 = (-0.65, 0, -0.45)$ $\mathbf{n}_A = (0.28, 0.5, 0.55)$ $\mathbf{n}_B = (-0.57, 0, 0.55)$ $\mathbf{n}_{AB} = (0, 0.52, 0)$ $\mathbf{c}_1 = (-0.66, 0, 0.35)$	$\tau_Q \mathbf{t}_A$ $+\tau_Q \mathbf{t}_B$ $+\tau_{QQ} \mathbf{t}_{AB}$ $= 0$
triangle–pentagon 		$V_3 = (-0.31, -0.53, 0.51)$ $V_7 = (-0.31, 0.53, 0.51)$ $\mathbf{n}_D = (0.78, 0, -0.16)$ $\mathbf{n}_N = (0, 0, 0.79)$ $\mathbf{n}_{DN} = (0.54, 0, 0.33)$ $\mathbf{c}_4 = (0, 1.06, 0)$	$\tau_P \mathbf{t}_D$ $+\tau_T \mathbf{t}_N$ $+\tau_{PT} \mathbf{t}_{DN}$ $= 0$

Table A.1: Edges on the tessellation

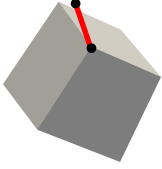
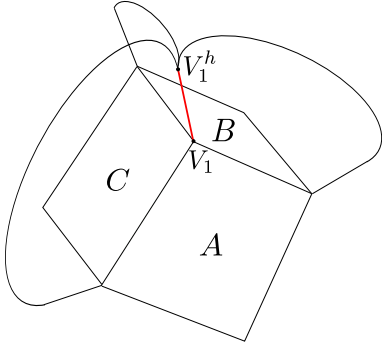
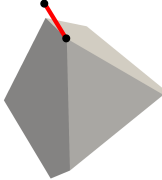
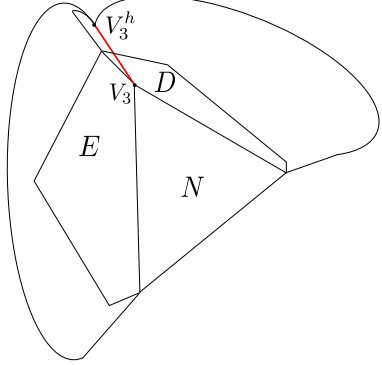
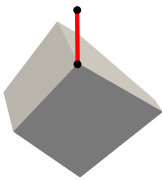
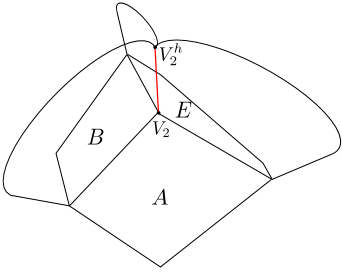
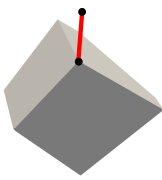
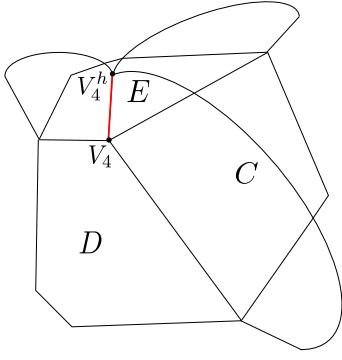
Interaction	Edges	Angles	Equation
quadrilateral– quadrilateral– quadrilateral 		$V_1^h = (0, 0, -0.79 - h_4)$ $\mathbf{n}_{AB} = (0, 0.52, 0)$ $\mathbf{n}_{BC} = (0.45, -0.26, 0)$ $\mathbf{n}_{CA} = (-0.45, -0.26, 0)$ $\mathbf{c}_5 = (0, 0, h_4)$	$\tau_{QQ} \mathbf{t}_{AB}^r$ $+ \tau_{QQ} \mathbf{t}_{BC}^r$ $+ \tau_{QQ} \mathbf{t}_{CA}^r$ $= 0$
pentagon– pentagon– triangle 		$V_3^h = (-0.31 - 0.39h_3,$ $-0.53 - 0.67h_3,$ $0.51 + 0.64h_3)$ $\mathbf{n}_{DE} = (-0.3, 0.13, 0)$ $\mathbf{n}_{DN} = (-0.27, 0.47, 0.33)$ $\mathbf{n}_{EN} = (-0.54, 0, 0.33)$ $\mathbf{c}_7 = (0.39h_3, 0.67h_3, -0.64h_3)$	$\tau_{PT} \mathbf{t}_{DN}^r$ $+ \tau_{PT} \mathbf{t}_{EN}^r$ $+ \tau_{PP} \mathbf{t}_{DE}^r$ $= 0$
quadrilateral– quadrilateral– pentagon 		$V_2^h = (-0.66 - 0.83h_1,$ $0,$ $-0.45 - 0.56h_1)$ $\mathbf{n}_{AB} = (0, 0.52, 0)$ $\mathbf{n}_{AE} = (-0.3, 0.31, 0.44)$ $\mathbf{n}_{BE} = (0.3, 0.31, -0.44)$ $\mathbf{c}_6 = (0.83h_1, 0, 0.56h_1)$	$\tau_{QQ} \mathbf{t}_{AB}^r$ $+ \tau_{PQ} \mathbf{t}_{AE}^r$ $+ \tau_{PQ} \mathbf{t}_{BE}^r$ $= 0$
pentagon– pentagon– quadrilateral 		$V_4^h = (-0.38 - 0.48h_1,$ $-0.67 - 0.84h_1,$ $0.20 + 0.25h_1)$ $\mathbf{n}_{DE} = (-0.23, 0.13, 0)$ $\mathbf{n}_{CD} = (-0.3, 0.31, 0.44)$ $\mathbf{n}_{CE} = (0.41, -0.17, 0.44)$ $\mathbf{c}_8 = (0.48h_1, 0.84h_1, -0.25h_1)$	$\tau_{PP} \mathbf{t}_{DE}^r$ $+ \tau_{PQ} \mathbf{t}_{CD}^r$ $+ \tau_{PQ} \mathbf{t}_{CE}^r$ $= 0$

Table A.2: Radial edges

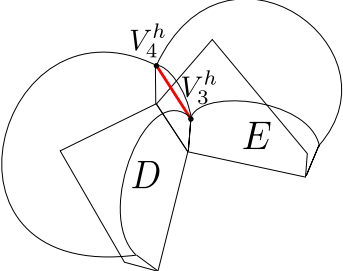
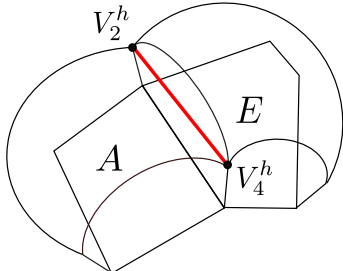
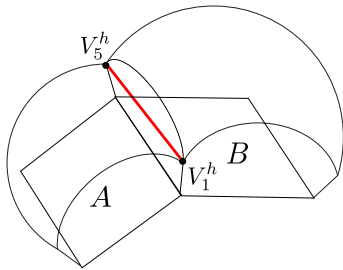
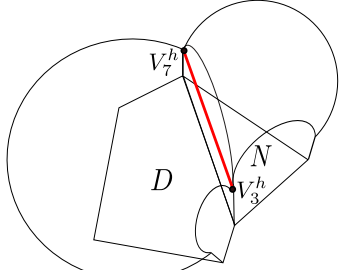
Interaction	Edges	Angles	Equation
pentagon– pentagon		$\mathbf{n}_{DE} = (-0.23, 0.13, 0)$ $\mathbf{c}_{11} = (0.078 + 0.1h_3,$ $0.14 + 0.17h_3,$ $0.3 + 0.38h_3)$	$\tau_P^s \mathbf{t}_D^s$ $+ \tau_P^s \mathbf{t}_E^s$ $+ \tau_{PP}^s \mathbf{t}_{DE}^s$ $= 0$
quadrilateral– pentagon		$\mathbf{n}_{AE} = (0.41, -0.17, 0.44)$ $\mathbf{c}_{10} = (-0.27 - 0.34h_1,$ $0.67 + 0.84h_1,$ $-0.65 - 0.82h_1)$	$\tau_P^s \mathbf{t}_E^s$ $+ \tau_Q^s \mathbf{t}_A^s$ $+ \tau_{PQ}^s \mathbf{t}_{AE}^s$ $= 0$
quadrilateral– quadrilateral		$\mathbf{n}_{AB} = (0, 0.52, 0)$ $\mathbf{c}_9 = (-0.66 - 0.82h_4,$ $0,$ $0.35 + 0.44h_4)$	$\tau_Q^s \mathbf{t}_A^s$ $+ \tau_Q^s \mathbf{t}_B^s$ $+ \tau_{QQ}^s \mathbf{t}_{AB}^s$ $= 0$
pentagon– triangle		$\mathbf{n}_{DN} = (-0.54, 0, 0.33)$ $\mathbf{c}_{12} = (0, -1.06 - 1.34h_3, 0)$	$\tau_P^s \mathbf{t}_D^s$ $+ \tau_T^s \mathbf{t}_N^s$ $+ \tau_{PT}^s \mathbf{t}_{DN}^s$ $= 0$

Table A.3: Edges on the free surface. The expressions of \mathbf{n}_i^s are reported at the beginning of this Appendix.

Tutti gli effetti della Natura sono soltanto conseguenze matematiche di un piccolo numero di leggi immutabili.

P. S. Laplace

3

Pattern formation in soft matter

The main focus of this Chapter is to propose new models to characterize active processes, such as growth and remodeling, in living matter.

First, we study the morphogenetic process behind the formation of folded structure in human brains. In Section 3.1.1, we justify the assumption of a solid model for brain organoids and we compute an estimation of the surface tension acting on a solid cellular aggregate. In Section 3.1.2 we develop a nonlinear elastic model of brain organoids based on the theory of morphoelasticity and we revisit the model proposed by [25] to overcome the limitations remarked by [131]. We describe organoids as nonlinear elastic bodies, com-

posed of a disk surrounded by a growing layer called cortex. The external boundary is subjected to a tissue surface tension due the intercellular adhesion forces. In Section 3.1.3, we perform a linear stability analysis of the radially symmetric configuration and in Section 3.1.4 we implement a finite element code to study the post-buckling behavior. We find that the process of gyrification is triggered by the cortex growth and modulated by the competition between two length scales: the radius of the organoid and the capillary length generated by surface tension. This competition causes a reduction of the cell stiffness and drives lissencephaly: the softening of the organoid strengthens the role of surface tension, delaying or even inhibiting the onset of a mechanical instability at the free boundary. Finally, in Section 3.1.5 we discuss the outcomes of our model together with some concluding remarks.

Secondly, in Section 3.2, we study the c -looping process in the heart tube, that is the first-symmetry breaking process in cardiac embryogenesis. Before septation processes shape its four chambers, the embryonic heart is a straight tube that spontaneously bends and twists breaking the left-right symmetry. First in Section 3.2.1, we propose a morphomechanical model for the torsion of the heart tube describing the heart tube (HT) as a nonlinear incompressible isotropic hollow cylinder. We hypothesize that this spontaneous looping can be modeled as a mechanical instability due to accumulation of residual stresses induced by the geometrical frustration of tissue remodeling, which mimics the cellular rearrangement within the heart tube. Second, in Section 3.2.2, we perform a linear stability analysis of the resulting nonlinear elastic boundary value problem to determine the onset of c -looping as a function of the aspect ratios of the tube and of the internal remodeling rate. Then, in Section 3.2.3, we perform numerical simulations to study the fully nonlinear morphological transition, showing that the soft tube develops a realistic self-contacting looped shape in the physiological range of geometrical parameters. Finally, in Section 3.2.4 we discuss the outcomes of our model together with some concluding remarks.

Then, in Section 3.3, we characterize Faraday waves in soft incompressible slabs. This phenomenon, known as Faraday instability, is now well understood for viscous fluids but surprisingly eluded any theoretical explanation for soft solids. Here, we characterize Faraday waves in soft incompressible slabs using the Floquet theory to study the onset of harmonic and subharmonic resonance eigenmodes. First, in Section 3.3.1, we show some recent experimental results highlighting the emergence of standing waves at the free surface of soft elastic bodies attached to a rigid oscillating substrate and subjected to critical values of forcing frequency and amplitude. Second, in Section 3.3.2, we define the nonlinear elastic problem and we identify its homogeneous solution as the ground state. Then, in Section 3.3.3, we derive the incremental boundary value problem that is solved using the Floquet theory, considering both harmonic and subharmonic resonance modes. In Section 3.3.4.1 we define the dimensionless parameters governing the onset of Faraday instability in soft solids, which characterize the interaction of elastic, gravity and capillary waves. In Section 3.3.4.2 we collect the numerical outcomes of the linear stability analysis and in Section 3.3.4.3 we discuss some analytical results of the linear stability analysis. Remarkably, we found that Faraday instability in soft solids is characterized by a harmonic resonance in the physical range of the material parameters, completely different to the subharmonic resonance that is known to characterize viscous fluids. Finally, in Section 3.3.5, we add few concluding remarks.

Finally, in Section 3.4, we derive the famous Aronson-Bénilan estimate in different L^p spaces, fundamental to provide analytical and numerical models for tissue growth. First, in Section 3.4.2, we introduce the typical single equation model of tissue growth, which is a “modified” porous-media equation, since an additional source term is taken into account, and it will be closed by considering, as equations of state, different pressure fields. Second, in Section 3.4.2.1, we briefly describe the mathematical setting to pass to the incompressible limit in a population-based model and then we carefully describe which kind of regu-

larity the Aronson-Bénilan estimate (AB-estimate) provides in a porous-media setting. In Section 3.4.4, we derive the L^1 -estimate without and with a reaction term G and we show the advantages and limitations of adding a weight h , in particular classical results hold just in 1D, since dissipative terms are missing. Then, in Section 3.4.5, we conduct similar computations in the L^∞ space proving that the additional weight helps in generalizing the AB-type estimate for all pressure laws. We use a similar technique as [102], where they studied the evolution of the Laplacian of the pressure, Δp , which satisfies an appropriate parabolic inequality. Upon introducing a suitable function $h(p)$ characterized a posteriori, they deduced the time estimate on the solution n . Different from [102], here, first we do not need any additional regularity on the quantities involved and then, we do not have to specify the shape of the weight: it solves an inequality, different from [102] where they impose the equality, and we just need to prove that the weight is bounded from above and below. Finally, thanks to Theorem 3.4.4, we are able to pass to the incompressible limit for all fields of pressure. In Section 3.4.6, we perform an L^2 -estimate showing that it can be obtained just for the a particular class of pressure laws. Finally, in Section 3.4.7, we add few concluding remarks.

The results of this Section lead to the following publications:

- D. Riccobelli, and G. Bevilacqua; *Surface tension controls the onset of gyrification in brain organoids*; J. Mech. Phys. Solids (2020) 134: 103745, doi:10.1016/j.jmps.2019.103745, [271].
- G. Bevilacqua, P. Ciarletta, A. Quarteroni; *Morphomechanical model of the torsional c-looping in the embryonic heart*; arxiv.org/pdf/2010.01006.pdf, under review, [46].
- G. Bevilacqua, X. Shao, J. R. Saylor, J. B. Bostwick and P. Ciarletta; *Faraday waves in soft elastic solids*; Proc. Royal Soc. A (2020) 476 no. 2241: 20200129, doi.org/10.1098/rspa.2020.0129, [51].

- X. Shao, G. Bevilacqua, P. Ciarletta, J. R. Saylor, and J. B. Bostwick; *Experimental observation of Faraday waves in soft gels*; under review, [288].
 - G. Bevilacqua, B. Perthame, and M. Schmidtchen; *The Aronson-Bénilan estimate in Lebesgue spaces*; preprint arxiv.org/pdf/2007.15267.pdf, under review, [50].
-

3.1 SURFACE TENSION CONTROLS THE ONSET OF GYRIFICATION IN BRAIN ORGANOIDS

The formation of folded structures in human and animal brains makes it possible to increase the extension of the cerebral cortex, packing a larger number of neurons in a limited space. The creation of these furrows and ridges called *sulci* and *gyri*, respectively, is fundamental for a healthy development of the brain in embryogenesis. The mechanics underlying this morphogenetic phenomenon is not still completely understood.

Recent experiments performed on human brain organoids [193], *i.e.* cell agglomerates cultured in vitro that reproduce the morphogenesis of organs, apparently confirm the hypothesis that sulci are generated by brain cortex buckling triggered by growth [280, 68, 34]. In [193], the authors observed an increased growth of the cortex with respect to the underlying lumen. In some pathological situations such as *lissencephaly*, a genetic mutation, the physiological generation of brain sulci is inhibited or even suppressed. This disease, caused by the LIS1 heterozygous (+/-) mutation, is correlated to nutritional disorders, alterations in muscle tone, severe psychomotor and mental retardation [122]. The mathematical description of brain sulci embryogenesis can provide new insights to understand the mechanisms underlying this disease.

A well developed framework to model mechanical instabilities induced by growth is the theory of *morphoelasticity* [161], where living tissues are treated as growing elastic materials. A spatially inhomogeneous growth generates microstructural misfits, leading to a geometrically incompatible relaxed configuration. The restoration of the compatibility requires elastically distorting the body and generating residual stresses [178, 276].

Differential growth and residual stresses are involved in the morphogenesis of tissues such as intestinal villi [23, 39, 92] and they enhance the mechanical strength of several biological structures, such as arteries [87].

A first model of the experiments on brain organoids [193] has been developed by [25]. The authors model the organoid as a nonlinear elastic material, where gyrification is triggered by a remodeling of the cortex and the contraction of the lumen. In their model, the selection of the critical wavelength is dictated by different mechanical properties of the lumen and the cortex. Despite the good agreement with experimental results, [131] noticed that brain organoids exhibit an unconventional behavior: the cortex is thinner in correspondence of sulci and thicker in correspondence of gyri, in contrast with the morphology predicted by elastic models.

In cellular aggregates, cohesion among cells is due to adhesion forces induced by adhesion molecules [315, 218]. Internal cells are surrounded by other cells, so that the sum of all these forces is zero and each cell is in mechanical equilibrium. Conversely, cells at the boundary of the agglomerate possess a portion of their membrane which is not in contact with other cells: the total adhesion force acting on such cells is non null and it is perpendicular to the free surface of the cellular agglomerate (see Fig. 3.1 for a graphical representation). These forces generate deformation and the appearance of a boundary layer at the periphery that can be treated as a surface effect called *tissue surface tension* [296].

This phenomenon is reminiscent of the mechanics of surface tension in fluids and soft gels [299]. Since organoids and embryos are characterized by small length scales, surface

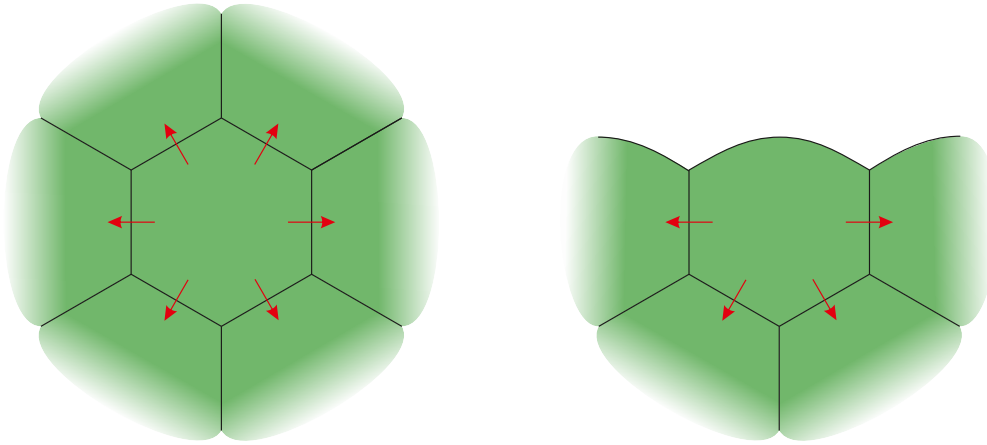


Figure 3.1: Cells in the bulk (left) and on the free surface (right) of a cellular lattice. Adhesion forces generated by the surrounding cells are denoted by the red arrows. The sum of all these forces on an internal cell is zero, while it is non-zero and perpendicular to the boundary for a cell on the free surface.

effects arising from cohesion forces cannot be neglected. The presence of tissue surface tension has been used in fluid models of cellular agglomerates [141, 111, 138] but it is usually overlooked in solid models.

Surface tension has been used within the framework of the theory of nonlinear elasticity to regularize the [55] instability, *i.e.* the buckling instability of an elastic half-space under compression. Without taking into account surface tension, all the wrinkling modes become unstable at the same compression rate [38]. Non-linear elasticity and particularly models based on elastic bilayers [207, 78, 189, 191] have been widely employed to model growth phenomena in living tissues, such as the morphogenesis of intestinal villi [39, 92] and of brain sulci [305, 179]. The majority of the literature (see for instance [190, 27] for solid cylindrical bi-layers) focuses their attention on growth induced instability without considering surface tension. A remarkable exception is provided by the work of [119], where surface tension is introduced in a cylindrical bi-layer as a regularization of the Biot instability: when the substrate is much more rigid than the coating, the critical wavelength goes to zero. A possible method to regularize this instability is to introduce a small surface tension that introduces a new length scale (the capillary length), leading to a finite critical

wavelength (see [38]). At small length scales, elasto-capillary forces can deform soft gel beams [234, 233] even inducing mechanical instabilities [304, 325]. Surface tension can also enhance the resistance to fracture in soft solids [210, 182].

3.1.1 INTERCELLULAR ADHESION GENERATES SURFACE TENSION IN CELLULAR AGGREGATES

At the micro-scale, cellular aggregates are composed by several constituents that, in bulk, have a solid or a fluid-like mechanical nature, like cells, the extracellular matrix, the interstitial fluid. From a macroscopic point of view, these agglomerates can be treated as continuum media but their rheology is still a matter of debate. In fact, cellular aggregates are frequently modeled as fluids [140, 225] that can bear external loading thanks to the tissue surface tension. Another point of view is that cellular aggregates behave as active viscoelastic solids [201, 11, 193].

Some important features of biological tissues mechanics cannot be reproduced by fluid-like models. First, there are experimental evidences that cell mitosis and apoptosis (*i.e.* the cell division and death respectively) are regulated by mechanical stress [231, 230]. In particular, in [85], the authors report an increased cell duplication in the regions where the compressive stress exerted by the surrounding material on the tumor spheroid is minimum. This spatially inhomogeneous growth can be explained only by using a solid description of the cellular agglomerate: the stress tensor of a fluid at rest corresponds to an hydrostatic pressure which is independent on the spatial position [11].

Furthermore, contrarily to fluids, solids can store mechanical stress even in the absence of external loads. These stresses are called residual [178] and they are created when differential growth in solid matter develops microstructural misfits. These geometrical incompatibilities are restored by elastic distortions of the body, generating mechanical stress [276, 161, 270].

Contrary to the fluid approach, the tissue surface tension of cellular aggregates is frequently neglected in solid models. Nonetheless, solids possess surface tension too [299]: it can play an important role, when the aggregate is very soft or has a small size. In fact, surface tension introduces a new length scale in the problem: let μ be the shear modulus of the cellular agglomerate and γ the surface tension, then the capillary length ℓ is defined as [233, 299]

$$\ell = \frac{\gamma}{\mu}.$$

Whenever this length scale is of the same order as the characteristic length of the body (e.g. the radius of a spheroid) surface tension cannot be neglected: it can produce a non-negligible deformation [233, 298, 236] and it can even induce mechanical instabilities [234, 304, 325]. Cellular aggregates are very soft and the effect of the surface tension can be highly relevant, as we show in the following.

3.1.1.1 ESTIMATION OF THE SURFACE TENSION

There are experimental evidences that a tensile skin, having the thickness of a couple of cells, generates an isotropic compression inside multicellular aggregates [205]. This phenomenon can be explained as a manifestation of tissue surface tension induced by intercellular adhesion: the tensile skin is indeed very thin and such boundary layer can be treated as a surface tension.

Modeling the unloaded multicellular spheroid as a ball occupying the domain

$$\Omega_s = \{ \mathbf{X} \in \mathbb{R}^3 \mid |\mathbf{X}| < R_o \},$$

we assume that the spheroid is composed of an incompressible elastic material. Let \mathbb{T} be

the Cauchy stress tensor, the balance of the linear and angular momentum reads

$$\operatorname{div} \mathbb{T} = \mathbf{0}. \quad (3.1)$$

If the spheroid is subjected to a tissue surface tension γ , the boundary condition reads [299]

$$\mathbb{T}\mathbf{n} = \gamma\mathcal{K}\mathbf{n}, \quad \text{at } R = R_o \quad (3.2)$$

where R denotes the radial position, \mathcal{K} is twice the mean curvature, and \mathbf{n} is the external normal.

We now show that the undeformed reference configuration is in mechanical equilibrium. Experimental observations [205] lead us to state that residual stresses are absent. The Cauchy stress is then given by [243]

$$\mathbb{T} = -p\mathbb{I}$$

where \mathbb{I} is the identity and p is the pressure field that enforces the incompressibility constraint. A constant pressure field p satisfies the equilibrium equation (3.1). By imposing Eq. (3.2), we get

$$p = \frac{2\gamma}{R_o}$$

which is nothing but the Young-Laplace equation. We invert the previous equation with respect to γ , obtaining

$$\gamma = \frac{pR_o}{2}. \quad (3.3)$$

From the work of [205], we get that the typical radius of a spheroid is $\sim 400 \mu\text{m}$ and the internal pressure p is about 500 Pa (Fig. 5d in [205]). From these data and from Eq. (3.3), we estimate that the surface tension acting on the spheroid is $\gamma \simeq 0.1 \text{ N/m}$.

Remark 3.1.1. In this Section, we have estimated the tissue surface tension acting on

a spheroid. Unfortunately, up to our knowledge, there are not similar experimental data that can be used to perform the same computation for brain organoids. There are some measurements of the surface tension acting on different embryonic tissues when they are treated as fluids [285]. In their work, all the measured values have the same order of magnitude. From these data, we can assume that $\gamma \simeq 0.1 \text{ N/m}$ is a qualitative estimate of tissue surface tension acting on a brain organoid.

3.1.2 ELASTIC MODEL OF BRAIN ORGANOID

In this Section, we illustrate a model of brain organoids, described as growing hyperelastic bodies subjected to surface tension.

3.1.2.1 KINEMATICS

We denote by \mathbf{X} the material position coordinate. Since brain organoids are cell aggregates confined in a narrow space by a coverslip and a membrane [193], we model them as two dimensional objects. Let

$$\Omega_0 = \{ \mathbf{X} = [R \cos \Theta, R \sin \Theta] \in \mathbb{R}^2 \mid 0 \leq R < R_o \text{ and } 0 \leq \Theta < 2\pi \}$$

be the reference configuration of the organoid. We indicate with $\varphi : \Omega_0 \rightarrow \mathbb{R}^2$ the deformation field, so that the actual configuration of the body Ω is given by $\varphi(\Omega_0)$. Let $\mathbf{x} = \varphi(\mathbf{X})$ be the actual position of the point \mathbf{X} and the displacement vector is defined as $\mathbf{u}(\mathbf{X}) = \varphi(\mathbf{X}) - \mathbf{X}$. Let \mathbf{F} be the deformation gradient, *i.e.* $\mathbf{F} = \text{Grad } \varphi$. We exploit a multiplicative decomposition of the deformation gradient (known as Kröner-Lee decomposition [196, 204]) to model the growth of the organoid, so that

$$\mathbf{F} = \mathbf{F}_e \mathbf{G}$$

where the growth tensor \mathbf{G} accounts for the local inelastic distortion due to the body growth, while \mathbf{F}_e describes the elastic distortion necessary to maintain the geometrical compatibility of the body and to balance the external and internal forces [276]. As commonly done for biological tissues, it is reasonable to model organoids as incompressible media, namely we enforce that

$$\det \mathbf{F}_e = 1. \quad (3.4)$$

In [193], the authors identified two distinct regions in brain organoids: an internal lumen and an external ring, called cortex, the latter being characterized by a faster growth. Indicating with R_i the radius of the lumen, we denote these two regions by Ω_{0L} and Ω_{0R} :

$$\Omega_{0L} = \{\mathbf{X} \in \Omega \mid R < R_i\}, \quad \Omega_{0C} = \{\mathbf{X} \in \Omega \mid R_i < R < R_o\},$$

and their images through φ are denoted by Ω_L and Ω_R respectively.

We assume that the growth tensor \mathbf{G} takes diagonal form

$$\mathbf{G} = \begin{cases} 1 & \text{if } R < R_i, \\ g\mathbf{I} & \text{if } R_i < R < R_o, \end{cases} \quad (3.5)$$

where the scalar quantity g is the growth rate of the cortex with respect to the lumen.

Tissue surface tension acts at both the interfaces organoid-coverslip and organoid-membrane.

Let us call γ_{membrane} and $\gamma_{\text{coverslip}}$ the tension acting on the organoid at the interface with these two surfaces. Their contribution to the total energy is given by

$$E_{\text{interface}} = \int_{\Omega} [\gamma_{\text{membrane}} + \gamma_{\text{coverslip}}] dv = (\gamma_{\text{membrane}} + \gamma_{\text{coverslip}}) |\Omega_0| \det \mathbf{F}.$$

Since the deformation is isochoric, $\det \mathbf{F} = \det \mathbf{G}$. The contribution of the surface tension acting on both the membrane and the coverslip, given by $E_{\text{interface}}$, does not change when

the organoid undergoes an elastic deformation and it does not influence either the stability or the morphology of the organoid. This agrees with the observations of [193]: the authors tried different coverslips and membranes, each one characterized by a different adhesion to the organoid and they did not notice remarkable differences (see Fig. S9 of the supplementary material of [193]). From now on, since $E_{\text{interface}}$ does not influence the deformation of the body, it is not explicitly included in the total energy.

We now introduce some mechanical constitutive assumptions.

3.1.2.2 MECHANICAL CONSTITUTIVE ASSUMPTIONS AND FORCE BALANCE EQUATIONS

We assume that the organoids are composed of a homogenous hyperelastic material, having strain energy density W . The first Piola–Kirchhoff stress \mathbf{P} and the Cauchy stress tensors \mathbf{T} are then given by

$$\mathbf{P} = (\det \mathbf{G})\mathbf{G}^{-1} \frac{\partial W_0(\mathbf{F}_e)}{\partial \mathbf{F}_e} - p\mathbf{F}^{-1} \quad \mathbf{T} = \frac{1}{\det \mathbf{F}}\mathbf{F}\mathbf{P}$$

where p is the Lagrange multiplier enforcing the incompressibility constraint (3.4). The balance of the linear and angular momentum reads

$$\text{Div } \mathbf{P} = \mathbf{0} \text{ in } \Omega_{0L}, \Omega_{0C}, \quad \text{or} \quad \text{div } \mathbf{T} = \mathbf{0} \text{ in } \Omega_L, \Omega_C \quad (3.6)$$

in the material and actual reference frame, respectively.

We assume that the center of the organoid is fixed, *i.e.*

$$\mathbf{u}(\mathbf{0}) = \mathbf{0} \quad (3.7)$$

while a constant surface tension γ acts at the external boundary of the organoid, so that

[299]

$$\mathbb{T}\mathbf{n} = \gamma\mathcal{K}\mathbf{n} \quad (3.8)$$

where \mathbf{n} is the outer normal in spatial coordinates and \mathcal{K} is the oriented curvature of the boundary curve \mathcal{L} parametrized clockwise, *i.e.*

$$\mathcal{L}(\Theta) = \varphi ([R_o \cos(\Theta), R_o \sin(-\Theta)]). \quad (3.9)$$

The Lagrangian form of the boundary condition (3.8) is obtained performing a pull-back

$$\mathbf{P}^T \mathbf{N} = (\det \mathbf{F}) \gamma \mathcal{K} \mathbf{F}^{-T} \mathbf{N}. \quad (3.10)$$

Finally, we enforce the continuity of the stress at the interface $R = R_i$, so that

$$\lim_{R \rightarrow R_i^-} \mathbf{P}^T \mathbf{N} = \lim_{R \rightarrow R_i^+} \mathbf{P}^T \mathbf{N}. \quad (3.11)$$

We can assume that brain organoids behave as isotropic media, since they are composed of neural progenitors and not fully developed neurons [193]. Moreover, in the fully developed brain, both the gray and the white matter are essentially isotropic [66, 67]. As it concerns the internal structure, brain organoids are complex cell agglomerates composed of different biological materials, such as the extra-cellular matrix, cells, interstitial fluid. According to the observations reported in [193], the extra cellular matrix and the cellular cytoskeleton account for the elasticity of the organoid. We have assumed that the two elastic phases in the organoids generate a homogeneous hyperelastic material. There are several works which show a very good fit of the experimental data by assuming a Mooney–Rivlin model (especially when the stretches are moderate [120, 27]). Such an energy reduces to the neo-Hookean one whenever the deformation is planar. Hence, the strain energy density is given

by

$$W(\mathbf{F}) = \det(\mathbf{G})W_0(\mathbf{F}_e) = (\det \mathbf{G})\frac{\mu}{2}(\text{tr}(\mathbf{F}_e^T \mathbf{F}_e) - 2). \quad (3.12)$$

The first Piola–Kirchhoff and Cauchy stress tensors read, respectively,

$$\begin{cases} \mathbf{P} = \mu(\det \mathbf{G})\mathbf{G}^{-1}\mathbf{G}^{-T}\mathbf{F}^{-T} - p\mathbf{F}^{-1}, \\ \mathbf{T} = \mu\mathbf{F}\mathbf{G}^{-1}\mathbf{G}^{-T}\mathbf{F}^T - pl. \end{cases} \quad (3.13)$$

Summing up, Eqs. (3.4) and (3.6), together with the kinematic constraint Eq. (3.7) and the boundary condition Eq. (3.10) define the nonlinear elastic problem. In the next Section we look for a radially symmetric solution.

3.1.2.3 EQUILIBRIUM RADIALY-SYMMETRIC SOLUTION

Let (r, θ) be the actual radial and polar coordinates of a point. Let $(\mathbf{E}_R, \mathbf{E}_\Theta)$ and $(\mathbf{e}_r, \mathbf{e}_\theta)$ be the local vector basis in polar coordinates in the Lagrangian and Eulerian reference frame, respectively. We look for a radially-symmetric solution of the form

$$\boldsymbol{\varphi}(\mathbf{X}) = r(R)\mathbf{e}_r.$$

The deformation gradient expressed in polar coordinates reads

$$\mathbf{F} = \text{diag}\left(r', \frac{r}{R}\right). \quad (3.14)$$

It is immediate to notice that

$$r(R) = R \quad \text{for } R < R_i,$$

where $r_i = r(R_i) = R_i$. In the cortex, from the incompressibility constraint given by Eq. (3.4), we get

$$r'r = g^2 R.$$

Performing an integration and imposing that $R_i = r_i$, we get

$$r(R) = g \sqrt{R^2 + \left(\frac{1}{g^2} - 1\right) R_i^2}. \quad (3.15)$$

It remains to determine the pressure field p . First, we notice that, inverting and differentiating (3.15), we obtain

$$\begin{cases} R = \frac{1}{g} \sqrt{r^2 + (g^2 - 1) R_i^2}, \\ r' = g \frac{\sqrt{r^2 + (g^2 - 1) R_i^2}}{r}, \end{cases} \quad \text{in } R_i < R < R_o \quad (3.16)$$

respectively. The curvature of the boundary line is $-r_o^{-1}$, where

$$r_o = r(R_o) = g \sqrt{R_o^2 + \left(\frac{1}{g^2} - 1\right) R_i^2}.$$

The boundary condition Eq. (3.8) reads

$$\mathbb{T} \mathbf{e}_r = -\frac{\gamma}{r_o} \mathbf{e}_r.$$

Since the deformation depends only on the radial position r , the balance of the linear and angular momentum in polar coordinates reads

$$\frac{dT_{rr}}{dr} + \frac{T_{rr} - T_{\theta\theta}}{r} = 0 \quad (3.17)$$

where T_{ij} are the components of the Cauchy stress tensor \mathbb{T} in polar coordinates. From

Eqs. (3.13), (3.14) and (3.16), the Cauchy stress in the cortex reads

$$\mathbb{T} = \text{diag} \left(\frac{\mu (R_i^2 (g^2 - 1) + r^2)}{r^2} - p, \frac{\mu r^2}{R_i^2 (g^2 - 1) + r^2} - p \right). \quad (3.18)$$

We can integrate Eq. (3.17) from r to r_o , obtaining

$$T_{rr}(r) = -\frac{\gamma}{r_o} + \int_r^{r_o} \left[\frac{\mu \left(-\frac{\rho^4}{R_i^2 (g^2 - 1) + \rho^2} + R_i^2 (g^2 - 1) + \rho^2 \right)}{\rho^3} \right] d\rho. \quad (3.19)$$

We can find the pressure field in the cortex (*i.e.* for $r_i < r < r_o$) by plugging Eq. (3.18) into Eq. (3.19), obtaining

$$\begin{aligned} p = f_p(r) := & \frac{1}{2} \left(\mu \left(\frac{R_i^2 (g^2 - 1)}{r^2} + 2 \right) + \right. \\ & + \mu \left(-\log (R_i^2 (g^2 - 1) + r^2) + \log (R_i^2 (g^2 - 1) + r_o^2) + 2 \log \left(\frac{r}{r_o} \right) \right) + \\ & \left. + \frac{\mu R_i^2 (g^2 - 1) + 2\gamma r_o}{r_o^2} \right). \end{aligned} \quad (3.20)$$

Finally, we impose the continuity of the stress Eq. (3.11) at $r = r_i = R_i$ to get the pressure for $r < r_i$. Since the lumen remains undeformed, the Cauchy stress reads

$$\mathbb{T} = -p_L \mathbf{1}.$$

Using Eq. (3.18) and Eq. (3.20), we can write the solution

$$\begin{cases} r = R \\ p = p_L := f_p(r_i) + \mu - g^2 \mu \end{cases} \quad \text{for } r < r_i, \quad (3.21)$$

$$\begin{cases} r = g \sqrt{R^2 + \left(\frac{1}{g^2} - 1\right) R_i^2} \\ p = p_C := f_p(r) \end{cases} \quad \text{for } r_i < r < r_o. \quad (3.22)$$

In the next section a linear stability analysis of the solution given by Eqs. (3.21)-(3.22) is performed, but first we remark some important aspects regarding the boundary conditions.

Remark 3.1.2. In this model, we have assumed that the only force acting on the boundary of the organoid is due to tissue surface tension. We remark that, in the experiments reported in [193], organoids are embedded in Matrigel. Karzbrun and co-authors tried different concentration of the gel, without registering remarkable changes to the morphology of the wrinkling (see Fig. S9 [193]), so that we are lead to conjecture that Matrigel has a negligible effect on the onset of the instability.

Matrigel is characterized by an elastic modulus of the same order as the organoid one (500 Pa [294]). In each experiment, eleven organoids are placed in a dish having a diameter of 6 cm, so that the distance among organoids is of the order of centimeters. The distance among organoids is much larger than the displacement induced by the organoid growth, so that the response of the Matrigel is linear and can be modeled as the action of linear springs acting at the boundary, as done for similar motivations in [273]. We have verified through this approach that the role of Matrigel is negligible. For the readers interested in the modeling of the Matrigel embedment, we expose in Appendix B.2 some details on the linear stability analysis in the presence of linear springs at the boundary.

3.1.3 LINEAR STABILITY ANALYSIS

3.1.3.1 INCREMENTAL EQUATIONS

We apply the theory of incremental deformations superposed on finite strains [243] to investigate the stability of the radially symmetric solution. Let $\delta\mathbf{u}$ be the incremental displacement field and let $\Gamma = \text{grad } \delta\mathbf{u}$. We introduce the push-forward of the incremental Piola-Kirchhoff stress in the axisymmetric deformed configuration, given by

$$\delta\mathbf{P} = \mathcal{A}_0 : \Gamma + p\Gamma - \delta p\mathbf{I} \quad (3.23)$$

where \mathcal{A}_0 is the fourth order tensor of instantaneous elastic moduli, δp is the increment of the Lagrangian multiplier that imposes the incompressibility constraint. The two dots operator ($:$) denotes the double contraction of the indices

$$(\mathcal{A}_0 : \Gamma)_{ij} = (A_0)_{ijhk} \Gamma_{kh},$$

where the convention of summation over repeated indices is used. The components of the tensor \mathcal{A}_0 for a neo-Hookean material are given by

$$(A_0)_{ijhk} = \mu \delta_{ik} (B_e)_{jh}$$

where $B_e = F_e F_e^T$ and δ_{ik} is the Kronecker Delta. The incremental equilibrium equation and the linearized form of the incompressibility constraint read respectively

$$\begin{cases} \text{Div } \delta\mathbf{P} = \mathbf{0} & \text{in } \Omega_{0L}, \Omega_{0C}, \\ \text{tr } \Gamma = 0 & \text{in } \Omega_{0L}, \Omega_{0C}. \end{cases} \quad (3.24)$$

The linearized form of the kinematic constraint (3.7) and of the boundary condition (3.8) complement the incremental equations

$$\delta \mathbf{u}(\mathbf{0}) = \mathbf{0}, \quad (3.25)$$

$$\delta \mathbf{P} \mathbf{e}_r = \gamma \delta \mathcal{K} \mathbf{e}_r - \gamma \mathcal{K} \Gamma^T \mathbf{e}_r, \quad (3.26)$$

where $\delta \mathcal{K}$ is the increment of the curvature. Finally, we enforce the continuity of the incremental displacement of the stress at the interface

$$\begin{cases} \lim_{r \rightarrow R_i^-} \delta \mathbf{u} = \lim_{r \rightarrow R_i^+} \delta \mathbf{u}, \\ \lim_{r \rightarrow R_i^-} \delta \mathbf{P}^T \mathbf{e}_r = \lim_{r \rightarrow R_i^+} \delta \mathbf{P}^T \mathbf{e}_r. \end{cases} \quad (3.27)$$

In the following, we rewrite the incremental problem given by the Eqs. (3.24)-(3.26) into a more convenient form using the [297] formulation.

3.1.3.2 STROH FORMULATION

We rewrite the incremental problem in non-dimensional form adopting as the characteristic length scale and shear modulus R_o and μ respectively. The behavior of the problem is governed by the non-dimensional parameters

$$\alpha_\gamma = \frac{\ell}{R_o} = \frac{\gamma}{\mu R_o}, \quad \alpha_R = \frac{R_i}{R_o}, \quad (3.28)$$

in addition to the growth parameter g .

For the sake of brevity, we introduce the multi-index $W = \{L, C\}$. The quantities with subscript L are computed in the lumen, while the ones in the cortex have the subscript C.

We denote with u_W and v_W the components of $\delta \mathbf{u}_W$ while δP_{rr}^W and $\delta P_{r\theta}^W$ are the com-

ponents of the incremental stress along the radial direction \mathbf{e}_r . We can reduce the system of partial differential equations (3.24) into a system of ordinary differential equations by assuming the following ansatz for the incremental displacement, pressure and stress:

$$u_W(r, \theta) = U_W(r) \cos(m\theta), \quad (3.29)$$

$$v_W(r, \theta) = V_W(r) \sin(m\theta), \quad (3.30)$$

$$\delta P_{rr}^W(r, \theta) = s_{rr}^W(r) \cos(m\theta), \quad (3.31)$$

$$\delta P_{r\theta}^W(r, \theta) = s_{r\theta}^W(r) \sin(m\theta), \quad (3.32)$$

$$\delta p_{r\theta}^W(r, \theta) = Q^W(r) \cos(m\theta), \quad (3.33)$$

where $m \in \{n \in \mathbb{N} \mid n \geq 2\}$ is the circumferential wavenumber. By substituting Eq. (3.31) into Eq. (3.24), we obtain the following expression for Q^L and Q^C

$$\begin{aligned} Q^L(r) &= -s_{rr}^L(r) + p_L U_L'(r), \\ Q^C(r) &= U_C'(r) \left(\frac{\alpha_R^2 (g^2 - 1)}{r^2} + p_C + 1 \right) - s_{r\theta}^C(r), \end{aligned}$$

where p_L, p_C are defined in Eq. (3.22).

By the choices (3.29)-(3.32) and using a well established procedure, the incremental problem can be rewritten in the [297] form

$$\frac{d\boldsymbol{\eta}_W}{dr} = \frac{1}{r} \mathbf{N}_W \boldsymbol{\eta}_W \quad \text{with } W = \{L, C\}, \quad (3.34)$$

where $\boldsymbol{\eta}_W$ is the *displacement-traction vector* defined as

$$\boldsymbol{\eta}_W = [\mathbf{U}_W, r \boldsymbol{\Sigma}_W] \quad \text{where} \quad \begin{cases} \mathbf{U}_W = [U_W, V_W], \\ \boldsymbol{\Sigma}_W = [s_{rr}^W, s_{r\theta}^W]. \end{cases}$$

The matrix $\mathbf{N}_W \in \mathbb{R}^{4 \times 4}$ is the *Stroh matrix* and it has the following sub-block form

$$\mathbf{N}_L = \begin{bmatrix} \mathbf{N}_1^W & \mathbf{N}_2^W \\ \mathbf{N}_3^W & \mathbf{N}_4^W \end{bmatrix}.$$

For the lumen ($r < r_i$), the sub-blocks read:

$$\begin{aligned} \mathbf{N}_1^L &= \begin{bmatrix} -1 & -m \\ mp_L & p_L \end{bmatrix}, & \mathbf{N}_3^L &= \begin{bmatrix} -p_L^2 m^2 + m^2 + 2p_L + 2 & m(-p_L^2 + 2p_L + 3) \\ 1 & -mp_L \end{bmatrix}, \\ \mathbf{N}_2^L &= \begin{bmatrix} 0 & 0 \\ 0 & 1 \end{bmatrix}, & \mathbf{N}_4^L &= \begin{bmatrix} m(-p_L^2 + 2p_L + 3) & (2m^2 - p_L + 1)(p_L + 1) \\ m & -p_L \end{bmatrix}. \end{aligned} \quad (3.35)$$

In the cortex ($r_i < r < r_o$), the sub-blocks are given by

$$\begin{aligned} \mathbf{N}_1^C &= \begin{bmatrix} -1 & -m \\ mp_C \beta_C & p_C \beta_C \end{bmatrix}, & \mathbf{N}_2^C &= \begin{bmatrix} 0 & 0 \\ 0 & \beta_C \end{bmatrix}, & \mathbf{N}_4^C &= \begin{bmatrix} 1 & -mp_C \beta_C \\ m & -p_C \beta_C \end{bmatrix}, \\ \mathbf{N}_3^C &= \begin{bmatrix} 1/\beta_C + (1 + m^2)\beta_C + p_C(2 - mp_C \beta_C) & m\beta_C(2 + 1/\beta_C^2 + 2p_C/\beta_C - p_C^2) \\ m\beta_C(2 + 1/\beta_C^2 + 2p_C/\beta_C - p_C^2) & m^2/\beta_C + (1 + m^2)\beta_C + 2m^2 p_C - p_C^2 \beta_C \end{bmatrix}; \end{aligned} \quad (3.36)$$

where

$$\beta_C = \frac{r^2}{r^2 + (g^2 - 1)\alpha_R^2}.$$

We remark that the coefficient of the Stroh matrix are constant in the lumen (see Eq. (3.35)).

This allows us to solve analytically the incremental problem for $r < r_i$.

3.1.3.3 INCREMENTAL SOLUTION FOR THE LUMEN

We follow the procedure proposed in [119] and in [25]. Since Eq. (3.34) with $W = L$ is a system of ODEs with constant coefficients, its solution can be rewritten in terms of eigen-

values and eigenvectors of \mathbf{N}_L . The eigenvalues of \mathbf{N}_L are $\lambda_1 = m - 1$, $\lambda_2 = m + 1$, $\lambda_3 = -m + 1$ and $\lambda_4 = -m - 1$. The general integral of Eq. (3.34) is given by

$$\boldsymbol{\eta}_L = c_1 \mathbf{w}_1 r^{m-1} + c_2 \mathbf{w}_2 r^{m+1} + c_3 \mathbf{w}_3 r^{-m+1} + c_4 \mathbf{w}_4 r^{-m-1}, \quad (3.37)$$

where \mathbf{w}_i are the eigenvectors of \mathbf{N}_L associated with the eigenvalues λ_i , $i = 1, \dots, 4$. Since the incremental solution must satisfy the kinematic constraint Eq. (3.25), we immediately get that $c_3 = c_4 = 0$ while

$$\begin{aligned} \mathbf{w}_1 &= [-1, 1, -(m-1)(1+p_L), (m-1)(1+p_L)] \\ \mathbf{w}_2 &= [-m, m+2, -(m+1)(m(1+p_L)-4), (m+1)((m+2)+(m-2)p_L)]. \end{aligned} \quad (3.38)$$

The two constants c_1 and c_2 will be fixed by imposing the continuity of the displacement and of the stress at $r = r_i$ (*i.e.* by enforcing Eq. (3.27)).

3.1.3.4 NUMERICAL PROCEDURE FOR THE SOLUTION IN THE CORTEX

The incremental problem in the cortex cannot be solved analytically since the coefficient of the Stroh matrix \mathbf{N}_C given by Eq. (3.36) are not constant. To overcome this difficulty, we implement a numerical code based on the impedance matrix method [59, 60].

We first introduce the *conditional impedance matrix*, defined as

$$r \boldsymbol{\Sigma}_C(r) = \mathbf{Z}_C(r, r_o) \mathbf{U}_C(r). \quad (3.39)$$

Such a matrix is called conditional since its expression depends on an auxiliary condition at $r = r_o$, in this case the boundary condition Eq. (3.26). In the following paragraphs we expose a procedure to construct the matrix $\mathbf{Z}_C(r, r_o)$. The incremental boundary condition

Eq. (3.26) reads

$$\delta \mathbf{P}^T \mathbf{e}_r = \alpha_\gamma \delta \mathcal{K} \mathbf{e}_r + \frac{\alpha_\gamma}{r_o} \Gamma^T \mathbf{e}_r, \quad \text{at } r = r_o. \quad (3.40)$$

where the incremental curvature $\delta \mathcal{K}$ is given by (see the Appendix B.1 for the details of the computation):

$$\delta \mathcal{K} = \frac{1}{r_o^2} \left(\frac{\partial u}{\partial \theta} + \frac{\partial^2 u}{\partial \theta^2} \right), \quad \text{at } r = r_o.$$

From the ansatz of variable separation in Eqs.(3.29)-(3.30) and using the incremental form of the incompressibility constraint Eq. (3.24), the boundary condition Eq. (3.40) is equivalent to

$$\delta \mathbf{P}^T \mathbf{e}_r = -\frac{\alpha_\gamma}{r_o^2} \left[(m^2 U_C + m V_C) \cos(m\theta), (m U_C + V_C) \sin(m\theta) \right] \quad \text{at } r = r_o. \quad (3.41)$$

We can now define the *auxiliary impedance matrix* [242] as

$$\mathbf{Z}_o^C = -\frac{\alpha_\gamma}{r_o} \begin{bmatrix} m^2 & m \\ m & 1 \end{bmatrix}, \quad (3.42)$$

so that the boundary condition Eq. (3.41) is equivalent to the equation

$$r_o \boldsymbol{\Sigma}_C(r_o) = \mathbf{Z}_o^C \mathbf{U}(r_o). \quad (3.43)$$

We introduce the matricant

$$\mathbf{M}^C(r, r_o) = \begin{bmatrix} \mathbf{M}_1^C(r, r_o) & \mathbf{M}_2^C(r, r_o) \\ \mathbf{M}_3^C(r, r_o) & \mathbf{M}_4^C(r, r_o) \end{bmatrix}, \quad \mathbf{M}^C(r, r_o) \in \mathbb{R}^{4 \times 4}$$

called *conditional matrix*, defined as the solution of the problem

$$\begin{cases} \frac{d\mathbf{M}^C}{dr} = \frac{1}{r}\mathbf{N}_C\mathbf{M}^C(r, r_o) \\ \mathbf{M}^C(r_o, r_o) = \mathbf{I}. \end{cases} \quad (3.44)$$

From Eq. (3.44), the Stroh form of the incremental problem given by Eq. (3.34) and Eq. (3.43), we get

$$\begin{cases} \mathbf{U}_C(r) = (\mathbf{M}_1^C(r, r_o) + r_o\mathbf{M}_2^C(r, r_o)\mathbf{Z}_o)\mathbf{U}_C(r_o), \\ r\mathbf{\Sigma}_C(r) = (\mathbf{M}_3^C(r, r_o) + r_o\mathbf{M}_4^C(r, r_o)\mathbf{Z}_o)\mathbf{U}_C(r_o), \end{cases}$$

so that

$$r\mathbf{\Sigma}_C(r) = (\mathbf{M}_3^C(r, r_o) + r_o\mathbf{M}_4^C(r, r_o)\mathbf{Z}_o)(\mathbf{M}_1^C(r, r_o) + r_o\mathbf{M}_2^C(r, r_o)\mathbf{Z}_o)^{-1}\mathbf{U}_C(r). \quad (3.45)$$

From Eq. (3.45), the conditional impedance matrix is given by

$$\mathbf{Z}_C(r, r_o) = (\mathbf{M}_3^C(r, r_o) + r_o\mathbf{M}_4^C(r, r_o)\mathbf{Z}_o)(\mathbf{M}_1^C(r, r_o) + r_o\mathbf{M}_2^C(r, r_o)\mathbf{Z}_o)^{-1}.$$

From now on, we omit the dependence of \mathbf{Z}_C wherever convenient for sake of simplicity. By using Eq. (3.39), we can rewrite the Stroh problem given by Eq. (3.34) into a differential Riccati equation. Indeed, from Eq. (3.34), we get

$$\frac{d\mathbf{U}_C}{dr} = \frac{1}{r}(\mathbf{N}_1^C\mathbf{U}_C + \mathbf{N}_2^C\mathbf{Z}_C\mathbf{U}_C), \quad (3.46)$$

$$\frac{d\mathbf{Z}_C}{dr}\mathbf{U}_C + \mathbf{Z}_C\frac{d\mathbf{U}_C}{dr} = \frac{1}{r}(\mathbf{N}_3^C\mathbf{U}_C + \mathbf{N}_4^C\mathbf{Z}_C\mathbf{U}_C). \quad (3.47)$$

Substituting Eq. (3.46) into Eq. (3.47) we get the following differential Riccati equation

$$\frac{d\mathbf{Z}_C}{dr} = \frac{1}{r}(\mathbf{Z}_C\mathbf{N}_1^C - \mathbf{Z}_C\mathbf{N}_2^C\mathbf{Z}_C + \mathbf{N}_3^C + \mathbf{N}_4^C\mathbf{Z}_C). \quad (3.48)$$

We integrate Eq. (3.48) from r_o to r_i , using as initial condition the auxiliary impedance matrix defined in Eq. (3.42), *i.e.*

$$Z_C(r_o, r_o) = Z_o^C.$$

To construct a bifurcation criterion, we follow [25]: from the continuity of the displacement-traction vector $\boldsymbol{\eta}_C(r_i) = \boldsymbol{\eta}_L(r_i)$ Eq. (3.27) we get

$$r_i \boldsymbol{\Sigma}_L(r_i) = r_i \boldsymbol{\Sigma}_C(r_i) = Z_C(r_i, r_o) \mathbf{U}_C(r_i) = Z_C(r_i, r_o) \mathbf{U}_L(r_i),$$

so that non-null solutions of the incremental problem exist if and only if

$$\det[\mathbf{A} - Z_C(r_i, r_o) \mathbf{B}] = 0, \quad (3.49)$$

where

$$A_{ij} = (w_i)_{j+2} \quad B_{ij} = (w_i)_j, \quad i, j = 1, 2,$$

with \mathbf{w}_i defined in Eq. (3.38). For a fixed value of the control parameter g we integrate the Riccati Eq. (3.48) from $r = r_o$ up to $r = r_i$ making use of the the software MATHEMATICA 11.3 (Wolfram Research, Champaign, IL, USA). We iteratively increase the control parameter g until the bifurcation criterion Eq. (3.49) is satisfied.

3.1.3.5 DISCUSSION OF THE RESULTS

First, we need to identify an interval of interest for the dimensionless parameter α_γ . We have estimated the surface tension of cellular aggregates in Section 3.1.1.1. From the stress profiles reported by [205], we obtain a surface tension of the order of 10^{-1} N/m. According to [193], the shear modulus of the wild-type brain organoid is $\mu \simeq 900$ Pa (Young modulus $E \simeq 2.7$ kPa) while $\mu \simeq 333$ Pa (Young modulus $E \simeq 1$ kPa) for the unhealthy ones, afflicted

by lissencephaly (*i.e.* when the mutation LIS1 +/- is present). Provided that the typical radius of the organoid is about $R_o = 400 \mu\text{m}$ [193], α_γ ranges between 0.25 for the wild-type organoids and 0.75 for the ones affected by lissencephaly.

Let us now discuss the results of the linear stability analysis. For fixed values of the dimensionless parameters α_R and α_γ , we denote by g_m the first value of g such that the bifurcation criterion (3.49) is satisfied for the wavenumber m . We define the critical threshold g_{cr} as the minimum g_m for $m \geq 2$ and the critical mode m_{cr} as the wavenumber corresponding to g_{cr} .

In Fig. 3.2, we plot the critical values g_{cr} and m_{cr} versus α_γ for two different values of α_R , *i.e.* in the first one $\alpha_R = 0.9$, while in the other one $\alpha_R = 0.95$. We observe that, for relatively small values of α_γ , the marginal stability threshold g_{cr} increases monotonously as α_γ increases, while the critical wavenumber m_{cr} decreases. There is a change in the behavior of the instability when the parameter α_γ is sufficiently large: the critical wavenumber m_{cr} increases suddenly and the marginal stability threshold g_{cr} remains nearly constant about $g_{\text{cr}} \simeq 2.5$.

The threshold at which this transition occurs strongly depends on α_R , as shown in Fig. 3.2.

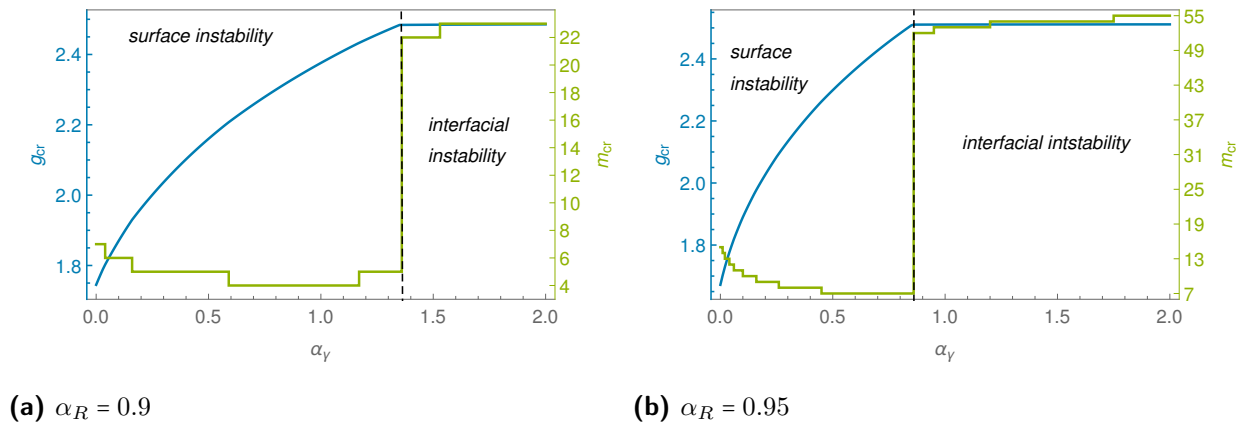


Figure 3.2: Plot of the marginal stability threshold g_{cr} and of the critical mode m_{cr} versus α_γ for (a) $\alpha_R = 0.9$ and (b) $\alpha_R = 0.95$.

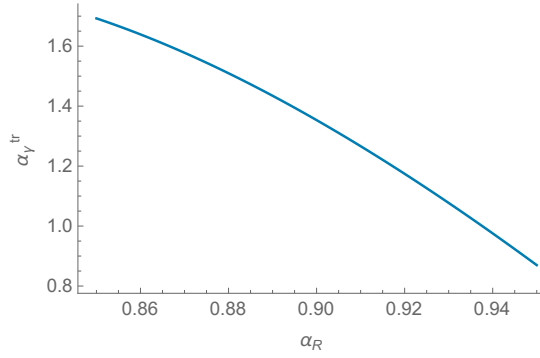


Figure 3.3: Plot of the critical value $\alpha_\gamma^{\text{tr}}$ at which the instability moves from the external surface to the interface versus α_R .

Indeed, when $\alpha_R = 0.9$, g_{cr} increases from 1.745 to 2.481 with $\alpha_\gamma \in (0, 1.34)$, while when $\alpha_R = 0.95$, g_{cr} increases in approximately the same range as for $\alpha_R = 0.9$, *i.e.* (1.671, 2.510), but α_γ varies in a smaller interval, *i.e.* $\alpha_\gamma \in (0, 0.86)$.

To study the morphology of the critical mode, we have integrated Eq. (3.46) to compute the incremental displacement field, as described in [121]. We depict in Tab. 3.1 a morphological diagram where we show the solution of the incremental problem for different values of α_γ and α_R . For small values of α_γ , we observe that the instability mainly releases elastic energy at the free boundary, displaying a wrinkling pattern: as we increase α_γ the wavenumber decreases and the critical mode displays a more rounded boundary. Furthermore, for larger values of α_γ there is a drastic change in the features of the instability: the morphological transition localizes at the interface between the cortex and the lumen with a high critical wavenumber. Let us call $\alpha_\gamma^{\text{tr}}$ the smallest value at which, fixing α_R , the instability localizes at the interface between the cortex and the lumen. We plot in Figure 3.3 $\alpha_\gamma^{\text{tr}}$ versus α_R . Interestingly, the transition from a surface to an interfacial instability can take place only if surface tension is relatively large. It is to be remarked that, whenever a surface instability takes place, the stretch induced by growth is quite large at the boundary between cortex and lumen. It is possible that, instead of wrinkles with short wave-

length, interfacial creases appear. However, the nucleation of sharp creases is the result of a nonlinear instability, not detectable by a linear analysis [94].

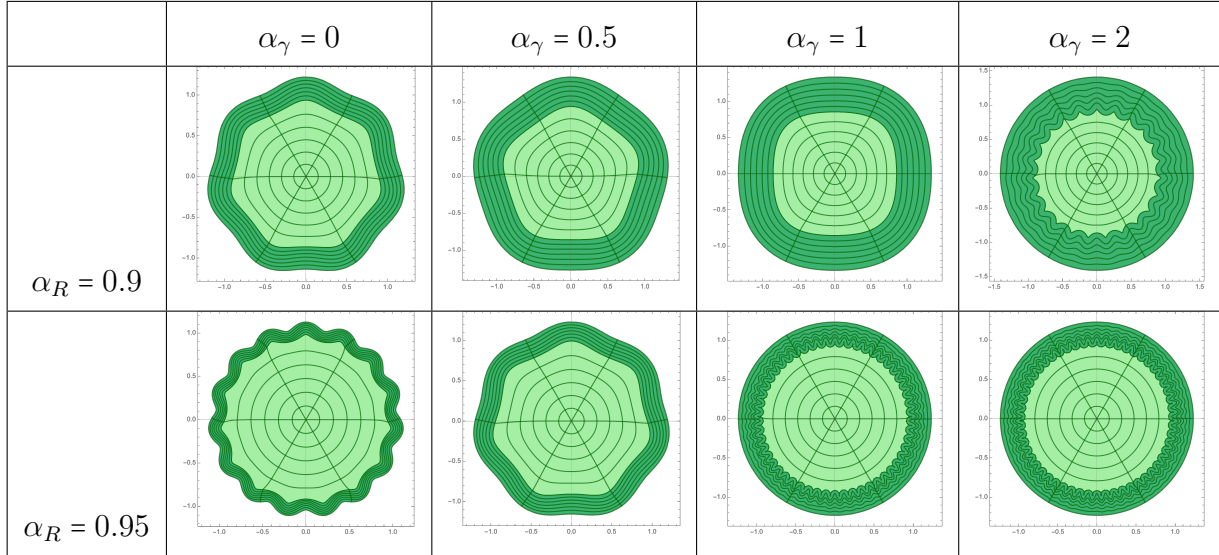


Table 3.1: Solutions of the linearized incremental problem at different α_R and different α_γ . The amplitude of the incremental radial displacement has been set equal to $0.05R_o$ for the sake of graphical clarity.

We also investigate the influence of α_R on the instability by fixing α_γ (see Fig. 3.4). In the absence of surface tension (*i.e.* $\alpha_\gamma = 0$), we observe that g_{cr} decreases monotonously as α_R increases (see Fig. 3.4a). The behavior is the opposite in the presence of surface tension, where the marginal stability threshold g_{cr} monotonously increases with α_R . For the range of parameters in which the critical mode displays an interfacial instability, we observe that g_{cr} increases linearly with α_R .

As regards the critical wavenumber m_{cr} , we can see that it increases in all the cases, both in the presence and in the absence of surface tension.

We observe that our model captures the main features of organoid development. First, for small values of α_γ , a morphological transition takes place at the free boundary, giving rise to a wrinkling pattern: as α_γ increases, we observe a decrease of the critical wavenumber and a higher marginal stability threshold. This is in agreement with the experiments

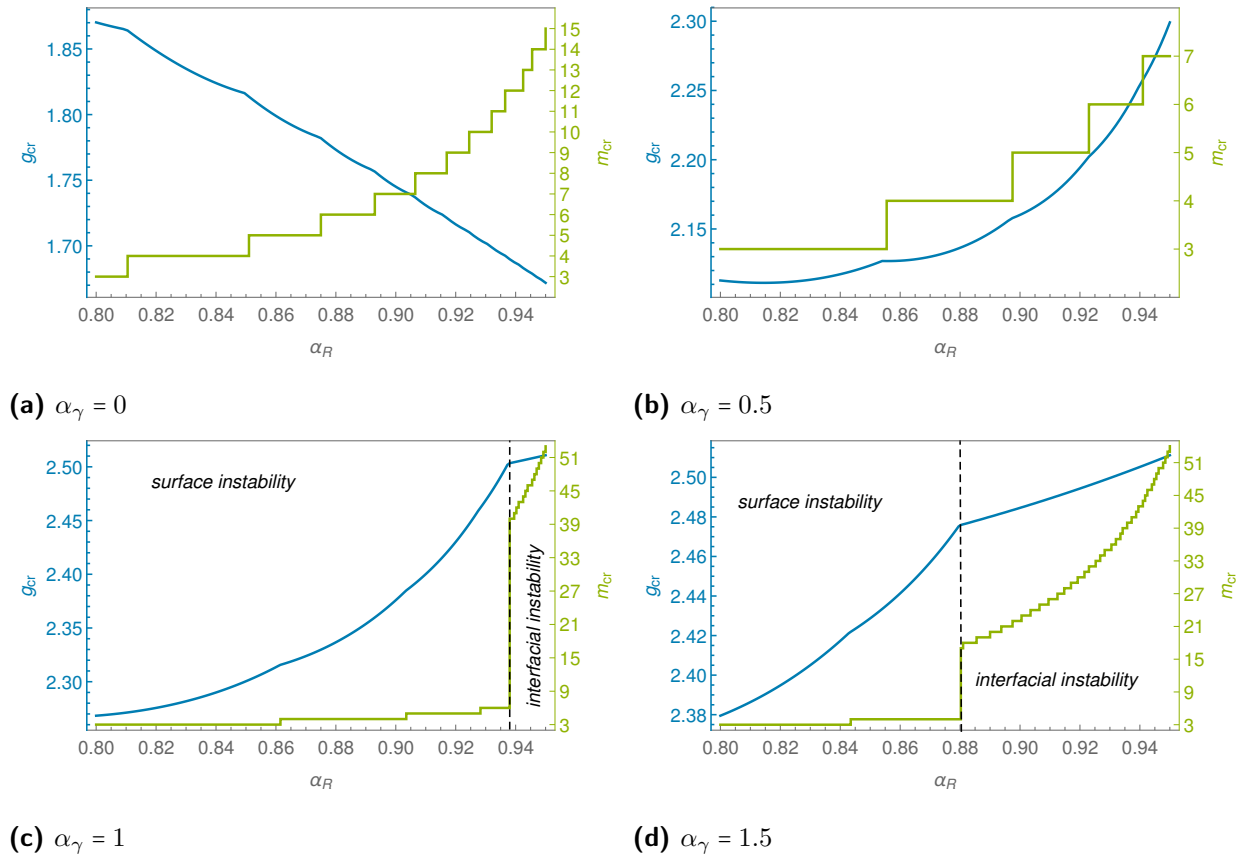


Figure 3.4: Plot of the marginal stability threshold g_{cr} and of the critical mode m_{cr} versus α_R for (a) $\alpha_\gamma = 0$, (b) $\alpha_\gamma = 0.5$, (c) $\alpha_\gamma = 1$, (d) $\alpha_\gamma = 1.5$.

of [193]: if the cells have the LIS1 +/- mutation, the authors measured that the elastic modulus of the cells is 2.7 times lower than the one of healthy cells. In our model this reduction of the stiffness is equivalent to an increase of α_γ . They have also reported a reduction of the number of folds in organoids affected by lissencephaly. As one can observe from the plots of Figs. 3.2-3.4 and from the morphological diagram of Table 3.1, as we increase α_γ the number of wrinkles decreases and the critical threshold increases, in accordance with [193]'s experiments (these results are shown in [193], Figure 5). Furthermore, for large values of α_γ , wrinkles at the free surface are completely absent, as happens in the most serious case of lissencephaly.

Compared to the model proposed by [25], in which the authors do not take into account

the tissue surface tension, our theoretical description presents some advantages. In fact, we do not introduce different shear moduli for the cortex and the lumen to modulate the critical wavenumber and the critical growth threshold. This choice is motivated by the experimental results of [193]: the authors reported a unique value of elastic modulus for the organoid and they did not experimentally measure a change in the shear moduli between the cortex and the lumen.

In our model the selection of the critical wavenumber is controlled by the competition between surface capillary energy and bulk elasticity. Furthermore, we are able to justify the complete absence of surface wrinkles in the most severe cases of lissencephaly, which corresponds to the case of large α_γ : large values of α_γ corresponds to both a high value of surface tension and a very soft material, the shear modulus is decreasing.

Notwithstanding the good agreement with the experimental results of our model, it is to be reported that models based on solid mechanics of brain organoids have been recently criticized by [131]. The authors observe that the folds of the cortex display an “anti-wrinkling” behavior: the cortex is thicker in correspondence of furrows and thinner at the ridges of wrinkles. The authors claim that solid models do not show this feature and, thus, they are inadequate to model multicellular aggregates. In the next section we implement a numerical code to approximate the fully non-linear problem and we show that the “anti-wrinkling” phenomenon is provoked by tissue surface tension.

3.1.4 POST-BUCKLING ANALYSIS

3.1.4.1 DESCRIPTION OF THE NUMERICAL METHOD

In this section we show the results of the numerical approximation of the non-linear problem given by Eqs. (3.6)-(3.7)-(3.10) to investigate the post-buckling behavior of the organoid. We use as computational domain the rectangle obtained through the conformal mapping

corresponding to the polar coordinate transformation, as done in [274]: let

$$\Omega_n = (0, 1) \times (0, \pi).$$

Given $\mathbf{X}_n \in \Omega_n$, the components represent the referential radial coordinate normalized with respect to the external radius, and the referential polar angle, respectively:

$$\begin{cases} X_1^n = \frac{R}{R_o}, \\ X_2^n = \Theta, \end{cases}$$

as represented in Fig. 3.5. The function

$$\mathbf{g}(\mathbf{X}_n) = [R_o X_1^n \cos(X_2^n), R_o X_1^n \sin(X_2^n)]$$

maps the computational domain to a half circle, which represent half of the reference configuration. The full domain can be obtained thanks to the axial symmetry of the problem.

We discretise the computational domain through the software GMSH [151]. We use a triangular grid, with a progressive refinement of the elements from $X_1^n = 0$ up to $X_1^n = \alpha_R$.

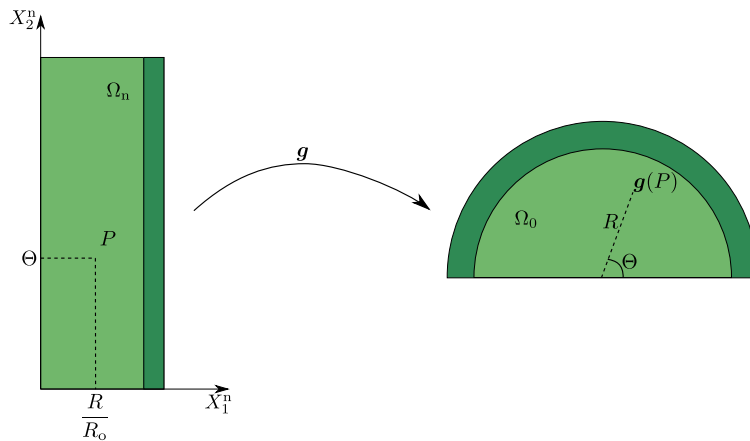


Figure 3.5: Representation of the conformal mapping g that maps the computational domain Ω_n to the reference configuration Ω_0

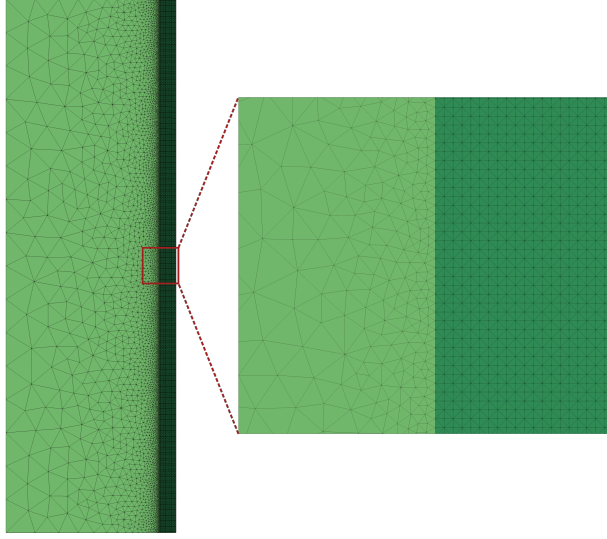


Figure 3.6: Mesh generated through GMSH for $\alpha_R = 0.9$. The maximum diameter of this mesh elements is 0.2488 while the minimum diameter is 0.0017.

In the cortex we instead use a structured mesh (*i.e.* for $\alpha_R < X_1^n < 1$), see Fig. 3.6.

We implement a numerical code based on the mixed finite element method to enforce the incompressibility constraint (3.4). We discretise the displacement field \mathbf{u} using continuous, piecewise quadratic functions, while we approximate the pressure through piecewise constant functions. The corresponding mixed finite element is the $\mathbf{P}_2 - P_0$ element, which is numerically stable for the incompressible hyperelastic problem [61]. We use an index h when we refer to the discretised counterpart of the mathematical quantities. We dimensionalise the system of equation with respect to μ and R_o as we did at the continuum level. We set the following discrete boundary conditions

$$\left\{ \begin{array}{ll} \mathbf{u}_h = \mathbf{0} & \text{if } X_1^n = 0, \\ \mathbf{u}_h \cdot \mathbf{e}_2 = 0 & \text{if } X_2^n = 0 \text{ or } X_2^n = \pi, \\ \mathbf{P}_h^T \mathbf{e}_2 \cdot \mathbf{e}_1 = 0 & \text{if } X_2^n = 0 \text{ or } X_2^n = \pi, \\ \mathbf{P}_h^T \mathbf{e}_1 = \det \mathbf{F}_h \alpha_\gamma \mathcal{K}_h \mathbf{F}_h^{-T} \mathbf{e}_1 & \text{if } X_1^n = 1, \end{array} \right.$$

where $(\mathbf{e}_1, \mathbf{e}_2)$ represents the canonical vector basis.

We solve the discretised form of the equilibrium equation (3.6) in the Lagrangian form using a Newton method. The control parameter g is incremented of δg when the Newton method converges, the numerical solution is used as initial guess for the following Newton cycle. The increment δg is automatically reduced near the theoretical marginal stability threshold and when the Newton method does not converge. The numerical simulation is stopped when $\delta g < 10^{-6}$. To trigger the mechanical instability, a small perturbation of an amplitude of $\sim 10^{-5}$, having the shape of the critical mode computed in Section 3.1.3, is applied at the free boundary of the mesh. We have numerically verified that the wavelength of the buckled pattern is not sensitive to the applied imperfection and the only effect is a slight anticipation of the instability threshold.

The numerical algorithm is implemented in Python through the open-source computing platform FEniCS (version 2018.1) [211]. The computation of the weak form and of the Jacobian necessary to solve each step of the Newton method are computed from the total energy through the library UFL [7]. Surface tension is introduced in the numerical algorithm following the implementation proposed in [233]. We use PETSc [22] as linear algebra back-end and MUMPS [12] as linear solver.

3.1.4.2 RESULTS OF THE FINITE ELEMENT SIMULATIONS

In this section, we discuss the results of the numerical simulations for $\alpha_R = 0.9$. In Fig. 3.7, we plot the buckled configuration of the organoid. As predicted by the critical modes of the linear stability analysis plotted in Table 3.1, in presence of surface tension (Fig. 3.7b) the free boundary is smoother and rounded.

We define Δr as the amplitude of the pattern at the free surface

$$\Delta r = \max_{\Theta \in [0, \pi]} r(R_o, \Theta) - \min_{\Theta \in [0, \pi]} r(R_o, \Theta)$$

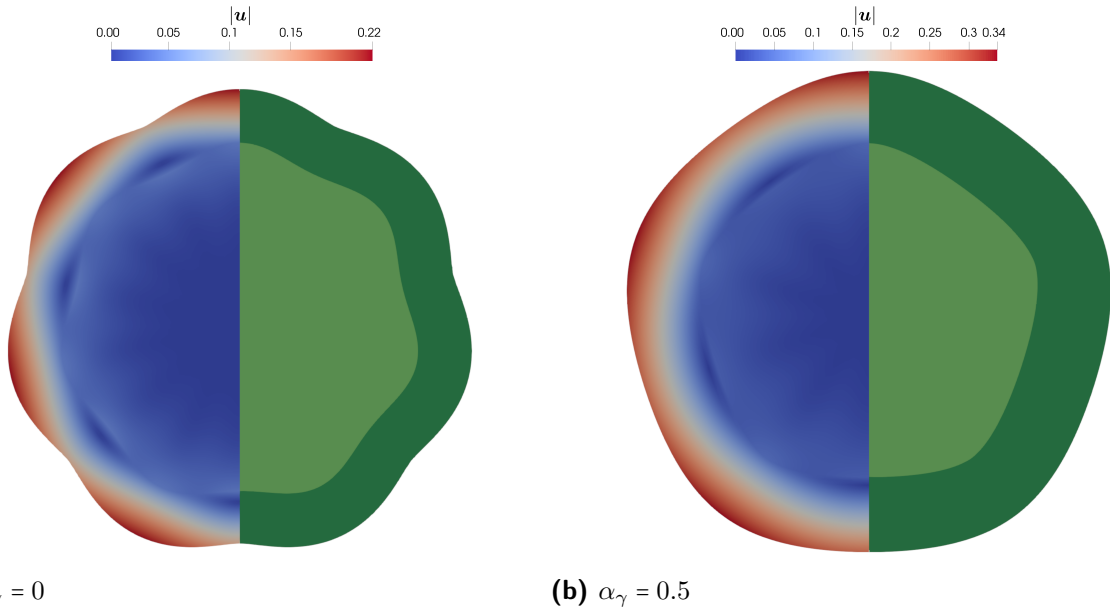


Figure 3.7: Buckled configuration for (a) $\alpha_\gamma = 0$ and $g = 1.7556$ and (b) $\alpha_\gamma = 0.5$ and $g = 2.1646$.

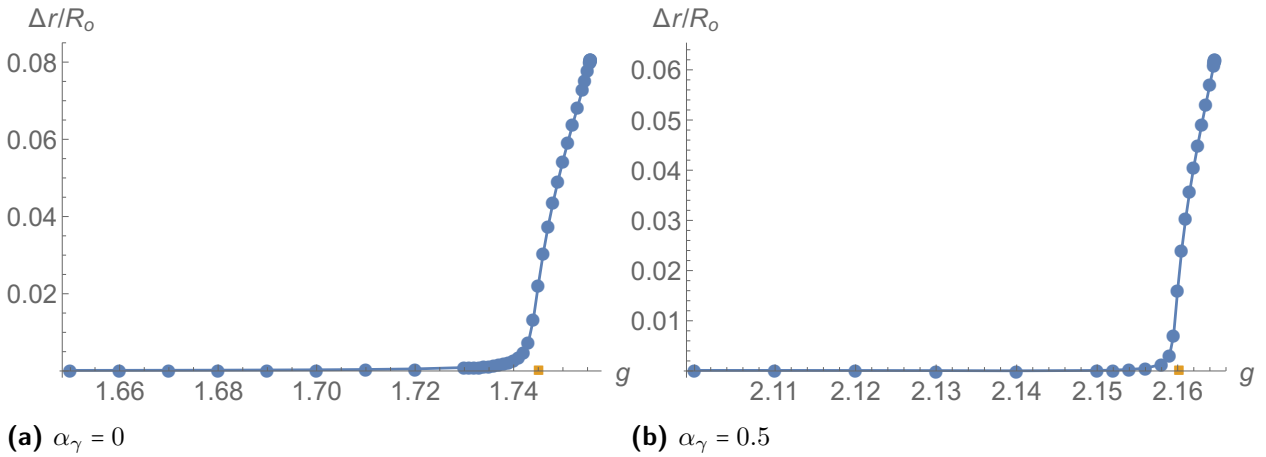


Figure 3.8: Bifurcation diagrams for (a) $\alpha_\gamma = 0$ and (b) $\alpha_\gamma = 0.5$. The orange square denotes the theoretical marginal stability threshold computed as exposed in Section 3.1.3. The good agreement between the linear stability analysis and the finite element code outcomes validates the numerical algorithm.

where r denotes the actual radial position of the point with polar coordinates (R, Θ) .

In Fig. 3.8, we show how the amplitude of the pattern Δr evolves with respect to the growth rate g . We observe that there is an excellent agreement with the marginal stability thresholds computed in the previous section, proving the consistence of the numerical code with respect to the theoretical predictions. Both the bifurcation diagrams exhibit a con-

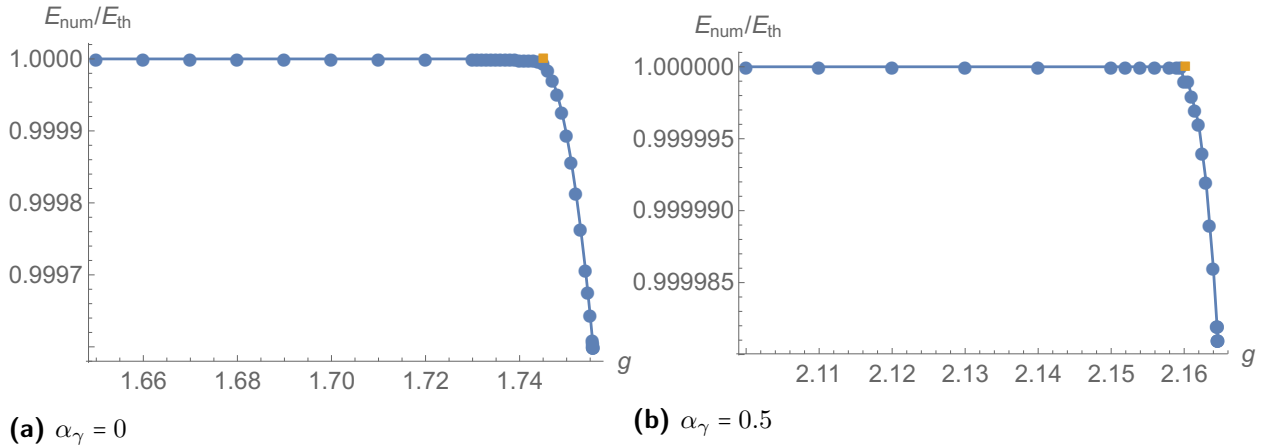


Figure 3.9: Plot of the ratio $E_{\text{num}}/E_{\text{th}}$ for (a) $\alpha_\gamma = 0$ and (b) $\alpha_\gamma = 0.5$. The orange square denotes the theoretical marginal stability threshold computed as exposed in Section 3.1.3.

tinuous transition from the unbuckled to the buckled configuration, displaying the typical behavior of a supercritical pitchfork bifurcation. Let

$$E = \int_{\Omega} W(\mathbf{F}) dV + \gamma \int_{\partial\Omega} |\mathbf{F}^{-T} \mathbf{N}| dS$$

be the total mechanical energy of the organoid. We compute the ratio of the energy E_{th} of the base solution given by Eqs. (3.21)-(3.22) and the energy E_{num} arising from the numerical simulations.

In Fig. 3.9 we plot the ratio $E_{\text{num}}/E_{\text{th}}$ versus the control parameter g for both $\alpha_\gamma = 0$ and $\alpha_\gamma = 0.5$. In both cases, the buckled configuration exhibits a total lower mechanical energy with respect to the unbuckled state. Furthermore we observe that the energy lowers continuously, confirming that the bifurcation is supercritical.

Finally, we compute the thickness of the cortex at the ridges and at the furrows of the buckled configuration (which correspond to the gyri and the sulci of the fully developed brain respectively). We observe that the thickness of the ridges is higher than the one of the furrows for $\alpha_\gamma = 0$ (see Fig. 3.10a), while the behavior is the opposite in the case of $\alpha_\gamma = 0.5$ (see Fig. 3.10b). The latter case is typical of brain organoids, as observed in [131].

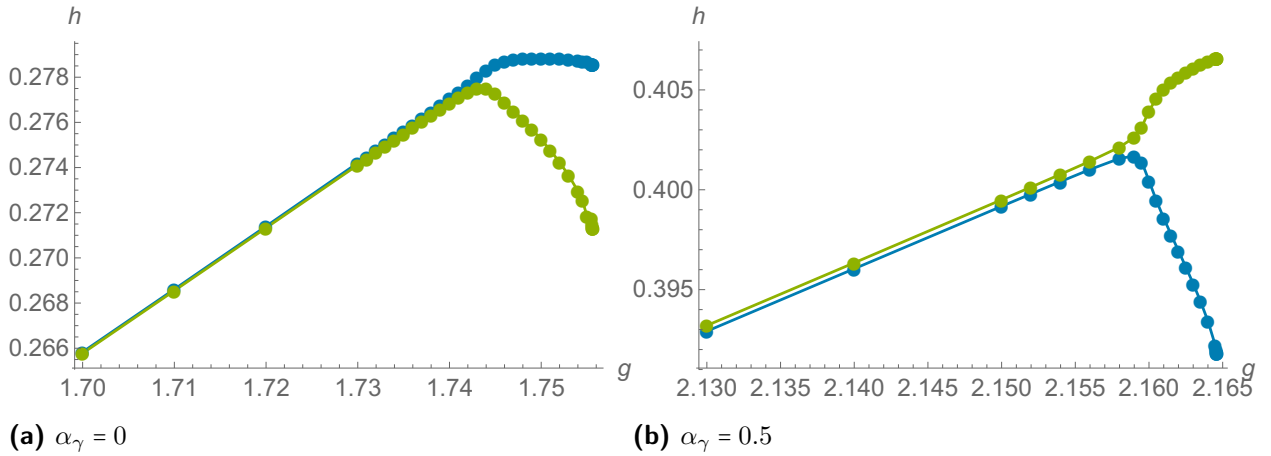


Figure 3.10: Thickness of the cortex of ridges (blue) and furrows (green) for (a) $\alpha_\gamma = 0$ and (b) $\alpha_\gamma = 0.5$. The latter situation, in which the the thickness of ridges is higher that the one of furrows, corresponds to the “antiwrinkling” behavior described in [131].

These numerical results suggest that the “antiwrinkling” behavior, as named by [131], is due to the presence of surface tension, which is highly relevant due to the small radius of a brain organoid. If we consider a fully developed brain, its typical size is of order of decimeters. In this case, keeping γ and μ fixed, α_γ is reduced by five order of magnitudes with respect to the case of the organoid and the contribution of surface tension to the total energy becomes negligible. Experimental results show that gyri are thicker than sulci [179], differently from what happens at the small length scales of the brain organoid. This is in agreement with the outcomes of our model in the case $\alpha_\gamma = 0$, confirming that the “antiwrinkling” behavior is caused by the competition of bulk elastic energy and the surface tension.

However, our numerical algorithm has some limitations. The Newton method does not converge anymore slightly past the marginal stability threshold. In fact, the bifurcation diagrams of Fig. 3.8 show that the amplitude of the pattern increases very rapidly beyond the marginal stability threshold. As one can observe in Fig. 3.7a, the deformation tends to localize near the furrows, highlighting a possible subcritical transition to a folded state, which would be in agreement with the experimental observations of [193]. The numeri-

cal approximation of a layer growing on a substrate with similar mechanical properties is particularly tricky, even numerically [145]. Future efforts will be devoted to the improvement of the numerical scheme, implementing an arclength continuation method to study the wrinkle-to-fold transition in brain organoids.

3.1.5 DISCUSSION AND CONCLUDING REMARKS

In this work, we have developed a model of brain organoids to describe the formation of cerebral sulci and to investigate the influence of surface tension on such a morphogenetic process. In Section 3.1.1 we have computed that the tissue surface tension acting on a solid multicellular spheroid is $\gamma = 10^{-1}$ N/m, using the data reported in [205]. We exploit this measure as a qualitative estimate of tissue surface tension of a generic cellular aggregate. In fact, measures performed on different embryonic tissues modeled as fluids all have the same order of magnitude [285]. Thus, we do not expect that the tissue surface tension acting on brain organoids dramatically differs from the one acting on multicellular spheroids.

Then, we have built in Section 3.1.2 an elastic model of brain organoids. They are described as disks surrounded by a growing rim and subjected to a surface tension generated by intercellular adhesion forces [225]. We have assumed that the two regions (disk and outer rim) are composed of the same incompressible neo-Hookean material. The system is governed by the dimensionless parameters g , *i.e.* the growth rate of the cortex with respect to the lumen, α_R and α_γ , which are the lumen radius and the capillary length, normalized with respect to the initial radius of the organoid, respectively.

We have computed a radially symmetric solution and we have studied its linear stability in Section 3.1.3 using the theory of incremental deformations. We have rewritten the linear stability analysis into an optimal Hamiltonian system using the Stroh formulation [144]. The impedance matrix method is adapted to take into account the boundary contribution

of surface tension.

The outcomes are discussed in Section 3.1.3.5. The introduction of a tissue surface tension of the same order as the estimate computed in Section 3.1.1.1 strongly influence the stability of the base solution and alters the critical wavelength. This result suggests that the interplay between elasticity and tissue surface tension plays a crucial role in controlling pattern selection in embryo morphogenesis. The predicted critical wavelength is always finite (see Fig. 3.4a). In our model the softening of cells, due to lissencephaly, corresponds to an increase of the parameter α_γ , strengthening the role of tissue surface tension and leading to a lower critical wavenumber. Experimental observations of [193] report a similar behavior: when the LIS1 +/- mutation is present, the shear modulus of the organoid is reduced and the wavenumber decreases compared with the healthy organoids. This suggest that the reduction of brain sulci due to lissencephaly is due to the competition between elastic and surface energies in early embryogenesis. Moreover, we have observed that, for larger α_γ , a transition from a surface to an interfacial instability occurs: buckling localizes at the interface between the cortex and the lumen. In this case the cortex remains smooth as one can observe in the most severe cases of lissencephaly. The results are reported in Figs. 3.2-3.3-3.4 and in Tab. 3.1.

Finally, in Section 3.1.4, we have implemented a finite element code to approximate the fully non-linear problem. The algorithm is based on a mixed variational formulation and the Newton method. The outcomes of the numerical simulations are reported in Fig. 3.7-3.10. These results show that tissue surface tension rounds the external boundary. Both in the presence and in the absence of surface energy, the bifurcation is supercritical, displaying a continuous transition from the unbuckled to the buckled state. Contrarily to the bilayer model without surface tension, our model reproduces “antiwrinkling” behavior of the cortex (namely the thickness of the outer layer is larger in the furrows). This suggests that this unconventional variation of cortex thickness is due to tissue surface energy. This

strengthens the importance of considering surface tension in the modelling of cellular aggregates.

Summing up, our model suggests a possible purely mechanical explanation of a number of open questions:

- brain sulci in organoids are generated by a mechanical instability triggered by cortex growth;
- the “anti-wrinkling” behavior is induced by the presence of surface tension which tends to reduce the perimeter of the organoid as proved by the numerical simulations;
- the reduction of stiffness of the cell decreases the role of elasticity and enhances the effect of surface tension (leading to an increased α_γ while keeping γ constant). A reduction of stiffness of the organoid has different consequences: the onset of bifurcation is delayed, the critical wavelength increases, the cortex is thicker and, in the most severe cases, the surface instability is absent.

This work opens the path to other studies, such as the analysis of the effect of surface tension on the growth of embryos and tumor spheroid. It proposes a theoretical explanation of purely mechanical nature of known experiments; of course further investigations will be needed to validate it. What emerges from our model is that tissue surface tension cannot be disregarded whenever a living tissue is characterized by relatively small length scales or by small elastic moduli. Future efforts will include the improvement of the numerical scheme in order to capture possible secondary bifurcations. Possible extensions include the implementation of an arclength continuation method to improve the numerical convergence in presence of turning points. From an experimental point of view, it would be important to quantitatively measure the surface tension acting on the organoid cor-

tex. Another possible line of research is the study of the influence of surface tension on the growth of cellular aggregates.

3.2 MORPHOMECHANICAL MODEL OF THE TORSIONAL C-LOOPING IN THE EMBRYONIC HEART

In human embryos, the heart is the first functioning organ. Around 17 days post-conception, the heart is essentially a single, relatively straight, muscle-wrapped tube [301]. In the next stage, the heart tube (HT) bends and twists developing a curved shape towards the right side of the embryo. Cardiac looping represents the first visible sign of left-right asymmetry in vertebrate embryos. Its inception received much attention in clinics, since spontaneous abortions (miscarriage) during the first trimester may occur for cardiac malformations caused by serious structural defects and abnormalities induced by minor looping perturbations [295]. After that looping is complete, the heart reaches the required configuration for further development into a four-chambered pump.

Collecting well-defined images of the human embryo in its first days of formation is a challenging procedure due to the necessity to avoid invasive procedures on the mother's body and to its very small size [318]. In order to circumvent these difficulties, researchers used chick embryos for studying cardiac morphogenesis, since the development of the chick heart has the same characteristic duration as the human one. The chick development takes approximately 21 days and it has been well-studied by Hamilton and Hamburger, who divided this morphological development into 46 chronological stages, starting from laying of the egg and ending with a newly hatched chick [171]. Moreover, the chick embryo can be cultured both *in-vivo* and *in-vitro* to better understand the underlying biological and physical mechanisms [117, 318, 302].

In the first stages (1 – 8), the primitive shapes of the cranial and caudal parts of the chick embryo develop, together with the beginning of the construction of the neural sys-

tem [171, 222]. Looping of the HT begins at stage 10 and consists of two main phases: *c-looping* and *s-looping* [246, 221]. During normal *c-looping* (stages 9 – 12), the heart tube transforms from a straight tube Fig. 3.11 (A), into a *c*-shaped one, see Fig. 3.11 (C), via two main deformations: a ventral bending Fig. 3.11 (B), and a dextral (rightward) torsion Fig. 3.11 (C) [301, 221, 291]. Hence, the looped HT looks like a helix [223] since the original ventral surface of the straight heart tube becomes the outer curvature (convex surface) of the looped heart, while the original dorsal side becomes the inner curvature (concave surface). During *s-looping* (stages 12 – 16), the primitive ventricle from its post *c*-loop cranial position moves to its definitive caudal position Fig. 3.11 (D), and induces a shortening of the distance between the conotruncus (outflow tract) and the atrium Fig. 3.11 (E) [262, 261]. At the end of the looping process, the obtained configuration is not yet a four-chambered pump, see Fig. 3.11 (F). Finally, during stages 18 – 26, septation processes divide the tube into four chambers. In the later stages (20 – 46), the embryonic length increases until the morphology of the limbs and of the face is well defined [171, 222].

In the following, we primarily focus on the *c*-looping of the HT. Since previous works mostly focused on biological and genetic aspects [219, 186, 318, 317], the looping remain poorly understood from the mechanical point of view. Indeed, it has been highlighted that internal and external physical forces direct bending and torsion in the embryo [300, 292]. Concerning the HT bending, the main idea is that it is driven by differential growth: cells on the dorsal side growth primarily by hypertrophy (bigger cells) than by hyperplasia (more cells), in contrast to what happens on the ventral surface. Hence, on the ventral surface the size of the cells is smaller than the ones on the dorsal one [291]. The physical origin of dextral torsion is openly debated. The HT is covered by a membrane, called splanchnopleure (SPL), which exerts a pressure on the heart. At the end of the tube there are two veins called omphalomesenteric vein (OVs), one on the right side and the other on the left. Before the onset of *c*-looping, the stress in the OVs is different in its caudal and

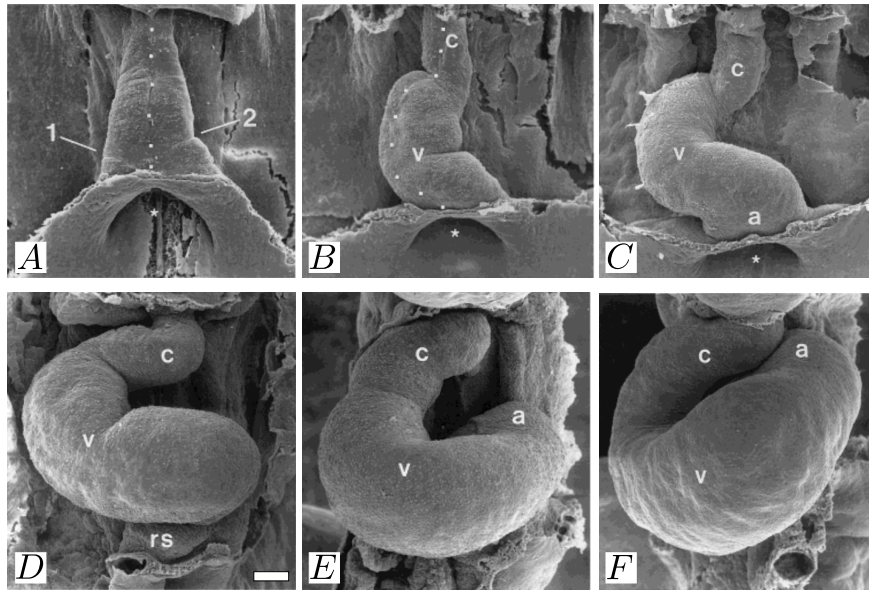


Figure 3.11: Ventral views showing the positional and morphological changes of the embryonic heart tube between its first morphological appearance at Hamburger Hamilton (HH)-stage 10 [171] (A), the beginning of the c-looping, HH-stage 12/13 [171] (C), the end of the phase of dextral-looping at HH-stage 13 [171] and the transformation from the c-shaped loop into the s-shaped one (D)-(F). [c], primitive conus; [v], primitive ventricular bend; [a], primitive atria. Scale bar 100 μ m. Figures adapted from [221].

cranial part, due to the different geometry of the veins and to the migration of precardiac cells from the OVs to the HT [317]. At stage 9, when c-looping process starts, the one on the right has a larger diameter than the other one. This phenomenon represents a break of symmetry in the structure which coupled with the action of the SPL pressure might cause the torsion and the position of the heart in the left part of the body [318, 317, 302, 292]. However, there are several candidate mechanisms for symmetry break in such a complex process. For instance, the SPL membrane has been removed in recent experiments [317]. The resulting HT rotation is inhibited but not eliminated, proving that looping involves a combination of different morphogenetic mechanisms, some of which can be redundant [300, 302].

Motivated by these experimental results, in this work, for the first time, we propose an original contribution to the mathematical modeling of a fundamental process about car-

diac shaping: we introduce a morphomechanical model for the torsion of the HT. We hypothesize that this spontaneous morphological transition can be modeled as a mechanical instability due to accumulation of residual stresses because of the geometrical frustration imposed by tissue remodelling. Precisely, we assume that the HT is a nonlinear elastic, homogeneous, incompressible body that is subjected to a torsional remodelling, which mimics the cells flux in the HT [291]. We assume that the tube undergoes a finite torsion by accumulating such a geometrical frustration, and we perform a linear stability analysis of the nonlinear elastic boundary value problem to determine the onset of c-looping as a function of the geometrical parameters of the HT. Then, we perform numerical simulations to study the post-buckling behaviour in the fully nonlinear morphological transition.

3.2.1 MATHEMATICAL MODEL

In this Section, we define the morphomechanical model of the HT, described as a hyperelastic body subjected to torsional remodeling.

3.2.1.1 KINEMATICS

Let

$$\Omega_0 = \{ \mathbf{X} = [R \cos \Theta, R \sin \Theta, Z] \in \mathbb{R}^3 \mid R_i \leq R < R_o \text{ and } 0 \leq \Theta < 2\pi \text{ and } 0 < Z < L \},$$

be the reference configuration of the HT, where R_i and R_o are respectively the internal and the external radius of the cylinder, L is the height of the hollow cylinder and \mathbf{X} is the material position coordinate. Although the HT is composed by different layers, for sake of simplicity, we assume that the HT is a homogeneous one-layered tissue. By experimental evidences, the HT can be modeled as a hollow cylinder since there is a small lumen in the middle. We indicate with $\varphi : \Omega_0 \rightarrow \mathbb{R}^3$ the deformation field, so that the actual config-

uration of the body Ω is given by $\varphi(\Omega_0)$. Let $\boldsymbol{x} = \varphi(\boldsymbol{X})$ be the actual position and the displacement vector is defined as $\boldsymbol{u}(\boldsymbol{X}) = \varphi(\boldsymbol{X}) - \boldsymbol{X}$. Let \mathbf{F} be the deformation gradient, i.e. $\mathbf{F} = \text{Grad } \varphi$.

In order to describe the finite torsion induced by tissue remodelling, we consider the multiplicative decomposition of the deformation gradient [196, 203, 277], such as

$$\mathbf{F} = \mathbf{F}_e \mathbf{G}, \quad (3.50)$$

where \mathbf{G} describes the metric distortion induced by the applied torsion and \mathbf{F}_e is the elastic deformation of the material restoring the geometrical compatibility of the current configuration. Defining γ as the finite torsion rate resulting from the remodelling processes, we choose \mathbf{G} as

$$\mathbf{G} = \begin{pmatrix} 1 & 0 & 0 \\ 0 & 1 & -\gamma R \\ 0 & 0 & 1 \end{pmatrix}. \quad (3.51)$$

We further assume that the cylinder cannot elongate along the z -direction, *i.e.*

$$z(Z = 0) = 0, \quad z(Z = L) = L. \quad (3.52)$$

Since no relevant growth processes occur in the stages of interest of c-looping ($\det \mathbf{G} = 1$) and the tissue is mainly composed by water, we model the HT as incompressible media, namely we enforce that

$$\det \mathbf{F}_e = 1. \quad (3.53)$$

We now introduce the mechanical constitutive assumptions.

3.2.1.2 BOUNDARY-VALUE PROBLEM (BVP)

Since we are describing the first stage of development and fibers are not yet present [171], it is reasonable to model the HT as an isotropic body. We assume that the HT is composed of a homogeneous hyperelastic material, having strain energy density W . The first Piola-Kirchhoff stress tensor \mathbf{P} and the Cauchy stress tensors \mathbf{T} are then given by

$$\mathbf{P} = \det \mathbf{G} \frac{\partial W(\mathbf{F}\mathbf{G}^{-1})}{\partial \mathbf{F}} - p\mathbf{F}^{-1} \quad \mathbf{T} = \frac{1}{\det \mathbf{F}} \mathbf{F}\mathbf{P}$$

where p is the Lagrange multiplier enforcing the incompressibility constraint, i.e. physically p is the necessary hydro-static pressure to enforce the incompressibility constraint $\det \mathbf{F}_e = 1$. Assuming quasi-static conditions in absence of external body forces, the balance of the linear momentum reads

$$\text{Div } \mathbf{P} = \mathbf{0} \text{ in } \Omega_0, \quad \text{or} \quad \text{div } \mathbf{T} = \mathbf{0} \text{ in } \Omega \quad (3.54)$$

where Div and div denote the divergence operator in material and current frame, respectively. The nonlinear system of equations (3.54) is complemented by the following Neumann condition on the inner and outer boundaries

$$\begin{cases} \mathbf{T} \cdot \mathbf{n} = \mathbf{0} & \text{on } r = r_i \\ \mathbf{T} \cdot \mathbf{n} = \mathbf{0} & \text{on } r = r_o \end{cases}, \quad (3.55)$$

where \mathbf{n} is the outer normal in spatial coordinates, and r_i, r_o are the spatial inner and outer radius, respectively. By performing a pull-back of Eq. (3.55), the Lagrangian form

of the boundary condition is given by

$$\begin{cases} \mathbf{P}^T \cdot \mathbf{N} = \mathbf{0} & \text{on } R = R_i \\ \mathbf{P}^T \cdot \mathbf{N} = \mathbf{0} & \text{on } R = R_o \end{cases} \quad (3.56)$$

where \mathbf{N} is the material outer normal. To keep the model as simple as possible, we assume that the tube behaves as a neo-Hookean material with the strain energy density given by

$$W(\mathbf{F}) = \det(\mathbf{G})W_0(\mathbf{F}_e) = (\det \mathbf{G})\frac{\mu}{2}(\text{tr}(\mathbf{F}_e^T \mathbf{F}_e) - 3). \quad (3.57)$$

The first Piola–Kirchhoff and Cauchy stress tensors read respectively

$$\begin{cases} \mathbf{P} = \mu(\det \mathbf{G})\mathbf{G}^{-1}\mathbf{G}^{-T}\mathbf{F}^T - p\mathbf{F}^{-1}, \\ \mathbf{T} = \mu\mathbf{F}\mathbf{G}^{-1}\mathbf{G}^{-T}\mathbf{F}^T - p\mathbf{l}, \end{cases} \quad (3.58)$$

where \mathbf{l} is the identity tensor. Eqs. (3.53), (3.54) and (3.56) define the nonlinear elastic BVP.

We now compute a solution of the BVP using the symmetry of the problem.

3.2.1.3 RADIALLY-SYMMETRIC SOLUTION

Let $(\mathbf{E}_R, \mathbf{E}_\Theta, \mathbf{E}_Z)$ and $(\mathbf{e}_r, \mathbf{e}_\theta, \mathbf{e}_z)$ be the unit vectors in material and spatial polar coordinates, respectively. Denoting (r, θ, z) the polar coordinates of a point, we search for a radially-symmetric solution

$$\boldsymbol{\varphi}(\mathbf{X}) = r(R)\mathbf{e}_r + Z\mathbf{e}_z.$$

so that the geometrical and the elastic deformation gradient read

$$\mathbf{F} = \text{diag} \left(\frac{\partial r(R)}{\partial R}, \frac{r}{R}, 1 \right), \quad \mathbf{F}_e = \mathbf{F}\mathbf{G}^{-1} = \begin{pmatrix} \frac{\partial r(R)}{\partial R} & 0 & 0 \\ 0 & \frac{r}{R} & \gamma r \\ 0 & 0 & 1 \end{pmatrix}. \quad (3.59)$$

From Eq. (3.59) and the incompressibility constraint Eq. (3.53), we get $r'r = R$, where $'$ denotes differentiation. By integrating, we obtain

$$r(R) = \sqrt{R^2 + r_i^2 - R_i^2}. \quad (3.60)$$

The balance of the linear momentum in polar coordinates imposes

$$\frac{dT_{rr}}{dr} + \frac{T_{rr} - T_{\theta\theta}}{r} = 0 \quad (3.61)$$

where T_{hk} , with h, k spanning over (r, θ, z) , are the components of the Cauchy stress tensor \mathbf{T} in polar coordinates. Using Eqs. (3.59) and (3.58), the Cauchy stress tensor is given by

$$\mathbf{T} = \begin{pmatrix} \frac{\mu(r^2 - r_i^2 + R_i^2)}{r^2} - p & 0 & 0 \\ 0 & \mu r^2 \left(\gamma^2 + \frac{1}{r^2 - r_i^2 + R_i^2} \right) - p & \gamma \mu r \\ 0 & \gamma \mu r & \mu - p \end{pmatrix}. \quad (3.62)$$

As regarding the current radii, by using Eq. (3.60), the expression of the external radius r_o is given by

$$r_o = \sqrt{R_o^2 + r_i^2 - R_i^2}, \quad (3.63)$$

while for the internal one, we have to integrate Eq. (3.61) from r_o to r_i , use the boundary

conditions Eq. (3.55) to get

$$\frac{1}{2}\mu \left((R_i^2 - R_o^2) \left(\gamma^2 + \frac{r_i^2 - R_i^2}{r_i^2 (r_i^2 - R_i^2 + R_o^2)} \right) + \log \left(\frac{r_i^2 - R_i^2 + R_o^2}{R_o^2} \right) + \log \left(\frac{R_i^2}{r_i^2} \right) \right) = 0 \quad (3.64)$$

which is an implicit relation to derive first r_i and then r_o from Eq. (3.63). Fixing the torsion rate γ and the initial geometry of the hollow tube, Eq. (3.64) is solved using the Newton method.

Finally, for the Lagrange multiplier p , we can integrate Eq. (3.61) from r to r_o , obtaining

$$T_{rr}(r) = \int_r^{r_o} \left[\frac{\mu (\rho^2 - r_i^2 + R_i^2)}{\rho^3} - \mu \rho \left(\gamma^2 + \frac{1}{\rho^2 - r_i^2 + R_i^2} \right) \right] d\rho. \quad (3.65)$$

Hence, solving Eq. (3.65) with respect to p , we obtain

$$p(r) = \frac{1}{2}\mu \left(\gamma^2 (-r^2 + r_i^2 - R_i^2 + R_o^2) + \frac{R_i^2 - r_i^2}{r^2} + \frac{R_i^2 - r_i^2}{r_i^2 - R_i^2 + R_o^2} + \log \left(\frac{r^2}{r^2 - r_i^2 + R_i^2} \right) + \log \left(\frac{R_o^2}{r_i^2 - R_i^2 + R_o^2} \right) + 2 \right). \quad (3.66)$$

Eqs. (3.60) and (3.66) represent the radially symmetric solution of the BVP.

Remark 3.2.1. It is useful to recall that a finite torsion on an hollow cylinder can be sustained by surface tractions alone, namely it is sufficient to apply an axial force F_z and a torque M on the end surfaces S , given by

$$F_z = \int_S T_{zz} dS = \frac{1}{2}\pi\mu R_i^2 \log \left(\frac{r_i^2 R_o^2}{R_i^2 (r_i^2 - R_i^2 + R_o^2)} \right) + \frac{\pi\mu (R_i^2 - R_o^2) [\gamma^2 (R_o^2 - R_i^2) (r_i^2 + R_o^2 - R_i^2) + 2 (R_i^2 - r_i^2)]}{4 (r_i^2 - R_i^2 + R_o^2)}, \quad (3.67)$$

while the torque M

$$M = \int_S T_{z\theta} r dS = \frac{1}{2}\pi\gamma\mu (R_o^2 - R_i^2) (2r_i^2 - R_i^2 + R_o^2). \quad (3.68)$$

Both surface tractions depend nonlinearly on the geometric parameters, namely R_o and R_i , while only M is linearly dependent on γ . In Fig. 3.12, we plot the two quantities defined in Eqs. (3.67) - (3.68) versus the torsion rate γ varying the ratio $\frac{R_o}{R_i}$. In Fig. 3.12a,

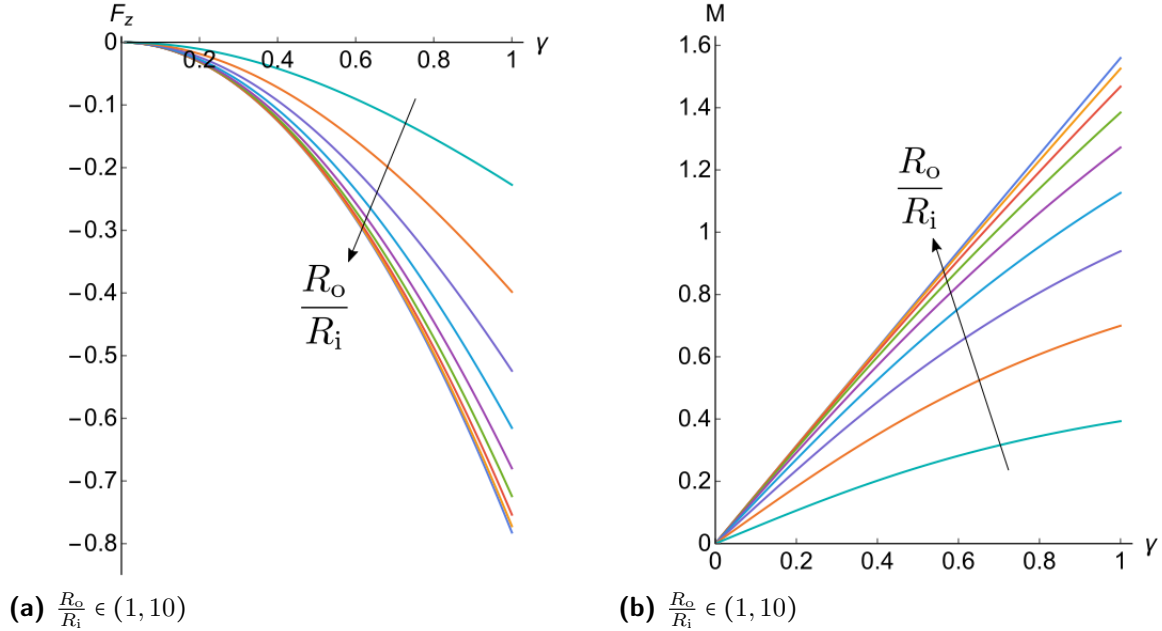


Figure 3.12: Plot of (a) the axial force F_z and (b) the torque M versus the torsion rate γ fixing the external radius $R_o = 1$, the shear modulus $\mu = 1$, computing r_i through Eq. (3.64) and varying the ratio between the external and the internal radii within the range $\frac{R_o}{R_i} \in (1, 10)$.

we notice that the axial force is compressive, showing the characteristic Poynting effect that favors buckling as the torsion rate increases [164, 148, 162].

In the following section, we study the linear stability analysis of the radially symmetric solution given by Eqs. (3.60) and (3.66).

3.2.2 LINEAR STABILITY ANALYSIS

In this section we study the linear stability of the finitely deformed tube by using the method of incremental deformations superposed on a finite strain [243]. We rewrite the resulting incremental BVP into the Stroh formulation that is solved using the impedance matrix method.

3.2.2.1 INCREMENTAL BVP

We apply the theory of incremental deformations superposed on finite strains to investigate the stability of the radially symmetric solution. Let $\delta\mathbf{u}$ be the incremental displacement field and let $\Gamma = \text{grad } \delta\mathbf{u}$. We introduce the push-forward of the incremental Piola-Kirchhoff stress tensor $\delta\mathbf{P}_0$ in the axis-symmetric deformed configuration, given by

$$\delta\mathbf{P} = \mathcal{A}_0 : \Gamma + p\Gamma - \delta p\mathbf{l}, \quad (3.69)$$

where \mathcal{A}_0 is the fourth order tensor of instantaneous elastic moduli, δp is the increment of the Lagrangian multiplier that imposes the incompressibility constraint. The two dots operator $(:)$ denotes the double contraction of the indices

$$(\mathcal{A}_0 : \Gamma)_{rs} = (A_0)_{rshk}\Gamma_{kh},$$

where the convention of summation over repeated indices is used. The components of the tensor \mathcal{A}_0 for a neo-Hookean material are given by

$$(A_0)_{rshk} = \mu\delta_{rk}(B_e)_{sh}$$

where $B_e = F_e F_e^T$ and δ_{rk} is the Kronecker delta. The incremental equilibrium equation and the linearised form of the incompressibility constraint read respectively

$$\begin{cases} \text{Div } \delta\mathbf{P} = \mathbf{0} & \text{in } \Omega, \\ \text{tr } \Gamma = 0 & \text{in } \Omega. \end{cases} \quad (3.70)$$

This system of partial differential equations is complemented by the following boundary conditions

$$\begin{cases} \delta \mathbf{P}^T \mathbf{e}_r = 0 & \text{on } r = r_i, \\ \delta \mathbf{P}^T \mathbf{e}_r = 0 & \text{on } r = r_o. \end{cases} \quad (3.71)$$

Now, we reformulate the BVP given by Eqs. (3.70) - (3.71) using the Stroh formulation to implement a robust numerical procedure.

3.2.2.2 STROH FORMULATION

We denote with u , v and w the components of δu in cylindrical coordinates and with δP_{rr} , $\delta P_{r\vartheta}$ and δP_{rz} the components of the incremental stress tensor. Following [297], we rewrite the system of partial differential equations Eq. (3.70) into a system of ordinary differential equations, by assuming the following variable separation ansatz for the incremental fields [92, 24, 327]

$$u(r, \vartheta, z) = U(r) \cos(kz - m\vartheta), \quad (3.72)$$

$$v(r, \vartheta, z) = V(r) \sin(kz - m\vartheta) \quad (3.73)$$

$$w(r, \vartheta, z) = W(r) \sin(kz - m\vartheta), \quad (3.74)$$

$$\delta P_{rr}(r, \vartheta, z) = s_{rr}(r) \cos(kz - m\vartheta) \quad (3.75)$$

$$\delta P_{r\vartheta}(r, \vartheta, z) = s_{r\vartheta}(r) \sin(kz - m\vartheta), \quad (3.76)$$

$$\delta P_{rz}(r, \vartheta, z) = s_{rz}(r) \sin(kz - m\vartheta), \quad (3.77)$$

$$\delta p(r, \vartheta, z) = Q(r) \cos(kz - m\vartheta), \quad (3.78)$$

where m and $k = (2n\pi)/L$ are respectively the circumferential and axial wavenumbers, with $m, n \in \mathbb{N}$. By substituting Eq. (3.75) into Eq. (3.69), we get

$$Q(r) = \frac{U'(r)(r^2 p(r) + r^2 - r_i^2 + R_i^2)}{r^2} - s_{rr}(r),$$

where $p(r)$ is defined in Eq. (3.66). Following a similar and well established procedure [24], the incremental problem can be rewritten into the Stroh form [297], such as

$$\frac{d\boldsymbol{\eta}}{dr} = \frac{1}{r} \mathbf{N}\boldsymbol{\eta}, \quad (3.79)$$

where $\boldsymbol{\eta}$ is the *displacement-traction vector* defined as

$$\boldsymbol{\eta} = [\mathbf{U}, r\boldsymbol{\Sigma}] \quad \text{where} \quad \begin{cases} \mathbf{U} = [U, V, W], \\ \boldsymbol{\Sigma} = [s_{rr}, s_{r\theta}, s_{rz}]. \end{cases}$$

The matrix $\mathbf{N} \in \mathbb{R}^{6 \times 6}$ is the *Stroh matrix* and it has the following sub-block form

$$\mathbf{N} = \begin{bmatrix} \mathbf{N}_1 & \mathbf{N}_2 \\ \mathbf{N}_3 & \mathbf{N}_4 \end{bmatrix},$$

such that $\mathbf{N}_i \in \mathbb{R}^3 \times \mathbb{R}^3$, $\mathbf{N}_1 = -\mathbf{N}_4^T$, $\mathbf{N}_2 = \mathbf{N}_2^T$ and $\mathbf{N}_3 = \mathbf{N}_3^T$, which means that the Stroh matrix has an Hamiltonian structure [144]. The expression of the four blocks is given by

$$\mathbf{N}_1 = \begin{bmatrix} -1 & m & -kr \\ -m\sigma p & \sigma p & 0 \\ krp\sigma & 0 & 0 \end{bmatrix}, \quad \mathbf{N}_2 = \begin{bmatrix} 0 & 0 & 0 \\ 0 & \sigma & 0 \\ 0 & 0 & \sigma \end{bmatrix}, \quad \mathbf{N}_3 = \begin{bmatrix} \kappa_{11} & \kappa_{12} & \kappa_{13} \\ \kappa_{12} & \kappa_{22} & \kappa_{23} \\ \kappa_{13} & \kappa_{23} & \kappa_{33} \end{bmatrix}, \quad (3.80)$$

where

$$\begin{aligned}
\kappa_{11} &= 1/\sigma + r^2\delta_1 + 2p + \delta_3\sigma & \kappa_{12} &= \sigma m(1/\sigma^2 - 2 + p^2) + \delta_2 \\
\kappa_{13} &= k/r(\sigma + rp) & \kappa_{22} &= r^2(k + \gamma^2 - 2m\gamma k) + \sigma(1 - p^2) + m^2(2 + \sigma\delta_5 + \sigma\gamma R) \\
\kappa_{23} &= -km(\sigma/r + 2pr) & \kappa_{33} &= m^2(\sigma + r\gamma^2) + r^2k\delta_4
\end{aligned}$$

and

$$\begin{aligned}
\sigma &= \frac{r^2}{R} & \delta_1 &= \gamma^2 + k^2 - 2\gamma km + \gamma^2 m^2 & \delta_2 &= -p^2(k^2 r^2 + m^2) + m^2 + 1 \\
\delta_3 &= 2r^2\gamma(k - m\gamma) - 2mp & \delta_4 &= k(1 + 1/\sigma - 2p) + 2m\gamma & \delta_5 &= (R_i^2 - r_i^2)^2/r^4,
\end{aligned}$$

with r and p defined in Eq. (3.60) and Eq. (3.66), respectively. Eq. (3.79) with the boundary condition $\Sigma = \mathbf{0}$ at $r = r_i$ and $r = r_o$ define the incremental BVP.

Eqs. (3.72) - (3.78) do not fulfill the boundary condition Eq. (3.52) at the bases, imposing $w = 0$ at $Z = 0, L$ [123, 130]. This difference in boundary conditions will likely appear as an end effect in proximity of the two bases at $Z = 0$ and $Z = L$, that becomes increasingly relevant as the tube is short with respect to its length.

The incremental BVP is hard to solve, hence, different numerical techniques have been introduced in literature to overcome the problem, e.g. *the compound matrix method* [175], *the determinantal method* [9] or *the Adams-Moulton method* [331]. We employ the *impedance matrix method* to transform the differential problem into a Riccati equation, that is easier to solve numerically [59, 60].

3.2.2.3 IMPEDENCE MATRIX METHOD

Following a similar procedure used in [24], we introduce the matricant

$$\mathbf{M}(r, r_o) = \begin{bmatrix} \mathbf{M}_1(r, r_o) & \mathbf{M}_2(r, r_o) \\ \mathbf{M}_3(r, r_o) & \mathbf{M}_4(r, r_o) \end{bmatrix}, \quad \mathbf{M}(r, r_o) \in \mathbb{R}^{6 \times 6},$$

defined as the solution of the problem

$$\frac{d\mathbf{M}}{dr} = \frac{1}{r}\mathbf{N}\mathbf{M}(r, r_o), \quad \mathbf{M}(r_o, r_o) = \mathbf{I}. \quad (3.81)$$

Since the solution of the Stroh problem Eq. (3.79) can be expressed as

$$\boldsymbol{\eta}(r) = \mathbf{M}(r, r_o)\boldsymbol{\eta}(r_o)$$

and no traction loads are applied on the external surface, i.e. $\boldsymbol{\Sigma}(r_o) = \mathbf{0}$, we can define the *conditional impedance matrix* $\mathbf{Z}(r, r_o)$ [242] as

$$\mathbf{Z}(r, r_o) = \mathbf{M}_3(r, r_o)\mathbf{M}_3^{-1}(r, r_o), \quad (3.82)$$

where the term *conditional* refers to the dependence on the boundary condition at r_o .

Omitting the explicit dependence of \mathbf{Z} on r and r_o , such a matrix satisfy the following relation

$$r\boldsymbol{\Sigma} = \mathbf{Z}\mathbf{U} \quad \forall r \in (r_i, r_o) \quad (3.83)$$

By using Eq. (3.83), we can rewrite the Stroh problem given by Eq. (3.79) into a differential Riccati equation, such as

$$\frac{d\mathbf{U}}{dr} = \frac{1}{r} (\mathbf{N}_1 + \mathbf{N}_2\mathbf{Z}) \mathbf{U}, \quad (3.84)$$

$$\frac{d\mathbf{Z}}{dr} \mathbf{U} + \mathbf{Z} \frac{d\mathbf{U}}{dr} = \frac{1}{r} (\mathbf{N}_3 + \mathbf{N}_4\mathbf{Z}) \mathbf{U}. \quad (3.85)$$

Substituting Eq. (3.84) into Eq. (3.85) we get the following differential Riccati equation

$$\frac{d\mathbf{Z}}{dr} = \frac{1}{r} (\mathbf{N}_3 + \mathbf{N}_4\mathbf{Z} - \mathbf{Z}\mathbf{N}_1 - \mathbf{Z}\mathbf{N}_2\mathbf{Z}). \quad (3.86)$$

We integrate Eq. (3.86) from r_o to r_i , using as starting condition the fact that there are no applied loads at $r = r_o$, i.e.

$$\mathbf{Z}(r_o, r_o) = \mathbf{0}.$$

To construct a bifurcation criterion, we use the fact that there are no applied loads in $r = r_i$: non-null solutions of the incremental problem exist if and only if

$$\det \mathbf{Z}(r_i) = 0. \quad (3.87)$$

Fixing the initial geometry of the HT, making outer iterations on the wavenumbers m and k , for a fixed value of the torsion control parameter γ we integrate the Riccati Eq. (3.86) from $r = r_o$ up to $r = r_i$ making use of the the software MATHEMATICA 11.3 (Wolfram Research, Champaign, IL, USA). We iteratively increase the torsion control parameter γ following its stable solution [92] until the bifurcation criterion Eq. (3.87) is satisfied.

3.2.2.4 MARGINAL STABILITY THRESHOLDS

In this section we collect and discuss the results of the linear stability analysis. First of all, we introduce the dimensionless parameters which govern the boundary value problem, i.e.

$$\tilde{\gamma} = \gamma R_o \quad \tilde{k} = k R_o \quad \alpha_R = \frac{R_o}{R_i} \quad \alpha_L = \frac{L}{R_o}, \quad (3.88)$$

where $\tilde{\gamma}$ represents the dimensionless torsion rate, \tilde{k} the dimensionless axial wavenumber, α_R and α_L are geometrical parameters, representing the thickness and the slenderness ratios, respectively. Given a material length L , the admissible axial wavenumber \tilde{k} is given by

$$\tilde{k} = \frac{2\pi n}{\alpha_L} \quad n \in \mathbb{N}. \quad (3.89)$$

In the following, first we aim at characterizing the torsion deformation during the c-looping by considering suitable biological values of the two parameters involved, i.e. the initial thickness ratio α_R of the HT and its slenderness ratio α_L .

In human embryo, looping begins approximately around 23 – 28 days after the fertilization, when the length is about 1 – 2 mm [163]. A lot of experiments have been performed on animals whose cardiovascular system is similar to humans, for instance the chick embryo [317, 328, 263, 223, 291], whose size is comparable with the human one; being about 3–4 mm. From these experimental results, a physiologically relevant range for both α_R and α_L is

$$\alpha_R = [1.35, 2.85] \quad \alpha_L = [7, 10]. \quad (3.90)$$

Second, we use a wider range of dimensionless parameters to investigate to a further ex-

tent the effect of geometry on pattern selection and nonlinear development.

In the following, we vary the thickness ratio $\alpha_R \in (1, +\infty)$, since neither $\alpha_R = 1$ nor $\alpha_R \rightarrow +\infty$ represent a hollow cylinder. In Figs. 3.13 - 3.14, we plot the marginal stability threshold $\tilde{\gamma}_{\text{cr}}$, the circumferential m_{cr} and the axial \tilde{k}_{cr} critical wavenumbers versus the thickness ratio α_R .

Considering the infinite cylinder, i.e. $\tilde{k} \in \mathbb{R}$, in Fig. 3.13a, we plot the critical circumferential number m_{cr} versus α_R and we notice that there is a cut-off thickness at which the morphological transition of the HT completely changes: for thin cylinder, i.e. $\alpha_R < 2$, the critical circumferential wavenumber $m_{\text{cr}} = 2$, while for $\alpha_R > 2$, i.e. considering thicker cylinders, the critical circumferential number is $m_{\text{cr}} = 1$. From a biological standpoint, this result implies that c-looping is controlled by the geometry of the embryonic tube. Moreover, from a mathematical point of view, geometrical nonlinearity dominates the post-bifurcation behavior [162, 159, 290].

Considering an infinite cylinder, i.e. $\tilde{k} \in \mathbb{R}$, we plot the critical axial wavenumber \tilde{k}_{cr} and the marginal stability threshold $\tilde{\gamma}_{\text{cr}}$, see respectively Figs. 3.13b - 3.13c, versus the thickness parameter α_R in the range of thin cylinders, i.e. $\alpha_R \in (1, 2)$. Both the marginal stability threshold $\tilde{\gamma}_{\text{cr}}$ and the critical axial wavenumber \tilde{k}_{cr} increase as α_R increases as already pointed out in [24], compare their Figs. 7a - 8a with our Figs. 3.13c - 3.13b.

Since thicker cylinders, i.e. $\alpha_R \gg 1$, immediately buckle for a very small value of the torsion control parameter $\tilde{\gamma}$, we study finite hollow thick tubes varying $\alpha_R \in (2, 10)$ and $\alpha_L = \{4, 4.5, 5, 6, 7, 15, 30\}$. From Fig. 3.13d and Fig. 3.13e, we notice that both the circumferential m_{cr} and the axial \tilde{k}_{cr} critical wavenumbers are affected by the slenderness ratio α_L . For small values of α_L and α_R , the critical circumferential wavenumber $m_{\text{cr}} = 2$ and there is a doubling period for the critical axial wavenumber, i.e. $\tilde{k}_{\text{cr}} = 4\pi/\alpha_L$. Fixing the slenderness ratio and increasing α_R , we find that $m_{\text{cr}} = 1$ and $\tilde{k}_{\text{cr}} = 2\pi/\alpha_L$, in accordance to what happens for an infinite cylinder.

In Fig. 3.14, we plot the marginal stability threshold $\tilde{\gamma}_{\text{cr}}$ versus α_R for different values of α_L . For graphical scaling of the parameters, we change the range of $\alpha_L = \{14, 14.5, 15, 15.5, 16\}$: similar to what happens for thin cylinder, i.e. $\alpha_R < 2$, $\tilde{\gamma}_{\text{cr}}$ increases as α_R increases, see the inset in Fig. 3.14.

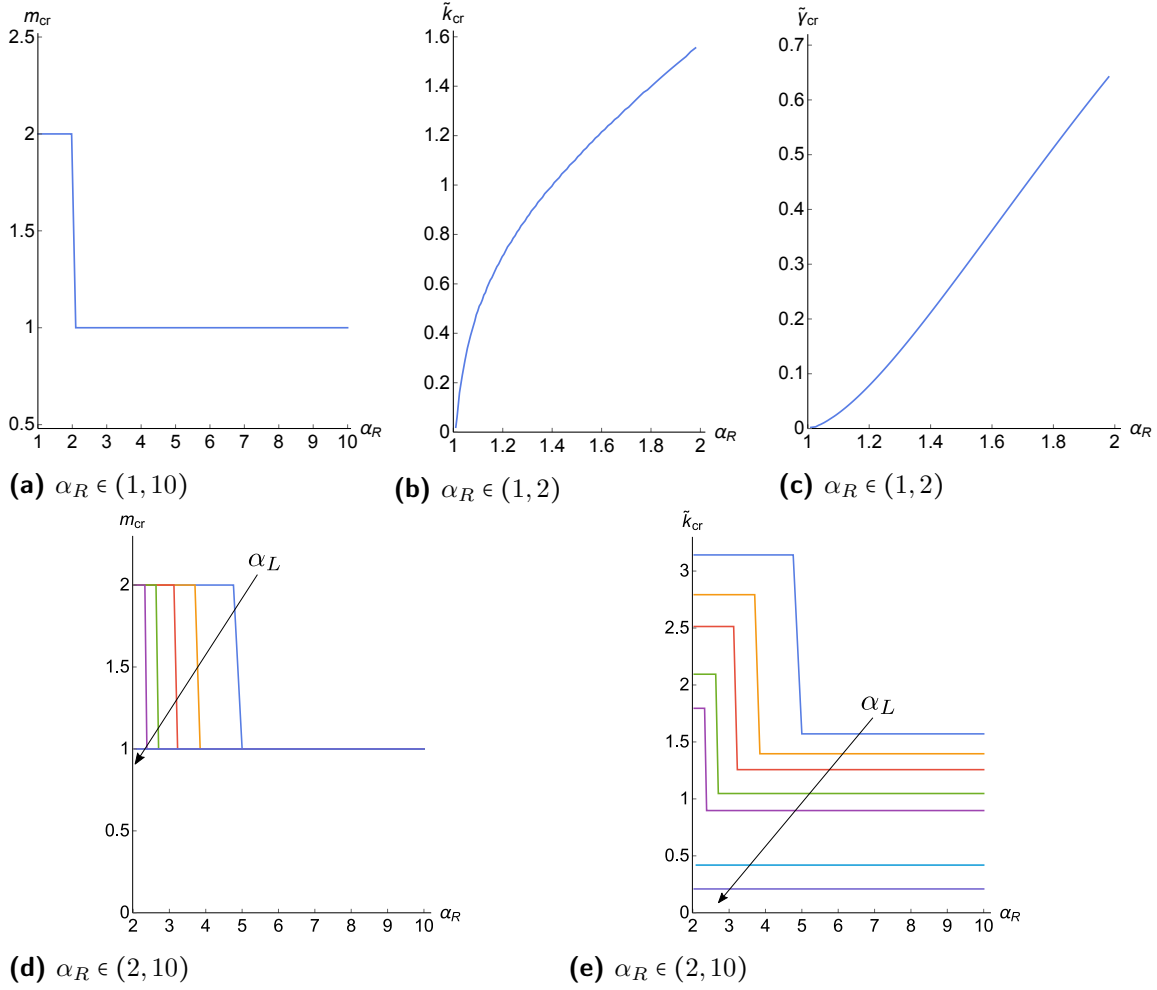


Figure 3.13: Plot of the critical values versus α_R , varying the initial thickness ratio $\alpha_R \in (1, 10]$. (a) Plot of the circumferential critical wavenumber m_{cr} versus α_R . Varying $\alpha_R \in (1, 2)$ and $\alpha_L = +\infty$, (b) plot of the critical axial wavenumber \tilde{k}_{cr} and (c) of the marginal stability threshold $\tilde{\gamma}_{\text{cr}}$ versus α_R . Varying $\alpha_R \in (2, 10)$, (d) plot of the critical circumferential wavenumber m_{cr} and (e) of the critical axial wavenumber \tilde{k}_{cr} versus α_R having chosen different values of $\alpha_L = \{4, 4.5, 5, 6, 7, 15, 30\}$.

The parameter α_L also affects the marginal stability thresholds of the HT. In Fig. 3.15, fixing the thickness ratio $\alpha_R = 2.85$, first we notice that the critical circumferential wavenum-

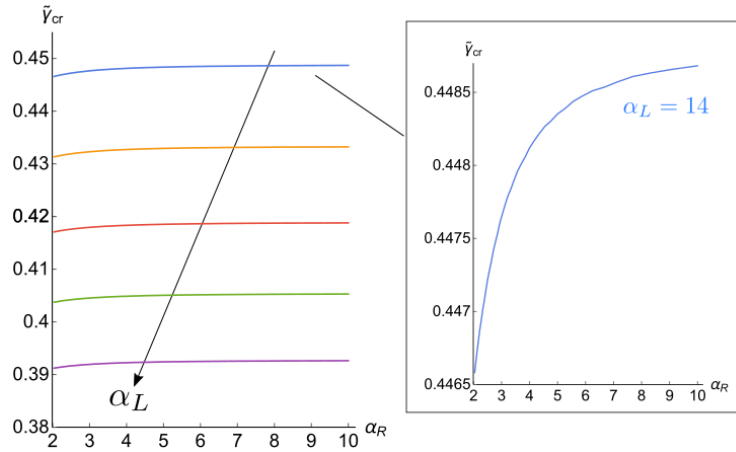


Figure 3.14: Plot of the marginal stability threshold $\tilde{\gamma}_{cr}$ versus α_R for thick cylinders, $\alpha_R \in (2, 10)$, varying $\alpha_L = \{14, 14.5, 15, 15.5, 16\}$. The inset shows a zoom of the curve with $\alpha_L = 14$.

ber m_{cr} is always $m_{cr} = 1$ for all α_L (see Fig. 3.15a). Then, in Figs. 3.15b - 3.15c, we plot the marginal stability threshold $\tilde{\gamma}_{cr}$ and the critical axial wavenumber \tilde{k}_{cr} versus α_L . Both the curves are coherent with the typical mechanical behavior of a twisted Euler rod: as we increase the slenderness ratio as the cylinder buckles earlier and the emerging pattern is an helix of pitch $1/\tilde{k}$ [164, 148].

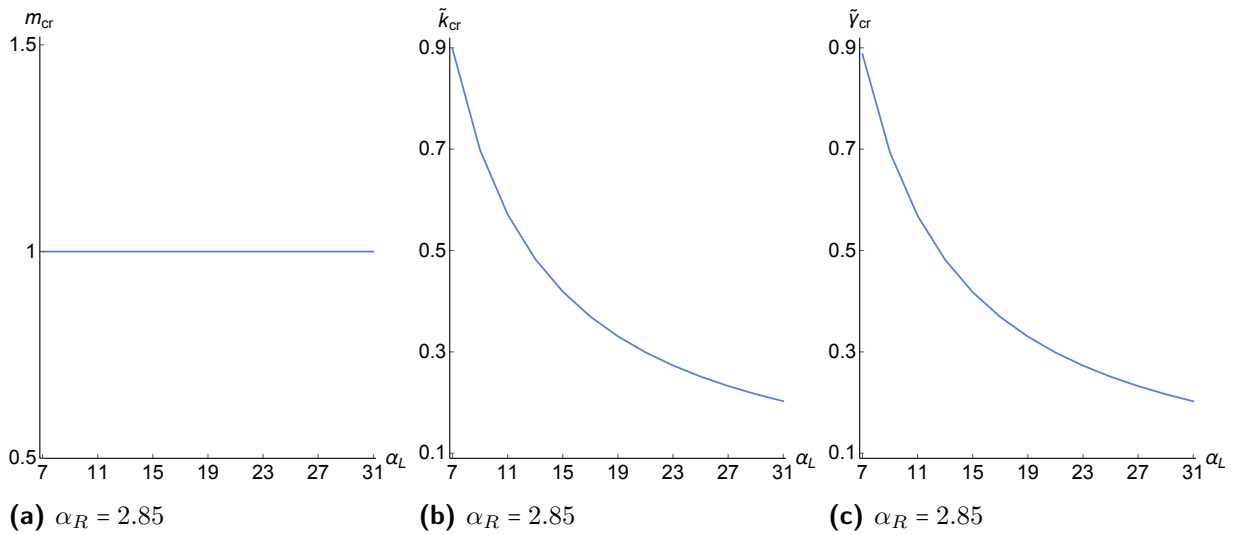


Figure 3.15: Plot of critical wavenumbers and the marginal stability threshold versus α_L , fixing the initial thickness ratio $\alpha_R = 2.85$. (a) The critical circumferential wavenumber is $m_{cr} = 1$. (b) The critical axial wavenumber \tilde{k}_{cr} and (c) of the marginal stability threshold $\tilde{\gamma}_{cr}$ decrease as α_L increases.

Figs. 3.13-3.15 characterize the loss of marginal stability as a function of the thickness ratio α_R and the slenderness ratio α_L . By using these characteristic values, in the next section we study the development of the looped configuration far beyond the marginal stability threshold: we implement a finite element code to discretize and numerically solve the fully nonlinear BVP given by Eqs. (3.54)-(3.56).

3.2.3 NUMERICAL SIMULATIONS

The boundary value problem is implemented by using FEniCS, an open source tool for solving partial differential equations [212]. We generate as a computational domain a hollow cylinder with a non-structured tetrahedral mesh created through the module MSHR [212], see Fig. 3.16, where we refine the mesh around the two bases $z = 0$ and $z = \alpha_L$, see Fig. 3.16b. Since the cylinder is finite, to solve the non linear elastic BVP Eqs. (3.53),

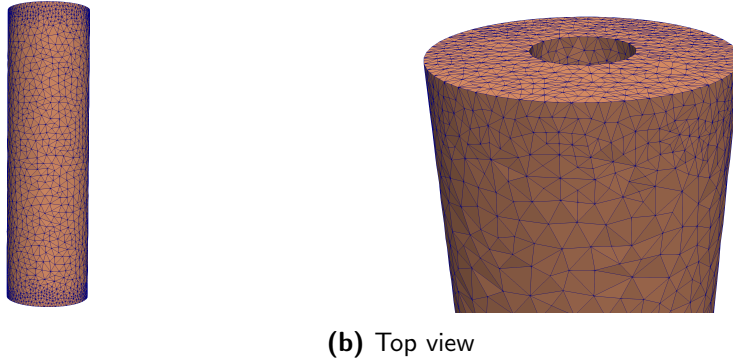


Figure 3.16: Mesh generated through MSHR for $\alpha_R = 2.85$ with local refinement.

(3.54) and (3.56), we need to impose suitable boundary conditions on the top and bottom bases. First, we assume a stronger form of (3.52), imposing

$$\mathbf{u} = 0 \quad \text{on } z = 0, z = \alpha_L. \quad (3.91)$$

We discretize the computational domain by using a mesh composed by 78338 elements and to solve the problem, we use the Taylor-Hood $\mathbf{P}_2 - P_1$ element, i.e. the displacement field is given by a continuous, piecewise quadratic function while the pressure field by a continuous, piecewise linear function. The choice of this particular element is motivated by its stability for non-linear elastic problems [21]. We introduce an additional term to stabilize the numerical scheme which penalizes the volumetric deformations, since at the discrete level the use of \mathbf{P}_2 -elements can result in unphysical values for the determinant of F_e [21]. Second, in order to evaluate the effect of the boundary conditions on the top and the bottom surfaces, we perform further simulations imposing a weaker form of (3.52), precisely

$$\begin{cases} \mathbf{u} \cdot \mathbf{e}_r & = 0 \quad \text{on } z = 0, z = \alpha_L, \\ \mathbf{u} \cdot \mathbf{e}_\vartheta & = 0 \quad \text{on } z = 0, z = \alpha_L, \\ \int_{z=i} \mathbf{u} \cdot \mathbf{e}_z & = 0 \quad \text{where } i = 0, \alpha_L. \end{cases} \quad (3.92)$$

In this case, the mesh is composed by 78426 elements. We solve the discretised form of the equilibrium equation Eq. (3.54) in the Lagrangian form using a Newton method. The torsion control parameter $\tilde{\gamma}$ is incremented of $\delta\tilde{\gamma}$ when the Newton method converges, the numerical solution is used as initial guess for the following Newton cycle. The increment $\delta\tilde{\gamma}$ is automatically reduced near the theoretical marginal stability threshold and when the Newton method does not converge. The numerical simulation is stopped when $\delta\tilde{\gamma} < 10^{-6}$. To trigger the mechanical instability, a small perturbation of an amplitude of $10^{-5}R_o$, having the shape of the critical mode computed in Section 3.2.2, is applied at the free boundary of the mesh. The numerical algorithm is implemented in Python through the open-source computing platform FEniCS (version 2018.1) [212]. We use PETSc [22] as linear algebra back-end and MUMPS [12] as linear solver.

3.2.3.1 SIMULATION RESULTS

In this section, we discuss the results of the numerical simulations varying the two physical parameters α_R and α_L firstly within the biological range given by the experimental papers, and secondly outside this range to further understand the role of geometrical parameters in pattern selection, validating the results against some known features in the limiting case of solid cylinder.

TORSIONAL C-LOOPING NUMERICAL RESULTS In this section, we discuss the nonlinear pattern formation fixing the geometry of the cylinder within the range of dimensionless parameters given by the experimental results.

In Fig. 3.17, we plot the looping development of the HT for a hollow cylinder with $\alpha_R = 2.85$, $\alpha_L = 7$, imposing Eq. (3.91) on the top and bottom bases. We show the actual configuration for several values of the torsion control parameter $\tilde{\gamma}$. As $\tilde{\gamma}$ increases, the cylinder displays an helical pattern and the simulation stops around $\tilde{\gamma} \simeq 1.4$ because the lumen closes with an incipient self-contact, see Fig. 3.18a. This phenomenon is consistent with the chronological development of the HT: in later stages 13 – 18 the blood starts flowing in the tube and the open and the close of the lumen represents the primitive valve in the heart [224, 158, 229].

In order to study the amplitude of the helical pattern, we cut the cylinder with a plane $z = c$, where c is a constant. To respect the symmetry of the system, we select the central section $c = \alpha_L/2 = 3.5$. Hence, we define

$$\Delta r = \text{dist}(C_c - O), \tag{3.93}$$

where C_c is the centroid of the considered section, the red dot in Fig. 3.18a and $O = (0, 0, c)$ the centroid of the original HT, the black dot in Fig. 3.18a. In Fig. 3.18b, we plot $\Delta r/R_o$

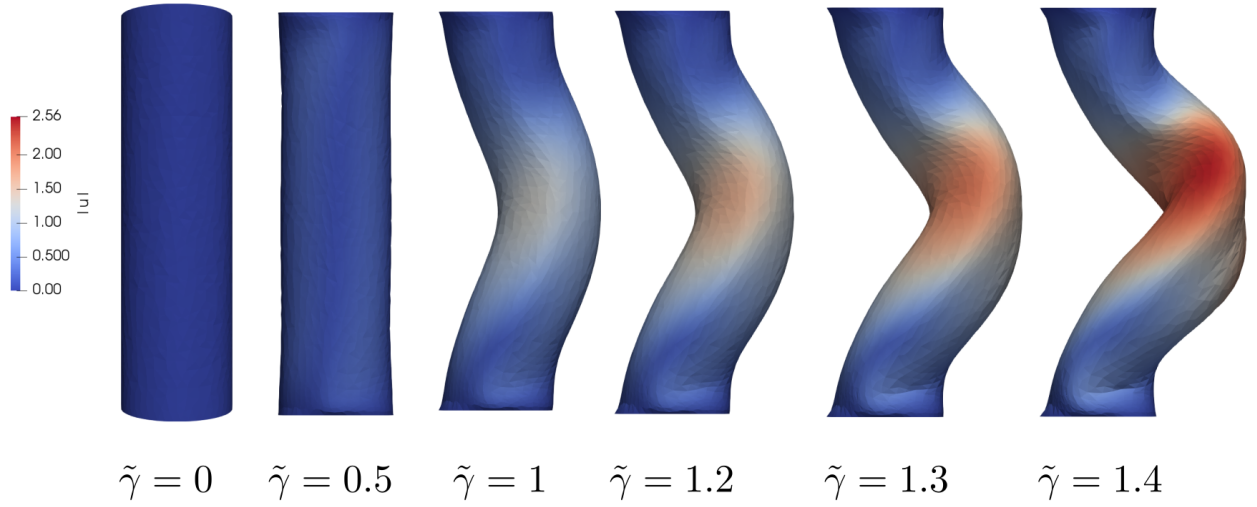


Figure 3.17: Actual configuration of the buckled tube when $\alpha_R = 2.85$, $\alpha_L = 7$ and Eq. (3.91) is taken as the boundary condition at $z = 0, \alpha_L$. For such values, the linear stability analysis gives $\tilde{\gamma}_{cr} \simeq 0.881748$.

versus $\tilde{\gamma}$ to measure the distance of the centroid of the section from the z -axis. We observe that there is an excellent agreement with the marginal stability thresholds computed in the previous section, verifying the results obtained by the numerical code against the theoretical predictions. Both bifurcation diagrams exhibit a continuous transition from the axis-symmetric to the buckled configuration, displaying the typical behaviour of a supercritical pitchfork bifurcation.

Finally, in Fig. 3.19, we perform the convergence analysis on our numerical simulations. We run several simulations at fixed geometry whilst increasing the number of the tetrahedra in the mesh, precisely we vary the numbers of faces on the side of the cylinder [212]. As the mesh gets finer and finer, as all the curves collapse on the same curve, and the numerical instability threshold is delayed for a coarser mesh, as expected due to the lower accuracy of the numerical approximation.

In Fig. 3.20, we fix the same geometry, i.e. $\alpha_R = 2.85$ and $\alpha_L = 7$, we solve again the fully nonlinear BVP Eqs. (3.53), (3.54) and (3.56), but we change the boundary condition on the two bases, substituting Eq. (3.91) with Eq. (3.92). As in the previous case, the

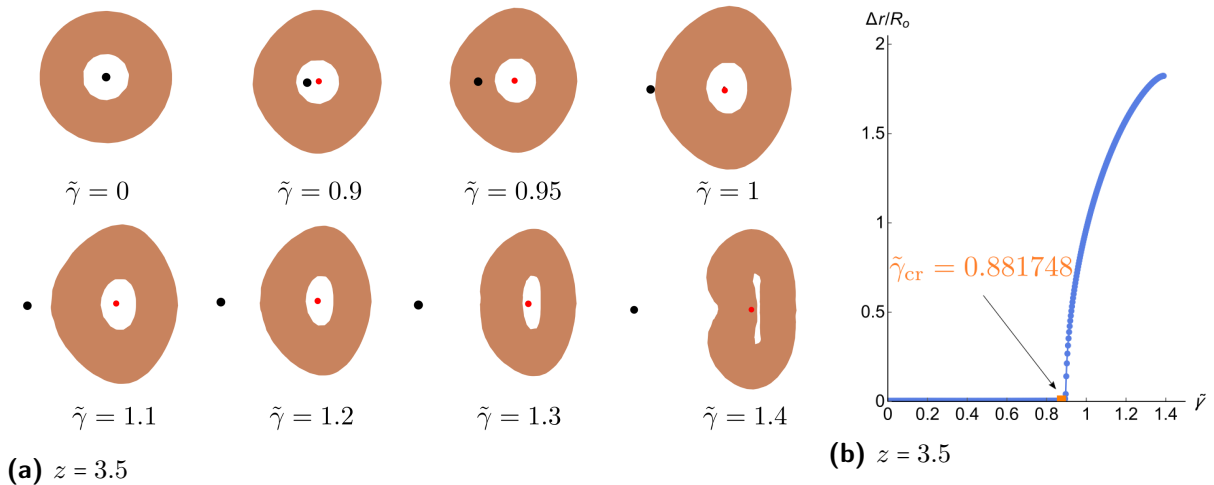


Figure 3.18: (a) Plot of the different shapes of the mid-section $z = \alpha_L/2 = 3.5$ at different values of the torsion control parameter $\tilde{\gamma}$. The black dot is $O = (0, 0, \alpha_L/2)$, i.e. the centroid of the initial midsection of the original HT, while the red one is the centroid of the midsection in the current configuration. The shape of the section changes and the lumen is getting smaller causing the stop of the numerical simulation. (b) Bifurcation diagram where we show the dimensionless parameter $\Delta r/R_o$ defined in Eq. 3.93 versus the torsion control parameter $\tilde{\gamma}$ when $\alpha_R = 2.85$ and $\alpha_L = 7$. The numerical simulation is validated against the marginal stability threshold computed with the linear stability analysis (orange square, $\tilde{\gamma}_{cr} \approx 0.881748$).

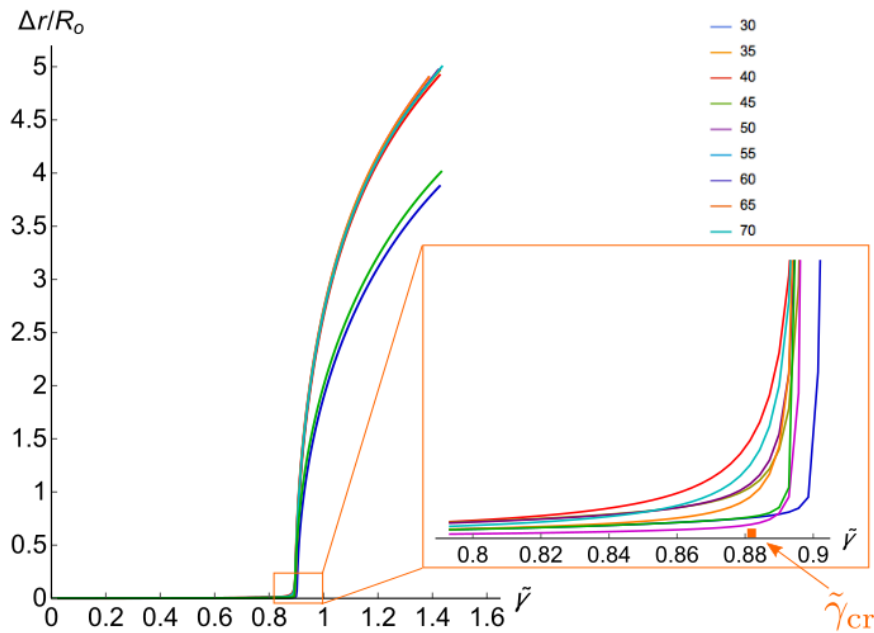


Figure 3.19: Plot of the bifurcation diagram varying the numbers of faces 30, 35, 40, 45, 50, 60, 70, 80 on the side of the cylinder [212]. In the inset, we highlight the behavior near the marginal stability threshold.

simulation stops because the lumen closes and the internal surfaces enters in self-contact approximately at the same value of the torsion control parameter $\tilde{\gamma} \simeq 1.4$ as in the previous case. Thus, the two different choices of the boundary conditions for the top and bottom

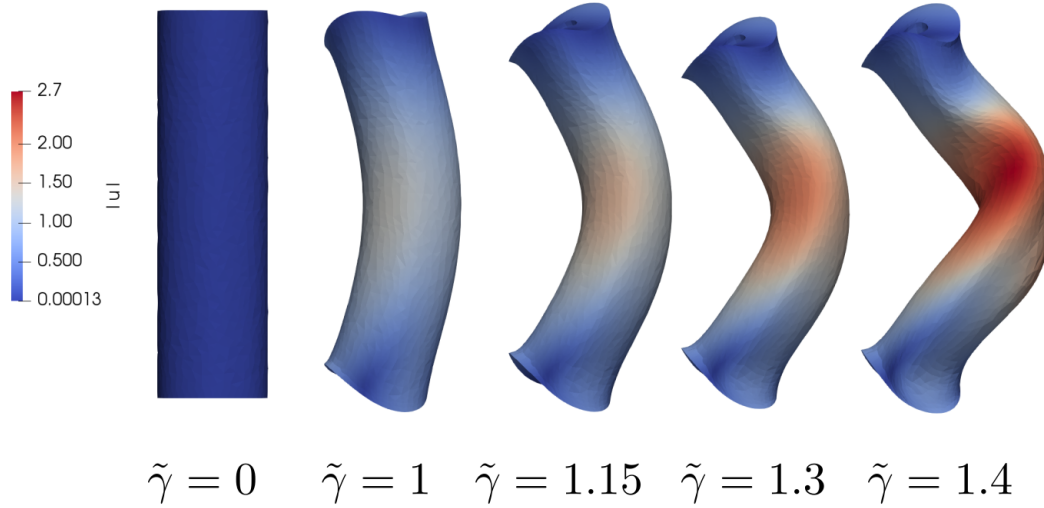


Figure 3.20: Actual configuration of the looped tube when $\alpha_R = 2.85$, $\alpha_L = 7$ and Eq. (3.92) is taken as boundary condition at $z = 0, \alpha_L$. In such conditions $\tilde{\gamma}_{cr} \simeq 0.881748$.

ends of the HT result in a small deviation of the onset of the bifurcation.

Let

$$E = \int_{\Omega_0} W(\mathbf{F}) dV \quad (3.94)$$

be the total elastic energy of the hollow cylinder. We compute the ratio of the energy E_{th} of the axis-symmetric solution given by Eqs. (3.60) and (3.66) and the energy E_{num} computed through the finite elements computation. In Fig. 3.21, we plot the ratio E_{num}/E_{th} versus the control parameter $\tilde{\gamma}$ fixing $\alpha_R = 2.85$ and $\alpha_L = 7$ for the two different boundary conditions on the two bases, respectively Eq. (3.91) - (3.92). As expected, the buckled configuration exhibits in both cases a total mechanical energy lower than the one in the unbuckled state. In Fig. 3.21a, we fixed the whole displacement field $\mathbf{u} = 0$, and the instability is a bit delayed with respect to the theoretical marginal stability threshold $\tilde{\gamma}_{cr}$.

In Fig. 3.21b we require that the displacement along z is zero in a weaker way, and the threshold is closer to the theoretical prediction. Furthermore we observe that the energy decays continuously as $\tilde{\gamma}$ grows beyond thresholds, confirming that the bifurcation is in both cases supercritical, see Figs. 3.18 and 3.19.

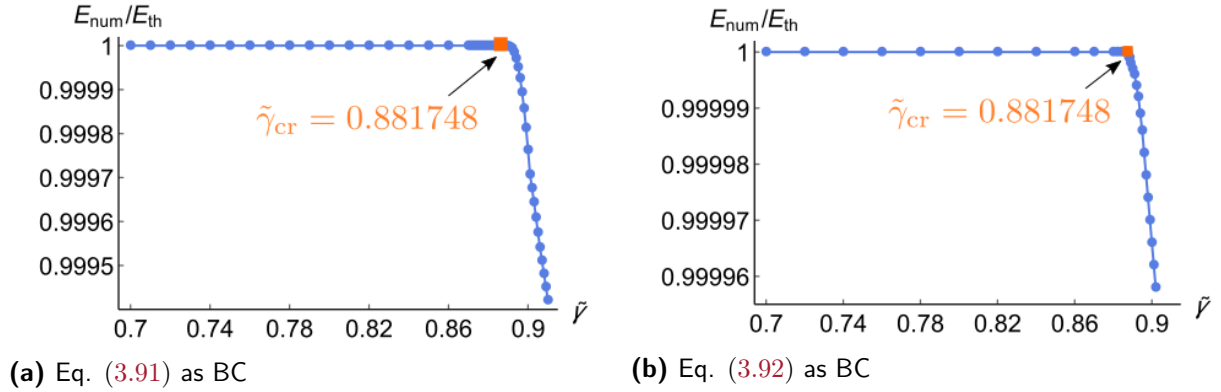


Figure 3.21: Plot of the ratio $E_{\text{num}}/E_{\text{th}}$ for (a) $\alpha_R = 2.85$ and Eq. (3.91) as boundary condition and (b) $\alpha_R = 2.85$ and (3.92) on the two bases versus the torsion control parameter $\tilde{\gamma}$. The orange square denotes the theoretical marginal stability threshold computed in Section 3.2.2.

NUMERICAL RESULTS FOR A WIDER RANGE OF GEOMETRICAL PARAMETERS We now investigate how the geometry, i.e. varying α_R and α_L , influences the buckled configuration in a wider range of dimensionless parameters, extending the linear stability analysis for some cases illustrated in Section 3.2.2.

First, let us consider the same thickness ratio $\alpha_R = 2.85$ as in the torsion c-looping case and increase the slenderness ratio setting $\alpha_L = 12$. From the linear stability analysis, we obtain that the marginal stability threshold decreases, i.e. $\tilde{\gamma}_{\text{cr}} = 0.52159$, and the critical circumferential and axial wavenumbers are $m_{\text{cr}} = 1$ and $\tilde{k}_{\text{cr}} = 2\pi/\alpha_L$, respectively. In Fig. 3.22, we plot the buckled configuration of the cylinder having imposed Eq. (3.91) on the two bases. We show the actual configuration for several values of the torsion control parameter $\tilde{\gamma}$. As $\tilde{\gamma}$ increases, the cylinder displays the expected helical pattern with a higher amplitude with respect to the one obtained fixing $\alpha_L = 7$, see the scale-bar of Fig. 3.22.

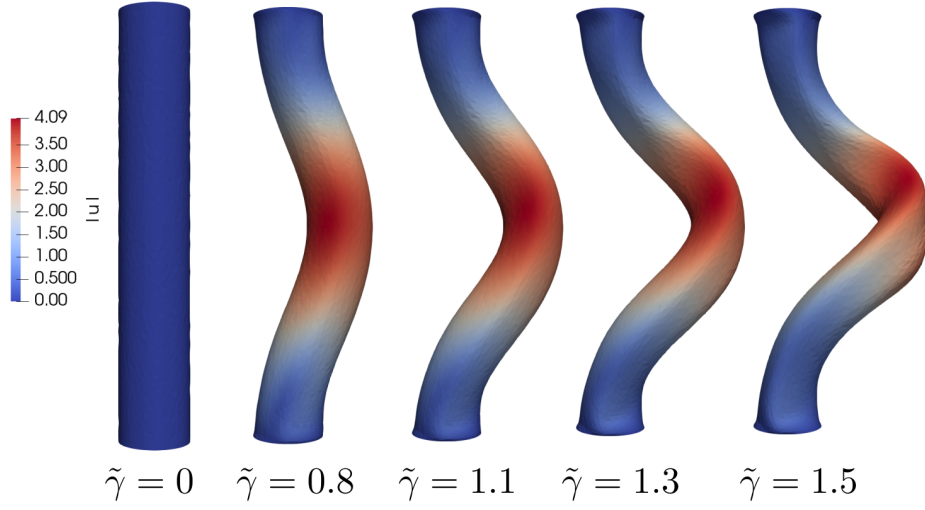


Figure 3.22: Actual configuration of the buckled tube for when $\alpha_R = 2.85$ and $\alpha_L = 12$ and Eq. (3.91) is taken as BC. In such conditions $m_{cr} = 1$, $\tilde{k}_{cr} = 2\pi/\alpha_L$ and $\tilde{\gamma}_{cr} = 0.521594$.

To quantify the amplitude of the helical pattern, in Fig. 3.23b, we plot the quantity $\Delta r/R_0$ defined in Eq. (3.93) versus the torsion control parameter $\tilde{\gamma}$, where in this case $O = (0, 0, 6)$. Comparing this picture with Fig. 3.18b, we notice a higher amplitude of the emerging helical loop, see Fig. 3.23b. In Fig. 3.23a, we plot the ratio of the energy E_{th} of the axis-symmetric solution given by Eqs. (3.60) and (3.66) and the energy E_{num} computed through the finite elements computation. We observe, first, the typical continuous transition from the unbuckled to the buckled configuration, confirming the supercritical pitchfork bifurcation and then a little delay on the onset of the instability due to the imposed boundary conditions Eq. (3.91).

Second, let us consider the same slenderness ratio α_L as in the torsional c -looping case, i.e. $\alpha_L = 7$, and consider a different initial thickness ratio $\alpha_R = 1.35$. With this choice we want to visualize the effect of the geometrical parameters on the nonlinear development of the looped patterns.

Imposing the boundary condition Eq. (3.91) on the two bases, we plot in Fig. 3.24 the resulting buckled configuration. As expected from the linear stability analysis, the critical

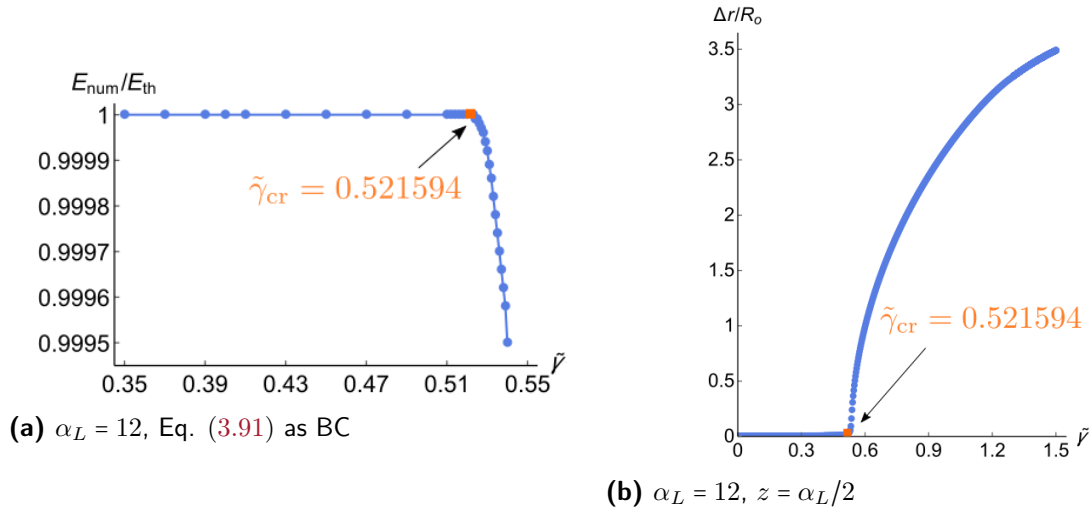


Figure 3.23: (a) Plot of the ratio $E_{\text{num}}/E_{\text{th}}$ for $\alpha_R = 2.85$, $\alpha_L = 12$ and Eq. (3.91) is taken as boundary condition versus the torsion control parameter $\tilde{\gamma}$. (b) Bifurcation diagram where we show the dimensionless parameter $\Delta r/R_o$ versus the torsion control parameter $\tilde{\gamma}$ when $\alpha_R = 2.85$, $\alpha_L = 12$ and $z = \alpha_L/2 = 6$. The orange square denotes the theoretical marginal stability threshold computed in Section 3.2.2, i.e. $m_{\text{cr}} = 1$, $\tilde{k}_{\text{cr}} = 2\pi/\alpha_L$ and $\tilde{\gamma}_{\text{cr}} = 0.521594$.

circumferential number is $m_{\text{cr}} = 2$, while the critical axial wavenumber is $2\pi/\alpha_L$.

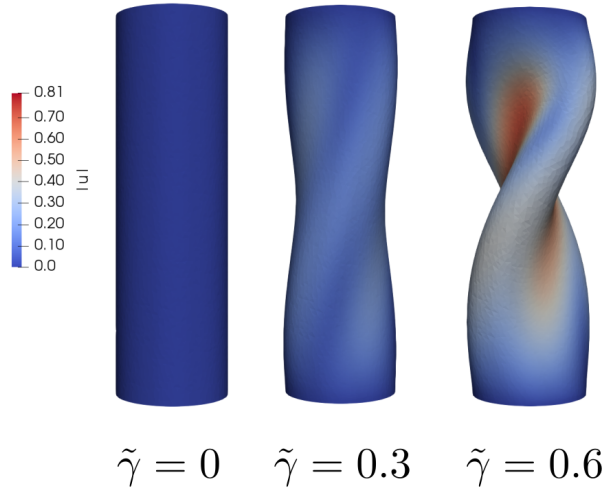


Figure 3.24: Actual configuration of the buckled tube when $\alpha_R = 1.35$, $\alpha_L = 7$ and Eq. (3.91) is taken as BC. In such conditions $m_{\text{cr}} = 2$, $\tilde{k}_{\text{cr}} = 2\pi/\alpha_L$ and $\tilde{\gamma}_{\text{cr}} \simeq 0.177001$.

Finally, if we consider a solid cylinder, that is characterized by $m_{\text{cr}} = 1$, we validate our numerical results against the classical problem of a twisted Euler rod, forming an helix of pitch $1/\tilde{k}$. For a Neo-Hookean material, this solution has been first presented by Green

and Spencer in [164]. Then, Gent and Hua [148] investigated the evolution of this instability: it can evolve with the sudden onset of a sharply bent ring, or knot. Up to our knowledge, this section is the first one which aims at reproducing the 3D numerical simulation of a finite torsion rate on a soft solid cylinder.

Let us fix the geometry of the solid cylinder, $\alpha_L = 12$ and impose the boundary condition Eq. (3.91) on the two bases, we plot in Fig. 3.25 the buckled configuration of the full cylinder. We show the actual configuration for several values of the torsion control parameter $\tilde{\gamma}$. As $\tilde{\gamma}$ increases, as the cylinder displays an helical pattern with a higher amplitude compared to the one of hollow cylinders, we can compare Fig. 3.17 and Fig. 3.23 with Fig. 3.25. The simulation stops around $\tilde{\gamma} \simeq 2.45$ probably due to the excessive distortion of the elements. Unfortunately, our simulation does not display the expected knot, since we should consider a longer cylinder which, however, requires a fine mesh, hence a bigger computational effort. Future efforts will be devoted in improving the performance of the numerical simulations, taking also into account for the self-contact.

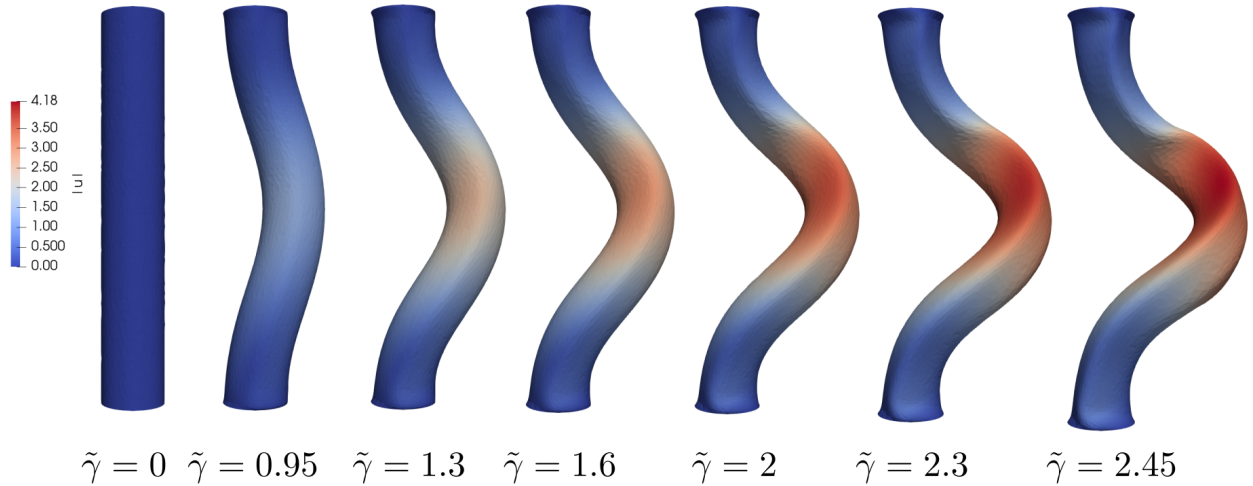


Figure 3.25: Actual configuration of the buckled tube for when $\alpha_R \rightarrow \infty$, $\alpha_L = 12$ and Eq. (3.91) is taken as BC. We choose $m_{cr} = 1$ and $\tilde{k}_{cr} = 2\pi/\alpha_L$.

In order to reduce the distortion of the tetrahedra, we refine the mesh near the two

bases and around $z = \alpha_L/2$, where we noticed the greatest concentration of elongated elements. The used mesh is presented in Fig. 3.26a. The linear stability analysis performed

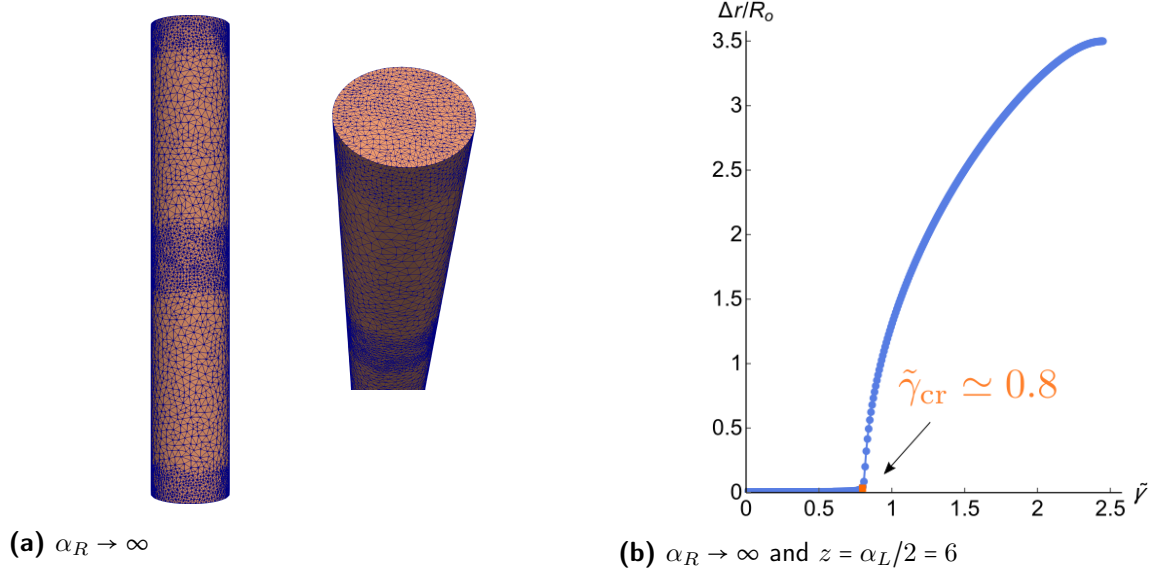


Figure 3.26: (a) Mesh generated through MSHR for $\alpha_R \rightarrow \infty$ with local refinements. (b) Bifurcation diagram showing the dimensionless parameter $\Delta r/R_0$ versus the torsion control parameter $\tilde{\gamma}$ when $\alpha_R \rightarrow \infty$, $\alpha_L = 12$ and $z = \alpha_L/2 = 6$. The orange square denotes the marginal stability threshold $\tilde{\gamma}_{\text{cr}} \simeq 0.8$ [164], with $m_{\text{cr}} = 1$ and $\tilde{k}_{\text{cr}} = 2\pi/\alpha_L$.

in Section 3.2.2 is no longer valid for a solid cylinder since the structure of the Stroh formulation changes in the absence of the lumen [92]. In order to assess our numerical results, we compare the marginal stability threshold obtained from our numerical simulations with the theoretical one computed by Green and Spencer [164]. In particular, we found that the critical torsion is around $\tilde{\gamma}_{\text{cr}} = 0.8$ for $\tilde{k} = 2\pi/\alpha_L$. In Fig. 3.26b, we plot the dimensionless quantity $\Delta r/R_0$ defined in eq. (3.93) versus the control parameter $\tilde{\gamma}$ where in this case $O = (0, 0, 6)$.

3.2.4 CONCLUSIONS

In this work, we have developed a simple morphomechanical model to describe the dextral torsion during the c-looping of the HT, which represents the first asymmetry during the

embryogenesis of the human heart. In Section 3.2.1, we have proposed a nonlinear elastic model of the HT undergoing torsional remodelling. The HT is described as a hollow cylinder whose thickness and slenderness ratios are obtained by experimental observations [302]. The elastic BVP is governed by the dimensionless parameters $\tilde{\gamma}$, i.e. the finite torsion rate induced by the remodelling cell flow, α_R , the ratio between outer and inner radius, and α_L , the ratio between the length and the outer radius of the HT. We have computed a radially symmetric solution and we have studied its linear stability in Section 3.2.2 using the theory of incremental deformations [243]. We have rewritten the linear stability analysis into an optimal Hamiltonian system using the Stroh formulation, following a procedure similar to that proposed in [24].

The marginal stability thresholds are discussed in Section 3.2.2.4. Both the critical circumferential and axial modes strongly depend on the geometrical parameters α_R and α_L . In particular, we recover some known results in the limit of thin tubes, as shown in Fig. 3.13a, showing a cut-off thickness at which the circumferential critical mode of the HT completely changes [162, 159, 290]. We also highlight that increasing α_L lowers the instability threshold [164, 148], as shown in Fig. 3.15.

Finally, we have implemented in Section 3.2.3 a finite element code to approximate the fully non-linear BVP. We use a mixed variational formulation whose linearization is based on the Newton method. The outcomes of our numerical simulations are reported in Figs. 3.17 - 3.26. We have considered both a physiological range of the geometrical parameters with experimental data, see Figs. 3.17 - 3.21, different geometrical data to validate our code, see Figs. 3.22 - 3.24 and the solid cylinder limit, see Figs. 3.25 - 3.26. These results show how the geometry of the cylinder, both the thickness and the slenderness ratio, strongly affect the looping onset and its nonlinear development. In all the cases, the bifurcation is supercritical, displaying a continuous transition from the axis-symmetric to the looped configurations, see Figs. 3.18, 3.21, 3.23 and 3.26b. We finally performed a grid

convergence analysis showing that our numerical results do not change any longer if a further mesh refinement is operated, as shown in Fig. 3.19.

In conclusion, our simple morphomechanical model suggests that a torsional internal remodelling alone can drive the spontaneous onset and the fully nonlinear development of the c-looping of the HT within its physiological range of geometrical parameters. This work aims to prove that mechanical features are as important as biological and chemical processes during this stage of heart embryogenesis. Further developments will be directed to investigate if the symmetry break results from the cell flow remodelling or may be directed from external constraints. We also aim to perform numerical simulations using a more realistic geometry extracted from bioimaging data.

3.3 FARADAY WAVES IN SOFT ELASTIC SOLIDS

In 1831 Faraday first observed standing capillary waves at the free surface of several fluids on a thin plate subjected to a periodic vertical oscillation [134]. Notably, he remarked that the characteristic frequency of the emerging patterns was half that of the driving frequency of the imposed vibration. This seminal observation of subharmonic resonance, later, inspired Lord Rayleigh in 1883 to propose a theoretical explanation based on a parametric oscillator governed by the Mathieu equation [266]. The analytic solution of the linear stability analysis for an ideal fluid was given after several decades by Benjamin and Ursell, showing a marginal stability diagram alternating loci of subharmonic and harmonic (*i.e.* isochronous) resonance [41].

The later analysis for a viscous fluid has shown that the dominance of a resonance mode over the other is mainly controlled by the ratio between the basin height and the typical length-scale of the viscous fluid at the free surface [199, 52]. Subharmonic resonance dominates in the nearly inviscid case, whilst bicritical points where both modes emerge si-

multaneously are encountered in shallow basins since the viscous effects are enhanced by the presence of the bottom rigid substrate [198]. The emergence of Faraday waves having a critical wavenumber is observed when the acceleration of the vertical oscillation reaches a critical threshold. Cubic terms are the weakest nonlinearities allowed to resonate with subharmonic linear eigenmodes in the associated amplitude equations, thus controlling the morphological transition to a large variety of ordered patterns [125]. Similar to other supercritical fluid instabilities [104], in the subharmonic regime the selection and the weakly nonlinear development of such patterns is mainly driven by the shape of the edge constraints of the basin [124, 108]. In the case where subharmonic and harmonic eigenmodes compete near the instability threshold, the patterns can arrange to a superlattice, localize in space and display chaotic motion on a slow timescale [95]. In experimental conditions with flexible boundaries, Faraday waves enable a localized wave particle interaction reminiscent of quantum mechanics, resulting into complex dynamics of self-propagation [99, 259].

The elastic behavior of the medium has been recently found to have a dramatic regularizing effect on some well-known dynamic phenomena in fluid mechanics, such as Rayleigh-Plateau [234, 303] or Rayleigh-Taylor instabilities [235, 83, 272]. Despite the recent experimental interest in this subject, very little is known about the elastic effects on the propagation of Faraday waves. For Non-Newtonian solutions of polymers, it has been observed that the instability threshold increases with respect to the Newtonian case as the driving frequency increases, suggesting that viscosity of the solution conversely decreases [267]. For linear viscoelastic fluids, the resonant mode becomes harmonic in the range where elastic forces are of the same order as the surface tension at the free boundary [319, 240]. Moreover, the corresponding instability diagram is strongly affected by variations of the liquid relaxation time [200]. For soft solids, recent experiments reported the dispersion relations of standing waves in soft agarose gels [289], paving the way for a positive use

of Faraday instability to measure the rheological properties of complex matter at scales where capillary-gravity and Rayleigh waves interact.

3.3.1 EXPERIMENTAL INVESTIGATION OF FARADAY WAVES IN SOFT MATERIALS

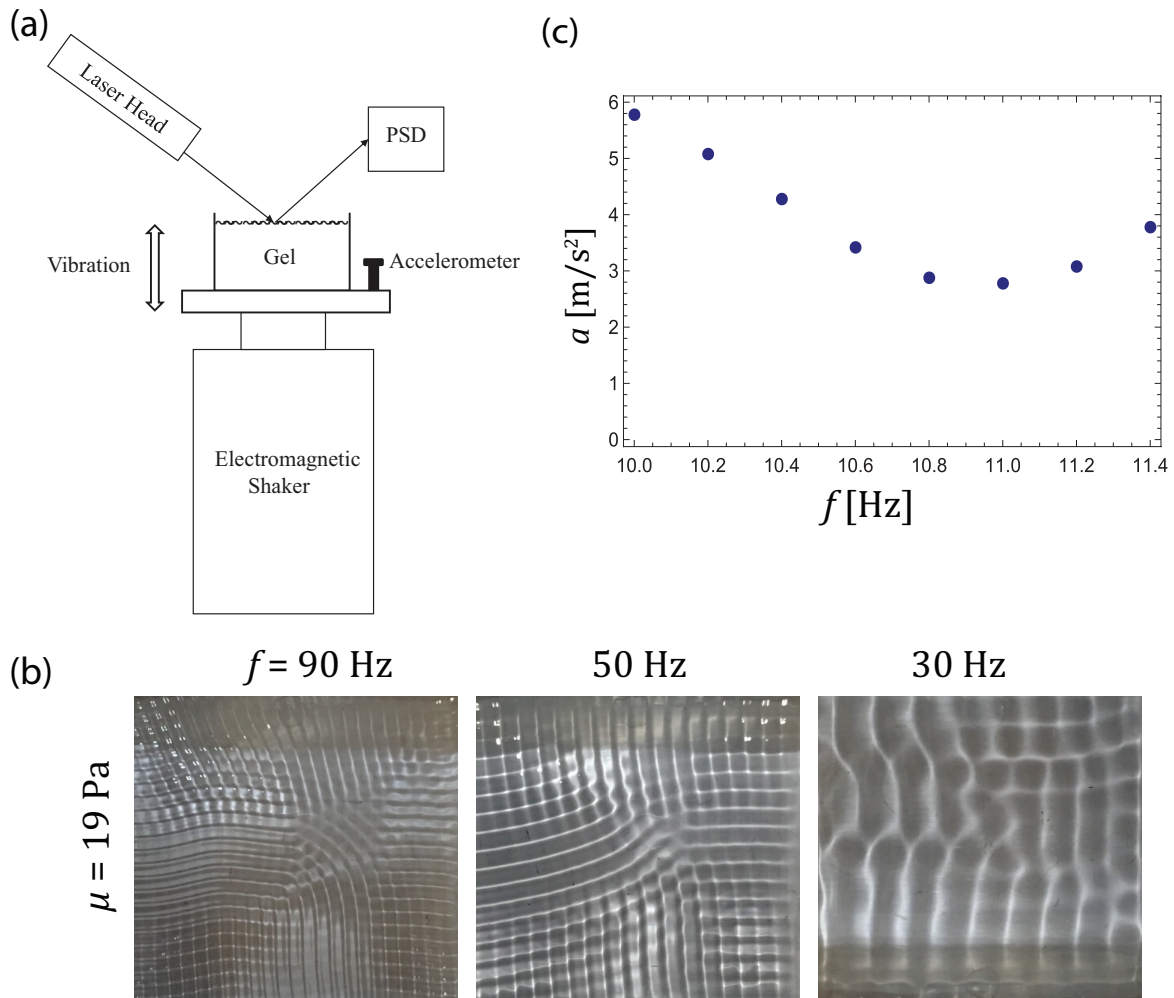


Figure 3.27: Faraday waves in soft gels: (a) schematic of experimental setup, (b) typical wave pattern for a gel with shear modulus $\mu = 19 \text{ Pa}$ in a square container, as it depends upon driving frequency f , and (c) typical instability tongue plotting critical acceleration a against frequency f for a given mode in a circular container.

We have observed Faraday waves on agarose gels using the experimental setup shown in Fig. 3.27(a). Here a square plexiglass container with edge length 9 cm is affixed to a

mechanical shaker which vertically drives the container over a range of frequencies $f_d = 30 - 90$ Hz to give the images presented in Fig. 3.27(b). The amplified signal of a function generator is used to drive the shaker, and the container acceleration is measured using an accelerometer mounted to the tank support. The soft materials used in these experiments are agarose gels made by dissolving agarose powder (Sigma Aldrich Type VI-A) in warm deionized water. The liquid is then allowed to gel in a container having a height $h = 24$ mm. The rheology of the gels are measured using an Anton Paar MCR-302 rheometer which admits a complex modulus $G' + iG''$. The storage modulus is typically many orders of magnitude larger than the loss modulus $G' \gg G''$ implying that these gels behave as an elastic solid with shear modulus in the range $\mu = 1-300$ Pa. Because our gels are soft, they are also subject to surface tension effects and the observed properties of the Faraday waves depend upon the resistance to motion caused by both shear modulus μ and surface tension γ with the relative importance quantified by the elastocapillary length $\ell = \gamma/\mu$. An advantage of exploring these soft agarose hydrogels is that these materials are often used in cell-printing applications for tissue engineering because they are capable of sustaining biological function. Studying Faraday wave formation in these gels may facilitate methods for patterning cells in a hydrogel matrix.

Above a critical acceleration threshold, waves appear on the gel surface as shown in Fig. 3.27(b), which tend to exhibit square-wave symmetry and align with the container geometry. For low driving frequency the surface wave exhibits a discrete mode number and finite bandwidth over which that mode can be excited [125, 124]. The bandwidth is illustrated in the typical instability tongue shown in Fig. 3.27(c). Here the resonance frequency ≈ 11 Hz coincides with the minimum value of the threshold acceleration. In general, for high driving frequency, the instability tongues become clustered closer together, there is no longer a finite bandwidth, the spatial wavenumber k is continuous, and the container geometry does not affect the wave pattern, as shown by [129] using irregular container ge-

ometries. The wavenumber k increases with the driving frequency and for accelerations much above threshold the waves lose their symmetry and become chaotic in nature. In our theoretical development, we assume the wavenumber is continuous and this corresponds to the high-frequency limit. We have also measured the critical acceleration for Faraday wave onset using essentially the same setup shown in Fig. 3.27, except using a circular tank. The HeNe laser beam (632.8 nm) shown in the figure is directed at the gel surface, and the reflected beam is captured by a position sensitive detector (PSD). The PSD output gives the location of the centroid of the light striking the detector which, in these experiments, is essentially the location of the laser spot on the detector. The vertically oscillating gel surface results in an oscillating signal from the PSD whose frequency is obtained via an FFT to yield the surface wave frequency f_o . In our experiments, we observe that $f_o = 0.5f_d$, a subharmonic response which is a signature of Faraday waves. We have obtained Faraday wave tongues by fixing f_d , performing an amplitude sweep and locating the threshold acceleration a_c . By repeating this for a range of f_d , Faraday wave tongues are traced out in $a - f_d$ space. An example of such a tongue is presented in Fig. 3.27(c) for the case of an agarose gel having an elasticity of $\mu = 3.5$ Pa.

Recently [288], apart of this seminal result, some experiments have been conducted to study the appearance of Faraday waves on the surface of an agarose gel which is mechanically-vibrated in a cylindrical container. We characterize the shape of the instability tongue and show the complex dependence upon material properties can be understood as an elasto-capillary effect highlighting the role of solid surface tension in soft gels.

3.3.2 THE NONLINEAR ELASTIC PROBLEM AND ITS GROUND STATE

We consider a soft hyperelastic body with a reference domain $\Omega_0 \in \mathbb{R}^3$ in its undeformed state. The body is infinitely long along the Z direction, so that a plane strain assumption

can be made, hence

$$\Omega_0 = \{\mathbf{X} = [X, Y, Z] \in \mathbb{R}^3 : X \in (0, L), Y \in (0, H), Z \in \mathbb{R}\},$$

where H is the reference height, L is the reference length, and \mathbf{X} is the material position vector. The body is attached to a rigid substrate at $Y = 0$ and free to slide at the lateral walls $X = 0, X = L$, being subjected to its own weight and to a vertical sinusoidal oscillation of amplitude a and frequency ω , as sketched in Fig. 3.28. We consider in the following a Cartesian coordinate system that is fixed with the rigid substrate, with unit material vectors \mathbf{E}_i , with $i = X, Y, Z$.

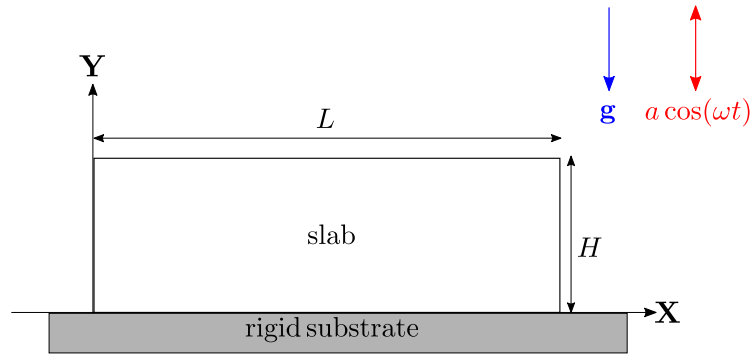


Figure 3.28: Sketch of the reference configuration of the model: L is the reference length of the elastic slab and H is its reference height. It is clamped to a rigid substrate and it is subjected to its own weight and to a vertical sinusoidal oscillation with amplitude a and frequency ω .

The actual position vector is given by $\mathbf{x} = \varphi(\mathbf{X}, t)$, where $\varphi : \Omega_0 \rightarrow \Omega \in \mathbb{E}^3$ is a one-to-one mapping at time t , so that the kinematics of motion is described by the geometrical deformation tensor $\mathbf{F} = \text{Grad } \mathbf{x} = \frac{\partial \mathbf{x}}{\partial \mathbf{X}}$. We also assume that the body is made of an incompressible neo-Hookean material with strain energy density given by

$$W(\mathbf{F}) = \frac{\mu}{2} (\text{tr } \mathbf{C} - 2) - p(\det \mathbf{F} - 1), \quad (3.95)$$

where μ is the shear modulus, $\mathbf{C} = \mathbf{F}^T \mathbf{F}$ is the right Cauchy–Green tensor and p is the La-

grangian multiplier enforcing the internal constraint of incompressibility. Using the constitutive assumption in Eq. (3.95), the nominal stress tensor \mathbf{P} and the Cauchy stress tensors \mathbf{T} are given respectively by [243]

$$\mathbf{P} = \frac{\partial W(\mathbf{F})}{\partial \mathbf{F}} - p\mathbf{F}^{-1} = \mu\mathbf{F}^T - p\mathbf{F}^{-1}, \quad \mathbf{T} = \mathbf{F}\mathbf{P}. \quad (3.96)$$

Thus, the balance of linear momentum for the elastic body reads

$$\text{Div } \mathbf{P} + \rho G(t) \mathbf{E}_y = \rho \frac{\partial^2 \mathbf{u}}{\partial t^2} \quad \text{in } \Omega_0, \quad (3.97)$$

where Div is the material divergence operator, ρ is the material density, $\mathbf{u}(\mathbf{X}) = \boldsymbol{\varphi}(\mathbf{X}) - \mathbf{X}$ is the displacement vector, $G(t) = g - a \cos(\omega t)$ is the time-dependent gravitational acceleration in the moving framework.

The nonlinear elastic problem is complemented by the following boundary conditions:

$$\left\{ \begin{array}{ll} \mathbf{u} \cdot \mathbf{E}_X = (\lambda_x - 1) X, \quad \mathbf{u} \cdot \mathbf{E}_Y = 0 & \text{for } Y = 0 \\ \mathbf{P}^T \mathbf{E}_Y = \gamma \mathcal{K} \mathbf{F}^{-T} \mathbf{E}_Y & \text{for } Y = H \\ \mathbf{E}_Y \cdot \mathbf{P}^T \mathbf{E}_X = 0 & \text{for } X = 0, X = L \\ \mathbf{u} \cdot \mathbf{E}_X = 0 & \text{for } X = 0 \\ \mathbf{u} \cdot \mathbf{E}_X = (\lambda_x - 1) L & \text{for } X = L, \end{array} \right. \quad (3.98)$$

where λ_x is the applied horizontal stretch at the side boundaries $X = 0$ and $X = L$, γ is the surface tension at the free boundary $Y = H$ and \mathcal{K} is the oriented curvature of the free surface due to the Young-Laplace law [33]. The homogeneous deformation field \mathbf{u}_0 solving

the boundary value problem Eqs. (3.97) - (3.98) is given by

$$\mathbf{u}_0 = \boldsymbol{\varphi}_0(\mathbf{X}) - \mathbf{X} = \begin{cases} u_x = (\lambda_x - 1)X \\ u_y = \left(\frac{1}{\lambda_x} - 1\right)Y \end{cases}. \quad (3.99)$$

This basic solution maps the ground state with the geometrical deformation tensor \mathbf{F}_0 given by

$$\mathbf{F}_0 = \begin{bmatrix} \lambda_x & 0 \\ 0 & \frac{1}{\lambda_x} \end{bmatrix}. \quad (3.100)$$

From Eq. (3.97) and the second boundary condition in Eq. (3.98), with $\mathcal{K}_0 = 0$ due to the imposed deformation field \mathbf{F}_0 in Eq. (3.100), the expression of the Lagrange multiplier p_0 in the ground state is given by

$$p_0(X, Y, t) = \frac{\mu}{\lambda_x^2} + \frac{\rho}{\lambda_x} (a \cos(\omega t) + g)(Y - H), \quad (3.101)$$

so that the body is subjected to a hydrostatic pressure linearly dependent on Y and periodically oscillating over the time t .

3.3.3 INCREMENTAL EQUATIONS

In order to investigate the stability of such a homogeneous deformation, the theory of incremental deformations superposed on finite strains will be used [243]. Let us superpose an infinitesimal displacement $\delta\mathbf{u}$ over the finite strain mapping the homogeneous ground state $\mathbf{x} = \boldsymbol{\varphi}_0(\mathbf{X})$, as follows

$$\bar{\mathbf{x}} = \mathbf{x} + \delta\mathbf{u} = \boldsymbol{\varphi}_0(\mathbf{X}) + \boldsymbol{\varphi}^1(\mathbf{x}), \quad (3.102)$$

where $\bar{\mathbf{x}}$ is the perturbed position vector and $\boldsymbol{\varphi}^1(\mathbf{x}) : \Omega \rightarrow \Omega'$ is the incremental mapping that takes the finitely deformed position vector \mathbf{x} into the perturbed configuration Ω' . Let

$\Gamma = \text{grad } \varphi^1(\mathbf{x}) = \frac{\partial \varphi^1(\mathbf{x})}{\partial \mathbf{x}}$ be the spatial displacement gradient associated to the incremental deformation. Hence, we can define the perturbed deformation gradient

$$\bar{\mathbf{F}} = \mathbf{F}_0 + \delta\mathbf{F} = \mathbf{F}_0 + \Gamma\mathbf{F}_0, \quad (3.103)$$

where $\delta\mathbf{F}$ is the increment of the basic deformation gradient \mathbf{F} . The perturbed Nominal stress tensor is given by

$$\bar{\mathbf{P}} = \mathbf{P}_0 + \delta\mathbf{P}_0, \quad (3.104)$$

where $\mathbf{P}_0 = \mathbf{P}(F_0, p_0)$ is the stress tensor in the ground state given in Eq. (3.96) and $\delta\mathbf{P}_0$ is its increment. In particular, we can compute the push-forward of the increment $\delta\mathbf{P}_0$, such as

$$\delta\mathbf{P} = \mathbf{F}_0 \delta\mathbf{P}_0 = \mathcal{A}_0 : \Gamma + p_0 \delta\mathbf{F}_0 - \delta p \mathbf{l},$$

where, using [91],

$$(\mathcal{A}_0)_{jikl} = \mu \mathbf{B}_{jk} \delta_{il}$$

is the forth-order tensor of the instantaneous elastic moduli, $\mathbf{B} = \mathbf{F}_0 \mathbf{F}_0^T$ the left Cauchy-Green tensor, δ_{il} is the Kronecher-delta, the operator $(:)$ denotes the double contraction of the indices, *i.e.* $(\mathcal{A}_0 : \Gamma)_{ij} = (\mathcal{A}_0)_{ijhk} \Gamma_{kh}$, \mathbf{l} is the identity tensor and δp is the increment of the Lagrangian multiplier.

With respect with the finitely deformed coordinates $x = \lambda_x X$ and $y = Y/\lambda_x$, the incremental equilibrium equations and the incremental incompressibility constraint read, respectively,

$$\begin{cases} \text{div } \delta\mathbf{P} = \rho \frac{\partial^2 \delta \mathbf{u}}{\partial t^2} & \text{in } \Omega \\ \text{tr } \Gamma = 0 & \text{in } \Omega. \end{cases} \quad (3.105)$$

$$(3.106)$$

Using $\mathcal{K}_0 = 0$, the incremental boundary conditions read

$$\left\{ \begin{array}{ll} \delta \mathbf{u} = \mathbf{0} & \text{for } y = 0 \end{array} \right. \quad (3.107)$$

$$\left\{ \begin{array}{ll} \delta \mathbf{P}^T \mathbf{E}_Y = \gamma \delta \mathcal{K} \mathbf{E}_Y & \text{for } y = H/\lambda_x \end{array} \right. \quad (3.108)$$

$$\left\{ \begin{array}{ll} \mathbf{E}_y \cdot \delta \mathbf{P}^T \mathbf{E}_x = 0 & \text{for } x = 0, x = \lambda_x L \end{array} \right. \quad (3.109)$$

$$\left\{ \begin{array}{ll} \delta \mathbf{u} \cdot \mathbf{E}_x = 0 & \text{for } x = 0, x = \lambda_x L, \end{array} \right. \quad (3.110)$$

where the expression of the incremental curvature can be obtained by a standard variational argument following [8] and it is given by

$$\delta \mathcal{K} = \frac{1}{\lambda_x^3} \frac{\partial^2 u_y}{\partial x^2}$$

Since the effective gravitational acceleration is a periodic function, the solutions to the boundary value problem given by Eqs. (3.105) - (3.108) are assumed to be of the Floquet form. By imposing the incompressibility constraint, *i.e.* $\text{tr} \Gamma = 0$, we can introduce a stream function $\psi(x, y, t)$ [80, 90] such that the incremental displacement $\delta \mathbf{u}$ is given by

$$\delta \mathbf{u} = \frac{\partial \psi(x, y, t)}{\partial y} \mathbf{e}_x - \frac{\partial \psi(x, y, t)}{\partial x} \mathbf{e}_y. \quad (3.111)$$

In particular, we make the following ansatz of the Floquet type:

$$\psi(x, y, t) = e^{\eta t} (e^{ikx} + e^{-ikx}) \sum_{n=-\infty}^{+\infty} \psi_{1,n}(y) e^{in\omega t}, \quad (3.112)$$

where k is the horizontal spatial wavenumber, ω is the frequency of the external oscillation imposed and η is the Floquet exponent equal to

$$\eta = s + i\alpha\omega, \quad (3.113)$$

with $s = s(k)$ and $\alpha = \alpha(k)$ being real and having finite values. Such a functional dependence along the x direction suitably describes both the infinite geometry, where k is assumed to be a continuous variable, and a finite length L , so that $k = 2\pi m/(\lambda_x L)$, with any integer mode m . The mathematical formulation of ψ implies that we are considering a linear superposition of waves with different amplitudes along the y directions, multiple frequencies of ω and the same wavelength along the x -direction.

Since we are interested in the onset of Faraday instability in this system model, we set $s = 0$ and we consider both the subharmonic and the harmonic resonance modes in the following.

3.3.3.1 SUBHARMONIC RESONANCE

In the subharmonic case (*SH*), *i.e.* setting $\alpha = 1/2$, the stream function and the incremental Lagrange multiplier read:

$$\psi(x, y, t) = e^{\frac{i\omega t}{2}} (e^{ikx} + e^{-ikx}) \sum_{n=-\infty}^{+\infty} \Psi_{1,n}(y) e^{in\omega t}, \quad (3.114)$$

$$\delta p(x, y, t) = e^{\frac{i\omega t}{2}} (e^{ikx} + e^{-ikx}) \sum_{n=-\infty}^{+\infty} p_{1,n}^{SH}(y) e^{in\omega t}, \quad (3.115)$$

where the eigenmodes satisfy the reality conditions

$$\Psi_{1,-n} = \Psi_{1,n-1}^*; \quad p_{1,-n}^{SH} = (p_{1,n-1}^{SH})^* \quad \text{SUBHARMONIC (SH)}, \quad (3.116)$$

and the superscript $*$ denotes the complex conjugate. The unknowns of the incremental problem are $p_{1,n}^{SH}$ and the amplitude of the n -wave, *i.e.* $\Psi_{1,n}$. From the first component of

Eq. (3.105), we obtain the expression for $p_{1,n}^{SH}$, such as

$$\begin{aligned}
p_{1,n}^{SH}(y) = & -\frac{i}{4k^3\lambda_x^2} \left(4ak^2\lambda_x^2\rho\Psi_{1,n-1}(y) + 4ak^2\lambda_x^2\rho\Psi_{1,n+1}(y) + 4gk^2\lambda_x^2\rho\Psi_{1,n}(y) \right. \\
& -4k^2\lambda_x^4\mu(\Psi_{1,n}(y))' + 4\lambda_x^2n^2\rho\omega^2(\Psi_{1,n}(y))' + 4\lambda_x^2n\rho\omega^2(\Psi_{1,n}(y))' \\
& \left. + \lambda_x^2\rho\omega^2(\Psi_{1,n}(y))' + 4\mu(\Psi_{1,n}(y))''' \right). \tag{3.117}
\end{aligned}$$

Then, by substituting Eq. (3.117) into the second component of Eq. (3.105), we obtain a fourth-order differential equation given by

$$A_{SH}(\Psi_{1,n})''''(y) + B_{SH}(\Psi_{1,n})''(y) + C_{SH}\Psi_{1,n}(y) = 0, \tag{3.118}$$

where

$$A_{SH} = \frac{\mu}{k^3\lambda_x^2}; \quad B_{SH} = \frac{\rho(2n\omega + \omega)^2}{4k^3} - \frac{(\lambda_x^4 + 1)\mu}{k\lambda_x^2}; \quad C_{SH} = \frac{(4k^2\lambda_x^2\mu - \rho(2n\omega + \omega)^2)}{4k}.$$

The general solutions of Eq. (3.118) is

$$\Psi_{1,n}(y) = S_{1,n} \cosh(Q_n y) + S_{2,n} \sinh(Q_n y) + S_{3,n} \cosh(ky) + S_{4,n} \sinh(ky), \tag{3.119}$$

where

$$Q_n = \frac{\lambda_x}{H} \sqrt{k^2 H^2 \lambda_x^2 - \frac{(1 + 2n)^2 \omega^2 H^2}{4} \frac{\mu}{\rho}}. \tag{3.120}$$

To find the expressions for the constant $S_{i,n}$ with $i = 1, 2, 3, 4$, we have to impose Eq. (3.107) and Eq. (3.108). Accordingly, $S_{i,n}$ with $i = 1, 2, 3$ can be rewritten as a function of

$S_{4,n}$, such as

$$S_{1,n} = -S_{3,n}; \quad S_{2,n} = -\frac{k S_{4,n}}{Q_n}; \quad S_{3,n} = S_{4,n} G_n, \quad (3.121)$$

where

$$G_n = -\frac{k \left(k^2 \sinh\left(\frac{H Q_n}{\lambda_x}\right) - 2k Q_n \sinh\left(\frac{H k}{\lambda_x}\right) + Q_n^2 \sinh\left(\frac{H Q_n}{\lambda_x}\right) \right)}{k^2 Q_n \left(\cosh\left(\frac{H Q_n}{\lambda_x}\right) - 2 \cosh\left(\frac{H k}{\lambda_x}\right) \right) + Q_n^3 \cosh\left(\frac{H Q_n}{\lambda_x}\right)}. \quad (3.122)$$

Finally, from the second component of Eq. (3.108), we get the following recursion relation

$$\zeta_n S_{4,n} = a (\tau_n S_{4,n-1} + \sigma_n S_{4,n+1}), \quad (3.123)$$

where the complete form of $\zeta_n, \tau_n, \sigma_n$ are reported in Appendix B.3.

Following the linear analysis for viscous fluids [198], we can rewrite the recursion rela-

tion Eq. (3.123) into a matrix form, such as

$$\underbrace{\begin{bmatrix} \vdots & \vdots & \vdots & \vdots & \vdots & \vdots \\ \cdots & \zeta_{-2} & 0 & 0 & 0 & \cdots \\ \cdots & 0 & \zeta_{-1} & 0 & 0 & \cdots \\ \cdots & 0 & 0 & \zeta_0 & 0 & \cdots \\ \cdots & 0 & 0 & 0 & \zeta_1 & \cdots \\ \vdots & \vdots & \vdots & \vdots & \vdots & \vdots \end{bmatrix}}_{\mathcal{B}} \begin{bmatrix} \vdots \\ S_{4,-2} \\ S_{4,-1} \\ S_{4,0} \\ S_{4,1} \\ \vdots \end{bmatrix} = a \underbrace{\begin{bmatrix} \vdots & \vdots & \vdots & \vdots & \vdots & \vdots \\ \cdots & 0 & \sigma_{-1} & 0 & 0 & \cdots \\ \cdots & \tau_{-2} & 0 & \sigma_0 & 0 & \cdots \\ \cdots & 0 & \tau_{-1} & 0 & \sigma_1 & \cdots \\ \cdots & 0 & 0 & \tau_0 & 0 & \cdots \\ \vdots & \vdots & \vdots & \vdots & \vdots & \vdots \end{bmatrix}}_{\mathcal{C}} \begin{bmatrix} \vdots \\ S_{4,-2} \\ S_{4,-1} \\ S_{4,0} \\ S_{4,1} \\ \vdots \end{bmatrix}, \quad (3.124)$$

or in a compact way as

$$\mathcal{B}S_{4,n} = a\mathcal{C}S_{4,n}. \quad (3.125)$$

An ordinary eigenvalue problem can be easily constructed from Eq. (3.125) by inverting \mathcal{B} , such as

$$\mathcal{M}^{SH}S_{4,n} = \frac{1}{a}S_{4,n}, \quad (3.126)$$

where $\mathcal{M}^{SH} = \mathcal{B}^{-1}\mathcal{C}$. Thus, the subharmonic resonance condition imposes that an eigenvalue of \mathcal{M}^{SH} be equal the inverse of the forcing amplitude a .

3.3.3.2 HARMONIC RESONANCE

In the harmonic case (H), *i.e.* setting $\alpha = 0$, the stream function and the incremental Lagrange multiplier read:

$$\psi(x, y, t) = (e^{ikx} + e^{-ikx}) \sum_{n=-\infty}^{+\infty} \Phi_{1,n}(y) e^{in\omega t}, \quad (3.127)$$

$$\delta p(x, y, t) = (e^{ikx} + e^{-ikx}) \sum_{n=-\infty}^{+\infty} p_{1,n}^H(y) e^{in\omega t}, \quad (3.128)$$

where the eigenmodes satisfy the harmonic reality conditions

$$\Phi_{1,-n} = \Phi_{1,n}^* \quad p_{1,-n}^H = (p_{1,n}^H)^* \quad \text{HARMONIC (H)}. \quad (3.129)$$

We get a vectorial equation depending on n , which has to be solved at each n with respect to the unknowns $p_{1,n}^H$ and $\Phi_{1,n}$. The expression of $p_{1,n}^H$ is obtained from the first component of Eq. (3.105), *i.e.*

$$\begin{aligned} p_{1,n}^H(y) = & -\frac{i}{k^3 \lambda_x^2} (ak^2 \lambda_x^2 \rho \Phi_{1,n-1}(y) + ak^2 \lambda_x^2 \rho \Phi_{1,n+1}(y) + gk^2 \lambda_x^2 \rho \Phi_{1,n}(y) \\ & -k^2 \lambda_x^4 \mu (\Phi_{1,n}(y))' + \lambda_x^2 n^2 \rho \omega^2 (\Phi_{1,n}(y))' + \mu (\Phi_{1,n}(y))'''). \end{aligned} \quad (3.130)$$

By substituting Eq. (3.130) into the second component of Eq. (3.105), we obtain a fourth-order differential equation

$$A_H (\Phi_{1,n})''''(y) + B_H (\Phi_{1,n})''(y) + C_H \Phi_{1,n}(y) = 0, \quad (3.131)$$

where

$$A_H = \frac{\mu}{k^3 \lambda_x^2}; \quad B_H = \frac{n^2 \rho \omega^2}{k^3} - \frac{\lambda_x^2 \mu}{k} - \frac{\mu}{k \lambda_x^2}; \quad C_H = k \lambda_x^2 \mu - \frac{n^2 \rho \omega^2}{k}.$$

The general integral of Eq. (3.131) is given by

$$\Phi_{1,n}(y) = A_{1,n} \cosh(P_n y) + A_{2,n} \sinh(P_n y) + A_{3,n} \cosh(ky) + A_{4,n} \sinh(ky), \quad (3.132)$$

where

$$P_n = \frac{\lambda_x}{H} \sqrt{k^2 H^2 \lambda_x^2 - n^2 \frac{\omega^2 H^2}{\mu/\rho}}. \quad (3.133)$$

If $\lambda_x = 1$, in Eq. (3.133) the case $n = 0$ simplifies as

$$P_0 = k. \quad (3.134)$$

This means that, for $\lambda_x = 1$ and $n = 0$, k is a root of double multiplicity equal of the characteristic polynomial associated to the differential equation Eq. (3.131). Hence, for $\lambda_x = 1$, the general solution has to be correct and the right one is given by

$$\Phi_{1,n} \Big|_{\lambda_x=1}(y) = \begin{cases} A_{1,0} \cosh(ky) + A_{2,0} \sinh(ky) + A_{3,0} y \cosh(ky) + A_{4,0} y \sinh(ky) & \text{if } n = 0 \\ A_{1,n} \cosh(P_n y) + A_{2,n} \sinh(P_n y) + A_{3,n} \cosh(ky) + A_{4,n} \sinh(ky) & \text{if } n \neq 0 \end{cases}. \quad (3.135)$$

By imposing the boundary conditions Eq. (3.107) and the first component of Eq. (3.108), for $\lambda_x \neq 1$, we can express $A_{i,n}$ with $i = 1, 2, 3$ as a function of $A_{4,n}$, such as

$$A_{1,n} = -A_{3,n}; \quad A_{2,n} = -\frac{k A_{4,n}}{P_n}; \quad A_{3,n} = A_{4,n} J_n; \quad (3.136)$$

where

$$J_n = -\frac{k \left(k^2 \sinh\left(\frac{HP_n}{\lambda_x}\right) - 2kP_n \sinh\left(\frac{Hk}{\lambda_x}\right) + P_n^2 \sinh\left(\frac{HP_n}{\lambda_x}\right) \right)}{k^2 P_n \left(\cosh\left(\frac{HP_n}{\lambda_x}\right) - 2 \cosh\left(\frac{Hk}{\lambda_x}\right) \right) + P_n^3 \cosh\left(\frac{HP_n}{\lambda_x}\right)}. \quad (3.137)$$

In the other case, such as $\lambda_x = 1$, the constants $A_{i,n}$ with $i = 1, 2, 3$ are given by

$$A_{1,n} = \begin{cases} 0 & \text{if } n = 0 \\ -A_{3,n} & \text{if } n \neq 0 \end{cases}; \quad A_{2,n} = \begin{cases} -\frac{A_{3,0}}{P_0} & \text{if } n = 0 \\ -\frac{kA_{4,n}}{P_n} & \text{if } n \neq 0 \end{cases}; \quad A_{3,n} = \begin{cases} J_0 A_{4,0} & \text{if } n = 0 \\ J_n A_{4,n} & \text{if } n \neq 0 \end{cases};$$

where

$$J_n \Big|_{\lambda_x=1} = \begin{cases} \frac{k(-2HkP_0 \sinh(Hk) - 2P_0 \cosh(Hk))}{-k^2 \sinh(HP_0) + 2Hk^2 P_0 \cosh(Hk) + 2kP_0 \sinh(Hk) - P_0^2 \sinh(HP_0)} & \text{if } n = 0 \\ \frac{k \left(k^2 \sinh(HP_n) - 2kP_n \sinh(Hk) + P_n^2 \sinh(HP_n) \right)}{2k^2 P_n \cosh(Hk) - k^2 P_n \cosh(HP_n) + P_n^3 (-\cosh(HP_n))} & \text{if } n \neq 0 \end{cases}. \quad (3.138)$$

Finally, by imposing the second component of Eq. (3.108), we obtain the recursion relation in the harmonic case, such as

$$Z_n A_{4,n} = a (T_n A_{4,n-1} + \Sigma_n A_{4,n+1}) \quad (3.139)$$

where the complete expressions of Z_n , T_n , Σ_n are reported in Appendix B.4. We can rewrite Eq. (3.139) in a compact form, such as

$$\mathcal{D}A_{4,n} = a \mathcal{E}A_{4,n}, \quad (3.140)$$

where

$$\underbrace{\begin{bmatrix} \vdots & \vdots & \vdots & \vdots & \vdots & \vdots & \vdots \\ \cdots & Z_{-2} & 0 & 0 & 0 & 0 & \cdots \\ \cdots & 0 & Z_{-1} & 0 & 0 & 0 & \cdots \\ \cdots & 0 & 0 & Z_0 & 0 & 0 & \cdots \\ \cdots & 0 & 0 & 0 & Z_1 & 0 & \cdots \\ \cdots & 0 & 0 & 0 & 0 & Z_2 & \cdots \\ \vdots & \vdots & \vdots & \vdots & \vdots & \vdots & \vdots \end{bmatrix}}_{\mathcal{D}} \begin{bmatrix} \vdots \\ A_{4,-2} \\ A_{4,-1} \\ A_{4,0} \\ A_{4,1} \\ A_{4,2} \\ \vdots \end{bmatrix} = a \underbrace{\begin{bmatrix} \vdots & \vdots & \vdots & \vdots & \vdots & \vdots & \vdots \\ \cdots & 0 & \Sigma_{-1} & 0 & 0 & 0 & \cdots \\ \cdots & T_{-2} & 0 & \Sigma_0 & 0 & 0 & \cdots \\ \cdots & 0 & T_{-1} & 0 & \Sigma_1 & 0 & \cdots \\ \cdots & 0 & 0 & T_0 & 0 & \Sigma_2 & \cdots \\ \cdots & 0 & 0 & 0 & T_1 & 0 & \cdots \\ \vdots & \vdots & \vdots & \vdots & \vdots & \vdots & \vdots \end{bmatrix}}_{\mathcal{E}} \begin{bmatrix} \vdots \\ A_{4,-2} \\ A_{4,-1} \\ A_{4,0} \\ A_{4,1} \\ A_{4,2} \\ \vdots \end{bmatrix}. \quad (3.141)$$

The ordinary eigenvalue problem can be constructed from Eq. (3.140) by inverting \mathcal{D} , to get

$$\mathcal{M}^H A_{4,n} = \frac{1}{a} A_{4,n}, \quad (3.142)$$

where $\mathcal{M}^H = \mathcal{D}^{-1}\mathcal{E}$. Thus, the harmonic resonance condition imposes that an eigenvalue of \mathcal{M}^H be equal the inverse of the forcing amplitude a .

The results of the marginal stability analysis are collected in the next section.

3.3.4 MARGINAL STABILITY ANALYSIS

In this Section, we first identify the dimensionless parameters governing the nonlinear elastic problem. We later present a numerical procedure to solve robustly the eigenvalue problems in Eqs. (3.126) and (3.142) determining the influence of such parameters on the onset of Faraday instability. We finally perform some asymptotic limits to retrieve some known results for Rayleigh-Taylor instability.

3.3.4.1 DIMENSIONLESS PARAMETERS

Before solving the eigenvalue problems, we have rewritten the nonlinear elastic problem in a dimensionless form. The order parameter of the Faraday instability is the dimensionless quantity $\tilde{a} = \frac{a}{g}$, determining the relative intensity of the imposed gravitational acceleration. Moreover, we set the characteristic length of the system to be the height H of the elastic slab, so that $\tilde{k} = kH$ is taken to be the dimensionless wavenumber of the standing wave. The onset of the instability is characterized by the emergence of a marginally unstable wave with critical mode $\left(\frac{\omega H}{\sqrt{\mu/\rho}}\right)_{\text{cr}}$ when the forcing amplitude reaches a critical threshold \tilde{a}_{cr} . These critical values are controlled by the following dimensionless parameters:

$$\alpha_\omega = \frac{\omega}{\omega_{\text{car}}} = \frac{\omega H}{\sqrt{\mu/\rho}}; \quad \alpha_g = \frac{\rho g H}{\mu}; \quad \alpha_\gamma = \frac{\gamma}{\mu H}. \quad (3.143)$$

The parameter α_ω represents the ratio between the forcing frequency ω and the characteristic frequency $\omega_{\text{car}} = \frac{\sqrt{\mu/\rho}}{H}$ of shear waves inside the elastic material. It can be rewritten as $\alpha_\omega = \tilde{k}(c/c_s)$, where $c = \omega/k$ is the velocity of the standing wave and $c_s = \sqrt{\mu/\rho}$ is the velocity of the shear elastic wave. Since α_ω/\tilde{k} is the ratio of the velocities of the standing and shear waves, we expect a physical range of admissible solutions in the subsonic range, *i.e.* $\alpha_\omega/\tilde{k} < 1$.

The parameter α_g is the ratio between the characteristic value of the gravitational potential energy $\rho g H$ and of the elastic energy μ . Thus, if $\alpha_g \ll 1$ gravity waves are negligible with respect to shear waves, whilst if $\alpha_g = O(1)$ we expect the gravitation effects to be of the same order as the elastic ones.

Finally, α_γ is the ratio between the capillary length $\ell = \gamma/\mu$ and the characteristic height of the slab H . Thus, if $\alpha_\gamma \ll 1$ capillary waves are negligible with respect to shear waves, whilst if $\alpha_\gamma = O(1)$ we expect the surface tension effects to be of the same order as the elastic ones. Accordingly, α_g/α_γ represents the ratio between gravity and capillarity.

In the next section, we discuss the results of the linear stability analysis varying the physical parameters defined in Eq. (3.143) and the pre-stretch parameter λ_x .

3.3.4.2 MARGINAL STABILITY THRESHOLDS

In Eqs. (3.126) and (3.142), the two matrices \mathcal{M}^i with $i = SH, H$ possess infinite entrances. Following [198], we propose a robust numerical procedure for solving these eigenvalue problems considering truncated matrices involving only the first resonant mode, i.e. a 2×2 matrix for the SH mode and a 3×3 one for the H mode.

In particular, we implemented an iterative algorithm using the software Mathematica (Wolfram Inc., version 12), varying the physical parameters $\alpha_g, \alpha_\gamma, \alpha_\omega$ defined in Eq. (3.143), the pre-stretch λ_x , and the wavenumber \tilde{k} . We compute numerically using Arnoldi's method the largest eigenvalue of \mathcal{M}^{SH} in Eq. (3.126) and of \mathcal{M}^H in Eq. (3.142), and we obtain the smallest value of the marginal stability threshold $\tilde{a}(\tilde{k})$. The critical value \tilde{k}_{cr} is selected as the wavenumber corresponding to the smallest value $\tilde{a}_{cr} = \min(\tilde{a}(\tilde{k}))$ computed for all subsonic modes \tilde{k} at fixed physical parameters.

The subsonic regime can be explicitly identified in the limit $\alpha_g \ll 1$ and $\alpha_\gamma \ll 1$, *i.e.* when gravity and capillary effects become negligible with respect to elastic ones. By simple Taylor expansion of the eigenvalues of the truncated matrices \mathcal{M}^i with $i = SH, H$ we find that

the subsonic range is $\alpha_\omega \in [0, \frac{\pi}{2\lambda_x})$ for the H resonant mode, and $\alpha_\omega \in [0, \frac{\pi}{\lambda_x})$ for the SH resonant mode.

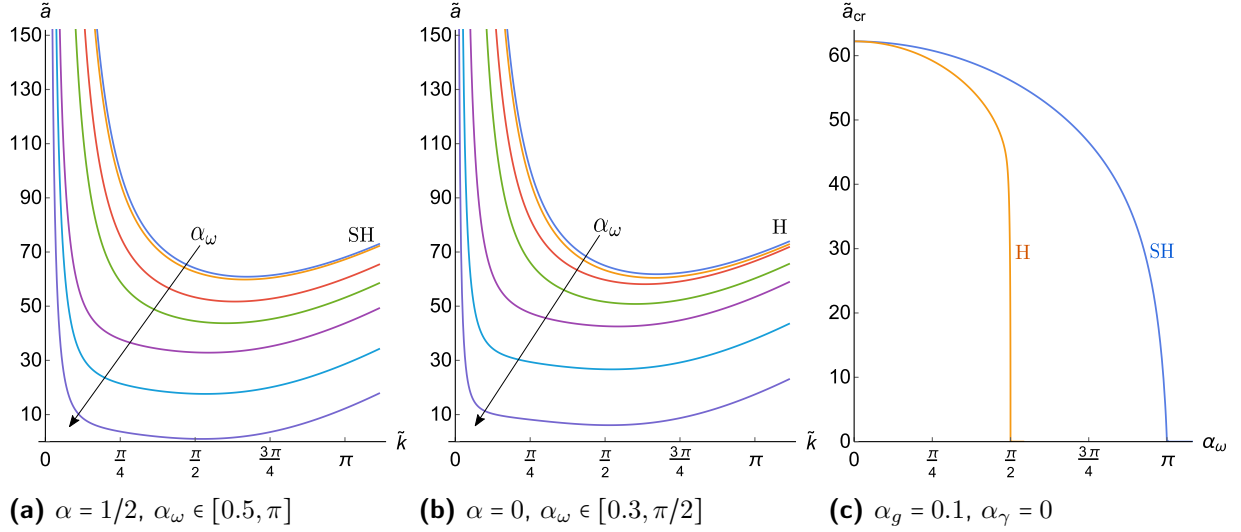


Figure 3.29: Marginal stability curves showing the order parameter \tilde{a} versus the horizontal wavenumber \tilde{k} where we fix $\lambda_x = 1, \alpha_\gamma = 0$ and $\alpha_g = 0.1$. (a) $\alpha = 1/2$ and $\alpha_\omega = \{0.5, 1, 2, 2.5, 3, 3.1, \pi\}$; (b) $\alpha = 0$ and $\alpha_\omega = \{0.3, 0.6, 0.9, 1.3, 1.5, 1.56, \pi/2\}$. (c) Critical threshold \tilde{a}_{cr} versus α_ω fixing $\lambda_x = 1, \alpha_\gamma = 0$ and $\alpha_g = 0.1$: the blue line is the subharmonic case $\alpha = 1/2$ (SH), while the yellow one is the harmonic resonant mode $\alpha = 0$ (H).

In Fig. 3.29a and in Fig. 3.29b, we plot the inverse of the largest eigenvalue \tilde{a} versus the wavenumber \tilde{k} setting $\lambda_x = 1, \alpha_\gamma = 0$ and $\alpha_g = 0.1$ at different values of α_ω in the subsonic regime for subharmonic and harmonic resonance modes, respectively. We notice that the dispersion curves are smooth and admit a minimum value representing the marginal stability threshold \tilde{a}_{cr} at the critical wavenumber \tilde{k}_{cr} . In Fig. 3.29c, fixing $\lambda_x = 1$, we depict the harmonic and subharmonic thresholds when $\alpha_g = 0.1$ and $\alpha_\gamma = 0$ to illustrate that harmonic resonance occurs before the subharmonic one. By these considerations, at fixed values of λ_x, α_g and α_γ , the eigenvalue problem has to be solved until the marginal stability threshold \tilde{a}_{cr} goes to zero.

We found that the first marginally stable eigenmode is the harmonic one for all physical ranges of the dimensionless parameters. This is completely different with respect to what happens in viscous fluids, see [198], where the subharmonic resonance dominates. This is

illustrated in Fig. 3.30a - 3.30b, for $\lambda_x = 1$, $\alpha_\gamma = 0$ and $\alpha_g = 0.001$, showing the critical values \tilde{a}_{cr} and \tilde{k}_{cr} versus the subsonic range of α_ω .

We further notice that both the harmonic and the subharmonic curves collapse on the same one in the limit $\alpha_\omega \ll 1$, suggesting the onset of a different kind of elastic bifurcation, *i.e.* an elastic Rayleigh-Taylor instability [233, 272].

In Figs. 3.30c - 3.30d, we plot the marginal stability threshold \tilde{a}_{cr} and the corresponding critical wavenumber \tilde{k}_{cr} versus α_ω in the critical H case varying α_g at fixed $\lambda_x = 1$ and $\alpha_\gamma = 0$. For graphic clarity, in Fig. 3.30c, we vary $\alpha_g \in [1, 5]$ step 0.5 and we notice that as we increase α_g , as the critical threshold \tilde{a}_{cr} decreased at fixed α_ω , and the physically admissible range of α_ω decreases. As depicted in Fig. 3.30d, the critical wavenumber does not depend on α_g even if the range of α_ω does, so that all the curves collapse on the same one.

Finally, the influence of surface tension is illustrated by the marginal stability curves in Figs. 3.30e - 3.30f. As expected the presence of a surface tension has a regularized effect on the onset of a Faraday instability, since it penalizes any morphological transition creating a non-flat free surface [234, 303]. The physical range of interest for the dimensionless parameter α_γ for soft solids with shear modulus in the range $\mu \in [10, 100]$ Pa made by hydrogels with $\gamma \in [0, 0.05]$ N/m [289] is about $\alpha_\gamma \in [0, 0.2]$. In Figs. 3.30e - 3.30f, we plot the marginal stability threshold \tilde{a}_{cr} and the corresponding critical wavenumber \tilde{k}_{cr} versus α_ω fixing $\lambda_x = 1$, $\alpha_g = 0.001$ and varying $\alpha_\gamma \in [0, 0.2]$ step 0.05. We only depict the first unstable resonant eigenmode that is always the harmonic case. We notice that by increasing α_γ , the critical wavenumber decreases, while the marginal stability threshold for the relative acceleration increases.

In Fig. 3.31, we show the effects of the pre-stretch λ_x on both the critical acceleration \tilde{a}_{cr} and the critical wavenumber \tilde{k}_{cr} as a function of α_ω . We find that the marginally stable Faraday wave is always given by the harmonic eigenmode in the physical range of $\alpha_\omega \in$

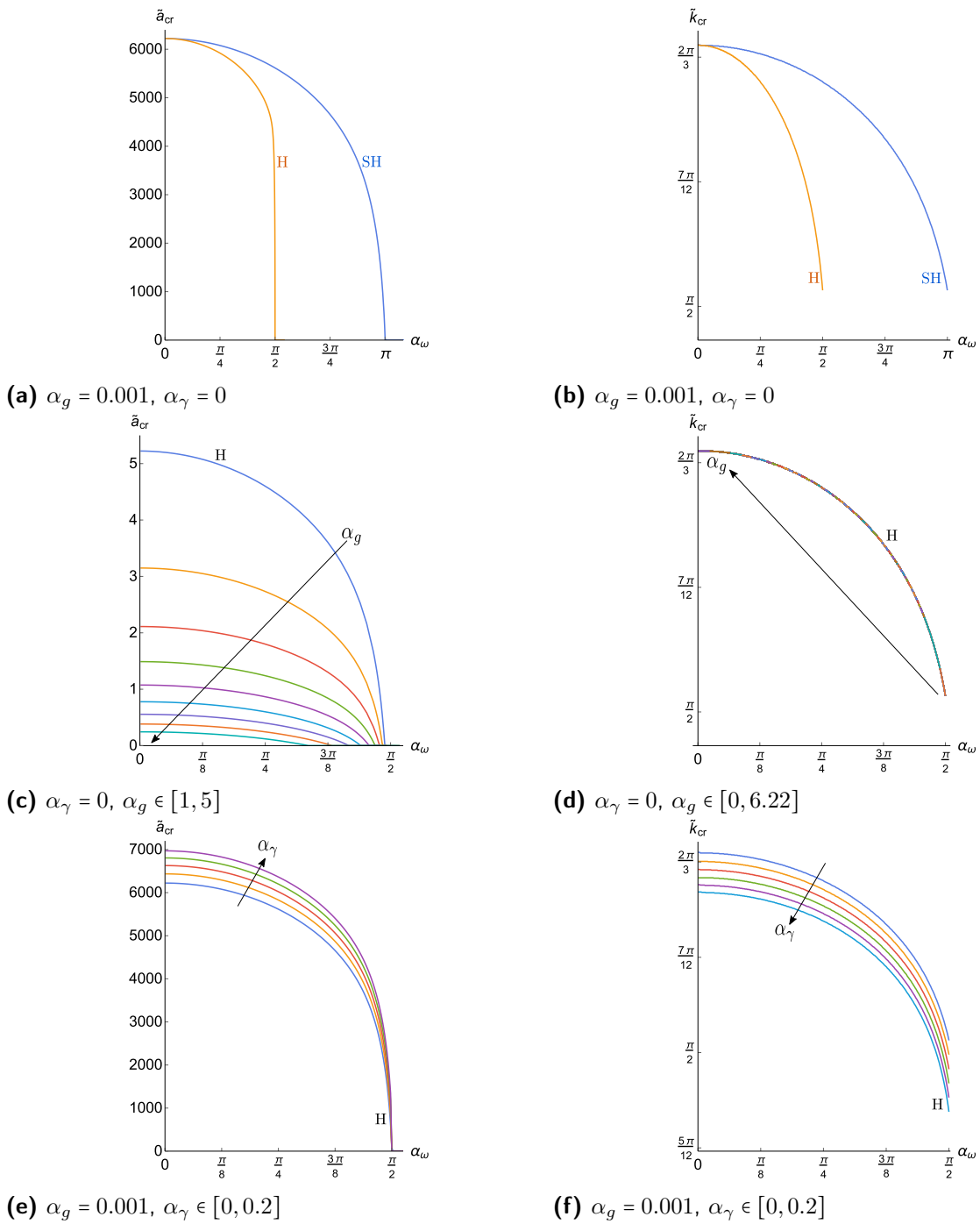
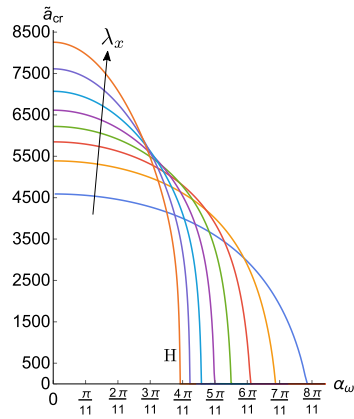
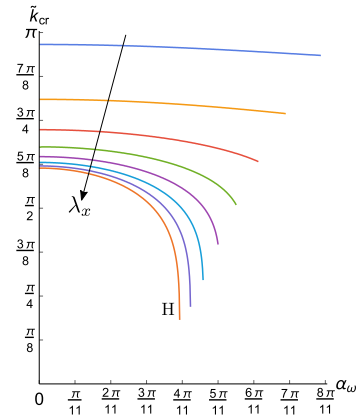


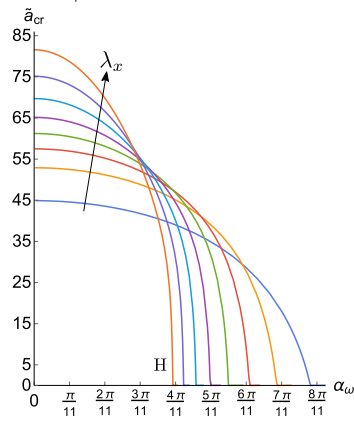
Figure 3.30: Plot of the critical value \tilde{a}_{cr} and the critical wavenumber \tilde{k}_{cr} versus α_ω fixing $\lambda_x = 1$ and varying the physical quantities. (a) - (b) $\alpha_\gamma = 0$ and $\alpha_g = 0.001$, (c) $\alpha = 0, \alpha_\gamma = 0$ and $\alpha_g \in [1, 5]$ step 0.5 for graphical reasons, (d) $\alpha = 0, \alpha_\gamma = 0$ and $\alpha_g \in [0, 6.22]$ step 0.2, (e) - (f) $\alpha = 0, \alpha_g = 0.001$ and $\alpha_\gamma \in [0, 0.2]$ step 0.05. In (a) - (b), the yellow line is the harmonic solution while the blue one is the subharmonic one.



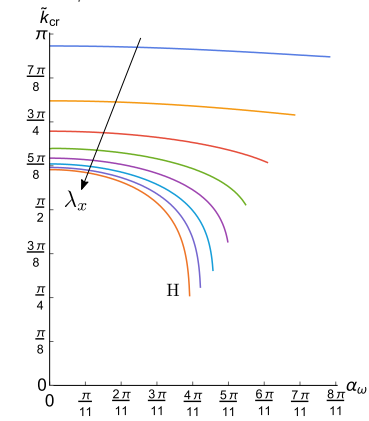
(a) $\alpha_g = 0.001, \alpha_\gamma = 0$



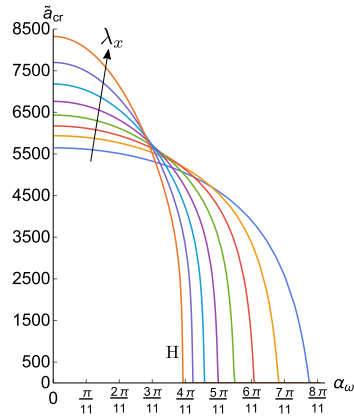
(b) $\alpha_g = 0.001, \alpha_\gamma = 0$



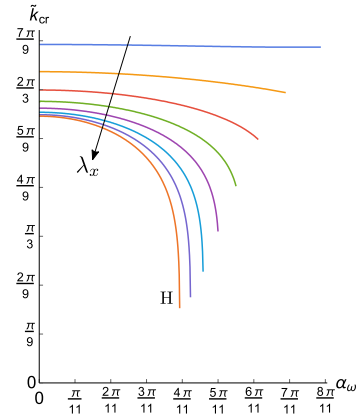
(c) $\alpha_g = 0.1, \alpha_\gamma = 0$



(d) $\alpha_g = 0.1, \alpha_\gamma = 0$



(e) $\alpha_g = 0.001, \alpha_\gamma = 0.05$



(f) $\alpha_g = 0.001, \alpha_\gamma = 0.05$

Figure 3.31: Plot of the critical values \tilde{a}_{cr} and the critical wavenumber \tilde{k}_{cr} versus α_ω fixing the first unstable resonant mode, i.e. $\alpha = 0$ and varying $\lambda_x \in [0.7, 1.4]$ step 0.1. (a) - (b) $\alpha_g = 0.001, \alpha_\gamma = 0$, (c) - (d) $\alpha_g = 0.1, \alpha_\gamma = 0$, (e) - (f) $\alpha_g = 0.001, \alpha_\gamma = 0.05$

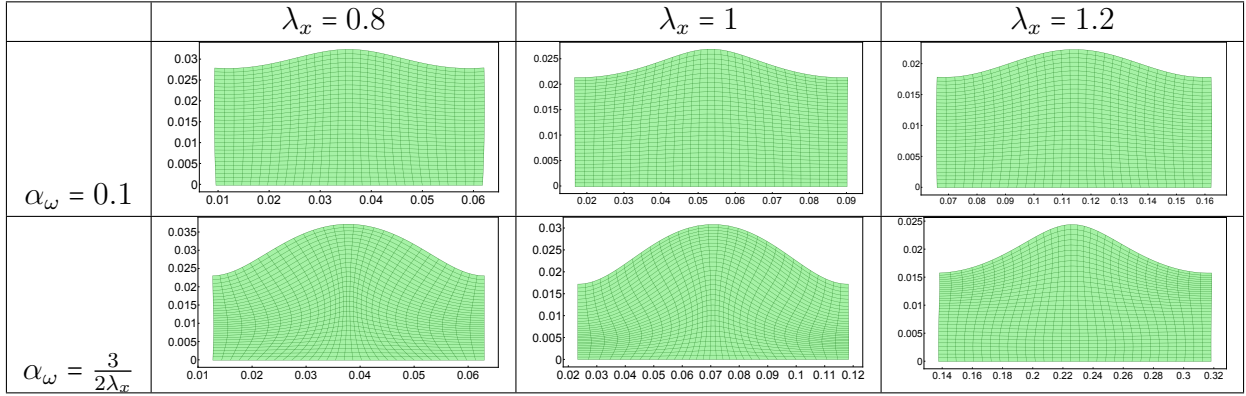


Table 3.2: Solutions of the linearised incremental problem at $\alpha_\gamma = 0$ and different λ_x where we fix $\alpha_g = 1$ and $\alpha_\omega = 0.1$ (top) and $\alpha_\omega = 3/(2\lambda_x)$ (bottom). The amplitude of the incremental displacement $A_{4,n}$ has been set equal to $0.05H$ for the sake of graphical clarity.

$[0, \pi/(2\lambda_x)]$. We consider a range of $\lambda_x \in [0.6, 1.5]$ that excludes the possibility of a surface (or Biot) instability in compression [55]. Comparing with Fig. 3.30a, where $\lambda_x = 1$, from Fig. 3.31a, we immediately notice that a compressive pre-stretch favours the onset of a Faraday instability, whilst a tensile pre-stretch has a stabilising effect. We further remark, by comparing Fig. 3.30b with Fig. 3.31b, that the critical wavenumber increases in compression and decreases in traction. Comparing Fig. 3.31a with Fig. 3.31e and Fig. 3.31b with Fig. 3.31f, we remark that an increase of the surface tension results into a decrease of the critical wavenumber while the marginal stability threshold \tilde{a}_{cr} increases.

Moreover, we consider $\alpha_g = 0.1$ and $\alpha_\gamma = 0$ in Figs. 3.31c - 3.31d. Compared to the results in Fig. 3.31a, we confirm that increasing α_g favours the onset of a Faraday instability.

Finally, we study the morphology of the emerging Faraday wave by computing the incremental displacement $\delta\mathbf{u}_x$ and $\delta\mathbf{u}_y$ defined in Eq. (3.111), where we substitute the expressions of $\Phi_{1,n}$ defined in Eq. (3.132) if $\lambda_x \neq 1$ and Eq. (3.135) if $\lambda_x = 1$ superposing the harmonic modes $n = 0, -1, 1, 2, -2, 3, -3$. We collect in Table 3.2 the resulting displacement fields over one critical wavelength of the eigenmode within the elastic slab. We depict the critical morphology for three different values of the pre-stretch parameter λ_x : one in com-

pression at $\lambda_x = 0.8$, one without pre-stretch at $\lambda_x = 1$ and one in extension at $\lambda_x = 1.2$. We fix $\alpha_g = 1$ and $\alpha_\gamma = 0$ and we consider two different values of α_ω .

3.3.4.3 ASYMPTOTIC LIMIT OF RAYLEIGH-TAYLOR INSTABILITY

In this section we give a few analytic results of the asymptotic behavior of the marginal stability curves for $\alpha_\omega \ll 1$, *i.e.* in the limit when the driving frequency of the oscillation is small and the imposed acceleration can induce a Rayleigh-Taylor instability.

(A1) If $\lambda_x = 1$ and $a = 0$, an elastic bifurcation occurs for $\alpha_g \simeq 6.22$ and $\tilde{k}_{\text{cr}} \simeq 2.11$.

Setting $\lambda_x = 1$ and $a = 0$, the undeformed elastic slab does not oscillate. Hence, the right-hand side terms in Eqs. (3.125) and (3.140) vanish. Thus, the dispersion relations simplify as the vanishing of the determinant of the matrix \mathcal{B} and the matrix \mathcal{D} . Performing a series expansion around $\alpha_\omega = 0$, both expression read at the leading order:

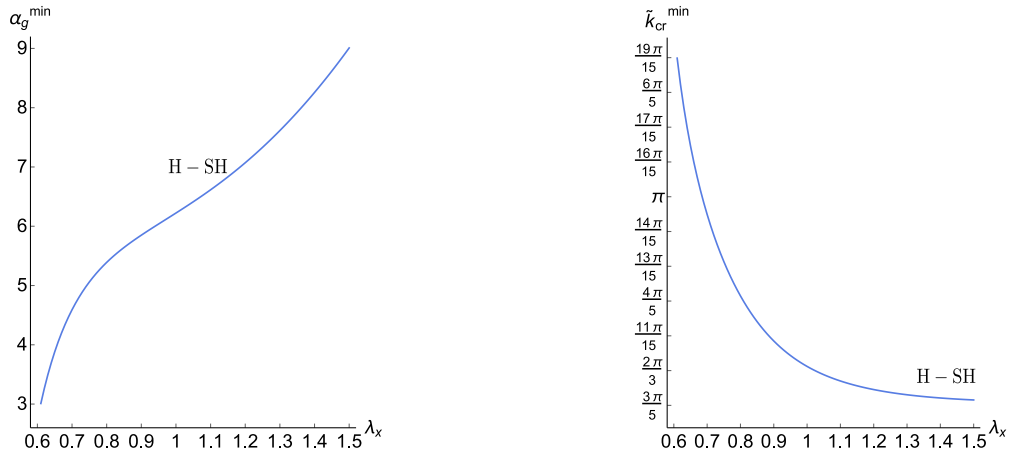
$$\alpha_g = \frac{2\tilde{k} (2\tilde{k}^2 + \cosh(2\tilde{k}) + 1)}{\sinh(2\tilde{k}) - 2\tilde{k}}, \quad (3.144)$$

which is the same expression reported in [233]. Eq. (3.144) has a minimum for $(\alpha_g)_{\text{min}} \simeq 6.22$ and the corresponding minimum wavenumber is $(\tilde{k})^{\text{min}} \simeq 2.11$, which is the known threshold for an elastic Rayleigh-Taylor instability.

If $\lambda_x \neq 1$, the dispersion relation reads

$$\alpha_g = \frac{\tilde{k} \left(-(\lambda_x^8 + 6\lambda_x^4 + 1) \sinh\left(\frac{\tilde{k}}{\lambda_x}\right) \sinh(\tilde{k}\lambda_x) + (\lambda_x^8 + 2\lambda_x^4 + 5) \lambda_x^2 \cosh\left(\frac{\tilde{k}}{\lambda_x}\right) \cosh(\tilde{k}\lambda_x) - 4(\lambda_x^6 + \lambda_x^2) \right)}{\lambda_x^2 (\lambda_x^4 - 1) \left(\lambda_x^2 \sinh\left(\frac{\tilde{k}}{\lambda_x}\right) \cosh(\tilde{k}\lambda_x) - \sinh(\tilde{k}\lambda_x) \cosh\left(\frac{\tilde{k}}{\lambda_x}\right) \right)}. \quad (3.145)$$

In Fig. 3.32, we plot the marginal stability threshold $(\alpha_g)^{\text{min}}$ and $(\tilde{k}_{\text{cr}})^{\text{min}}$ from Eq. (3.145) versus the applied pre-stretch λ_x .



(a) $a = 0, \alpha_\omega \ll 1$

(b) $a = 0, \alpha_\omega \ll 1$

Figure 3.32: Plot of the (a) critical values $(\alpha_g)^{\min}$ and (b) $(\tilde{k}_{\text{cr}})^{\min}$ versus λ_x in the limit of $\alpha_\omega \ll 1$ fixing $a = 0$ and $\alpha_\gamma = 0$.

(A2) If $\lambda_x = 1$ and $a \neq 0$, an elastic bifurcation occurs if the following relation holds

$$\tilde{a}_{\text{cr}} = \frac{6.22}{\alpha_g} - 1. \quad (3.146)$$

This asymptotic limit corresponds to a Rayleigh-Taylor instability corresponding to a maximum effective acceleration given by $G = (g + a)$. We obtain Eq. (3.146) by performing a series expansion of the matrices \mathcal{M}^i with $i = SH, H$ around $\alpha_\omega = 0$ and by computing the corresponding eigenvalues. The critical value \tilde{a}_{cr} given by Eq. (3.146) is physically relevant only if $\alpha_g < 6.22$. By imposing that, this threshold is an extremal point with respect to variations of the wavenumber. We also find that the expression of the critical wavenumber \tilde{k}_{cr} is independent on α_g .

3.3.5 CONCLUSIONS

This section has investigated the onset of Faraday instability in a pre-stretched elastic slab whose lateral sides are free to slide, that is attached at the bottom to a rigid substrate and subjected to a vertical oscillation with a forcing frequency ω and amplitude a . The soft

solid is assumed to behave as an incompressible hyperelastic material of the neo-Hookean type. We have used the Floquet theory to study the onset of harmonic and subharmonic resonance eigenmodes from the ground state corresponding to a finite homogeneous deformation of the elastic slab. The incremental boundary value problem is characterized by the three dimensionless parameters defined in Eq. (3.143), that characterize the interplay of gravity, capillary and elastic waves. Remarkably, we found that Faraday instability in soft solids is characterized by a harmonic resonance in the physical range of the material parameters, in contrast to the subharmonic resonance that is known to characterize viscous fluids and shearing motions in nonlinear elastodynamics [81, 258]. The dominance of harmonic modes was earlier observed in viscoelastic fluids [319, 240], but it first proved here for nonlinear elastic solids. Moreover, the critical threshold for the relative acceleration decreases by increasing the parameter α_g , demonstrating that gravity waves can favour the instability when their potential energy is of the same order as the elastic strain energy. On the contrary, the presence of surface tension has a stabilizing effect by introducing an energy penalty to the emergence of standing waves at the free boundary. Interestingly, both harmonic and subharmonic eigenmodes become simultaneously unstable in the limit of small driving frequency, highlighting the transition towards an elastic bifurcation of the Rayleigh-Taylor type. Precisely, this phenomenon, together with the stabilizing effect of the surface tension have been recovered by some experiments on agarose gel [288]. Since the material is very soft, it can be excited just by using lower frequency, *i.e.* $\omega \in (0, 30)$ Hz, causing that the visualized resonant eigenmode is the subharmonic one. Moreover, the typical effect of the surface tension, *i.e.* it penalizes any morphological transition creating a non-flat free surface, is also obtained from the experimental results. Indeed, the critical acceleration \tilde{a}_{cr} decreases with decreasing α_γ , see Fig. 3.30e and Fig. 5 of [288]. Noteworthy, we found that the application of a finite pre-stretch can alter significantly the marginal stability curves and the morphology of the emerging standing waves.

In particular, a compressive pre-stretch favors the onset of Faraday instability with shorter critical wavelength. This novel result suggests a new path for the experimental characterization of soft materials using Faraday waves. The application of a wide range of controlled pre-stretch indeed allows to measure the corresponding dispersion relations of the standing waves, thus inferring the mechanical parameters of the soft matter. Since Faraday waves are found to be controlled by radically different resonance modes for viscous liquids and elastic matter, this precise and robust experimental method may be suitable to distinguish solid-like from fluid-like responses of soft matter at different scales.

Further analysis will be focused on extending the proposed analysis to study pattern formation in a 3D experimental setting, considering the weakly nonlinear interactions of linear eigenmodes traveling in different directions.

3.4 POROUS MEDIA MODEL OF TISSUE GROWTH: ANALYTICAL ESTIMATES IN THE FREE BOUNDARY LIMIT

In the last few decades, the study of cancer development improve due to new analytical tools and due to the introduction of new numerical methods [36, 142, 37, 216, 118, 35]. The main difficulty in studying these phenomena is the vast biological complexity related to the presence of different kinds of inter-specifically and intra-specifically interacting cells. Describing the tumor at the macroscopic level, we can distinguish two categories. On the one hand, we can devise partial differential equations (PDEs) of type , used primarily to model tumor growth [166, 70, 269, 256, 63, 93], in which cells are represented by densities. On the other hand, tissue growth can be described by devising a free boundary model [165, 105, 143], where tissue growth is due to the motion of its boundary. Each of these approaches have their advantages: the first approach, also called mechanical models, is widely studied with many numerical and analytical tools. Regarding the second

approach, it is closer to the biological vision of the tissue and allows to study its motion and dynamics. There is a well-developed technique to establish a link between the two approaches, the so-called incompressible limit, which implies that the pressure becomes stiff [250, 251, 176, 227, 65, 86, 208, 194].

3.4.1 THE ARONSON-BÉNILAN ESTIMATE AND REGULARITY THEORY OF THE PME

The Aronson-Bénilan estimate is fundamental in proving and obtaining much more regularity in the PME. Indeed, in [72], the authors prove that the unique generalised solution to the porous medium equation in two (or more) dimension, a result due to [282], is continuous. Moreover, they give an explicit expression for the modulus of continuity in space and time, *cf.* [72, Theorem 1.1], thus extending the known one-dimensional result on the Hölder-regularity in space by Aronson, *cf.* [16, Theorem, p.465]. It is important to stress that the regularity theory of Caffarelli and Friedman heavily relies on the AB-estimate. On the one hand, it allows them, in some sense, to quantify how the density at the centre of small balls changes in small time instance, *cf.* [72, Lemmas 2.2 & 2.3], and derive an explicit modulus of continuity for the multi-dimensional porous medium equation. On the other hand, it allows them to study the regularity of the free boundary in any dimension, *cf.* [74], generalising the one-dimensional results of [18, 73]. In doing so, they need to quantify how fast the density begins to intrude a previously unoccupied domain, *cf.* [74, Lemma 2.1], which uses the multi-dimensional AB-estimate. One of the key findings in their paper is the Hölder-regularity of the free boundary, $t = f(x)$, which allows them to improve the modulus of continuity solutions which are established to be Hölder-continuous, too, [72, Section 4]. Eight years later, in [75], the authors prove that the free boundary is in fact Lipschitz continuous for all times larger than the first time that the solution contains a ball which includes the initial data. For smaller time instance, however, Hölder regularity is optimal due to so-called focusing phenomena, [20, 13, 75]. The focusing problem is

dedicated to understanding how areas of vacuum in the initial data are filled by the evolution of the porous medium equation. While solutions are Hölder continuous, the pressure gradient can blow up in time, *cf.* [20].

A hard problem is to perform a linear limit of the PME, to recover the heat equation. Indeed, the mentioned Hölder regularity for the solution of the PME cannot be obtained. Only in recent works [149, 150], the authors prove that given an initial data with low regularity, the solution is L^p in time and belongs to a fractional Sobolev space in \mathbb{R}^d with $d > 1$. Moreover, using the Barenblatt solution, the authors prove that this result is the optimal one.

3.4.2 POPULATION-BASED DESCRIPTION OF TISSUE GROWTH

The simplest way to model tumor growth is introducing a single equation describing the evolution of the abnormal cell density, $n(x, t)$, where $x \in \mathbb{R}^d$ and $t \in \mathbb{R}^+$ which evolves under pressure forces and cell multiplication according to the equation [69, 250]

$$\frac{\partial n}{\partial t} - \operatorname{div}(n \nabla p) = nG(p), \quad (3.147)$$

where $p = p(n)$ is the pressure field and $G := G(p)$ models the proliferation of cells and it is called growth function. Suitable assumptions have to be imposed on G , for instance

$$G'(p) < 0, \quad \text{and} \quad G(p_M) = 0, \quad (3.148)$$

which imply that the increasing number of the cells is limited by the pressure p and $p_M > 0$ is called the *homeostatic pressure* [69]. Concerning the pressure, in many papers [250, 251, 176, 65, 208, 194], there is an explicit and assigned relation between p and n . In the

following, to be as general as possible, we only assume that

$$p = p(n), \quad p(0) = 0, \quad p'(n) > 0, \quad (3.149)$$

for $n > 0$. We have two examples in mind, the classical Power-law case, where

$$p(n) = n^\gamma, \quad (3.150)$$

see [249, 65, 110] and the pressure used in [116] (called DHV throughout) where

$$p(n) = \varepsilon \frac{n}{1-n}, \quad (3.151)$$

cf. [116]. For a general pressure law, the quantity p satisfies the evolution equation given by

$$\partial_t p = |\nabla p|^2 + qw, \quad (3.152)$$

where

$$q(p) := np'(n), \quad \text{and} \quad w := \Delta p + G(p). \quad (3.153)$$

The aforementioned examples give

$$q(p) = \gamma p \quad (\text{polytropic law}), \quad \text{and} \quad q(p) = p \left(1 + \frac{p}{\varepsilon} \right) \quad (\text{DHV law}).$$

They differ deeply near $p = 0$ in their behaviors as $\varepsilon \rightarrow 0$ and $\gamma \rightarrow \infty$ and this is a major issue if one wants to study these limits and establish the Hele-Shaw free boundary problem.

For $G \equiv 0$, Aronson and Bénilan build their estimate on the observation that one can

obtain an equation for w [19]. Their argument can be extended to include G and leads to the equation

$$\partial_t w = 2 \sum_{i,j=1}^N (\partial_{ij}^2 p)^2 + 2 \nabla p \cdot \nabla w - G'(p) |\nabla p|^2 + \Delta(qw) + G'(p)qw.$$

Because

$$2 \sum_{i,j=1}^N (\partial_{ij}^2 p)^2 \geq \frac{2}{N} (\Delta p)^2 = \frac{2}{N} (w - G)^2,$$

and since we assume $G' \leq 0$, *i.e.* Eq. (3.148), we may also write

$$\partial_t w \geq \frac{2}{N} w^2 + 2 \nabla p \cdot \nabla w + \Delta(qw) + \left[G'(p)q - \frac{4}{N}G \right] w. \quad (3.154)$$

This inequality, which is self-contained when $G \equiv 0$, is the very basis of estimates on $|w|_- = \max(0, -w)$ which we analyze in different L^p spaces.

3.4.2.1 FREE BOUNDARY-BASED DESCRIPTION OF TISSUE GROWTH

Besides its huge impact on the regularity theory of solutions to the porous medium equation and the free boundaries thereof, the AB-estimate proves to be a crucial tool for building a bridge between a density-based description and a geometric description of tissue growth. The link between the two models is established through a rigorous study of the *incompressible limit* of the porous medium pressure equation, *cf.* Eq. (3.152), as the pressure law becomes stiffer and stiffer, *i.e.*, $\gamma \rightarrow \infty$ or $\varepsilon \rightarrow 0$, in the respective pressure law (Eqs. (3.150), (3.151)). As a result an incompressible model is obtained, satisfying two relations. The first, $p(n-1) = 0$, implies the absence of any pressure in zones that are not saturated ($\{n < 1\}$), while the second one, also referred to as *complementarity relation*,

yields an equation satisfied by the pressure on $\{p > 0\}$, which is of the form

$$p(\Delta p + G(p)) = 0.$$

It is immediately apparent that strong regularity is needed to obtain such an expression, which is provided by (adaptations) of the AB-estimate — bounds on the Laplacian of the pressure are enough to infer strong compactness of the pressure gradient. This was first observed in [250] to be equivalent to being able to pass to the limit in the porous medium pressure equation and obtain the incompressible limit.

3.4.3 EXTENSION TO TWO SPECIES

Let us highlight that the mathematical theory of the limit for equations like Eq. (3.147) is well studied both with $G \neq 0$, *cf.* [250, 116, 194], and without G , *cf.* [40, 152, 153], as well as in the case where nutrients and viscosity are included, *cf.* [251, 115, 114, 110]. The limit model turns out to be a free boundary model of Hele-Shaw type. The model of a single evolution equation, which describes the tumor cell distribution, can be complemented by another species consisting of healthy tissue, and it is given by

$$\frac{\partial n^{(i)}}{\partial t} - \operatorname{div}(n^{(i)} \nabla p) = n^{(1)} F^{(i)}(p) + n^{(2)} G^{(i)}(p), \quad (3.155)$$

where $i = 1, 2$, $n^{(1)}, n^{(2)}$ denote the population densities and $G^{(i)}, F^{(i)}$ model the reaction or growth phenomena, which are assumed to depend exclusively on the pressure according to experimental observations [69, 264]. The system structure of Eq. (3.155) causes serious analytical difficulties, *cf.* [79, 169, 65, 257, 128], due to its hyperbolic flavour. The careful study of the pressure equation helps in proving the existence of solutions and obtaining uniform estimates with respect to the stiffness parameter, *i.e.* γ in the classical Power-law

case, $p = n^\gamma$ [249, 227, 169]. Due to the insufficient regularity of the pressure, the incompressible limit can be achieved just in 1D using Sobolev embedding. For the DHV pressure law, *i.e.* assuming that the pressure blows up at a finite threshold, *cf.* [176, 86, 116], similar mathematical difficulties arise: in order to pass to the limit, strong restrictions have to be imposed.

While the incompressible limit for multiple species remains an interesting open problem for the Darcy law, including viscosity of cells in the model changes the analytical properties of the model drastically and recently. In case of the so-called *Brinkmans law* [3], the model reads

$$\begin{cases} \frac{\partial n^{(i)}}{\partial t} - \operatorname{div}(n^{(i)} \nabla W) = n^{(1)} F^{(i)}(p) + n^{(2)} G^{(i)}(p) \\ -\nu \Delta W + W = p, \end{cases} \quad (3.156)$$

where $i = 1, 2$ and ν is the viscosity parameter. On the one hand, the idea to couple the two equations for the individual species through Brinkmans law changes the behavior dramatically as mentioned before, *i.e.* classical techniques used in the one-specie model fail [251], but on the other hand the pressure field gains regularity and some mathematical difficulties can be overcome. Recently, two results have been obtained in this direction: in [115], the authors are able to establish the incompressible limit in the one dimensional case by establishing uniform BV-bounds for the two species; then in [114], since the BV-strategy fails in higher dimensions, by employing a non-local compactness criterion [188], the passage to the incompressible limit can be accomplished.

3.4.4 L^1 -TYPE ESTIMATE

The form of Eq. (3.154) is well adapted to perform L^1 -estimates of the second-order quantity w because it generates, thanks to the Kato inequality, the following inequality

$$\partial_t |w|_- \leq -\frac{2}{N} |w|_-^2 + 2\nabla p \cdot \nabla |w|_- + \Delta(q|w|_-) + \left[G'(p)q - \frac{4}{N}G \right] |w|_-. \quad (3.157)$$

It turns out that further manipulations lead to restrictions which are more demanding than expected. To explain that, we first treat the case $G \equiv 0$. The extension to the case $G \geq 0$ is stated in the second corresponding subsection.

3.4.4.1 L^1 -ESTIMATES WHEN $G \equiv 0$

When $G \equiv 0$, $w = \Delta p$ and a simple integration of Eq. (3.154) yields,

$$\frac{d}{dt} \int_{\mathbb{R}^N} |w|_- dx \leq 2 \frac{N-1}{N} \int_{\mathbb{R}^N} |w|_-^2 dx.$$

Because of the quadratic growth of the right-hand side, this inequality provides us with an L^1 control only in dimension $N = 1$. We thus adopt a different strategy. By adding a positive weight function, $h = h(p)$, we aim to study whether or not it helps improve the above result. We shall establish the

Theorem 3.4.1 (Case $G \equiv 0$, L^1 -theory). *Assume the pressure law is such that for $p > 0$*

$$\alpha_1(p) := \int_0^p \left[q(\cdot)h'(\cdot) + \frac{1}{N}h(\cdot) \right] d\rho > 0, \quad \text{with} \quad h(p) := \int_0^p e^{\int_0^\rho \frac{1}{q}} d\rho. \quad (3.158)$$

Then, the following a priori estimates hold true

$$\int_{\mathbb{R}^N} h(p) |\Delta p(t)|_- dx + 2 \int_0^t \int_{\mathbb{R}^N} \alpha_1(p(s)) |\Delta p(s)|_-^2 dx ds \leq \int_{\mathbb{R}^N} h(p) |\Delta p(0)|_- dx, \quad (3.159)$$

and for all $t \leq T$

$$\int_{\mathbb{R}^N} h(p) |\Delta p(t)|_- dx \leq \frac{A(T)}{t} \quad \text{with} \quad A = \frac{1}{2} \sup_{0 \leq t \leq T} \int_{\mathbb{R}^N} \frac{h(p)^2}{\alpha_1(p)} dx. \quad (3.160)$$

Estimate (3.159) also holds when $N = 1$ with $h \equiv 1$ and $\alpha_1 \equiv 0$.

Notice that, because $q'(p)p'(n) = p'(n) + np''(n)$, the condition $\alpha_1 > 0$ is satisfied when, for instance, $p(n)$ is a convex function.

However, it turns out that the result of this theorem is rather weak compared of L^∞ -type estimate. Indeed, the calculation forces us to choose $h(0) = 0$, therefore the estimate is weak near the free boundary $\{p = 0\}$. However, for the pressure laws we have introduced before, when γ is large or ε is small, the decay rate scales correctly with γ or ε , and allows for a uniform control of $\partial_t p$. To see this we may give the corresponding expressions of α_1 , h , A , explicitly:

For the Power-law, we have $q(p) = \gamma p$ and

$$h(p) = \frac{\gamma}{\gamma+1} p^{\frac{\gamma+1}{\gamma}}, \quad \alpha_1(p) = \gamma \left[1 - \frac{N-1}{N} \frac{1}{\gamma+1} \right] p^{\frac{\gamma+1}{\gamma}} > 0, \quad \text{and} \quad A = \mathcal{O}(\gamma^{-1}).$$

For the DHV law, the situation is similar and we find

$$h(p) = \varepsilon p - \varepsilon^2 \ln \left(1 + \frac{p}{\varepsilon} \right), \quad \alpha_1(p) = p^2 + \varepsilon \frac{N-1}{N} \left[\varepsilon \ln \left(1 + \frac{p}{\varepsilon} \right) - p \right] > 0, \quad \text{and} \quad A = \mathcal{O}(\varepsilon^2).$$

Proof. Hence, integrating over \mathbb{R}^N , we get

$$\begin{aligned}
\frac{d}{dt} \int_{\mathbb{R}^N} h(p) |w|_- dx &= \int_{\mathbb{R}^N} \left(h'(p) |w|_- \left(\frac{\partial p}{\partial t} \right) + h(p) \left(\frac{\partial |w|_-}{\partial t} \right) \right) dx \\
&\leq \int_{\mathbb{R}^N} h'(p) |\nabla p|^2 |w|_- dx - \int_{\mathbb{R}^N} h'(p) q(p) |w|_-^2 dx - \int_{\mathbb{R}^N} \frac{2h}{N} |w|_-^2 dx \quad (3.161) \\
&\quad + \underbrace{\int_{\mathbb{R}^N} h(p) \Delta(q(p) |w|_-) dx}_{I_1} + 2 \underbrace{\int_{\mathbb{R}^N} h(p) \nabla p \cdot \nabla |w|_- dx}_{I_2}.
\end{aligned}$$

We next estimate separately the integral terms I_1 and I_2 . Beginning with I_1 , integrating by parts twice, we obtain

$$\begin{aligned}
I_1 &= \int_{\mathbb{R}^N} q(p) |w|_- \Delta h(p) dx \\
&= \int_{\mathbb{R}^N} q(p) h''(p) |\nabla p|^2 |w|_- dx - \int_{\mathbb{R}^N} h'(p) q(p) |w|_-^2 dx.
\end{aligned}$$

As for the second term, I_2 , we integrate by parts once, which yields

$$I_2 = -2 \int_{\mathbb{R}^N} h'(p) |\nabla p|^2 |w|_- dx - 2 \int_{\mathbb{R}^N} h(p) |w|_-^2 dx.$$

Substituting the expressions for the two integral terms I_1 and I_2 into Eq. (3.161), we obtain

$$\frac{d}{dt} \int_{\mathbb{R}^N} h(p) |w|_- dx \leq -2 \int_{\mathbb{R}^N} \alpha_1 |w|_-^2 dx + \int_{\mathbb{R}^N} \beta_1 |w|_- |\nabla p|^2 dx, \quad (3.162)$$

where

$$\alpha_1 := h'q - h \left(1 - \frac{1}{N} \right), \quad \text{and} \quad \beta_1 := qh'' - h'. \quad (3.163)$$

In dimension $N = 1$ we can choose $h = 1$, $\alpha_1 = \beta_1 = 0$ which provides us with and L^1 -

estimate of $|\Delta p|_-$ and proves the last statement of Theorem 3.4.1.

In higher dimension, we are unable to do that and we solve $\beta_1(p) = 0$ instead, which gives the expression of h and α_1 in (3.158). Then, integrating Eq. (3.162) in t gives the announced estimate (3.159).

To obtain estimate (3.160), we use the Cauchy-Schwarz inequality to write

$$\left(\int_{\mathbb{R}^N} h|w|_- \right)^2 dx \leq A \int_{\mathbb{R}^N} \alpha_1 |w|_-^2 dx, \quad A := \frac{1}{2} \int_{\mathbb{R}^N} \frac{h^2}{\alpha_1} dx.$$

Substituting this information into Eq. (3.162), we get

$$\frac{d}{dt} \int_{\mathbb{R}^N} h(p) |w|_- dx \leq -A^{-1} \left(\int_{\mathbb{R}^N} h|w|_- dx \right)^2.$$

Since $U(t) = \frac{A}{t}$ is a solution, we conclude that

$$\int_{\mathbb{R}^N} h(p) |w|_- dx \leq A/t,$$

which proves the statement (3.160) and concludes the proof of Theorem 3.4.1. \square

3.4.4.2 L^1 -ESTIMATES WITH $G \neq 0$

With the notations of Theorem 3.4.1, we define

$$\bar{\delta}_1 = \max_{0 \leq p \leq p_M} \left\{ G \left[2 \frac{N-2}{N} - \frac{h'q}{h} \right] + G'q \right\}.$$

Theorem 3.4.2 (Case $G' \leq 0$, L^1 -theory). *With the notations and assumptions of Theorem 3.4.1, $G' \leq 0$ and $\bar{\delta}_1$ as above, the following a priori estimates hold true*

$$\int_{\mathbb{R}^N} h(p) |w(t)|_- dx + \int_0^t e^{\bar{\delta}_1(t-s)} \int_{\mathbb{R}^N} \alpha_1(p) |w|_-^2 dx ds \leq e^{\bar{\delta}_1 t} \int_{\mathbb{R}^N} h(p) |w(0)|_- dx, \quad (3.164)$$

and

$$\int_{\mathbb{R}^N} h(p)|w(t)|_- dx \leq A \frac{\bar{\delta}_1 e^{\bar{\delta}_1 t}}{e^{\bar{\delta}_1 t} - 1}. \quad (3.165)$$

with A as in Eq. (3.160). Estimate (3.164) also holds when $N = 1$ with $h \equiv 1$ and $\alpha_1 \equiv 0$.

Notice that the sign of $\bar{\delta}_1$ does not play a role here.

Proof. Still building on the inequality (3.154) and using a positive weight, $h = h(p)$, the evolution in time of the quantity hw is given by

$$\begin{aligned} \partial_t (h|w|_-) &= h'|w|_- \partial_t p + h \partial_t |w|_- \\ &\leq h'|w|_- (|\nabla p|^2 + qw) \\ &\quad + h \left\{ -\frac{2}{N} |w|_-^2 + 2\nabla p \cdot \nabla |w|_- + \Delta(q|w|_-) + \left[G'(p)q - \frac{4}{N}G \right] |w|_- \right\} \end{aligned}$$

Integrating, we get

$$\begin{aligned} \frac{d}{dt} \int_{\mathbb{R}^N} h|w|_- dx &\leq \int_{\mathbb{R}^N} h'|\nabla p|^2 |w|_- dx - \int_{\mathbb{R}^N} h'q|w|_-^2 dx - \int_{\mathbb{R}^N} \frac{2h}{N} |w|_-^2 dx \\ &\quad + \int_{\mathbb{R}^N} h\Delta(q|w|_-) dx + 2 \int_{\mathbb{R}^N} h\nabla p \cdot \nabla |w|_- dx - \int_{\mathbb{R}^N} \left[\frac{4}{N}G - G'q \right] h |w|_- dx \\ &\leq \int_{\mathbb{R}^N} h'|\nabla p|^2 |w|_- dx - \int_{\mathbb{R}^N} \left[\frac{2h}{N} + h'q \right] |w|_-^2 dx - \int_{\mathbb{R}^N} \left[\frac{4}{N}G - G'q \right] h |w|_- dx \\ &\quad + \underbrace{\int_{\mathbb{R}^N} q|w|_- \Delta h dx}_{I_1} - 2 \underbrace{\int_{\mathbb{R}^N} [\nabla h \cdot \nabla p + h\Delta p] |w|_- dx}_{I_2}. \end{aligned}$$

Integrating by parts twice, the term I_1 can be rewritten as

$$\begin{aligned} I_1 &= \int_{\mathbb{R}^N} [h''|\nabla p|^2 + h'\Delta p] q|w|_- dx \\ &= \int_{\mathbb{R}^N} h''q|\nabla p|^2 |w|_- dx - \int_{\mathbb{R}^N} h'q|w|_-^2 dx - \int_{\mathbb{R}^N} h'qG|w|_- dx. \end{aligned}$$

Next we simplify the term I_2 . Integrating by parts and using the chain rule we obtain

$$I_2 = \int_{\mathbb{R}^N} h' |\nabla p|^2 |w|_- dx - \int_{\mathbb{R}^N} h |w|_-^2 dx - \int_{\mathbb{R}^N} hG |w|_- dx.$$

Substituting I_1 and I_2 back into our main inequality, we get

$$\frac{d}{dt} \int_{\mathbb{R}^N} h |w|_- dx \leq -2 \int_{\mathbb{R}^N} \alpha_1^h |w|_-^2 dx + \int_{\mathbb{R}^N} \beta_1^h |w|_- |\nabla p|^2 dx + \int_{\mathbb{R}^N} \delta_1^h h |w|_- dx,$$

where

$$\alpha_1^h = h'q - h \frac{N-1}{N}, \quad \beta_1^h = h''q - h', \quad \text{and} \quad \delta_1^h = G \left[2 \frac{N-2}{N} - \frac{h'q}{h} \right] + G'q \leq \bar{\delta}_1.$$

To control the terms on the right-hand side, we argue as in the case $G \equiv 0$. In dimension $N = 1$, we can choose $h = 1$, $\alpha_1^h = \beta_1^h = 0$. Otherwise, it is sufficient to impose that

$$\alpha_1^h(p) > 0, \quad \text{and} \quad \beta_1^h(p) = 0,$$

as chosen in Theorem 3.4.1.

We rewrite the inequality, after using the Cauchy-Schwarz inequality, as

$$\frac{d}{dt} \int_{\mathbb{R}^N} h |w|_- dx \leq -A^{-1} \left(\int_{\mathbb{R}^N} h |w|_- \right)^2 dx + \bar{\delta}_1 \int_{\mathbb{R}^N} h |w|_- dx.$$

It remains to observe that $A \frac{\bar{\delta}_1 e^{\bar{\delta}_1 t}}{e^{\bar{\delta}_1 t} - 1}$ is a solution and we obtain the statements of Theorem

3.4.2. □

3.4.5 L^∞ -TYPE ESTIMATE

The other extreme L^p -space is that used in the original paper, and establishes a bound in L^∞ of $|w|_-$. To show the AB in this space, we use a similar technique first proposed in [102]. They study the evolution of the Laplacian of the pressure, Δp , which satisfies an appropriate parabolic inequality. Upon introducing a suitable function $h(p)$ characterized a posteriori, they deduce the time estimate on the solution n . Here, we are able to weaken the condition on the the function ϕ , *i.e.* we do not need to impose their Eq. (3). Precisely, our needed condition to get the AB-type estimate are the same as the ones in [102]. There are two main differences: first they are not addressing the incompressible limit and then, to assume their Eq. (3), they are forced to select a specific form of the weight which also ensures that a specific power of ϕ is convex. In the following, first we do not need any additional regularity on the quantities involved and we do not have to specify the shape of the weight: it solves an inequality, different from [102] where they impose the equality, and we just need to prove that the weight is bounded from above and below. Finally, thanks to Theorem 3.4.4, we are able to pass to the incompressible limit for all fields of pressure.

It uses the strong form of the equation satisfied by w . Namely, starting from Eq. (3.154), we can write

$$\partial_t w \geq \frac{2}{N} w^2 + 2\nabla(p+q) \cdot \nabla w + q\Delta w + w\Delta q + \left[G'(p)q - \frac{4}{N}G \right] w.$$

Using that

$$\Delta q = q''(p)|\nabla p|^2 + q'(p)\Delta p = q''(p)|\nabla p|^2 + q'(p)(w - G),$$

we find

$$\partial_t w \geq \left[q' + \frac{2}{N} \right] w^2 + 2\nabla(p+q) \cdot \nabla w + q''|\nabla p|^2 w + q\Delta w + \left[G' q - \left(\frac{4}{N} + q' \right) G \right] w. \quad (3.166)$$

A first result that can be deduced directly from this calculation is

Theorem 3.4.3 (Lower bound on Δp , special case). *Assume that $q'' \geq 0$ and assume there are constants $\bar{\delta} \in \mathbb{R}$, $\alpha_0 > 0$ such that $G' q - (\frac{4}{N} + q')G \leq \bar{\delta}$ and $q' + \frac{2}{N} \geq \alpha_0$, then we have*

$$\Delta p + G \geq -\frac{1}{\alpha_0} \frac{\bar{\delta} e^{\bar{\delta} t}}{e^{\bar{\delta} t} - 1}.$$

This result applies to homogeneous pressure laws $q(p) = \gamma p$ and $\alpha_0 = O(\gamma)$ and matches that of [250], see [250, Eqs. (2.14)]. It also applies to DHV law, $q = p + \varepsilon^{-1} p^2$, $q' = 1 + 2\varepsilon^{-1} p$ and $q'' = 2\varepsilon^{-1}$, but then $\alpha_0 = O(1)$ (when $p \approx 0$) does not give a uniform decay as $\frac{1}{\varepsilon}$) as needed to study the Hele-Shaw limit.

To treat more general pressure laws we can refine the argument and as in the L^1 -case, we begin with the porous-medium equation and then we include the growth term.

3.4.5.1 L^∞ -ESTIMATES WHEN $G \equiv 0$

We begin with estimating the Laplacian of the pressure, $w = \Delta p$, when $G \equiv 0$. We are going to prove the following theorem

Theorem 3.4.4 (Lower bound on Δp , $G \equiv 0$). *1. Assume that*

$$\left(\frac{q}{p}\right)' \geq 0, \quad \text{and} \quad \tilde{\alpha}_0 := \min_{0 \leq p \leq p_M} \frac{p q'(p)}{q(p)} > 0,$$

then

$$\frac{q(p)}{p} \Delta p \geq -\frac{1}{\tilde{\alpha}_0 t}.$$

2. Assume that $q'(p) > -1$ for $p \in [0, p_M]$, and

$$\tilde{\alpha}_0 = \frac{\min_{0 \leq p \leq p_M} q'(p)}{1 + \max_{0 \leq p \leq p_M} q'(p)} + \frac{2}{N} \frac{1 + q'(0)}{(1 + \max_{0 \leq p \leq p_M} q'(p))^2} > 0.$$

Then, we have

$$\left(1 + \min_{0 \leq p \leq p_M} q'(r)\right) \Delta p \geq -\frac{1}{\tilde{\alpha}_0 t}.$$

With the first set of assumptions, the estimate is compatible with the Hele-Shaw asymptotics in the two examples of Power-Law (then $\tilde{\alpha}_0 = 1$ and $\frac{q}{p} = \gamma$) and DHV law (then $\tilde{\alpha}_0 = 1$ and $\frac{q}{p} = \frac{p+\varepsilon}{\varepsilon}$). The second set of assumption is an explicit example motivated by [102].

To understand if there is some slack in the estimate, we compute the evolution of the quantity hw , where $h = h(p)$ is assumed to be a positive weight function. We obtain

$$\begin{aligned} \frac{\partial(hw)}{\partial t} &= wh' \frac{\partial p}{\partial t} + h \frac{\partial w}{\partial t} \\ &\geq wh'(|\nabla p|^2 + qw) \\ &\quad + h \left(\left[q' + \frac{2}{N} \right] w^2 + q'' |\nabla p|^2 w + 2\nabla(p+q) \cdot \nabla w + q\Delta w \right), \end{aligned}$$

where we used the equation satisfied by the pressure, Eq. (3.152), and Eq. (3.166) for w .

Upon rearranging the terms, we get

$$\frac{\partial(hw)}{\partial t} \geq w^2 \left[hq' + qh' + \frac{2}{N} \right] + w|\nabla p|^2 (h' + q''h) + q \underbrace{h\Delta w}_{I_1} + \underbrace{2h(1+q')\nabla p \cdot \nabla w}_{I_2}. \quad (3.167)$$

The terms involving the linear operators have to be rewritten in terms of the new quantity

hw rather than w . Therefore, from the first term we get

$$\begin{aligned}
I_1 &= \Delta(hw) - w\Delta h - 2\nabla h \cdot \nabla w \\
&= \Delta(hw) - w(h''|\nabla p|^2 + h'w) - 2h'\nabla p \cdot \nabla w \\
&= \Delta(hw) - w(h''|\nabla p|^2 + h'w) - 2\frac{h'}{h}\nabla p \cdot (\nabla(hw) - w\nabla h) \\
&= \Delta(hw) - 2\frac{h'}{h}\nabla p \cdot \nabla(hw) - w(h''|\nabla p|^2 + h'w) + 2(hw)\frac{(h')^2}{h^2}|\nabla p|^2 \\
&= \Delta(hw) - 2\frac{h'}{h}\nabla p \cdot \nabla(hw) + w|\nabla p|^2\left(2\frac{(h')^2}{h} - h''\right) - h'w^2.
\end{aligned}$$

For the second one we have

$$\begin{aligned}
I_2 &= 2\nabla(p+q) \cdot h\nabla w \\
&= 2\nabla(p+q) \cdot (\nabla(hw) - h'w\nabla p) \\
&= 2\nabla(p+q) \cdot \nabla(hw) - 2(1+q')h'w|\nabla p|^2.
\end{aligned}$$

Substituting the simplified expressions of I_1 and I_2 into Eq. (3.167), we have

$$\frac{\partial(hw)}{\partial t} \geq \alpha_\infty^h(hw)^2 + \beta_\infty^h(hw)|\nabla p|^2 + \mathcal{L}_\infty^h(hw), \quad (3.168)$$

where

$$\alpha_\infty^h = \frac{q'}{h} + \frac{2}{Nh^2}, \quad \text{and} \quad \beta_\infty^h = q'' - \frac{qh''}{h} + 2\frac{q(h')^2}{h^2} - 2\frac{q'h'}{h} - \frac{h'}{h},$$

as well as

$$\mathcal{L}_\infty^h(hw) = q\Delta(hw) + 2\left(1 + q' - \frac{qh'}{h}\right)\nabla p \cdot \nabla(hw).$$

In order to find a sub-solution and to close the estimate, it is enough to ensure that

$$\alpha_\infty^h = \frac{q'}{h} + \frac{2}{Nh^2} \geq \alpha_0 > 0, \quad \frac{\beta_\infty^h}{h} = \left(\frac{q}{h}\right)'' + \left(\frac{1}{h}\right)' \leq 0, \quad (3.169)$$

where α_0 is a constant. We propose two strategies to fulfill these requirements.

1. ASSUME $\left(\frac{q}{p}\right)' \geq 0$. With this assumption, we can simply choose

$$h = \frac{q}{q'(0)p}, \quad \left(\frac{q}{h}\right)' = q'(0),$$

because $\frac{1}{h}$ is non-increasing. Then we compute,

$$\alpha_0 := q'(0) \simeq \min_{0 \leq p \leq p_M} \left[\frac{p q'(p)}{q(p)} + \frac{2}{N} \frac{q'(0)p^2}{q(p)^2} \right],$$

and this gives our first statement in Theorem 3.4.4 after simplifying a coefficient $q'(0)$.

2. ASSUME $q'(p) > -1$. Then we impose, from Eq. (3.169)

$$\left(\frac{q}{h}\right)' + \frac{1}{h} = 1 + q'(0), \quad \text{and} \quad h(0) = 1. \quad (3.170)$$

Because of the degeneracy at $p = 0$, the condition $h(0) = 1$ is imposed since we can compute

$$1 + q'(0) = \frac{q'(0)}{h(0)} + q(0)(h^{-1})'(0) + \frac{1}{h(0)} = \frac{q'(0) + 1}{h(0)}.$$

We can analyze the differential equation (3.170).

Lemma 3.4.5. *Assume that $q'(p) > -1$ for $p \in [0, p_M]$. Then, the solution of (3.170)*

satisfies,

$$\frac{1 + \min_{0 \leq r \leq p} q'(r)}{1 + q'(0)} \leq h(p) \leq \frac{1 + \max_{0 \leq r \leq p} q'(r)}{1 + q'(0)}, \quad \forall p \in (0, p_M).$$

Remark 3.4.6 (Power-law, DHV Pressure, General Pressure Laws). Notice that if q is smooth as in DHV, $q'(0) = 1$ but for the Power-law, $q'(0) = \gamma$. As a matter of fact, for the Power-law pressure and the singular pressure we are able to provide explicit expressions for h , *i.e.*

$$h_\gamma(p) = 1, \quad \text{and} \quad h_\varepsilon(p) = 1 + p - \varepsilon \log(p + \varepsilon) + \varepsilon \log \varepsilon. \quad (3.171)$$

However, we also emphasize that the bounds established in the preceding theorem allow to prove an Aronson-Bénilan type estimate for more general pressure-laws $p = p(n)$, under rather weak assumptions on q , thus extending the known cases.

Proof. First, we change variables and set, in Eq. (3.170),

$$u(p) := \frac{1}{h(p)},$$

In the new variable, it becomes

$$qu' + (q' + 1)u = 1 + q'(0), \quad (3.172)$$

with $u(0) = 1$. The rest of the argument, *i.e.* the proof of the upper and lower bound on h , is by contradiction. To this end, we define

$$U(p) = a \frac{1 + q'(0)}{1 + \max_{0 \leq r \leq p} q'(r)}.$$

By construction, it is a non-increasing function and it satisfies $u(0) = 1 > U(0) = a$. Assume there exists a point $p^* \in (0, p_M)$, that we can choose to be minimal, such that

$$u(p^*) = U(p^*). \quad (3.173)$$

Therefore, at this point we have to have $u'(p^*) \leq 0$, as well as $(1 + q'(p^*))u(p^*) = (1 + q'(p^*))U(p^*)$. Revisiting Eq. (3.172), we see that

$$\begin{aligned} 1 + q'(0) &= (qu)'(p^*) + u(p^*) \\ &= q(p^*)u'(p^*) + (q(p^*) + 1)u(p^*) \\ &\leq (1 + q(p^*))U(p^*) \\ &\leq a(1 + q'(0)), \end{aligned}$$

having used the fact that $qu'(p^*) \leq 0$ and the definition of U . It is clear that this is a contradiction, since $0 < a < 1$ and proves that $u > aU$. Finally, taking $a \rightarrow 1$, we obtain the upper bound. The lower bound is obtained in the same way. \square

The derivation of Theorem 3.4.4 is now as usual because $-\frac{1}{\alpha_0 t}$ is a sub-solution of Eq. (3.168) and, using Lemma 3.4.5, we can choose

$$\alpha_0 = \min_{0 \leq p \leq p_M} q'(p) \frac{1 + q'(0)}{1 + \max_{0 \leq p \leq p_M} q'(p)} + \frac{2}{N} \left(\frac{1 + q'(0)}{1 + \max_{0 \leq p \leq p_M} q'(p)} \right)^2.$$

Then, using Lemma 3.4.5 a second time,

$$\frac{1 + \min_{0 \leq r \leq p} q'(r)}{1 + q'(0)} w \geq \min_p h(p) w \geq -\frac{1}{\alpha_0 t},$$

which gives the result of Theorem 3.4.4.

3.4.5.2 L^∞ -ESTIMATES WHEN $G \neq 0$

Next, we proceed by incorporating reaction terms, *cf.* Eq. (3.147) and prove the

Theorem 3.4.7 (Lower bound on Δp , general G). *With the assumptions and notations of Theorem 3.4.4, we have, with the constant δ_∞^h defined below*

$$\left(1 + \min_{0 \leq p \leq p_M} q'(r)\right) (\Delta p + G) \geq -\frac{1}{\tilde{\alpha}_0} \frac{\bar{\delta}_\infty^h e^{\bar{\delta}_\infty^h t}}{e^{\bar{\delta}_\infty^h t} - 1}.$$

Still using (3.166), we compute the evolution of the quantity hw , *i.e.*

$$\begin{aligned} \frac{\partial(hw)}{\partial t} &\geq h'|\nabla p|^2 w + \left(\frac{h'q}{h^2}\right)(hw)^2 + hq''|\nabla p|^2 w + \left(\frac{q'}{h}\right)(hw)^2 \\ &\quad + \underbrace{2h\nabla(p+q) \cdot \nabla w + q}_{I_1} \underbrace{h\Delta w}_{I_2} + (hw) \left(G'q - \left(\frac{4}{N} + q'\right)G\right). \end{aligned} \quad (3.174)$$

Next, we rewrite the terms I_1 and I_2 using the new variable, hw . The first term, I_1 , becomes

$$I_1 = 2\nabla(p+q) \cdot \nabla(hw) - 2w|\nabla p|^2(1+q')h'.$$

Regarding the second one, we obtain

$$\begin{aligned} I_2 &= \Delta(hw) - w\Delta h - 2\nabla h \cdot \nabla w \\ &= \Delta(hw) - w(h''|\nabla p|^2 + h'\Delta p) - 2h'\nabla p \cdot \nabla w \\ &= \Delta(hw) - w(h''|\nabla p|^2 + h'w - h'G) - 2\frac{h'}{h}\nabla p \cdot (\nabla(hw) - wh'\nabla p) \\ &= \Delta(hw) - 2\frac{h'}{h}\nabla p \cdot \nabla(hw) + w|\nabla p|^2\left(2\frac{h'^2}{h} - h''\right) - (hw)^2\left(\frac{h'}{h^2}\right) + (hw)\left(\frac{h'G}{h}\right). \end{aligned}$$

Substituting the terms I_1 and I_2 back into Eq. (3.174), we get

$$\frac{\partial(hw)}{\partial t} \geq \alpha_\infty^h (hw)^2 + \beta_\infty^h |\nabla p|^2 w + \mathcal{L}_\infty^h(hw) + \delta_\infty^h(hw), \quad (3.175)$$

where α_∞^h , β_∞^h and $\mathcal{L}_\infty^h(hw)$ are as in inequality (3.168), and

$$\delta_\infty^h(p) := G'q - \left(\frac{4}{N} + q'\right)G + \frac{qh'G}{h} \leq \bar{\delta}_\infty < \infty. \quad (3.176)$$

In order to close the L^∞ -type bound, it suffices to apply a slight variation of the proof of Theorem 3.4.4 incorporating additional terms related to the growth. Again, we have to require that

$$\alpha_\infty^h \geq \alpha_0 > 0, \quad \text{and} \quad \beta_\infty^h = 0, \quad (3.177)$$

which are identical to the conditions given by Eq. (3.169), (3.170).

Therefore Theorem 3.4.7 follows as in Section 3.4.4.2 because $-\frac{1}{\alpha_0} \frac{\bar{\delta}_\infty^h e^{\bar{\delta}_\infty^h t}}{e^{\bar{\delta}_\infty^h t-1}}$ is a sub-solution of the corresponding equation.

3.4.6 L^2 -TYPE ESTIMATE

We now investigate the L^2 space which has been used in situations where the L^∞ estimate cannot be applied because the growth term depends on other quantities and cannot be differentiated with uniform control. As we shall see, the advantage of working in L^2 is to provide additional dissipation terms which do not appear in L^1 or L^∞ while keeping an estimate compatible with the free boundary in opposition to L^1 .

We proceed again by departing from Eq. (3.154) which we write as

$$\partial_t \frac{|w|_-^2}{2} \leq -\frac{2}{N} |w|_-^3 + \nabla p \cdot \nabla |w|_-^2 + |w|_- \Delta(q|w|_-) + \left[G'q - \frac{4}{N}G\right] |w|_-^2. \quad (3.178)$$

And we distinguish the two cases $G \equiv 0$ or not.

3.4.6.1 L^2 -ESTIMATES WHEN $G \equiv 0$. NO WEIGHT.

We are going to prove the following theorem

Theorem 3.4.8. *Assume $\inf_{0 \leq p \leq p_M} \left(\frac{2}{N} - 1 + \frac{q'}{2} \right) =: \alpha_0 \geq 0$ and $q'' \leq 0$, then*

$$\int_{\mathbb{R}^N} |w(t)|_-^2 dx + 2 \int_0^t \int_{\mathbb{R}^N} \left(\frac{2}{N} - 1 + \frac{q'}{2} \right) |w(s)|_-^3 dx ds \leq \int_{\mathbb{R}^N} |w(t=0)|_-^2 dx.$$

When, for $t \in [0, T]$, we have $\alpha_0 > 0$, for solutions with compact support in x , it holds

$$\int_{\mathbb{R}^N} |w(t)|_-^2 dx \leq \frac{C(T)}{t^2} \quad \forall t \in [0, T].$$

For the Power-law, $q' = \gamma$, we recover the condition obtained in [169], that is

$$\gamma \geq 2 - \frac{4}{N}.$$

In the case of the DHV pressure, cf. Eq. (3.151), the assumption $q'' \leq 0$ is not met.

Notice also that the argument can be localized, see [110], and this allows to remove the compact support assumption.

Proof. Integrating Eq. (3.178), and using two integration by parts, we obtain

$$\frac{d}{dt} \int_{\mathbb{R}^N} \frac{|w|_-^2}{2} dx \leq -\frac{2}{N} \int_{\mathbb{R}^N} |w|_-^3 dx + \int_{\mathbb{R}^N} |w|_-^3 dx - \underbrace{\int_{\mathbb{R}^N} \nabla |w|_- \nabla (q|w|_-) dx}_I. \quad (3.179)$$

Integrating by parts, the first term, I , can be rewritten, *i.e.*

$$\begin{aligned} I &= - \int_{\mathbb{R}^N} |w|_- \nabla q \cdot \nabla |w|_- \, dx - \int_{\mathbb{R}^N} q |\nabla |w|_-|^2 \, dx \\ &= \frac{1}{2} \int_{\mathbb{R}^N} \Delta q |w|_-^2 \, dx - \int_{\mathbb{R}^N} q |\nabla |w|_-|^2 \, dx \\ &= \frac{1}{2} \int_{\mathbb{R}^N} q'' |\nabla p|^2 |w|_-^2 \, dx - \frac{1}{2} \int_{\mathbb{R}^N} q' |w|_-^3 \, dx - \int_{\mathbb{R}^N} q |\nabla |w|_-|^2 \, dx, \end{aligned}$$

where we used the chain rule $\Delta q = q'' |\nabla p|^2 + q' w$.

Substituting the simplified expressions for I into Eq. (3.179), we obtain

$$\frac{d}{dt} \int_{\mathbb{R}^N} \frac{|w|_-^2}{2} \, dx \leq - \int_{\mathbb{R}^N} \left(\frac{2}{N} - 1 + \frac{q'}{2} \right) |w|_-^3 \, dx + \frac{1}{2} \int_{\mathbb{R}^N} q'' |\nabla p|^2 |w|_-^2 \, dx - \int_{\mathbb{R}^N} q |\nabla |w|_-|^2 \, dx.$$

Since $q \geq 0$, this ensures that the estimate can be closed if $q' > 2 - \frac{4}{N}$, for all $p \in (0, p_M)$ and $q'' \leq 0$. Indeed, we deduce the inequality

$$\int_{\mathbb{R}^N} |w(t)|_-^2 \, dx \leq - \int_{\mathbb{R}^N} \alpha_0 |w(t)|_-^3. \quad (3.180)$$

The conclusions of the theorem follow by time integration (first estimate) or using a sub-solution $\frac{C(T)}{t^2}$ (second estimate with regularizing effect).

□

It is interesting to investigate if adding a weight can help us to include more general pressure laws.

3.4.6.2 L^2 -ESTIMATES WHEN $G \equiv 0$. WITH WEIGHTS.

In order to be as general as possible, we add a weight $h = h(p)$.

Theorem 3.4.9. *Assume there exists a positive weight, $0 < c \leq h(p) \leq c^{-1}$ such that the two*

differential inequalities

$$\alpha_2^h := \frac{4}{N} + \frac{2h'q}{h} - 2 + q' \geq 0, \quad \text{and} \quad \beta_2^h := \frac{h''q + q''h - h'}{h} \leq 0.$$

are met. Then

$$\int_{\mathbb{R}^N} h|w|_-^2(t) \, dx + \int_0^t \int_{\mathbb{R}^N} \alpha_2^h h|w|_-^3 \, dx \, dt \leq \int_{\mathbb{R}^N} h|w|_-^2(0) \, dx.$$

Note that the same regularization effect as in Theorem 3.4.8 can be obtained if $\alpha_2^h > \alpha_0$, for some constant $\alpha_0 > 0$.

Proof. Using the equation satisfied by the pressure, Eq. (3.152), and Eq. (3.178) for $|w|_-^2$, we compute the evolution in time of $h|w|_-^2$

$$\begin{aligned} \frac{\partial}{\partial t}(h|w|_-^2) &= h'|w|_-^2(|\nabla p|^2 + qw) + h\partial_t|w|_-^2 \\ &\leq h'|\nabla p|^2|w|_-^2 - h'q|w|_-^3 \\ &\quad + 2h\left(-\frac{2}{N}|w|_-^3 + 2|w|_- \nabla p \cdot \nabla|w|_- + |w|_- \Delta(q|w|_-)\right). \end{aligned} \tag{3.181}$$

Integrating over \mathbb{R}^N and with an integration by parts for the last two terms, we get

$$\begin{aligned} \frac{d}{dt} \int_{\mathbb{R}^N} (h|w|_-^2) \, dx &\leq \int_{\mathbb{R}^N} h'|\nabla p|^2|w|_-^2 \, dx - \int_{\mathbb{R}^N} \left(\frac{4}{N} + \frac{h'q}{h}\right) h|w|_-^3 \, dx \\ &\quad + 4 \int_{\mathbb{R}^N} h|w|_- \nabla p \cdot \nabla|w|_- \, dx - 2 \int_{\mathbb{R}^N} \nabla(h|w|_-) \nabla(q|w|_-) \, dx \\ &\leq - \int_{\mathbb{R}^N} h'|\nabla p|^2|w|_-^2 \, dx - \int_{\mathbb{R}^N} \left(\frac{4}{N} - 2 + \frac{h'q}{h}\right) h|w|_-^3 \, dx \\ &\quad - 2 \underbrace{\int_{\mathbb{R}^N} \nabla(h|w|_-) \nabla(q|w|_-) \, dx}_I. \end{aligned} \tag{3.182}$$

Next, we need to address the term I . We compute

$$\begin{aligned}
I &= \int_{\mathbb{R}^N} [h' \nabla p |w|_- + h \nabla |w|_-] \cdot [q' \nabla p |w|_- + q \nabla |w|_-] dx \\
&= \int_{\mathbb{R}^N} \left[h' q' |\nabla p|^2 |w|_-^2 + \frac{h' q + h q'}{2} \nabla p \cdot \nabla |w|_-^2 + h q |\nabla |w|_-|^2 \right] dx \\
&= \int_{\mathbb{R}^N} \left[h' q' |\nabla p|^2 |w|_-^2 + \frac{h' q + h q'}{2} |w|_-^3 - \left[\frac{h' q + h q'}{2} \right]' |\nabla p|^2 |w|_-^2 + h q |\nabla |w|_-|^2 \right] dx.
\end{aligned} \tag{3.183}$$

Reorganizing the terms, we get

$$I = \int_{\mathbb{R}^N} \left[\frac{h' q + h q'}{2} |w|_-^3 - \frac{h'' q + h q''}{2} |\nabla p|^2 |w|_-^2 + h q |\nabla |w|_-|^2 \right] dx$$

Finally, substituting I into Eq. (3.182), we obtain

$$\frac{d}{dt} \int_{\mathbb{R}^N} (h |w|_-^2) dx \leq - \int_{\mathbb{R}^N} \alpha_2^h h |w|_-^3 dx + \int_{\mathbb{R}^N} \beta_2^h |\nabla p|^2 h |w|_-^2 dx - 2 \int_{\mathbb{R}^N} h q |\nabla |w|_-|^2 dx,$$

where

$$\alpha_2^h = \frac{4}{N} + \frac{2h'q}{h} - 2 + q', \quad \text{and} \quad \beta_2^h = \frac{h''q + q''h - h'}{h}.$$

By assumption

$$\alpha_2^h \geq 0, \quad \text{and} \quad \beta_2^h \leq 0. \tag{3.184}$$

the statement holds true. \square

Remark 3.4.10. For the condition $\alpha_2^h \geq 0$, the weight h does not help when it is positive because the term generated by the weight, $\frac{2h'q}{h^3}$ vanishes for $p = 0$. However, loosing on the estimate near the free boundary, for instance we may choose $h = p$, then we improve the

range of possible parameters. For Power-law, we reach the conditions

$$\alpha_2^h = \frac{4}{p^2 N} + \frac{3\gamma}{p^2} - \frac{2}{p^2} \geq 0,$$

which is less restrictive than when $h = 1$, while the condition $\beta_2^h \leq 0$ is fulfilled.

It is unclear to us how to choose the weight h for DHV law in L^2 .

Adding the reaction term G , we do not gain anything. Precisely, without the weight h , we obtain the same conditions on q' and q'' as the ones in Theorem 3.4.8. Since G is bounded and decreasing, cf. Eq. (3.148), the term which involves G can always be controlled. We decide not to report all the calculations because they can be derived easily from the ones in Section 3.4.6.1.

To conclude the section, we decide to add the reaction term $G > 0$ and we can derive the L^2 -estimate for $h|w|_-$.

3.4.6.3 L^2 -ESTIMATES WHEN $G \neq 0$. WITH WEIGHTS

This section is dedicated to proving the following theorem.

Theorem 3.4.11. *Assume there exists a positive weight, $0 < c \leq h(p) \leq c^{-1}$ such that the two differential inequalities $\alpha_2^h \geq 0, \beta_2^h \leq 0$, are satisfied, with α_2^h and β_2^h defined as in Theorem 3.4.9.*

Then there holds

$$\int_{\mathbb{R}^N} h|w|_-^2(t) \, dx + \int_0^t \int_{\mathbb{R}^N} \alpha_2^h h|w|_-^3 \, dx \, dt \leq \int_{\mathbb{R}^N} h|w|_-^2(0) \, dx + \int_0^t \int_{\mathbb{R}^N} \bar{\delta}_2^h h|w|_-^2 \, dx \, dt,$$

where

$$\bar{\delta}_2^h = \sup_{0 \leq p \leq p_M} \left\{ 2G'q + G \left(2 \left(1 - \frac{4}{N} \right) - \frac{h'q + q'h}{h} \right) \right\}.$$

As before, the same regularization effect as in Theorem 3.4.8 is obtained if we can guarantee that $\alpha_2^h > \alpha_0$, for a positive constant $\alpha_0 > 0$. Theorem 3.4.11 proves that adding the reaction, the estimate does not gain anything.

Proof. Starting from Eq. (3.181) and including the additional growth terms G , the evolution of $h|w|_-^2$ becomes

$$\begin{aligned} \frac{\partial}{\partial t} (h|w|_-^2) &\leq h'|\nabla p|^2|w|_-^2 - h'q|w|_-^3 \\ &\quad + 2h \left(-\frac{2}{N}|w|_-^3 + \nabla p \cdot \nabla |w|_-^2 + |w|_- \Delta(q|w|_-) \right) \\ &\quad + 2h \left(G'q - \frac{4}{N}G \right) |w|_-^2. \end{aligned} \quad (3.185)$$

Integrating in space and by an integration by parts, we get

$$\begin{aligned} \frac{d}{dt} \int_{\mathbb{R}^N} h|w|_-^2 \, dx &\leq - \int_{\mathbb{R}^N} \left(\frac{4}{N} + \frac{qh'}{h} - 2 \right) h|w|_-^3 \, dx - \int_{\mathbb{R}^N} h'|w|_-^2 |\nabla p|^2 \, dx \\ &\quad - 2 \underbrace{\int_{\mathbb{R}^N} \nabla(h|w|_-) \cdot \nabla(q|w|_-) \, dx}_I + 2 \int_{\mathbb{R}^N} h|w|_-^2 \left(G'q + G \left(1 - \frac{4}{N} \right) \right) dx. \end{aligned} \quad (3.186)$$

Using Eq. (3.183) and the definition of w , cf. Eq. (3.153), the term I simplifies to

$$\begin{aligned} I &= \frac{1}{2} \int_{\mathbb{R}^N} (h'q + hq') |w|_-^3 \, dx - \frac{1}{2} \int_{\mathbb{R}^N} (h''q + hq'') |\nabla p|^2 |w|_-^2 \, dx \\ &\quad + \frac{1}{2} \int_{\mathbb{R}^N} (h'q + hq') G |w|_-^2 \, dx + \int_{\mathbb{R}^N} hq |\nabla |w|_-|^2 \, dx \end{aligned} \quad (3.187)$$

Substituting everything into Eq. (3.186), we obtain

$$\frac{d}{dt} \int_{\mathbb{R}^N} \frac{h|w|_-^2}{2} dx \leq - \int_{\mathbb{R}^N} \alpha_2^h h|w|_-^3 dx + \int_{\mathbb{R}^N} |\nabla p|^2 \beta_2^h h|w|_-^2 dx + \int_{\mathbb{R}^N} \delta_2^h h|w|_-^2 dx,$$

where

$$\alpha_2^h = \frac{4}{N} + \frac{2qh'}{h} - 2 + q', \quad \text{and} \quad \beta_2^h = \frac{h''q + q''h - h'}{h},$$

as well as

$$\delta_2^h = 2G'q + G \left(2 \left(1 - \frac{4}{N} \right) - \frac{h'q + q'h}{h} \right) \leq \bar{\delta}_2 < \infty,$$

where $\bar{\delta}_2$ is as in the statement. By assumption

$$\alpha_2^h \geq 0 \quad \text{and} \quad \beta_2^h \leq 0, \tag{3.188}$$

and the statement holds true. □

Remark 3.4.12. Different techniques have been used to perform an L^2 -bound. For instance, in [110], the authors compute exactly the square of the expression $(w - G)$ and then they apply the Young's inequality to the term

$$2 \left(1 - \frac{2}{N} \right) G|w|_-^2.$$

This choice allows them to get an additional small constant $\mu > 0$ in the expression of α_2^h which can help in getting a weaker condition to close the estimate. However, there is an

additional term which involves the growth term, *i.e.*

$$C \int_{\mathbb{R}^N} G^2 |w|_- \, dx,$$

with $C > 0$ a constant. Now the estimate can only be closed by assuming the standard conditions on G , *cf.* Eq. (3.148), plus an additional condition on the domain. Finally, the expression of δ_2^h change a bit, *i.e.*

$$(\delta_2^h)_Y = \frac{2G'q}{h} - G \left(\frac{h'q + q'h}{h^2} \right) \leq \tilde{\delta}_2 < \infty,$$

which can be bounded by controlling h' .

Remark 3.4.13. In the Power-law case, regarding the conditions on α_2^h and β_2^h , we can refer to Remark 3.4.10. The last one, substituting $q = p\gamma$ and $h(p) = c_1 + p$, δ_2^h becomes

$$\delta_2^h = \gamma p(2G' - c_1G) - (p + c_1)(G\gamma + 2G) < \infty. \quad (3.189)$$

Note that this expression is always non-positive for non-negative and decreasing growth terms, *cf.* Eq. (3.148).

3.4.7 CONCLUSIONS

The Aronson-Bénilan estimate has proven to be a fundamental tool in order to study regularity and asymptotic in several problems related to the porous media equations. Even if it has been used mainly to control the Laplacian of the pressure from below by a term as $\Delta p(t) \geq -\frac{C}{t}$, one may use it in other Lebesgue spaces. We have systematically studied the restrictions on the parameters and the conclusions that one can draw in L^1 , L^2 and L^∞ (original work of Aronson and Bénilan). In particular we considered two specific forms of the pressure law, the Power-law and DHV law.

Our conclusions are that the L^∞ setting provides the widest range of parameters, generating the strongest estimate. For instance, it can be applied to both pressure laws. On the other hand, the L^2 estimate requires restrictions on the parameters (which exclude DHV law) but is enough to estimate the Laplacian of the pressure for the Power-law. Because of integration by parts, and because a dissipation term occurs explicitly, it is however useful for some strongly coupled problem where L^∞ bounds are not possible. The L^1 estimate turns out to be the simplest but is only useful in space dimension $N = 1$.

When weights are included in order to treat more general equations of state, we improve the results in [102] and we obtain estimates correctly scaled with respect to the Hele-Shaw limit, which, with our notations, is expressed as $|w|_- \approx 0$ for $\gamma \gg 1$ or $\varepsilon \ll 1$.

If one wishes to estimate the quantity $p\Delta p(t)$, losing regularity near the free boundary, then one can drastically extend the range of possible pressure laws.

B

Appendix to Chapter 3

B.1 COMPUTATION OF THE INCREMENTAL CURVATURE

The external boundary in the actual incremental configuration is given by

$$\boldsymbol{\alpha}(\theta) = (r_o + u(r_o, \theta)) [\cos(\theta + v(r_o, \theta)), \sin(-\theta - v(r_o, \theta))], \quad (\text{B.1})$$

since the parametrization of $\boldsymbol{\alpha}$ is counter-clockwise (3.9). By differential geometry, the oriented curvature of $\boldsymbol{\alpha}$ is given by

$$\mathcal{K} = \frac{\alpha'_x(\theta)\alpha''_y(\theta) - \alpha'_y(\theta)\alpha''_x(\theta)}{|\boldsymbol{\alpha}'(\theta)|^3}, \quad (\text{B.2})$$

where with ' we denote the derivative with respect to θ . By combining Eq. (B.1) and Eq. (B.2) we obtain

$$\mathcal{K} = \frac{(v' + 1) \left((u + r_o) (u'' - (u + r_o) (v' + 1)^2) - 2u'^2 \right) - (u + r_o) u' v''}{(u'^2 + (u + r_o)^2 (v' + 1)^2)^{3/2}}. \quad (\text{B.3})$$

We can linearize the relation (B.3) with respect to u , v , and their derivatives to get the following expression of the incremental curvature

$$\delta\mathcal{K} = \frac{u'' + u}{r_o^2}.$$

B.2 ROLE OF THE MATRIGEL EMBEDMENT

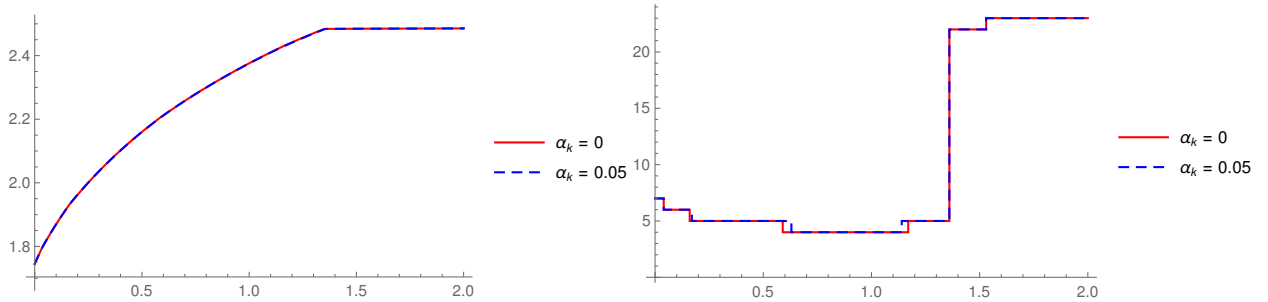


Figure B.1: Marginal stability threshold g_{cr} (top) and critical wavenumber m_{cr} (bottom) versus α_γ for $\alpha_R = 0.9$ and $\alpha_k = 0, 0.5$.

Let k_s be the elastic constant of the springs per unit length. Let $\mu_M \simeq \mu$ be the shear modulus of the Matrigel. The boundary condition Eq. (3.10) modifies into

$$\mathbf{P}^T \mathbf{N} = (\det \mathbf{F}) \gamma \mathcal{K} \mathbf{F}^{-T} \mathbf{N} - k_s \mathbf{u}.$$

The radially symmetric solution given by Eqs. (3.21)-(3.22) is still a solution of the modified problem, the only difference is that the pressure increases of a constant $k_s R_o (1 - R_o/r_o)$. Denoting by R_M the characteristic distance among the organoids, from a dimensional evaluation we obtain

$$k_s \simeq \frac{\mu}{R_M}.$$

We adimensionalize k_s with respect to μ and R_o , obtaining

$$\alpha_k = \frac{k_s R_o}{\mu} \simeq \frac{R_o}{R_M} \simeq \frac{500 \mu\text{m}}{1\text{cm}} = 0.05.$$

From this computation it is likely that the force exerted by the Matrigel on the organoid is negligible. To verify it, we have modified the linear stability of exposed in Section 3.1.3 to account for the Matrigel embedment.

Following the procedure exposed in [273], we can compute the marginal stability threshold using the same algorithm exposed in the manuscript by just modifying Eq. (3.43) into

$$Z_o = -\frac{\alpha \gamma}{r_o} \begin{bmatrix} m^2 & m \\ m & 1 \end{bmatrix} - \alpha_k \mathbf{I}.$$

The marginal stability threshold are only slightly influenced by the presence of the linear springs at the boundary, as shown by Fig. B.1. From these results, it is clear that the presence of Matrigel has very little influence on the behavior of the organoid, as observed in [193].

B.3 EXPRESSIONS OF $\zeta_n, \tau_n, \sigma_n$

We report the functions ζ_n, τ_n and σ_n we introduced in Eq. (3.123), such as

$$\begin{aligned}
\zeta_n &= \frac{1}{4k^3\lambda_x^3Q_n} \left(kQ_n \left(G_n \left((4gk\lambda_x^3\rho - 4\gamma k^3) \cosh\left(\frac{HQ_n}{\lambda_x}\right) + 4k \cosh\left(\frac{Hk}{\lambda_x}\right) (\gamma k^2 - g\lambda_x^3\rho) \right. \right. \right. \\
&\quad \left. \left. \left. + \lambda_x \sinh\left(\frac{Hk}{\lambda_x}\right) (4k^2(\lambda_x^4 + 1)\mu - \lambda_x^2(2n+1)^2\rho\omega^2) \right) - 4gk\lambda_x^3\rho \sinh\left(\frac{Hk}{\lambda_x}\right) + 4\gamma k^3 \sinh\left(\frac{Hk}{\lambda_x}\right) \right. \right. \\
&\quad \left. \left. + 4k^2\lambda_x^5\mu \cosh\left(\frac{Hk}{\lambda_x}\right) + 4k^2\lambda_x\mu \cosh\left(\frac{Hk}{\lambda_x}\right) - 4k^2\lambda_x^5\mu \cosh\left(\frac{HQ_n}{\lambda_x}\right) - 8k^2\lambda_x\mu \cosh\left(\frac{HQ_n}{\lambda_x}\right) \right. \right. \\
&\quad \left. \left. - \lambda_x^3\rho\omega^2 \cosh\left(\frac{Hk}{\lambda_x}\right) - 4\lambda_x^3n^2\rho\omega^2 \cosh\left(\frac{Hk}{\lambda_x}\right) - 4\lambda_x^3n\rho\omega^2 \cosh\left(\frac{Hk}{\lambda_x}\right) + 4\lambda_x^3n^2\rho\omega^2 \cosh\left(\frac{HQ_n}{\lambda_x}\right) \right. \right. \\
&\quad \left. \left. + 4\lambda_x^3n\rho\omega^2 \cosh\left(\frac{HQ_n}{\lambda_x}\right) + \lambda_x^3\rho\omega^2 \cosh\left(\frac{HQ_n}{\lambda_x}\right) \right) + 4k^3(g\lambda_x^3\rho - \gamma k^2) \sinh\left(\frac{HQ_n}{\lambda_x}\right) \right. \\
&\quad \left. - \lambda_x G_n Q_n^2 \sinh\left(\frac{HQ_n}{\lambda_x}\right) (4k^2(\lambda_x^4 + 2)\mu - \lambda_x^2(2n+1)^2\rho\omega^2) + 4\lambda_x\mu G_n Q_n^4 \sinh\left(\frac{HQ_n}{\lambda_x}\right) \right. \\
&\quad \left. + 4k\lambda_x\mu Q_n^3 \cosh\left(\frac{HQ_n}{\lambda_x}\right) \right) \\
\tau_n &= \frac{\rho G_{n+1} \cosh\left(\frac{Hk}{\lambda_x}\right)}{k} - \frac{\rho G_{n+1} \cosh\left(\frac{HQ_{n+1}}{\lambda_x}\right)}{k} + \frac{\rho \sinh\left(\frac{Hk}{\lambda_x}\right)}{k} - \frac{\rho \sinh\left(\frac{HQ_{n+1}}{\lambda_x}\right)}{Q_{n+1}} \\
\sigma_n &= \frac{\rho G_{n-1} \cosh\left(\frac{Hk}{\lambda_x}\right)}{k} - \frac{\rho G_{n-1} \cosh\left(\frac{HQ_{n-1}}{\lambda_x}\right)}{k} + \frac{\rho \sinh\left(\frac{Hk}{\lambda_x}\right)}{k} - \frac{\rho \sinh\left(\frac{HQ_{n-1}}{\lambda_x}\right)}{Q_{n-1}}
\end{aligned}$$

where Q_n and G_n are respectively defined in Eqs. (3.120) and (3.122)

B.4 EXPRESSIONS OF Z_n, T_n, Σ_n

We report the functions Z_n, T_n and Σ_n we introduced in Eq. (3.139), such as

$$\begin{aligned}
Z_n &= \frac{1}{k^3\lambda_x^3P_n} \left(kP_n \left(J_n \left((gk\lambda_x^3\rho - \gamma k^3) \cosh\left(\frac{HP_n}{\lambda_x}\right) + k \cosh\left(\frac{Hk}{\lambda_x}\right) (\gamma k^2 - g\lambda_x^3\rho) + \lambda_x \sinh\left(\frac{Hk}{\lambda_x}\right) \right. \right. \right. \\
&\quad \left. \left. \left. (k^2(\lambda_x^4 + 1)\mu - \lambda_x^2n^2\rho\omega^2) \right) - gk\lambda_x^3\rho \sinh\left(\frac{Hk}{\lambda_x}\right) + \gamma k^3 \sinh\left(\frac{Hk}{\lambda_x}\right) + k^2\lambda_x^5\mu \cosh\left(\frac{Hk}{\lambda_x}\right) \right. \right. \\
&\quad \left. \left. + k^2\lambda_x\mu \cosh\left(\frac{Hk}{\lambda_x}\right) - k^2\lambda_x^5\mu \cosh\left(\frac{HP_n}{\lambda_x}\right) - 2k^2\lambda_x\mu \cosh\left(\frac{HP_n}{\lambda_x}\right) - \lambda_x^3n^2\rho\omega^2 \cosh\left(\frac{Hk}{\lambda_x}\right) \right. \right. \\
&\quad \left. \left. + \lambda_x^3n^2\rho\omega^2 \cosh\left(\frac{HP_n}{\lambda_x}\right) \right) + k^3(g\lambda_x^3\rho - \gamma k^2) \sinh\left(\frac{HP_n}{\lambda_x}\right) - \lambda_x J_n P_n^2 \sinh\left(\frac{HP_n}{\lambda_x}\right) \right. \\
&\quad \left. (k^2(\lambda_x^4 + 2)\mu - \lambda_x^2n^2\rho\omega^2) + \lambda_x\mu J_n P_n^4 \sinh\left(\frac{HP_n}{\lambda_x}\right) + k\lambda_x\mu P_n^3 \cosh\left(\frac{HP_n}{\lambda_x}\right) \right) \\
T_n &= \frac{\rho J_{n+1} \cosh\left(\frac{Hk}{\lambda_x}\right)}{k} - \frac{\rho J_{n+1} \cosh\left(\frac{HP_{n+1}}{\lambda_x}\right)}{k} + \frac{\rho \sinh\left(\frac{Hk}{\lambda_x}\right)}{k} - \frac{\rho \sinh\left(\frac{HP_{n+1}}{\lambda_x}\right)}{P_{n+1}} \\
\Sigma_n &= \frac{\rho J_{n-1} \cosh\left(\frac{Hk}{\lambda_x}\right)}{k} - \frac{\rho J_{n-1} \cosh\left(\frac{HP_{n-1}}{\lambda_x}\right)}{k} + \frac{\rho \sinh\left(\frac{Hk}{\lambda_x}\right)}{k} - \frac{\rho \sinh\left(\frac{HP_{n-1}}{\lambda_x}\right)}{P_{n-1}}
\end{aligned}$$

where P_n and J_n are respectively defined in Eqs. (3.133) and (3.137).

In the case $\lambda_x = 1$, $Z_n|_{\lambda_x=1}$, $T_n|_{\lambda_x=1}$ and $\Sigma_n|_{\lambda_x=1}$ are given by

$$\begin{aligned}
 Z_n|_{\lambda_x=1} &= \begin{cases} -\frac{1}{k^3 P_0} (J_0(k^2 \sinh(HP_0)(\gamma k^2 - g\rho) + HkP_0(\cosh(Hk)(gk\rho - \gamma k^3) \\ -2k^2\mu \sinh(Hk)) + 3k^2\mu P_0 \cosh(HP_0) - \mu P_0^3 \cosh(HP_0)) \\ + HkP_0(k \sinh(Hk)(g\rho - \gamma k^2) - 2k^2\mu \cosh(Hk))) & \text{if } n = 0 \\ -\frac{1}{k^3 P_n} (kP_n \cosh(HP_n)(-gJ_n k\rho + \gamma J_n k^3 + 3k^2\mu - \rho\omega^2) \\ + J_n kP_n(\cosh(Hk)(gk\rho - \gamma k^3) + \sinh(Hk)(\rho\omega^2 - 2k^2\mu)) \\ + kP_n(k \sinh(Hk)(g\rho - \gamma k^2) + \cosh(Hk)(\rho\omega^2 - 2k^2\mu)) \\ + k^3 \sinh(HP_n)(\gamma k^2 - g\rho) + J_n P_n^2 \sinh(HP_n)(3k^2\mu - \rho\omega^2) \\ + J_n(-\mu)P_n^4 \sinh(HP_n) - k\mu P_n^3 \cosh(HP_n)) & \text{if } n \neq 0 \end{cases} \\
 T_n|_{\lambda_x=1} &= \begin{cases} -\frac{\rho}{kP_0} (J_0(\sinh(HP_0) - HP_0 \cosh(Hk)) - HP_0 \sinh(Hk)) & \text{if } n = 0 \\ -\frac{\rho}{kP_n} (J_n(P_n \cosh(HP_n) - P_n \cosh(Hk)) \\ - P_n \sinh(Hk) + k \sinh(HP_n)) & \text{if } n \neq 0 \end{cases} \\
 \Sigma_n|_{\lambda_x=1} &= \begin{cases} -\frac{\rho}{kP_0} (J_0(\sinh(HP_0) - HP_0 \cosh(Hk)) - HP_0 \sinh(Hk)) & \text{if } n = 0 \\ -\frac{\rho}{kP_n} (J_n(P_n \cosh(HP_n) - P_n \cosh(Hk)) \\ - P_n \sinh(Hk) + k \sinh(HP_n)) & \text{if } n \neq 0 \end{cases}
 \end{aligned}$$

with J_n is defined in Eq. (3.138).

*È assai più bello sapere un po' di tutto che
saper tutto di una cosa.*

B. Pascal

4

Conclusion and perspectives

This thesis has dealt with several physical problems concerning soft and active matter. We performed several investigations by proposing *ad hoc* models that have been solved using Mathematical and Physical methods and techniques.

More precisely, we focused on two main phenomena: self-organization and pattern formation in soft matter. The first one is a spontaneous process which gives to a disordered system a specific order, whereas pattern formation refers to the generation of complex configurations organized in space and time.

The main results are briefly summarized in the following.

SELF-ORGANIZATION IN SOFT MATTER In Chapter 2, we characterized the phenomenon of self-organization in soft matter.

First, we studied how Geometry and Mechanics have both a relevant role in determining the three-dimensional packing of eight soap bubbles, to mimic the mitotic process in the embryo and precisely the transition from eight-cells stage to sixteen-cells stage. We focused on a particular configuration of 8 bubbles and we investigated the mechanical distribution of forces. The toy model is composed by 7 identical spheres symmetrically surrounding a central one: their initial position is dictated by the solution of the Tammes problem [306], while the final one is obtained by a compaction process which results into a full tiling of the central sphere. The obtained rearrangement is an equilibrium one and by proving suitable physical criteria of optimality we might ensure that our polyhedron is the optimal one among all the possible convex polytopes inscribed into a sphere [64]. Fixing this geometrical arrangement, we looked for the force balance that realizes such a configuration. The obtained force field showed an anisotropy in its orientation, suggesting that difference in tensions might be crucial for next topological transitions. The power of this method is its non-destructive technique which will be perfect to design new metamaterials, where it is fundamental to know a priori the distribution of forces.

Secondly, we extended recent results of the Plateau problem, which in its simplest form studies the existence of a surface spanning a given boundary. Precisely, we solved the so-called Kirchhoff-Plateau problem, in which the fixed boundary is replaced by an elastic rod adding another unknown to the problem.

We started studying the equilibrium configuration of a system consisting by two Kirchhoff rods linked in an arbitrary way and tied by a soap film. The major difference with respect to [156] is the fact that the second loop did not have a fixed position in space, while the first had a prescribed frame at a point. For the energy functional of the system, we considered three contributions: the elastic and the potential energy for the link, since the

thickness is not zero, and the surface tension energy of the film. The main difficulty consisted in looking for a suitable definition of spanning surface, since we did not want to prescribe *a priori* the region of the boundary touched by the film. We used a proper definition introduced by Harrison [172] based on the concept of linking number and the reformulation of the concept *spanning* proposed by De Lellis [112], fundamental to gain the necessary regularity. Then, we proved the existence of a solution with minimum energy and we performed some experiments to confirm the kind of surface predicted by the model.

Second, we modified the previous model by introducing an additional contribution into the energy functional to describe the process of the absorption of a protein by a biological membrane. After constructing a system consisting of two Kirchhoff rods linked in an arbitrary way and also forming knots, constrained not to touch themselves by means of an electrical repulsion and tied by a soap film, we proved the existence of a solution with minimum total energy.

Finally, we studied what happens to the Kirchhoff-Plateau problem when the thickness of the rod vanishes, *i.e.* when the rod shrinks to a line, to try to recover the Plateau problem with an elastic boundary curve. After studying simple examples using the linear and the nonlinear elasticity to show that the limiting curve may retain some “memory” of the twisting, we conjectured that something more than the simple image of the curve must be given in order to model the associated elastic energy. Indeed, by using the Γ -convergence technique, we performed a dimensional reduction of the classical Kirchhoff-Plateau problem, obtaining that the limiting curve is the midline of the rod itself, *i.e.* it is a framed curve that can sustain bending and twisting. Hence, the approximating problems have minima which converge weakly to the minimum energy solution of the limit problem, as well as the corresponding value of the energy, showing that the Plateau solution with elastic boundary may be approximated by solutions of the problems with a rod boundary.

PATTERN FORMATION IN SOFT MATTER In Chapter 3, we modeled active processes and their consequences in living matter. In soft solids, the coupling between physical and geometrical nonlinearities leads to non-convex energies that admit multiple local minimizers. Thus, a morphological transition may occur as the result of the accumulation in the elastic body of mechanical residual stress. In porous media, the presence of an additional source term, introduced to mimic the cell proliferation in tissue growth, implied the introduction of an exhaustive regularity theory to correctly describe the evolution of tumor density cell over time.

First, to study the gyrification phenomenon, *i.e.* the formation of folded structures in brain organoids, we proposed a morphoelastic model in which brain organoids are described as disks surrounded by a growing rim and subjected to a surface tension generated by intercellular adhesion forces. We assumed that the two regions (disk and outer growing rim) are composed of the same incompressible neo-Hookean material, whose growth is modeled using the multiplicative decomposition of the deformation gradient. Computing a radially symmetric solution, we performed its linear stability analysis using the method of incremental deformation superposed on a finite stress. The introduction of a tissue surface tension strongly influences the stability of the base solution and alters the critical wavelength. The post-buckling morphology is studied using a mixed finite element formulation in the fully nonlinear regime. The obtained result suggests that the interplay between elasticity and tissue surface tension plays a crucial role in controlling pattern selection in embryo morphogenesis and it strengthens the importance of considering surface tension in modeling cellular aggregates.

Second, we developed a simple morphomechanical model to describe the dextral torsion during the *c*-looping of the heart tube (HT), which represents the first asymmetry during the embryogenesis of the human heart. We proposed a nonlinear elastic model of the HT undergoing torsional remodeling, describing it as a hollow cylinder whose aspect ratio

and length are obtained by experimental observations. We computed a radially symmetric solution, we studied its linear stability using the theory of incremental deformations and we solved the corresponding incremental problem using the Stroh formulation and the impedance matrix method. The geometry of the cylinder controls the onset of a bifurcation: both the critical circumferential and axial modes strongly depend on the aspect ratio and on the length of the cylinder itself. We implemented a finite element code using a mixed variational formulation whose linearization is based on the Newton method. Our morphomechanical model suggests that a torsional internal remodeling alone can drive the spontaneous onset and the fully nonlinear development of the c -looping of the heart tube.

Third, we investigated the onset of Faraday instability in a pre-stretched elastic slab, assumed to behave as a neo-Hookean material, attached at the bottom to a rigid substrate and subjected to a vertical oscillation. We used the Floquet theory to study the onset of harmonic and subharmonic resonance eigenmodes from a finite homogeneous deformation of the elastic slab. We found that Faraday instability in soft solids is characterized by a harmonic resonance in the physical range of the material parameters, in contrast to the subharmonic resonance that is known to characterize viscous fluids [81]. Noteworthy, we found that the application of a finite pre-stretch can alter significantly the marginal stability curves and the morphology of the emerging standing waves. This novel result suggests a new path for the experimental characterization of soft materials using Faraday waves to distinguish solid-like from fluid-like responses of soft matter at different scales.

Finally, to characterize cancer invasion we studied the evolution of a tumor cell density through a porous-media and we include an additional source term to model the cell division rate. Hence, we needed to extend the Aronson-Bénilan estimate on second order derivatives for the solution of the porous-media equation. Precisely, thanks to this control, two different approaches of tissue growth, *i.e.* the partial differential equations (PDEs) types, where tumor cells are represented by densities, and the free boundary approach, in

which tissue growth is due to the motion of its boundary, are linked using the so-called *incompressible limit*. We systematically studied the restrictions on the parameters and the conclusions that one can draw in L^1 , L^2 and L^∞ (original work of Aronson and Bénilan): the L^∞ setting provides the widest range of parameters, generating the strongest estimate since it can be applied to all the pressure laws; the L^2 estimate requires restrictions on the parameters and the L^1 estimate turns out to be the simplest but it is only useful in space dimension $N = 1$. When weights are included to treat more general equations of state, we improve the results of [102] but we pay in regularity near the free boundary.

FUTURE DEVELOPMENTS The research field concerning the formulation and analysis of mathematical models for soft biological matter is rapidly expanding and several open challenges have to be tackled. Beyond the few achievements provided in this thesis, there are several improvements that will be addressed in future works. Without pretending to give a full overview of the many open problems in the field, in the following I summarize some questions that are more directly related to the main object of this thesis.

For what concerns the formulation of the Plateau problem, in this thesis we mainly focus on looking for the minimum of the associated energy functional which can be physically visualized by putting a wire in a film solution, since it realizes a stable configuration. Future developments will be devoted in getting a complete characterization of the mechanical structure of the Plateau problem by classifying and computing all the critical points, *i.e.* all the equilibrium configurations. Recently, a new mathematical tool has been introduced to find first simple closed geodesics on spheres [103] and then to characterize minimal surfaces in the manifold environment [97]. Hence, a possible line of research that I am interesting in developing is using the *Min-max theory* to recover the already known minima, then to prove the existence and the stability of non-trivial critical points and finally, to visualize the obtained shapes using efficient numerical tools. Indeed, numerical

aspects of the Kirchhoff-Plateau problem are quite difficult due to its mathematical formulation, namely the intersection set between the boundary of the rod and the soap film is not known a priori. A big challenge that it will be interesting to study is finding a suitable mathematical characterization of this set which will open new paths in numerical investigations [57, 155].

Moreover, there is the necessity of further developing perturbative theories in a weakly non-linear regime in solid mechanics for a deeper theoretical understanding of pattern formations. Indeed, another interesting research line that I would like to develop is to try to extend theories coming from dynamical systems to nonlinear elasticity. These techniques have been recently developed to analyze the existence of periodic and quasi-periodic solutions (KAM Theory) of some equations arising from fluid dynamics [185, 28, 29]. In this thesis, we exploited only the linear behavior of Faraday waves in soft elastic solids and it will be interesting to analyze the nonlinear regime by using *normal form* procedure, in the spirit of KAM theory.

Finally, all the studied problems were motivated primarily by biological phenomena. The main drawback of studying a real phenomenon is the huge complexity in its description. For instance, we considered a simplified geometry or we reduced the dimension of the problem setting. It will be not only interesting but I think more useful to introduce more realistic models, to really help the medical community in understanding the biological process and overcoming possible related pathologies. It is my personal belief that future developments in this research field will be driven by interactions among different disciplines, including new analytical tools to investigate strong nonlinearities, more refined models to capture a wider physical complexity of modeled systems and efficient numerical methods to approximate accurately their solutions.

References

- [1] Acerbi, E. & Fusco, N. (1984). Semicontinuity problems in the calculus of variations. *Archive for Rational Mechanics and Analysis*, 86(2), 125–145.
- [2] Alberts, B., Johnson, A., Lewis, J., Walter, P., Raff, M., & Roberts, K. (2002). *Molecular biology of the cell* 4th edition: International student edition.
- [3] Allaire, G. (1991). Homogenization of the navier-stokes equations and derivation of brinkmans law. *Mathématiques appliquées aux sciences de l'ingénieur (Santiago, 1989)*, (pp. 7–20).
- [4] Almeida, L., Bubba, F., Perthame, B., & Pouchol, C. (2019). Energy and implicit discretization of the fokker-planck and keller-segel type equations. *Networks and Heterogeneous Media*, 14(1).
- [5] Almgren, F. J. (1968). Existence and regularity almost everywhere of solutions to elliptic variational problems among surfaces of varying topological type and singularity structure. *The Annals of Mathematics*, 87(2), 321.
- [6] Almgren, F. J. (1976). Existence and regularity almost everywhere of solutions to elliptic variational problems with constraints. *Memoirs of the American Mathematical Society*, 4(165), 0–0.
- [7] Alnæs, M. S., Logg, A., Ølgaard, K. B., Rognes, M. E., & Wells, G. N. (2014). Unified form language. *ACM Transactions on Mathematical Software*, 40(2), 1–37.
- [8] Amar, M. B. & Ciarletta, P. (2010). Swelling instability of surface-attached gels as a model of soft tissue growth under geometric constraints. *Journal of the Mechanics and Physics of Solids*, 58(7), 935–954.
- [9] Amar, M. B. & Goriely, A. (2005). Growth and instability in elastic tissues. *Journal of the Mechanics and Physics of Solids*, 53(10), 2284–2319.
- [10] Ambrosi, D., Ateshian, G. A., Arruda, E. M., Cowin, S., Dumais, J., Goriely, A., Holzapfel, G. A., Humphrey, J. D., Kemkemer, R., Kuhl, E., et al. (2011). Perspectives on biological growth and remodeling. *Journal of the Mechanics and Physics of Solids*, 59(4), 863–883.

- [11] Ambrosi, D., Pezzuto, S., Riccobelli, D., Stylianopoulos, T., & Ciarletta, P. (2017). Solid tumors are poroelastic solids with a chemo-mechanical feedback on growth. *Journal of Elasticity*, 129(1-2), 107–124.
- [12] Amestoy, P., Duff, I., & L’Excellent, J.-Y. (2000). Multifrontal parallel distributed symmetric and unsymmetric solvers. *Computer Methods in Applied Mechanics and Engineering*, 184(2-4), 501–520.
- [13] Angenent, S. & Aronson, D. (1995). The focusing problem for the radially symmetric porous medium equation. *Communications in Partial Differential Equations*, 20(7-8), 1217–1240.
- [14] Ansari, M. H. & Smolin, L. (2008). Self-organized criticality in quantum gravity. *Classical and Quantum Gravity*, 25(9), 095016.
- [15] Antman, S. S. (1995). *Nonlinear Problems of Elasticity*. Springer New York.
- [16] Aronson, D. G. (1969). Regularity properties of flows through porous media. *SIAM Journal on Applied Mathematics*, 17(2), 461–467.
- [17] Aronson, D. G. (1970a). Regularity properties of flows through porous media: A counterexample. *SIAM Journal on Applied Mathematics*, 19(2), 299–307.
- [18] Aronson, D. G. (1970b). Regularity properties of flows through porous media: The interface. *Archive for Rational Mechanics and Analysis*, 37(1), 1–10.
- [19] Aronson, D. G. & Bénilan, P. (1979). Régularité des solutions de l’équation des milieux poreux dans \mathbb{R}^n . *CR Acad. Sci. Paris Sér. AB*, 288(2), A103–A105.
- [20] Aronson, D. G. & Graveleau, J. (1993). A selfsimilar solution to the focusing problem for the porous medium equation. *European Journal of Applied Mathematics*, 4(1), 65–81.
- [21] Auricchio, F., Da Veiga, L. B., Lovadina, C., Reali, A., Taylor, R. L., & Wriggers, P. (2013). Approximation of incompressible large deformation elastic problems: some unresolved issues. *Computational Mechanics*, 52(5), 1153–1167.
- [22] Balay, S., Abhyankar, S., Adams, M., Brown, J., Brune, P., Buschelman, K., Dalcin, L., Dener, A., Eijkhout, V., Gropp, W., Kaushik, D., Knepley, M., May, D., McInnes, L. C., Munson, T., Rupp, K., Sanan, P., Smith, B., Zampini, S., Zhang, H., & Zhang, H. (2018). *PETSc Users Manual: Revision 3.10*. Technical report, Argonne National Lab.(ANL), Argonne, IL (United States).
- [23] Balbi, V. & Ciarletta, P. (2013). Morpho-elasticity of intestinal villi. *Journal of The Royal Society Interface*, 10(82), 20130109–20130109.

- [24] Balbi, V. & Ciarletta, P. (2015). Helical buckling of thick-walled, pre-stressed, cylindrical tubes under a finite torsion. *Mathematics and Mechanics of Solids*, 20(6), 625–642.
- [25] Balbi, V., Destrade, M., & Goriely, A. (2020). Mechanics of human brain organoids. *Physical Review E*, 101(2).
- [26] Balbi, V., Kuhl, E., & Ciarletta, P. (2015). Morphoelastic control of gastro-intestinal organogenesis: theoretical predictions and numerical insights. *Journal of the Mechanics and Physics of Solids*, 78, 493–510.
- [27] Balbi, V., Trotta, A., Destrade, M., & Annaihd, A. N. (2019). Poynting effect of brain matter in torsion. *Soft Matter*, 15(25), 5147–5153.
- [28] Baldi, P., Berti, M., Haus, E., & Montalto, R. (2018). Time quasi-periodic gravity water waves in finite depth. *Inventiones mathematicae*, 214(2), 739–911.
- [29] Baldi, P. & Montalto, R. (2020). Quasi-periodic incompressible euler flows in 3d. *arXiv preprint arXiv:2003.14313*.
- [30] Ball, J. M. (1976). Convexity conditions and existence theorems in nonlinear elasticity. *Archive for rational mechanics and Analysis*, 63(4), 337–403.
- [31] Barenblatt, G. I. (1952). On some unsteady motions of a liquid and gas in a porous medium. *Akad. Nauk SSSR. Prikl. Mat. Meh.*, 16, 67–78.
- [32] Barlow, S. M. & Raval, R. (2003). Complex organic molecules at metal surfaces: bonding, organisation and chirality. *Surface Science Reports*, 50(6-8), 201–341.
- [33] Batchelor, G. K. (2000). *An introduction to fluid dynamics*. Cambridge university press.
- [34] Bayly, P., Taber, L., & Kroenke, C. (2014). Mechanical forces in cerebral cortical folding: A review of measurements and models. *Journal of the Mechanical Behavior of Biomedical Materials*, 29, 568–581.
- [35] Bellomo, N., Bianca, C., & Delitala, M. (2009). Complexity analysis and mathematical tools towards the modelling of living systems. *Physics of Life Reviews*, 6(3), 144–175.
- [36] Bellomo, N. & De Agelis, E. (2003). Modeling and simulation of tumor development, treatment, and control. *Mathematical and computer modelling*, 37(11).
- [37] Bellomo, N., Li, N., & Maini, P. K. (2008). On the foundations of cancer modelling: selected topics, speculations, and perspectives. *Mathematical Models and Methods in Applied Sciences*, 18(04), 593–646.

- [38] Ben Amar, M. & Ciarletta, P. (2010). Swelling instability of surface-attached gels as a model of soft tissue growth under geometric constraints. *Journal of the Mechanics and Physics of Solids*, 58(7), 935–954.
- [39] Ben Amar, M. & Jia, F. (2013). Anisotropic growth shapes intestinal tissues during embryogenesis. *Proceedings of the National Academy of Sciences*, 110(26), 10525–10530.
- [40] Bénilan, P., Boccardo, L., & Herrero, M. A. (1989). On the limit of solutions of $u_t = \delta u^m$ as $m \rightarrow \infty$.
- [41] Benjamin, T. B. & Ursell, F. J. (1954). The stability of the plane free surface of a liquid in vertical periodic motion. *Proceedings of the Royal Society of London. Series A. Mathematical and Physical Sciences*, 225(1163), 505–515.
- [42] Berger, M. (2010). *Geometry revealed: a Jacob’s ladder to modern higher geometry*. Springer Science & Business Media.
- [43] Bernatzki, F. (1997). On the existence and regularity of mass-minimizing currents with an elastic boundary. *Annals of Global Analysis and Geometry*, 15(5), 379–399.
- [44] Bernatzki, F. & Ye, R. (2001). Minimal surfaces with an elastic boundary. *Annals of Global Analysis and Geometry*, 19(1), 1–9.
- [45] Bevilacqua, G. (2020). Symmetry break in the eight bubble compaction. *arXiv preprint arXiv:2007.15399*.
- [46] Bevilacqua, G., Ciarletta, P., & Quarteroni, A. (2020a). Morphomechanical model of the torsional c-looping in the embryonic heart. *arXiv preprint arXiv:2010.01006*.
- [47] Bevilacqua, G., Lussardi, L., & Marzocchi, A. (2018a). Soap film spanning an elastic link. *Quarterly of Applied Mathematics*, 77(3), 507–523.
- [48] Bevilacqua, G., Lussardi, L., & Marzocchi, A. (2018b). Soap film spanning electrically repulsive elastic protein links. *Atti della Accademia Peloritana dei Pericolanti-Classe di Scienze Fisiche, Matematiche e Naturali*, 96(S3), 1.
- [49] Bevilacqua, G., Lussardi, L., & Marzocchi, A. (2020b). Dimensional reduction of the kirchhoff-plateau problem. *Journal of Elasticity*, (pp. 1–14).
- [50] Bevilacqua, G., Perthame, B., & Schmidtchen, M. (2020c). The aronson-b\’enilan estimate in lebesgue spaces. *arXiv preprint arXiv:2007.15267*.
- [51] Bevilacqua, G., Shao, X., Saylor, J. R., Bostwick, J. B., & Ciarletta, P. (2020d). Faraday waves in soft elastic solids. *Proceedings of the Royal Society A*, 476(2241), 20200129.

- [52] Beyer, J. & Friedrich, R. (1995). Faraday instability: linear analysis for viscous fluids. *Physical Review E*, 51(2), 1162.
- [53] Bikerman, J. (1973). Formation and structure. In *Foams* (pp. 33–64). Springer.
- [54] Biot, M. A. (1938). Theory of elasticity with large displacements and rotations.
- [55] Biot, M. A. (1963). Surface instability of rubber in compression. *Applied Scientific Research, Section A*, 12(2), 168–182.
- [56] Biot, M. A. (1965). *Mechanics of incremental deformations*.
- [57] Biria, A. & Fried, E. (2014). Buckling of a soap film spanning a flexible loop resistant to bending and twisting. *Proceedings of the Royal Society A: Mathematical, Physical and Engineering Sciences*, 470(2172), 20140368.
- [58] Biria, A. & Fried, E. (2015). Theoretical and experimental study of the stability of a soap film spanning a flexible loop. *International Journal of Engineering Science*, 94, 86–102.
- [59] Biryukov, S. (1985). Impedance method in the theory of elastic surface waves. *Soviet Physics. Acoustic*.
- [60] Biryukov, S. V., Gulyaev, Y. V., Krylov, V. V., & Plessky, V. P. (1995). *Surface Acoustic Waves in Inhomogeneous Media*. Springer Berlin Heidelberg.
- [61] Boffi, D., Brezzi, F., & Fortin, M. (2013). *Mixed Finite Element Methods and Applications*. Springer Berlin Heidelberg.
- [62] Brakke, K. & Morgan, F. (2002). Instabilities of cylindrical bubble clusters. *The European Physical Journal E*, 9(1), 453–460.
- [63] Bresch, D., Colin, T., Grenier, E., Ribba, B., & Saut, O. (2010). Computational modeling of solid tumor growth: the avascular stage. *SIAM Journal on Scientific Computing*, 32(4), 2321–2344.
- [64] Brinkmann, G., McKay, B. D., et al. (2007). Fast generation of planar graphs. *MATCH Commun. Math. Comput. Chem*, 58(2), 323–357.
- [65] Bubba, F., Perthame, B., Pouchol, C., & Schmidtchen, M. (2020). Hele–shaw limit for a system of two reaction-(cross-) diffusion equations for living tissues. *Archive for Rational Mechanics and Analysis*, 236(2), 735–766.
- [66] Budday, S., Sommer, G., Birkl, C., Langkammer, C., Haybaeck, J., Kohnert, J., Bauer, M., Paulsen, F., Steinmann, P., Kuhl, E., & Holzapfel, G. (2017a). Mechanical characterization of human brain tissue. *Acta Biomaterialia*, 48, 319–340.

- [67] Budday, S., Sommer, G., Haybaeck, J., Steinmann, P., Holzapfel, G., & Kuhl, E. (2017b). Rheological characterization of human brain tissue. *Acta Biomaterialia*, 60, 315–329.
- [68] Budday, S., Steinmann, P., & Kuhl, E. (2014). The role of mechanics during brain development. *Journal of the Mechanics and Physics of Solids*, 72, 75–92.
- [69] Byrne, H. & Drasdo, D. (2009). Individual-based and continuum models of growing cell populations: a comparison. *Journal of mathematical biology*, 58(4-5), 657.
- [70] Byrne, H. M. & Chaplain, M. A. J. (1996). Modelling the role of cell-cell adhesion in the growth and development of carcinomas. *Mathematical and Computer Modelling*, 24(12), 1–17.
- [71] Caffarelli, L. & Evans, L. (1983). Continuity of the temperature in the two-phase stefan problem. *Archive for Rational Mechanics and Analysis*, 81(3), 199–220.
- [72] Caffarelli, L. & Friedman, A. (1979a). Continuity of the Density of a Gas Flow in a Porous Medium. *Transactions of the American Mathematical Society*, 252, 99.
- [73] Caffarelli, L. & Friedman, A. (1979b). Regularity of the free boundary for the one-dimensional flow of gas in a porous medium. *American Journal of Mathematics*, 101(6), 1193–1218.
- [74] Caffarelli, L. & Friedman, A. (1980). Regularity of the Free Boundary of a Gas Flow in an n-dimensional Porous Medium. *Indiana University Mathematics Journal*, 29, 361–391.
- [75] Caffarelli, L., Vázquez, J.-L., & Wolanski, N. (1987). Lipschitz continuity of solutions and interfaces of the n-dimensional porous medium equation. *Indiana University mathematics journal*, 36(2), 373–401.
- [76] Camazine, S., Deneubourg, J.-L., Franks, N. R., Sneyd, J., Bonabeau, E., & Theraula, G. (2003). *Self-organization in biological systems*. Princeton university press.
- [77] Cantat, I., Cohen-Addad, S., Elias, F., Graner, F., Höhler, R., Pitois, O., Rouyer, F., & Saint-Jalmes, A. (2013). *Foams: structure and dynamics*. OUP Oxford.
- [78] Cao, Y.-P., Li, B., & Feng, X.-Q. (2012). Surface wrinkling and folding of core-shell soft cylinders. *Soft Matter*, 8(2), 556–562.
- [79] Carrillo, J. A., Fagioli, S., Santambrogio, F., & Schmidtchen, M. (2018). Splitting schemes and segregation in reaction cross-diffusion systems. *SIAM Journal on Mathematical Analysis*, 50(5), 5695–5718.
- [80] Carroll, M. (2004). A representation theorem for volume-preserving transformations. *International journal of non-linear mechanics*, 39(2), 219–224.

- [81] Carroll, M. M. (1967). Some results on finite amplitude elastic waves. *Acta Mechanica*, 3(2), 167–181.
- [82] Cauchy, A.-L. (1813). Recherches sur les polyedres. *J. Ecole Polytechnique*, 9(16), 68–86.
- [83] Chakrabarti, A., Mora, S., Richard, F., Phou, T., Fromental, J.-M., Pomeau, Y., & Audoly, B. (2018). Selection of hexagonal buckling patterns by the elastic rayleigh-taylor instability. *Journal of the Mechanics and Physics of Solids*, 121, 234–257.
- [84] Chen, Y. C. & Fried, E. (2013). Stability and bifurcation of a soap film spanning a flexible loop. *Journal of Elasticity*, 116(1), 75–100.
- [85] Cheng, G., Tse, J., Jain, R. K., & Munn, L. L. (2009). Micro-environmental mechanical stress controls tumor spheroid size and morphology by suppressing proliferation and inducing apoptosis in cancer cells. *PLoS ONE*, 4(2), e4632.
- [86] Chertock, A., Degond, P., Hecht, S., & Vincent, J. (2019). Incompressible limit of a continuum model of tissue growth with segregation for two cell populations. *Mathematical biosciences and engineering: MBE*, 16(5), 5804.
- [87] Chuong, C. J. & Fung, Y. C. (1986). Residual stress in arteries. In *Frontiers in Biomechanics* (pp. 117–129). Springer New York.
- [88] Ciarlet, P. G. (1988). *Mathematical Elasticity: Volume I: three-dimensional elasticity*. North-Holland.
- [89] Ciarlet, P. G. & Nečas, J. (1987). Injectivity and self-contact in nonlinear elasticity. *Archive for Rational Mechanics and Analysis*, 97(3).
- [90] Ciarletta, P. (2011). Generating functions for volume-preserving transformations. *International Journal of Non-Linear Mechanics*, 46(9), 1275–1279.
- [91] Ciarletta, P. (2014). Wrinkle-to-fold transition in soft layers under equi-biaxial strain: A weakly nonlinear analysis. *Journal of the Mechanics and Physics of Solids*, 73, 118–133.
- [92] Ciarletta, P., Balbi, V., & Kuhl, E. (2014). Pattern selection in growing tubular tissues. *Physical Review Letters*, 113(24).
- [93] Ciarletta, P., Foret, L., & Ben Amar, M. (2011). The radial growth phase of malignant melanoma: multi-phase modelling, numerical simulations and linear stability analysis. *Journal of the Royal Society Interface*, 8(56), 345–368.
- [94] Ciarletta, P. & Truskinovsky, L. (2019). Soft nucleation of an elastic crease. *Physical Review Letters*, 122(24).

- [95] Ciliberto, S. & Gollub, J. (1985). Chaotic mode competition in parametrically forced surface waves. *Journal of Fluid Mechanics*, 158, 381–398.
- [96] Clare, B. & Kepert, D. (1986). The closest packing of equal circles on a sphere. *Proc. R. Soc. Lond. A*, 405(1829), 329–344.
- [97] Colding, T. & Lellis, C. d. (2003). The min-max construction of minimal surfaces. *Surveys in Differential Geometry*, 8(1), 75–107.
- [98] Coleman, B. D. & Noll, W. (1959). On the thermostatics of continuous media. *Archive for rational mechanics and analysis*, 4(1), 97–128.
- [99] Couder, Y., Protiere, S., Fort, E., & Boudaoud, A. (2005). Dynamical phenomena: Walking and orbiting droplets. *Nature*, 437(7056), 208.
- [100] Cox, S., Graner, F., Vaz, F., Monnereau-Pittet, C., & Pittet, N. (2003a). Minimal perimeter for n identical bubbles in two dimensions: calculations and simulations. *Philosophical Magazine*, 83(11), 1393–1406.
- [101] Cox, S., Vaz, M., & Weaire, D. (2003b). Topological changes in a two-dimensional foam cluster. *The European Physical Journal E*, 11(1), 29–35.
- [102] Crandall, M. G. & Pierre, M. (1982). Regularizing effects for $u_t = \Delta\varphi(u)$. *Trans. Amer. Math. Soc.*, 274(1), 159–168.
- [103] Croke, C. B. et al. (1988). Area and the length of the shortest closed geodesic. *Journal of Differential Geometry*, 27(1), 1–21.
- [104] Cross, M. C. & Hohenberg, P. C. (1993). Pattern formation outside of equilibrium. *Reviews of modern physics*, 65(3), 851.
- [105] Cui, S. & Escher, J. (2008). Asymptotic behaviour of solutions of a multidimensional moving boundary problem modeling tumor growth. *Communications in Partial Differential Equations*, 33(4), 636–655.
- [106] Dacorogna, B. (1989). *Direct Methods in the Calculus of Variations*. Springer Berlin Heidelberg.
- [107] Darcy, H. P. G. (1856). *Les Fontaines publiques de la ville de Dijon. Exposition et application des principes à suivre et des formules à employer dans les questions de distribution d'eau, etc.* V. Dalamont.
- [108] Daudet, L., Ego, V., Manneville, S., & Bechhoefer, J. (1995). Secondary instabilities of surface waves on viscous fluids in the faraday instability. *EPL (Europhysics Letters)*, 32(4), 313.

- [109] David, G. (2017). *Should We Solve Plateau’s Problem Again?* Princeton University Press.
- [110] David, N. & Perthame, B. (2020). Free boundary limit of tumor growth model with nutrient. *arXiv preprint arXiv:2003.10731*.
- [111] Davis, G. S., Phillips, H. M., & Steinberg, M. S. (1997). Germ-layer surface tensions and “tissue affinities” in *Rana pipiens* Gastrulae: Quantitative measurements. *Developmental Biology*, 192(2), 630–644.
- [112] De Lellis, C., Ghiraldin, F., & Maggi, F. (2017). A direct approach to plateau’s problem. *Journal of the European Mathematical Society*, 19(8).
- [113] De Philippis, G., De Rosa, A., & Ghiraldin, F. (2016). A direct approach to plateau’s problem in any codimension. *Advances in Mathematics*, 288, 59–80.
- [114] Debiec, T., Perthame, B., Schmidtchen, M., & Vauchelet, N. (2020). Incompressible limit for a two-species model with coupling through brinkman’s law in any dimension. *ArXiv*.
- [115] Debiec, T. & Schmidtchen, M. (2020). Incompressible limit for a two-species tumour model with coupling through brinkmans law in one dimension. *Acta Applicandae Mathematicae*, (pp. 1–19).
- [116] Degond, P., Hecht, S., Vauchelet, N., & and (2020). Incompressible limit of a continuum model of tissue growth for two cell populations. *Networks & Heterogeneous Media*, 15(1), 57–85.
- [117] DeHaan, R. L. (1967). Development of form in the embryonic heart an experimental approach. *Circulation*, 35(5), 821–833.
- [118] Deroulers, C., Aubert, M., Badoual, M., & Grammaticos, B. (2009). Modeling tumor cell migration: from microscopic to macroscopic models. *Physical Review E*, 79(3), 031917.
- [119] Dervaux, J. & Ben Amar, M. (2011). Buckling condensation in constrained growth. *Journal of the Mechanics and Physics of Solids*, 59(3), 538–560.
- [120] Destrade, M., Gilchrist, M., Murphy, J., Rashid, B., & Saccomandi, G. (2015). Extreme softness of brain matter in simple shear. *International Journal of Non-Linear Mechanics*, 75, 54–58.
- [121] Destrade, M., Ní Annaidh, A., & Coman, C. D. (2009). Bending instabilities of soft biological tissues. *International Journal of Solids and Structures*, 46(25-26), 4322–4330.

- [122] Dobyns, W. B. (1993). Lissencephaly. a human brain malformation associated with deletion of the LIS1 gene located at chromosome 17p13. *JAMA: The Journal of the American Medical Association*, 270(23), 2838–2842.
- [123] Donnell, L. H. (1935). Stability of thin-walled tubes under torsion.
- [124] Douady, S. (1990). Experimental study of the faraday instability. *Journal of fluid mechanics*, 221, 383–409.
- [125] Douady, S. & Fauve, S. (1988). Pattern selection in faraday instability. *EPL (Europhysics Letters)*, 6(3), 221.
- [126] Douglas, J. (1931). Solution of the problem of plateau. *Transactions of the American Mathematical Society*, 33(1), 263–321.
- [127] Drasdo, D. & Hoehme, S. (2012). Modeling the impact of granular embedding media, and pulling versus pushing cells on growing cell clones. *New Journal of Physics*, 14(5), 055025.
- [128] Druet, P.-E. & Jüngel, A. (2020). Analysis of cross-diffusion systems for fluid mixtures driven by a pressure gradient. *SIAM Journal on Mathematical Analysis*, 52(2), 2179–2197.
- [129] Edwards, W. S. & Fauve, S. (1994). Patterns and quasi-patterns in the faraday experiment. *Journal of Fluid Mechanics*, 278, 123–148.
- [130] Emuna, N. & Durban, D. (2020). Stability analysis of arteries under torsion. *Journal of biomechanical engineering*, 142(6).
- [131] Engstrom, T., Zhang, T., Lawton, A., Joyner, A., & Schwarz, J. (2018). Buckling without bending: A new paradigm in morphogenesis. *Physical Review X*, 8(4).
- [132] Evans, L. C. (2015). *Measure Theory and Fine Properties of Functions, Revised Edition*. Chapman and Hall/CRC.
- [133] Exerowa, D. & Kruglyakov, P. M. (1997). *Foam and foam films: theory, experiment, application*. Elsevier.
- [134] Faraday, M. (1831). Xvii. on a peculiar class of acoustical figures; and on certain forms assumed by groups of particles upon vibrating elastic surfaces. *Philosophical transactions of the Royal Society of London*, 121, 299–340.
- [135] Federer, H. (2014). *Geometric measure theory*. Springer.
- [136] Federer, H. & Fleming, W. H. (1960). Normal and integral currents. *Annals of Mathematics*, (pp. 458–520).

- [137] Fichera, G. (1973). Existence theorems in elasticity. In *Linear theories of elasticity and thermoelasticity* (pp. 347–389). Springer.
- [138] Forgacs, G., Foty, R. A., Shafrir, Y., & Steinberg, M. S. (1998). Viscoelastic properties of living embryonic tissues: a quantitative study. *Biophysical Journal*, 74(5), 2227–2234.
- [139] Fortes, M., Vaz, M. F., Cox, S., & Teixeira, P. (2007). Instabilities in two-dimensional flower and chain clusters of bubbles. *Colloids and Surfaces A: Physicochemical and Engineering Aspects*, 309(1-3), 64–70.
- [140] Foty, R. A., Forgacs, G., Pflieger, C. M., & Steinberg, M. S. (1994). Liquid properties of embryonic tissues: Measurement of interfacial tensions. *Physical Review Letters*, 72(14), 2298–2301.
- [141] Foty, R. A., Pflieger, C. M., Forgacs, G., & Steinberg, M. S. (1996). Surface tensions of embryonic tissues predict their mutual envelopment behavior. *Development*, 122(5), 1611–1620.
- [142] Friedman, A. (2004). A hierarchy of cancer models and their mathematical challenges. *Discrete & Continuous Dynamical Systems-B*, 4(1), 147.
- [143] Friedman, A. & Hu, B. (2008). Stability and instability of Liapunov-Schmidt and Hopf bifurcation for a free boundary problem arising in a tumor model. *Transactions of the American Mathematical Society*, 360(10), 5291–5342.
- [144] Fu, Y. (2007). Hamiltonian interpretation of the stroh formalism in anisotropic elasticity. *Proceedings of the Royal Society A: Mathematical, Physical and Engineering Sciences*, 463(2088), 3073–3087.
- [145] Fu, Y. B. & Ciarletta, P. (2015). Buckling of a coated elastic half-space when the coating and substrate have similar material properties. *Proceedings of the Royal Society A: Mathematical, Physical and Engineering Sciences*, 471(2178), 20140979–20140979.
- [146] Fung, Y. C. & Liu, S. Q. (1992). Strain distribution in small blood vessels with zero-stress state taken into consideration. *American Journal of Physiology-Heart and Circulatory Physiology*, 262(2), H544–H552.
- [147] Garofalo, E. (2015). Absidi poligonali e impianti basilicali della sicilia tardomedievale. *TRACCIATI. STORIA E COSTRUZIONE NEL MEDITERRANEO*, (pp. 169–185).
- [148] Gent, A. & Hua, K.-C. (2004). Torsional instability of stretched rubber cylinders. *International Journal of Non-Linear Mechanics*, 39(3), 483–489.

- [149] Gess, B. (2017). Optimal regularity for the porous medium equation. *arXiv preprint arXiv:1708.04408*.
- [150] Gess, B., Sauer, J., & Tadmor, E. (2019). Optimal regularity in time and space for the porous medium equation. *arXiv preprint arXiv:1902.08632*.
- [151] Geuzaine, C. & Remacle, J.-F. (2009). Gmsh: A 3-D finite element mesh generator with built-in pre- and post-processing facilities. *International Journal for Numerical Methods in Engineering*, 79(11), 1309–1331.
- [152] Gil, O. & Quirós, F. (2001). Convergence of the porous media equation to Hele-Shaw. *Nonlinear Analysis: Theory, Methods & Applications*, 44(8), 1111–1131.
- [153] Gil, O. & Quirós, F. (2003). Boundary layer formation in the transition from the porous media equation to a hele–shaw flow. *Annales de l'Institut Henri Poincaré (C) Non Linear Analysis*, 20(1), 13–36.
- [154] Giomi, L. & Mahadevan, L. (2012). Minimal surfaces bounded by elastic lines. *Proceedings of the Royal Society A: Mathematical, Physical and Engineering Sciences*, 468(2143), 1851–1864.
- [155] Giusteri, G. G., Franceschini, P., & Fried, E. (2016). Instability paths in the kirchhoff–plateau problem. *Journal of Nonlinear Science*, 26(4), 1097–1132.
- [156] Giusteri, G. G., Lussardi, L., & Fried, E. (2017). Solution of the kirchhoff–plateau problem. *Journal of Nonlinear Science*, 27(3).
- [157] Giverso, C. & Ciarletta, P. (2016). Tumour angiogenesis as a chemo-mechanical surface instability. *Scientific reports*, 6, 22610.
- [158] Goenezen, S., Rennie, M. Y., & Rugonyi, S. (2012). Biomechanics of early cardiac development. *Biomechanics and modeling in mechanobiology*, 11(8), 1187–1204.
- [159] Goktas, S., Yalcin, O., Ermek, E., Piskin, S., Capraz, C. T., Cakmak, Y. O., & Pekkan, K. (2017). Haemodynamic recovery properties of the torsioned testicular artery lumen. *Scientific reports*, 7(1), 1–9.
- [160] Gonzalez, O., Maddocks, J., Schuricht, F., & von der Mosel, H. (2002). Global curvature and self-contact of nonlinearly elastic curves and rods. *Calculus of Variations and Partial Differential Equations*, 14(1), 29–68.
- [161] Goriely, A. (2017). *The Mathematics and Mechanics of Biological Growth*. Springer New York.
- [162] Goriely, A., Vandiver, R., & Destrade, M. (2008). Nonlinear euler buckling. *Proceedings of the Royal Society A: Mathematical, Physical and Engineering Sciences*, 464(2099), 3003–3019.

- [163] Gray, H. (2009). *Gray's anatomy*. Arcturus Publishing.
- [164] Green, A. E. & Spencer, A. (1958). The stability of a circular cylinder under finite extension and torsion. *Journal of Mathematics and Physics*, 37(1-4), 316–338.
- [165] Greenspan, H. P. (1972). Models for the growth of a solid tumor by diffusion. *Studies in Applied Mathematics*, 51(4), 317–340.
- [166] Greenspan, H. P. (1976). On the growth and stability of cell cultures and solid tumors. *Journal of theoretical biology*, 56(1), 229–242.
- [167] Gurney, W. S. C. & Nisbet, R. M. (1975). The regulation of inhomogeneous populations. *Journal of Theoretical Biology*, 52(2), 441–457.
- [168] Gurtin, M. E. (1982). *An introduction to continuum mechanics*, volume 158. Academic press.
- [169] Gwiazda, P., Perthame, B., & Świerczewska-Gwiazda, A. (2019). A two-species hyperbolic–parabolic model of tissue growth. *Communications in Partial Differential Equations*, 44(12), 1605–1618.
- [170] Hales, T. C. (2001). The honeycomb conjecture. *Discrete & Computational Geometry*, 25(1), 1–22.
- [171] Hamburger, V. & Hamilton, H. L. (1951). A series of normal stages in the development of the chick embryo. *Journal of morphology*, 88(1), 49–92.
- [172] Harrison, J. (2012). Soap film solutions to plateau’s problem. *Journal of Geometric Analysis*, 24(1), 271–297.
- [173] Harrison, J. & Pugh, H. (2016). Existence and soap film regularity of solutions to plateau’s problem. *Advances in Calculus of Variations*, 9(4).
- [174] Hartman, P. (2002). *Ordinary Differential Equations*. Society for Industrial and Applied Mathematics.
- [175] Haughton, D. & Orr, A. (1997). On the eversion of compressible elastic cylinders. *International journal of solids and structures*, 34(15), 1893–1914.
- [176] Hecht, S. & Vauchelet, N. (2017). Incompressible limit of a mechanical model for tissue growth with non-overlapping constraint. *Communications in Mathematical Sciences*, 15(7), 1913–1932.
- [177] Hoang, T. & Fried, E. (2016). Influence of a spanning liquid film on the stability and buckling of a circular loop with intrinsic curvature or intrinsic twist density. *Mathematics and Mechanics of Solids*, 23(1), 43–66.

- [178] Hoger, A. (1985). On the residual stress possible in an elastic body with material symmetry. *Archive for Rational Mechanics and Analysis*, 88(3), 271–289.
- [179] Holland, M., Budday, S., Goriely, A., & Kuhl, E. (2018). Symmetry breaking in wrinkling patterns: Gyri are universally thicker than sulci. *Physical Review Letters*, 121(22).
- [180] Holzapfel, A. G. (2000). Nonlinear solid mechanics ii.
- [181] Huang, H. (1986). Deformation free energy of bilayer membrane and its effect on gramicidin channel lifetime. *Biophysical Journal*, 50(6).
- [182] Hui, C.-Y., Liu, T., & Schwaab, M.-E. (2016). How does surface tension affect energy release rate of cracks loaded in Mode I? *Extreme Mechanics Letters*, 6, 31–36.
- [183] Hutchings, M., Morgan, F., Ritoré, M., & Ros, A. (2002). Proof of the double bubble conjecture. *Annals of Mathematics*, (pp. 459–489).
- [184] Ilin, A. M., Kalashnikov, A. S., & Oleinik, O. A. (1962). Linear equations of the second order of parabolic type. *Russian Mathematical Surveys*, 17(3), 1143.
- [185] Iooss, G., Plotnikov, P. I., & Toland, J. F. (2005). Standing waves on an infinitely deep perfect fluid under gravity. *Archive for rational mechanics and analysis*, 177(3), 367–478.
- [186] Itasaki, N., Nakamura, H., Sumida, H., & Yasuda, M. (1991). Actin bundles on the right side in the caudal part of the heart tube play a role in dextro-looping in the embryonic chick heart. *Anatomy and embryology*, 183(1), 29–39.
- [187] Itô, Y. (1952). The growth form of populations in some aphids, with special reference to the relation between population density and the movements. *Researches on Population Ecology*, 1(1), 36–48.
- [188] Jabin, P. E. (2010). Differential equations with singular fields. *Journal de mathématiques pures et appliquées*, 94(6), 597–621.
- [189] Jia, F., Li, B., Cao, Y.-P., Xie, W.-H., & Feng, X.-Q. (2015). Wrinkling pattern evolution of cylindrical biological tissues with differential growth. *Physical Review E*, 91(1).
- [190] Jia, F., Pearce, S. P., & Goriely, A. (2018). Curvature delays growth-induced wrinkling. *Physical Review E*, 98(3), 033003.
- [191] Jin, L., Liu, Y., & Cai, Z. (2019). Post-buckling analysis on growing tubular tissues: A semi-analytical approach and imperfection sensitivity. *International Journal of Solids and Structures*, 162, 121–134.

- [192] Kalashnikov, A. S. (1967). The occurrence of singularities in solutions of the non-steady seepage equation. *USSR Computational Mathematics and Mathematical Physics*, 7(2), 269–275.
- [193] Karzbrun, E., Kshirsagar, A., Cohen, S. R., Hanna, J. H., & Reiner, O. (2018). Human brain organoids on a chip reveal the physics of folding. *Nature Physics*, 14(5), 515–522.
- [194] Kim, I. & Požár, N. (2017). Porous medium equation to hele-shaw flow with general initial density. *Transactions of the American Mathematical Society*, 370(2), 873–909.
- [195] Knops, R. J. & Payne, L. E. (2012). *Uniqueness theorems in linear elasticity*, volume 19. Springer Science & Business Media.
- [196] Kröner, E. (1959). Allgemeine kontinuumstheorie der versetzungen und eigenspannungen. *Archive for Rational Mechanics and Analysis*, 4(1), 273.
- [197] Krugman, P. (1996). *The self-organizing economy*. Number 338.9 KRU 1996. CIM-MYT.
- [198] Kumar, K. (1996). Linear theory of faraday instability in viscous liquids. *Proceedings of the Royal Society of London. Series A: Mathematical, Physical and Engineering Sciences*, 452(1948), 1113–1126.
- [199] Kumar, K. & Tuckerman, L. S. (1994). Parametric instability of the interface between two fluids. *Journal of Fluid Mechanics*, 279, 49–68.
- [200] Kumar, S. (1999). Parametrically driven surface waves in viscoelastic liquids. *Physics of Fluids*, 11(8), 1970–1981.
- [201] Kuznetsova, T. G., Starodubtseva, M. N., Yegorenkov, N. I., Chizhik, S. A., & Zhdanov, R. I. (2007). Atomic force microscopy probing of cell elasticity. *Micron*, 38(8), 824–833.
- [202] Landau, L. (1986). Em lifshitz theory of elasticity. *Course of theoretical physics*, 7.
- [203] Lee, E. H. (1968). *Elastic-Plastic deformation at finite strains*. Technical report.
- [204] Lee, E. H. (1969). Elastic-plastic deformation at finite strains. *Journal of Applied Mechanics*, 36(1), 1.
- [205] Lee, W., Kalashnikov, N., Mok, S., Halaoui, R., Kuzmin, E., Putnam, A. J., Takayama, S., Park, M., McCaffrey, L., Zhao, R., Leask, R. L., & Moraes, C. (2019). Dispersible hydrogel force sensors reveal patterns of solid mechanical stress in multicellular spheroid cultures. *Nature Communications*, 10(1).

- [206] Lellis, C. D., Rosa, A. D., & Ghiraldin, F. (2019). A direct approach to the anisotropic plateau problem. *Advances in Calculus of Variations*, 12(2), 211–223.
- [207] Li, B., Cao, Y.-P., Feng, X.-Q., & Gao, H. (2012). Mechanics of morphological instabilities and surface wrinkling in soft materials: a review. *Soft Matter*, 8(21), 5728.
- [208] Liu, J.-G., Tang, M., Wang, L., & Zhou, Z. (2019). Towards understanding the boundary propagation speeds in tumor growth models. *arXiv preprint arXiv:1910.11502*.
- [209] Liu, S. & Fung, Y. (1988). Zero-stress states of arteries. *Journal of biomechanical engineering*, 110(1), 82–84.
- [210] Liu, T., Long, R., & Hui, C.-Y. (2014). The energy release rate of a pressurized crack in soft elastic materials: effects of surface tension and large deformation. *Soft Matter*, 10(39), 7723–7729.
- [211] Logg, A., Mardal, K.-A., & Wells, G., Eds. (2012a). *Automated Solution of Differential Equations by the Finite Element Method*. Springer Berlin Heidelberg.
- [212] Logg, A., Mardal, K.-A., & Wells, G. (2012b). *Automated solution of differential equations by the finite element method: The FEniCS book*, volume 84. Springer Science & Business Media.
- [213] Lord, R. (1900). Investigation of the character of the equilibrium of an incompressible heavy fluid of variable density. *Scientific papers*, (pp. 200–207).
- [214] LORENZI, T., LORZ, A., & PERTHAME, B. (2017). On interfaces between cell populations with different mobilities. *Kinetic & Related Models*, 10(1).
- [215] Lorenzi, T., Perthame, B., & Ruan, X. (2020). Invasion fronts and adaptive dynamics in a model for the growth of cell populations with heterogeneous mobility. *arXiv preprint arXiv:2007.13084*.
- [216] Lowengrub, J. S., Frieboes, H. B., Jin, F., Chuang, Y.-L., Li, X., Macklin, P., Wise, S. M., & Cristini, V. (2009). Nonlinear modelling of cancer: bridging the gap between cells and tumours. *Nonlinearity*, 23(1), R1.
- [217] Maggi, F. (2012). *Sets of finite perimeter and geometric variational problems: an introduction to Geometric Measure Theory*. Number 135. Cambridge University Press.
- [218] Maître, J.-L., Niwayama, R., Turlier, H., Nédélec, F., & Hiiragi, T. (2015). Pulsatile cell-autonomous contractility drives compaction in the mouse embryo. *Nature Cell Biology*, 17(7), 849–855.
- [219] Manasek, F. (1976). Heart development: interactions involved in cardiac morphogenesis. *Cell surface reviews*.

- [220] Mangan, R., Destrade, M., & Saccomandi, G. (2016). Strain energy function for isotropic non-linear elastic incompressible solids with linear finite strain response in shear and torsion. *Extreme Mechanics Letters*, 9, 204–206.
- [221] Männer, J. (2000). Cardiac looping in the chick embryo: a morphological review with special reference to terminological and biomechanical aspects of the looping process. *The Anatomical Record*, 259(3), 248–262.
- [222] Männer, J. (2009). The anatomy of cardiac looping: a step towards the understanding of the morphogenesis of several forms of congenital cardiac malformations. *Clinical Anatomy: The Official Journal of the American Association of Clinical Anatomists and the British Association of Clinical Anatomists*, 22(1), 21–35.
- [223] Männer, J. & Bayraktar, M. (2014). Cardiac looping may be driven by compressive loads resulting from unequal growth of the heart and pericardial cavity. observations on a physical simulation model. *Frontiers in physiology*, 5, 112.
- [224] Männer, J., Thrane, L., Norozi, K., & Yelbuz, T. M. (2008). High-resolution in vivo imaging of the cross-sectional deformations of contracting embryonic heart loops using optical coherence tomography. *Developmental Dynamics*, 237(4), 953–961.
- [225] Manning, M. L., Foty, R. A., Steinberg, M. S., & Schoetz, E.-M. (2010). Coaction of intercellular adhesion and cortical tension specifies tissue surface tension. *Proceedings of the National Academy of Sciences*, 107(28), 12517–12522.
- [226] Mansfield, M. L. (1994). Are there knots in proteins? *Nature Structural & Molecular Biology*, 1(4).
- [227] Mellet, A., Perthame, B., & Quirós, F. (2017). A Hele-Shaw problem for tumor growth. *J. Funct. Anal.*, 273(10), 3061–3093.
- [228] Melnyk, T. W., Knop, O., & Smith, W. R. (1977). Extremal arrangements of points and unit charges on a sphere: equilibrium configurations revisited. *Canadian Journal of Chemistry*, 55(10), 1745–1761.
- [229] Midgett, M., Chivukula, V. K., Dorn, C., Wallace, S., & Rugonyi, S. (2015). Blood flow through the embryonic heart outflow tract during cardiac looping in hh13–hh18 chicken embryos. *Journal of The Royal Society Interface*, 12(111), 20150652.
- [230] Montel, F., Delarue, M., Elgeti, J., Vignjevic, D., Cappello, G., & Prost, J. (2012a). Isotropic stress reduces cell proliferation in tumor spheroids. *New Journal of Physics*, 14(5), 055008.
- [231] Montel, F., Delarue, M., Elgeti, J., Vignjevic, D., Cappello, G., Prost, J., & Joanny, J.-F. (2012b). Stress clamp experiments on multicellular tumor spheroids. *Biophysical Journal*, 102(3), 220a.

- [232] Mooney, M. (1940). A theory of large elastic deformation. *Journal of applied physics*, 11(9), 582–592.
- [233] Mora, S., Maurini, C., Phou, T., Fromental, J.-M., Audoly, B., & Pomeau, Y. (2013). Solid drops: large capillary deformations of immersed elastic rods. *Physical review letters*, 111(11), 114301.
- [234] Mora, S., Phou, T., Fromental, J.-M., Pismen, L. M., & Pomeau, Y. (2010). Capillarity driven instability of a soft solid. *Physical review letters*, 105(21), 214301.
- [235] Mora, S., Phou, T., Fromental, J.-M., & Pomeau, Y. (2014). Gravity driven instability in elastic solid layers. *Physical review letters*, 113(17), 178301.
- [236] Mora, S. & Pomeau, Y. (2015). Softening of edges of solids by surface tension. *Journal of Physics: Condensed Matter*, 27(19), 194112.
- [237] Morgan, F. (2016). *Geometric measure theory: a beginner's guide*. Academic press.
- [238] Morisita, M. (1950). Population density and dispersal of a water strider. *gerris lacustris*: Observations and considerations on animal aggregations. *Contributions on Physiology and Ecology, Kyoto University*, 65, 1–149.
- [239] Mukherjee, A. (2015). *Differential Topology*. Springer International Publishing.
- [240] Müller, H. & Zimmermann, W. (1999). Faraday instability in a linear viscoelastic fluid. *EPL (Europhysics Letters)*, 45(2), 169.
- [241] Munkres, J. R. (1963). *Elementary Differential Topology. (AM-54)*. Princeton University Press.
- [242] Norris, A. N. & Shuvalov, A. L. (2010). Wave impedance matrices for cylindrically anisotropic radially inhomogeneous elastic solids. *The Quarterly Journal of Mechanics and Applied Mathematics*, 63(4), 401–435.
- [243] Ogden, R. W. (1997). *Non-linear elastic deformations*. Courier Corporation.
- [244] Oleinik, O. A., Kalasinkov, A. S., & Czou, Y. (1958). The Cauchy problem and boundary problems for equations of the type of non-stationary filtration. *Izv. Akad. Nauk SSSR. Ser. Mat.*, 22, 667–704.
- [245] Omens, J. H. & Fung, Y. C. (1990). Residual strain in rat left ventricle. *Circulation Research*, 66(1), 37–45.
- [246] Patten, B. M. (2008). *Early embryology of the chick*. Wildside Press LLC.
- [247] Pattle, R. E. (1959). Diffusion from an instantaneous point source with a concentration-dependent coefficient. *The Quarterly Journal of Mechanics and Applied Mathematics*, 12(4), 407–409.

- [248] Pauw, T. D. (2009). Size minimizing surfaces. *Annales scientifiques de l'École normale supérieure*, 42(1).
- [249] Perthame, B., Quirós, F., Tang, M., & Vauchelet, N. (2014a). Derivation of a hele-shaw type system from a cell model with active motion. *Interfaces and Free Boundaries*, 16, 489–508.
- [250] Perthame, B., Quirós, F., & Vázquez, J.-L. (2014b). The Hele-Shaw asymptotics for mechanical models of tumor growth. *Archive for Rational Mechanics and Analysis*, 212(1), 93–127.
- [251] Perthame, B. & Vauchelet, N. (2015). Incompressible limit of a mechanical model of tumour growth with viscosity. *Phil. Trans. R. Soc. A*, 373(2050), 20140283.
- [252] Philippis, G. D., Rosa, A. D., & Ghiraldin, F. (2019). Existence results for minimizers of parametric elliptic functionals. *The Journal of Geometric Analysis*, 30(2), 1450–1465.
- [253] Plateau, J. (1869). *Recherches expérimentales et théoriques sur les figures d'équilibre d'une masse liquide sans pesanteur*, volume 391. sn.
- [254] Plateau, J. (1873). Experimental and theoretical statics of liquids subject to molecular forces only. *Gauthier-Villars, Paris*.
- [255] Preiss, D. (1987). Geometry of measures in \mathbb{R}^n : Distribution, rectifiability, and densities. *The Annals of Mathematics*, 125(3).
- [256] Preziosi, L. & Tosin, A. (2009). Multiphase modelling of tumour growth and extracellular matrix interaction: mathematical tools and applications. *Journal of mathematical biology*, 58(4-5), 625.
- [257] Price, B. & Xu, X. (2020). Global existence theorem for a model governing the motion of two cell populations. *arXiv preprint arXiv:2004.05939*.
- [258] Pucci, E. & Saccomandi, G. (2009). Parametric resonance in non-linear elastodynamics. *International Journal of Non-Linear Mechanics*, 44(5), 560–569.
- [259] Pucci, G., Fort, E., Amar, M. B., & Couder, Y. (2011). Mutual adaptation of a faraday instability pattern with its flexible boundaries in floating fluid drops. *Physical review letters*, 106(2), 024503.
- [260] Radó, T. (1930). The problem of the least area and the problem of plateau. *Mathematische Zeitschrift*, 32(1), 763–796.
- [261] Ramasubramanian, A., Capaldi, X., Bradner, S. A., & Gangi, L. (2019). On the biomechanics of cardiac s-looping in the chick: Insights from modeling and perturbation studies. *Journal of Biomechanical Engineering*, 141(5).

- [262] Ramasubramanian, A., Chu-Lagraff, Q. B., Buma, T., Chico, K. T., Carnes, M. E., Burnett, K. R., Bradner, S. A., & Gordon, S. S. (2013). On the role of intrinsic and extrinsic forces in early cardiac s-looping. *Developmental Dynamics*, 242(7), 801–816.
- [263] Ramasubramanian, A., Latacha, K. S., Benjamin, J. M., Voronov, D. A., Ravi, A., & Taber, L. A. (2006). Computational model for early cardiac looping. *Annals of biomedical engineering*, 34(8), 1355–1369.
- [264] Ranft, J., Basana, M., Elgeti, J., Joanny, J., Prost, J., & Jülicher, F. (2010). Fluidization of tissues by cell division and apoptosis. *Natl. Acad. Sci. USA*, 49, 657–687.
- [265] Rayleigh, L. (1879). On the capillary phenomena of jets. *Proc. R. Soc. London*, 29(196-199), 71–97.
- [266] Rayleigh, L. (1883). Vii. on the crispations of fluid resting upon a vibrating support. *The London, Edinburgh, and Dublin Philosophical Magazine and Journal of Science*, 16(97), 50–58.
- [267] Raynal, F., Kumar, S., & Fauve, S. (1999). Faraday instability with a polymer solution. *The European Physical Journal B-Condensed Matter and Complex Systems*, 9(2), 175–178.
- [268] Reifenberg, E. R. (1960). Solution of the plateau problem for m -dimensional surfaces of varying topological type. *Bulletin of the American Mathematical Society*, 66(4).
- [269] Ribba, B., Saut, O., Colin, T., Bresch, D., Grenier, E., & Boissel, J.-P. (2006). A multiscale mathematical model of avascular tumor growth to investigate the therapeutic benefit of anti-invasive agents. *Journal of theoretical biology*, 243(4), 532–541.
- [270] Riccobelli, D., Agosti, A., & Ciarletta, P. (2019). On the existence of elastic minimizers for initially stressed materials. *Philosophical Transactions of the Royal Society A: Mathematical, Physical and Engineering Sciences*, 377(2144), 20180074.
- [271] Riccobelli, D. & Bevilacqua, G. (2020). Surface tension controls the onset of gyrfication in brain organoids. *Journal of the Mechanics and Physics of Solids*, 134, 103745.
- [272] Riccobelli, D. & Ciarletta, P. (2017). Rayleigh–Taylor instability in soft elastic layers. *Philosophical Transactions of the Royal Society A: Mathematical, Physical and Engineering Sciences*, 375(2093), 20160421.
- [273] Riccobelli, D. & Ciarletta, P. (2018a). Morpho-elastic model of the tortuous tumour vessels. *International Journal of Non-Linear Mechanics*, 107, 1–9.
- [274] Riccobelli, D. & Ciarletta, P. (2018b). Shape transitions in a soft incompressible sphere with residual stresses. *Mathematics and Mechanics of Solids*, 23(12), 1507–1524.

- [275] Rivlin, R. (1948). Large elastic deformations of isotropic materials iv. further developments of the general theory. *Philosophical Transactions of the Royal Society of London. Series A, Mathematical and Physical Sciences*, 241(835), 379–397.
- [276] Rodriguez, E. K., Hoger, A., & McCulloch, A. D. (1994a). Stress-dependent finite growth in soft elastic tissues. *Journal of Biomechanics*, 27(4), 455–467.
- [277] Rodriguez, E. K., Hoger, A., & McCulloch, A. D. (1994b). Stress-dependent finite growth in soft elastic tissues. *Journal of biomechanics*, 27(4), 455–467.
- [278] Rolfsen, D. (2003). *Knots and Links*. American Mathematical Society.
- [279] Roman, B. & Bico, J. (2010). Elasto-capillarity: deforming an elastic structure with a liquid droplet. *Journal of Physics: Condensed Matter*, 22(49), 493101.
- [280] Ronan, L., Voets, N., Rua, C., Alexander-Bloch, A., Hough, M., Mackay, C., Crow, T. J., James, A., Giedd, J. N., & Fletcher, P. C. (2013). Differential tangential expansion as a mechanism for cortical gyrification. *Cerebral Cortex*, 24(8), 2219–2228.
- [281] Rosa, A. D. (2018). Minimization of anisotropic energies in classes of rectifiable varifolds. *SIAM Journal on Mathematical Analysis*, 50(1), 162–181.
- [282] Sabinina, E. S. (1961). On the cauchy problem for the equation of nonstationary gas filtration in several space variables. volume 136 (pp. 1034–1037).: Russian Academy of Sciences.
- [283] Sands, D. E. (1993). *Introduction to crystallography*. Courier Corporation.
- [284] Saye, R. I. & Sethian, J. A. (2013). Multiscale modeling of membrane rearrangement, drainage, and rupture in evolving foams. *Science*, 340(6133), 720–724.
- [285] Schötz, E.-M., Burdine, R. D., Jülicher, F., Steinberg, M. S., Heisenberg, C.-P., & Foty, R. A. (2008). Quantitative differences in tissue surface tension influence zebrafish germ layer positioning. *HFSP journal*, 2(1), 42–56.
- [286] Schuricht (2002). Global injectivity and topological constraints for spatial nonlinearly elastic rods. *Journal of Nonlinear Science*, 12(5).
- [287] Schütte, K. & Van der Waerden, B. (1951). Auf welcher kugel haben 5, 6, 7, 8 oder 9 punkte mit mindestabstand eins platz? *Mathematische Annalen*, 123(1), 96–124.
- [288] Shao, X., Bevilacqua, G., Ciarletta, P., Saylor, J., & Bostwick, J. (2020). Experimental observation of faraday waves in soft gels. *Physical Review E*, 102(6), 060602.
- [289] Shao, X., Saylor, J., & Bostwick, J. (2018). Extracting the surface tension of soft gels from elastocapillary wave behavior. *Soft matter*, 14(36), 7347–7353.

- [290] Sharzehee, M., Fatemifar, F., & Han, H.-C. (2019). Computational simulations of the helical buckling behavior of blood vessels. *International Journal for Numerical Methods in Biomedical Engineering*, 35(12), e3277.
- [291] Shi, Y., Yao, J., Xu, G., & Taber, L. A. (2014a). Bending of the looping heart: differential growth revisited. *Journal of biomechanical engineering*, 136(8), 081002.
- [292] Shi, Y., Yao, J., Young, J. M., Fee, J. A., Perucchio, R., & Taber, L. A. (2014b). Bending and twisting the embryonic heart: a computational model for c-looping based on realistic geometry. *Frontiers in physiology*, 5, 297.
- [293] Skalak, R., Dasgupta, G., Moss, M., Otten, E., Dullemeijer, P., & Vilmann, H. (1982). Analytical description of growth. *Journal of theoretical biology*, 94(3), 555–577.
- [294] Soofi, S. S., Last, J. A., Liliensiek, S. J., Nealey, P. F., & Murphy, C. J. (2009). The elastic modulus of matrigel™ as determined by atomic force microscopy. *Journal of Structural Biology*, 167(3), 216–219.
- [295] Srivastava, D. & Olson, E. N. (1997). Knowing in your heart what’s right. *Trends in Cell Biology*, 7(11), 447–453.
- [296] Steinberg, M. S. (1963). Reconstruction of tissues by dissociated cells. *Science*, 141(3579), 401–408.
- [297] Stroh, A. N. (1962). Steady state problems in anisotropic elasticity. *Journal of Mathematics and Physics*, 41(1-4), 77–103.
- [298] Style, R. W., Hyland, C., Boltyskiy, R., Wettlaufer, J. S., & Dufresne, E. R. (2013). Surface tension and contact with soft elastic solids. *Nature Communications*, 4(1).
- [299] Style, R. W., Jagota, A., Hui, C.-Y., & Dufresne, E. R. (2017). Elastocapillarity: Surface tension and the mechanics of soft solids. *Annual Review of Condensed Matter Physics*, 8(1), 99–118.
- [300] Taber, L. A. (2003). Biophysical mechanisms of cardiac looping. *International Journal of Developmental Biology*, 50(2-3), 323–332.
- [301] Taber, L. A., Lin, I.-E., & Clark, E. B. (1995). Mechanics of cardiac looping. *Developmental Dynamics*, 203(1), 42–50.
- [302] Taber, L. A., Voronov, D. A., & Ramasubramanian, A. (2010). The role of mechanical forces in the torsional component of cardiac looping. *Annals of the New York Academy of Sciences*, 1188, 103.

- [303] Taffetani, M. & Ciarletta, P. (2015a). Beading instability in soft cylindrical gels with capillary energy: weakly non-linear analysis and numerical simulations. *Journal of the Mechanics and Physics of Solids*, 81, 91–120.
- [304] Taffetani, M. & Ciarletta, P. (2015b). Elastocapillarity can control the formation and the morphology of beads-on-string structures in solid fibers. *Physical Review E*, 91(3).
- [305] Tallinen, T., Chung, J. Y., Biggins, J. S., & Mahadevan, L. (2014). Gyration from constrained cortical expansion. *Proceedings of the National Academy of Sciences*, 111(35), 12667–12672.
- [306] Tammes, P. M. L. (1930). On the origin of number and arrangement of the places of exit on the surface of pollen-grains. *Recueil des travaux botaniques néerlandais*, 27(1), 1–84.
- [307] Tanaka, T., Sun, S.-T., Hirokawa, Y., Katayama, S., Kucera, J., Hirose, Y., & Amiya, T. (1987). Mechanical instability of gels at the phase transition. *Nature*, 325(6107), 796–798.
- [308] Taylor, G. I. (1950). The instability of liquid surfaces when accelerated in a direction perpendicular to their planes. i. *Proceedings of the Royal Society of London. Series A. Mathematical and Physical Sciences*, 201(1065), 192–196.
- [309] Taylor, J. E. (1976). The structure of singularities in soap-bubble-like and soap-film-like minimal surfaces. *Annals of Mathematics*, (pp. 489–539).
- [310] Terpstra, F. J. (1939). Die darstellung biquadratischer formen als summen von quadraten mit anwendung auf die variationsrechnung. *Mathematische Annalen*, 116(1), 166–180.
- [311] Thomas, L. F. & Harri-Augstein, E. S. (1985). *Self-organised learning: Foundations of a conversational science for psychology*. Routledge Kegan & Paul.
- [312] Thomson, W. (1887). On the division of space with minimum partitional area. *The London, Edinburgh, and Dublin Philosophical Magazine and Journal of Science*, 24(151), 503–514.
- [313] Truesdell, C. (1966). Rational mechanics of materials. In *Six Lectures on Modern Natural Philosophy* (pp. 1–22). Springer.
- [314] Truesdell, C. & Noll, W. (2004). The non-linear field theories of mechanics. In *The non-linear field theories of mechanics* (pp. 1–579). Springer.
- [315] Turlier, H. & Maître, J.-L. (2015). Mechanics of tissue compaction. *Seminars in Cell & Developmental Biology*, 47-48, 110–117.

- [316] Vázquez, J.-L. (2007). *The porous medium equation: mathematical theory*. Oxford University Press.
- [317] Voronov, D. A., Alford, P. W., Xu, G., & Taber, L. A. (2004). The role of mechanical forces in dextral rotation during cardiac looping in the chick embryo. *Developmental biology*, 272(2), 339–350.
- [318] Voronov, D. A. & Taber, L. A. (2002). Cardiac looping in experimental conditions: effects of extraembryonic forces. *Developmental dynamics: an official publication of the American Association of Anatomists*, 224(4), 413–421.
- [319] Wagner, C., Müller, H., & Knorr, K. (1999). Faraday waves on a viscoelastic liquid. *Physical review letters*, 83(2), 308.
- [320] Weaire, D. & Phelan, R. (1994). A counter-example to Kelvin’s conjecture on minimal surfaces. *Philosophical Magazine Letters*, 69(2), 107–110.
- [321] Weaire, D., Vaz, M., Teixeira, P., & Fortes, M. (2007). Instabilities in liquid foams. *Soft Matter*, 3(1), 47–57.
- [322] Weaire, D. L. & Hutzler, S. (2001). *The physics of foams*. Oxford University Press.
- [323] West, D. B. et al. (2001). *Introduction to graph theory*, volume 2. Prentice hall Upper Saddle River.
- [324] Xie, J. P., Liu, S. Q., Yang, R. F., & Fung, Y. C. (1991). The zero-stress state of rat veins and vena cava. *Journal of Biomechanical Engineering*, 113(1), 36–41.
- [325] Xuan, C. & Biggins, J. (2016). Finite-wavelength surface-tension-driven instabilities in soft solids, including instability in a cylindrical channel through an elastic solid. *Physical Review E*, 94(2).
- [326] Yang, X.-S., Deb, S., Loomes, M., & Karamanoglu, M. (2013). A framework for self-tuning optimization algorithm. *Neural Computing and Applications*, 23(7-8), 2051–2057.
- [327] Ye, S., Yin, S.-F., Li, B., & Feng, X.-Q. (2019). Torsion instability of anisotropic cylindrical tissues with growth. *Acta Mechanica Solida Sinica*, 32(5), 621–632.
- [328] Zamir, E. A. & Taber, L. A. (2004). Material properties and residual stress in the stage 12 chick heart during cardiac looping. *Journal of Biomechanical Engineering*, 126(6), 823–830.
- [329] Zel’dovich, I. B. & Raizer, I. P. (1966). *Physics of shock waves and high-temperature phenomena*.

- [330] Zhang, B., Lee, F. K., Tsui, O. K., & Sheng, P. (2003). Liquid crystal orientation transition on microtextured substrates. *Physical review letters*, 91(21), 215501.
- [331] Zhu, Y., Luo, X., & Ogden, R. W. (2008). Asymmetric bifurcations of thick-walled circular cylindrical elastic tubes under axial loading and external pressure. *International Journal of Solids and Structures*, 45(11-12), 3410–3429.